

Optimal Strain Gage Locations for Experimental Determination of Stress Intensity Factors

**A Thesis Submitted
In Partial Fulfillment of the Requirements
for the Degree of**

DOCTOR OF PHILOSOPHY

by

Hrushikesh Sarangi

(08610307)



**Department of Mechanical Engineering
Indian Institute of Technology Guwahati
Guwahati-781 039, India
July, 2012**



Certificate

It is certified that the work contained in the Thesis entitled “**Optimal Strain Gage Locations for Experimental Determination of Stress Intensity Factors**” submitted by **Hrushikesh Sarangi** to the Indian Institute of Technology Guwahati for the award of the degree of Doctor of Philosophy has been carried out under our supervision in the Department of Mechanical Engineering, Indian Institute of Technology Guwahati. This work has not been submitted elsewhere for the award of any other degree.

4th July 2012

(K. S. R. Krishna Murthy)

Associate Professor
Department of Mechanical Engineering
Indian Institute of Technology Guwahati
Guwahati – 781 039

(Debabrata Chakraborty)

Professor
Department of Mechanical Engineering
Indian Institute of Technology Guwahati
Guwahati – 781 039



Dedicated to my parents

Father : Late Khetrabasi Sarangi

Mother : Late Sukadevi Sarangi

&
my sister

Late Sushama Pani

Acknowledgements

This thesis is the result of four years of work whereby I have been accompanied and supported by many people. It is a pleasant aspect that I have now the opportunity to express my gratitude for all of them.

I would like to express my greatest appreciation to my supervisors Dr K. S. R. K. Murthy and Dr Debabrata Chakraborty Department of Mechanical Engineering Department, IIT Guwahati for their professional guidance, valuable academic advice, encouragement and strong support during the doctoral degree course and the writing of this thesis. The research hadn't been possible without their support. I would also sincerely thank Prof P. S. Robi, for his valuable suggestions in my experimental work.

I would like to thanks my doctoral committee members, Prof S. K. Dwivedy, Prof S. Talukdar and Prof S. Senthilvelan for their valuable discussions.

I am grateful to all the faculty members of Mechanical Engineering Department of IIT Guwahati for giving me a comfortable and active environment for pursuing my research work. I am grateful to Wokshop Superintendent Mr. D. K. Sharma, and other technical staff of mechanical workshop Mr Nidul Saikia, Mr Lakhinath Gogoi, Mr Mrinal Sharma, Indian Institute of Technology Guwahati for their help for preparation of specimens. I would like to express my special thanks to Mr Sanjib Sharma and Mr Rituraj Saikia for helping me lot at the time of conducting experiments and also thanks Sajit, Amrita and all research scholars of Mechanical Engineering Department, Indian Institute of Technology Guwahati. I am also thankful to Mr. Pranjol Paul for assistance during the final thesis preparation.

I am really grateful to my wife, Mrs Shipra Sarangi for her constant encouragement and moral support during my research work. I am also very grateful to my elder brother Mr Kailash Chandra Sarangi who always inspires me from my childhood for higher study absorbing himself any problem and financial burden. I would like thank my son Master Priyanshu Sarangi who always asks me date of completion of this work. I would like to thank for financial support provided by the Naval Research Board (NRB), Ministry of Defence, India under Grant Number NRB-167/MAT/08-09 for my experimental work. At last but not least I am also grateful to QIP centre, Indian Institute of Technology Guwahati for providing financial support for my PhD programme.

4th July 2012
IIT Guwahati

Hrushikesh Sarangi



Contents

<i>Abstract</i>	vii
<i>Nomenclature</i>	ix
<i>List of Figures</i>	xi
<i>List of Tables</i>	xix
1 Introduction	1
1.1 Introduction to fracture mechanics	1
1.2 Importance of fracture mechanics approach to design	4
1.3 Methods of analysis: Linear elastic fracture mechanics	5
1.4 Elastic plastic fracture mechanics	6
1.5 Fracture mechanics parameters	6
1.5.1 Strain energy release rate	7
1.5.2 Stress intensity factor	7
1.5.3 J - integral	8
1.5.4 Crack opening displacement	8
1.6 Stress intensity factors for different modes of loading	8
1.7 Methods for the determination of stress intensity factors	10
1.7.1 Analytical methods	10
1.7.2 Numerical methods	11
1.7.3 Experimental methods	11
1.7.3.1 The method of caustics	12
1.7.3.2 Moire interferometry	12
1.7.3.3 Photoelasticity	13
1.7.3.4 Electrical resistance strain gage	13
1.8 Principle of operation of the electrical resistance strain gage	14

1.9	Bonded metallic foil strain gages	15
1.10	Motivation	17
1.11	Organization of the thesis	18
2	Literature review	20
2.1	Strain gage techniques for determination of mode I SIF	20
2.2	Strain gage techniques for determination of mode II SIFs	29
2.3	Strain gage techniques for determination of mixed mode (I/II) SIFs	30
2.4	Summary of literature review and objectives	33
3	Theoretical background and formulations	36
3.1	The generalized Westergaard approach	36
3.1.1	Leading terms for mode I loading	40
3.1.2	Leading terms for mode II loading	41
3.2	Dally and Sanford [22] technique for the determination of K_I	42
3.3	Proposed approach for the determination of optimal radial locations for strain gages for the determination of K_I	46
3.4	Dally and Berger [51] strain gage technique for determination of mixed mode SIFs K_I and K_{II}	50
3.5	Proposed modified Dally and Berger technique	56
3.6	Determination of maximum permissible radial location r_{\max} in mixed mode (I/II)	65
3.7	Finite element formulation	68
3.7.1	Eight noded quadrilateral element	69
3.7.2	Quarter point elements (QPEs)	73
3.7.3	Collapsed six-noded triangle quarter point elements	73
3.8	Summary	75

4	Determination of r_{\max} for Mode I Cases	76
4.1	Determination and convergence of r_{\max} for the center cracked plates	76
4.2	Effect of a/b ratio on r_{\max}	82
4.3	An in-depth investigation on dependence of r_{\max} on a/b of center cracked plates	85
4.4	Effect of Poisson's ratio on r_{\max}	89
4.5	Determination of r_{\max} for edge cracked plates	90
4.6	Effect of the crack length and proximity of boundary on the r_{\max}	95
4.7	Effect of state of stress on r_{\max}	99
4.8	Determination of r_{\max} for double edge cracked plates	101
4.9	Eccentric center cracked plate subjected to uniform tensile stress	103
4.10	Verification of gage locations used by earlier researchers [22, 33, 35, 39, 56]	107
4.11	Summary	110
5	Determination of r_{\max} for Mixed mode Cases	112
5.1	Problem definition	112
5.2	Determination of the r_{\max} for slant edge cracked plate	113
5.3	Validation of the present approach for determination of coefficients	124
5.4	Numerical validation of modified DB technique	129
5.5	Influence of a/b ratio on the r_{\max}	131
5.6	Effect of state of stress on r_{\max}	138
5.7	Summary	140
6	Experimental verification	141
6.1	Description of the test specimen	141
6.2	Experimental determination of material properties of PMMA	144

6.3	Experimental verification of optimal strain gage locations	150
6.3.1	Numerical evaluation of r_{\max} for mode I experimental specimen	151
6.3.2	Numerical evaluation of r_{\max} for mixed mode experimental specimen	155
6.3.3	Details of experiments	158
6.3.4	Experimental results for verification of optimal strain gage locations in mode I	163
6.3.4.1	Results for $a/b = 0.293$	165
6.3.4.2	Results for $a/b = 0.493$	171
6.3.4.3	Results for $a/b = 0.693$	177
6.3.5	Experimental results for verification of optimal strain gage locations in mixed mode (I/II)	182
6.4	Summary	197
7	Conclusions and Scope for the Future Work	199
7.1	General conclusions	199
7.2	Specific conclusions	200
7.2.1	Conclusions based on numerical analysis of mode I configurations	200
7.2.2	Conclusions based on numerical analysis of mixed-mode configurations	201
7.2.3	Conclusions based on experiments on mode I configurations	202
7.2.4	Conclusions based on experiments on mixed mode (I/II) configurations	203
7.3	Scope for future work	205
	References	206
	List of Publications from this thesis	213
	About the Author	215

Abstract

Stress intensity factor (SIF) is an important parameter in linear elastic fracture mechanics as its limiting value decides whether an existing crack in a component grows or not. Use of linear elastic fracture mechanics principles in predicting and preventing fracture of engineering components largely depends on the availability of accurate values of SIF. Among all the experimental techniques, strain gage techniques are relatively inexpensive, simple and easy to use for the determination of the SIFs. However, the location and orientation of strain gage(s) with respect to the crack tip are extremely important for accurate determination of SIFs using strain gages. Strain gages placed either very near or very far from the crack tip might lead to inaccurate determination of SIFs due to local effects near the crack tip or incorrect representation of the strain field respectively. The present work proposes methodologies for accurate estimation of maximum permissible radial location (r_{\max}) of strain gage (s) in both mode I and mixed mode I/II, which ensures optimal strain gage locations for accurate determination of SIFs. A finite element based approach supported by strong theoretical formulations has been proposed for accurate estimation of r_{\max} for different mode I and mixed mode experimental specimens. Further, a modified strain gage technique for experimental determination of mixed mode SIFs has also been proposed in the present investigation. The effect of crack length, net ligament length, Poisson's ratio and state of stress on the r_{\max} have been investigated in this work. Finally, the experimental verification of the theory and methodologies proposed in the present investigation has also been carried out by conducting number of experiments on both mode I and mixed mode specimens. Experimental investigations show that very accurate values of SIFs could be obtained when the strain gage(s) are placed optimally (within the r_{\max} , obtained using the proposed methodologies). It was also observed from the results of present experiments that the error in SIFs was very high when the gage(s) were not placed within the recommended value of r_{\max} , thereby reinforcing the importance of knowing the r_{\max} in experimental determination of SIFs using strain gages. The experimental results also confirm the dependence of r_{\max} on crack length and net ligament length as predicted by the proposed methodology.



Nomenclature

a	crack length
$b, 2b$	width of the plate
e	eccentricity
E	Young's modulus
G	Shear modulus
h	half height of the plate
r	radial distance from the crack tip
t	thickness
x, y	x and y coordinates of a point
z	complex variable
A_n, B_m	coefficients of series type complex analytic functions for mode I
C_n, D_m	coefficients of series type complex analytic functions for mode II
F_I	normalized stress intensity factors opening mode
F_{II}	normalized stress intensity factors shearing mode
K_I	mode I stress intensity factor
K_{II}	mode II stress intensity factor
K_{III}	mode III stress intensity factor
r_{\max}	upper limit for gage locations
r_{\min}	minimum radial distance
Z_I, Y_I	complex analytic functions for mode I
Z_{II}, Y_{II}	complex analytic functions for mode II
r_{\max}^+	upper limit for gage locations along the positive gage line
r_{\max}^-	upper limit for gage locations along the negative gage line
α	orientation angle of strain gage
ν	Poisson's ratio
θ	angular coordinate
$+\theta$	orientation of positive gage line with the crack axis

$-\theta$	orientation of negative gage line with the crack axis
ϕ_I	Airy stress function for mode I
ϕ_{II}	Airy stress function for mode II
σ_x	normal stress in x direction
σ_y	normal stress in y direction
τ_{xy}	shear stress in x - y plane
ϵ_x	normal strain in x direction
ϵ_y	normal strain in y direction
ϵ_{aa}	normal strain in positive direction of θ and α
ϵ_{bb}	normal strain in negative direction of θ and α
γ_{xy}	shear strain in x - y plane
CT	compact tension specimen
2D	two-dimensional
3D	three-dimensional
DS technique	Dally and Sanford single strain gage technique
DB technique	Dally and Berger multi strain gage mixed mode technique
FE	finite element
FEA	finite element analysis
SECP	slant edge cracked plate
Q8	eight noded isoparametric quadrilateral element
QPE	quarter point element
SIF	stress intensity factor
TBP	three point bend specimen

List of Figures

1.1	Three types of loading	9
1.2	Typical foil strain gage	15
1.3	Location of strain gage from the crack tip	17
3.1	The complex plane at the crack tip	37
3.2	Different zones at the crack tip [22]	43
3.3	Strain gage location and orientation	44
3.4	Gage lines and strain gage location for mode I	45
3.5	(a) Plot of $\ln(\varepsilon_{aa})$ versus $\ln(r)$ (b) linear and non-linear variation of $\ln(\varepsilon_{aa})$ and $\ln(r)$ along the gage line	48
3.6	Strain gage location and orientation for mixed mode	51
3.7	Gage lines and strain gage locations for mixed mode	55
3.8	Extrapolation technique for determination of A_0 and C_0	56
3.9	Proposed gage locations for a mixed mode cracked body	62
3.10	Eight noded quadrilateral isoparametric element represented in natural coordinates	69
3.11	Six noded quadrilateral isoparametric element with mid-side nodes at the quarter point [52]	74
4.1	(a) center cracked plate; (b) solution domain for the center cracked plate	77
4.2	Different finite element meshes used for the convergence study of r_{\max} of the center cracked specimen with $a/b = 0.2$.	78
4.3	Different finite element meshes used for the convergence study of r_{\max} of the center cracked specimen with $a/b = 0.5$.	79
4.4	Linear and nonlinear variation of $\ln(\varepsilon_{aa})$ with $\ln(r)$ along the gage line for the sequence of meshes of center cracked plate with $a/b = 0.2$	79

4.5	Linear and nonlinear variation of $\ln(\varepsilon_{aa})$ with $\ln(r)$ along the gage line for the sequence of meshes of center cracked plate with $a/b = 0.5$.	80
4.6	Percent relative error in computed values of $\ln(\varepsilon_{aa})$ for the center cracked configurations (a) $a/b = 0.2$ and (b) $a/b = 0.5$.	81
4.7	Finite element meshes for the center cracked plate employed to study the effect of a/b on r_{\max} .	83
4.8	Variation of $\ln(\varepsilon_{aa})$ with $\ln(r)$ along the gage-line for the center cracked plates with different values of a/b	84
4.9	Graph of the r_{\max} as a function of a/b for the center cracked plate	85
4.10	Finite element meshes for the center cracked plates used to study the effect of the crack length a on the r_{\max} .	86
4.11	Graph of $\ln(\varepsilon_{aa})$ versus $\ln(r)$ showing variation of the r_{\max} with the crack length when the boundary effects are absent.	86
4.12	Finite element meshes for the center cracked plates employed to study the effect of net ligament length on r_{\max} .	88
4.13	Graph of $\ln(\varepsilon_{aa})$ versus $\ln(r)$ showing variation of the r_{\max} with the net ligament length $(b - a)$	88
4.14	Graph of $\ln(\varepsilon_{aa})$ versus $\ln(r)$ showing variation of the r_{\max} with the Poisson's ratio ν .	90
4.15	(a) A typical edge cracked plate (b) solution domain for edge cracked plate	91
4.16	(a) Typical mesh used for edge cracked plate (b) enlarged view at the crack tip corresponding mesh	92
4.17	Variation of $\ln(\varepsilon_{aa})$ with $\ln(r)$ along the gage line for the edge cracked plates	93
4.18	Graph of the r_{\max} as a function of a/b (0.1-0.8) for the edge cracked plate	95

4.19	Variation of $\ln(\varepsilon_{aa})$ with $\ln(r)$ along the gage line for the edge cracked plates under plane stress condition with $a/b = 0.00625$ to 0.05	96
4.20	Variation of r_{\max} with a/b (0.00625 to 0.8) for edge cracked plates under plane stress condition	96
4.21	Variation of $\ln(\varepsilon_{aa})$ with $\ln(r)$ along the gage line for the edge cracked plates under plane strain conditions	99
4.22	Comparison of plane stress and plane strain r_{\max} values for the edge cracked plate	100
4.23	(a) Double edge cracked plate (b) solution domain for the double edge cracked plate	101
4.24	(a) Typical mesh used for double edge cracked plate (b) enlarged view at the crack tip corresponding mesh	102
4.25	Variation of $\ln(\varepsilon_{aa})$ with $\ln(r)$ along the gage line for the double edge cracked plates with $a/b = 0.2$ to 0.7	102
4.26	(a) Eccentric cracked plate; (b) solution domain for eccentric cracked plate	104
4.27	(a) Typical mesh used for eccentric cracked plate (b) enlarged view at the crack tip corresponding mesh	104
4.28	Variation of $\ln(\varepsilon_{aa})$ with $\ln(r)$ along the right gage line for 15% eccentricity ratio.	105
4.29	Variation of $\ln(\varepsilon_{aa})$ with $\ln(r)$ along the left gage line for 15% eccentricity ratio	105
4.30	Geometry of mode I specimens (a) TPB (b) CT (c) Edge/Dog bone specimen	107
4.31	Finite element meshes for numerical analysis	108
4.32	Plots showing the used strain gage locations by the earlier workers and their corresponding r_{\max} values for (a) CT specimen in Ref. [22] (b) Dog bone specimen in Ref. [33] (c) TPB specimen in Ref. [33] (d) Edge cracked plate specimen in Ref. [39] and (e) TPB specimen in Ref. [56]	109

5.1	(a) Geometry of SECP subjected to uniform tension (b) typical mesh used in the present investigation for FEA (c) enlarged view at the crack tip region with the gage lines.	113
5.2	SECP with $a/b = 0.5$: (a) determination of A_0, A_2 and B_1 using the best-fit linear regression (b) determination of C_0, C_1 and C_2 using the best-fit linear regression	115
5.3	SECP with $a/b = 0.5$: (a) Plot of $E\varepsilon_{aa}$ versus r on the positive gage line (b) determination of r_{\max}^+ for the positive gage line (c) Plot of $E\varepsilon_{bb}$ versus r on the negative gage line (d) determination of r_{\max}^- for the negative gage line (e) % relative error in FE solutions of $E\varepsilon_{aa}$ and (f) % relative error in FE solutions of $E\varepsilon_{bb}$	116
5.4	Different finite element meshes used for the convergence study of r_{\max} of SECP specimen with $a/b = 0.5$	119
5.5	SECP with $a/b = 0.5$ coarse mesh (a) determination of A_0, A_2 and B_1 using the best fit linear regression (b) determination of C_0, C_1 and C_2 using the best fit linear regression.	120
5.6	SECP with $a/b = 0.5$ coarse mesh (a) determination of r_{\max}^+ for the positive gage line (b) determination of r_{\max}^- for the negative gage line	121
5.7	SECP with $a/b = 0.5$ medium mesh (a) determination of A_0, A_2 and B_1 using the best fit linear regression (b) determination of C_0, C_1 and C_2 using the best fit linear regression	122
5.8	SECP with $a/b = 0.5$ medium mesh (a) determination of r_{\max}^+ for the positive gage line (b) determination of r_{\max}^- for the negative gage line	123
5.9	(a) Geometry of SECP subjected to uniform tension (b) mesh used for FEA	124

5.10	(a) determination of A_0, A_2 and B_1 using the best fit linear regression (b) determination of C_0, C_1 and C_2 using the best fit linear regression.	125
5.11	Validation of the present approach for determination of coefficients: (a) comparison of ε_{aa} along the positive gage line (b) comparison of ε_{bb} along the negative gage line	127
5.12	Comparison of errors due to the coefficients: (a) percentage relative error in ε_{aa} along the positive gage line (b) percentage relative error in ε_{bb} along the negative gage line	128
5.13	Simulation of the proposed modified Dally and Berger's method for SECP with $a/b = 0.5$: (a) best fit to the simulated data along the positive gage line (b) best fit plot to the simulated data along the negative gage line	130
5.14	Results for determination of the r_{\max} for SECP with $a/b = 0.3$: (a) determination of A_0, A_2 and B_1 (b) determination of C_0, C_1 and C_2 (c) determination of r_{\max}^+ for the positive gage line (d) determination of r_{\max}^- for the negative gage line	132
5.15	SECP with $a/b = 0.2$: (a) determination of A_0, A_2 and B_1 (b) determination of C_0, C_1 and C_2 (c) determination of r_{\max}^+ for the positive gage line (d) determination of r_{\max}^- for the negative gage line	133
5.16	SECP with $a/b = 0.4$: (a) determination of A_0, A_2 and B_1 (b) determination of C_0, C_1 and C_2 (c) determination of r_{\max}^+ for the positive gage line (d) determination of r_{\max}^- for the negative gage line	134
5.17	SECP with $a/b = 0.6$: (a) determination of A_0, A_2 and B_1 (b) determination of C_0, C_1 and C_2 (c) determination of r_{\max}^+ for the positive gage line (d) determination of r_{\max}^- for the negative gage line	135

5.18	Results for determination of the r_{\max} for SECP with $a/b = 0.7$: (a) determination of A_0, A_2 and B_1 ; (b) determination of C_0, C_1 and C_2 ; (c) determination of r_{\max}^+ for the positive gage line; (d) determination of r_{\max}^- for the negative gage line	136
5.19	SECP with $a/b = 0.8$: (a) determination of A_0, A_2 and B_1 ; (b) determination of C_0, C_1 and C_2 ; (c) determination of r_{\max}^+ for the positive gage line (d) determination of r_{\max}^- for the negative gage line	137
5.20	Plot of the r_{\max}/b as a function of a/b for plane stress condition	138
5.21	Comparison of the r_{\max}/b between plane stress and plane strain conditions as a function of a/b	139
6.1	(a) A typical mode I specimen; (b) mixed mode specimen	142
6.2	(a) Optical microscope setup; (b) enlarged view at crack tip	143
6.3	ASTM D638 specimen with extensometer setup	145
6.4	Rectangular specimens pasted with strain gages	146
6.5	Cantilever beam testing setup	146
6.6	Tensile testing data of case 1 specimen (ASTM D638 specimen)	147
6.7	Tensile testing data of case 2 specimen (rectangular specimen)	148
6.8	Tensile testing data of case 3 specimen (rectangular specimen)	149
6.9	Symmetric boundary conditions for mode I specimens	152
6.10	Finite element meshes of different mode I specimens	152
6.11	Plot of $\ln(\varepsilon_{aa})$ versus $\ln(r)$ for different mode I specimens	153
6.12	Variation of r_{\max} as a function of a/b	154
6.13	(a) Analysis domain for SECP specimen with boundary conditions and ; (b) Finite element discretization of the mixed mode specimen	156

6.14	SECP with $a/b = 0.497$ (a) determination of A_0, A_2 and B_1 using the best-fit linear regression; (b) determination of C_0, C_1 and C_2 using the best-fit linear regression	156
6.15	SECP with $a/b = 0.497$ (a) determination of r_{\max}^+ for the positive gage line; (b) determination of r_{\max}^- for the negative gage line	157
6.16	A typical 1 mm gage length, pre-wired TML strain gage	159
6.17	Profile projector for verification of orientation and location of a strain gage	160
6.18	DAQ assistant of LabVIEW programming for a typical experiment	161
6.19	Specimen with the spacer blocks in clevis	161
6.20	Checking of alignment of a specimen using plumb	162
6.21	Photograph of complete experimental setup	162
6.22	Photograph of different mode I specimens	164
6.23	Measured strain (ε_{aa}) at $r_1 = 10$ mm for $a/b = 0.293$ for three repeated tests	166
6.24	Measured strain (ε_{aa}) at $r_2 = 30$ mm for $a/b = 0.293$ for three repeated tests	167
6.25	Measured strain (ε_{aa}) at $r_1 = 17.5$ mm for $a/b = 0.493$ for three repeated tests	172
6.26	Measured strain (ε_{aa}) at $r_2 = 35$ mm for $a/b = 0.493$ for three repeated tests	173
6.27	Measured strain (ε_{aa}) at $r_3 = 50$ mm for $a/b = 0.493$ for three repeated tests	174
6.28	Measured strain (ε_{aa}) at $r_1 = 7$ mm for $a/b = 0.693$ for all the three repeated tests	178
6.29	Measured strain (ε_{aa}) at $r_2 = 27$ mm for $a/b = 0.693$ for all the three repeated tests	179

6.30	Photograph of mixed mode specimen	183
6.31	Measured strains (ε_{aa}) at r_1 on the positive gage line versus applied load for all the six repeated tests	185
6.32	Measured strain (ε_{aa}) versus applied load at different radii r_2 to r_6 on the positive gage line for the 1 st test	186
6.33	Measured strains (ε_{bb}) at r_1 on the negative gage line versus applied load for all the six repeated tests	187
6.34	Measured strain (ε_{bb}) versus applied load at different radii r_2 to r_6 on the negative gage line for the 1 st test	188
6.35	Variation of measured strains (ε_{aa}) and (ε_{bb}) with the radial distance from the crack tip	189
6.36	Scheme 1: (a) determination of A_0, A_2 and B_1 using the best-fit linear regression; (b) determination of C_0, C_1 and C_2 using the best-fit linear regression	191
6.37	Scheme 2: (a) determination of A_0, A_2 and B_1 using the best-fit linear regression; (b) determination of C_0, C_1 and C_2 using the best-fit linear regression	192
6.38	Scheme 3: (a) determination of A_0, A_2 and B_1 using the best-fit linear regression; (b) determination of C_0, C_1 and C_2 using the best-fit linear regression	194

List of Tables

4.1	Geometric and material parameters of center cracked plates	77
4.2	Convergence of the r_{\max} with the mesh refinement for the center cracked plate with $a/b = 0.2$ and 0.5 .	82
4.3	Variation of the r_{\max} with a/b of the center cracked plate ($b = 150$ mm).	84
4.4	Variation of the r_{\max} with the crack length a for the center cracked plate.	87
4.5	Variation of the r_{\max} with the net ligament length ($b - a$) for the center cracked plate	88
4.6	Geometric and material parameters of the edge cracked plate	91
4.7	Variation of the r_{\max} with crack length a of the edge cracked plate under plane stress condition ($b = 1200$ mm and $h/b = 3$	94
4.8	Variation of the r_{\max} with a/b for the double edge cracked plate subjected to uniform tensile stress ($b = 150$ mm and $h/b = 2$).	103
4.9	Geometric and material properties of eccentric center cracked plate	104
4.10	Variation of the r_{\max} with % eccentricity of center cracked plate	106
4.11	Specimens and material properties used by various researchers	108
5.1	Geometric and material parameters of the numerical examples of the present work.	114
5.2	Convergence of the r_{\max} with the mesh refinement for SECP $a/b = 0.5$ under plane stress condition	123
5.3	Comparison of coefficients	126
5.4	Variation of the r_{\max} with a/b of SECP under plane stress condition	138

6.1	Details of test specimens for determination of E and ν of PMMA	145
6.2	Experimental results of material properties	150
6.3	Details of experimental specimens for mode I and mixed mode loading	151
6.4	r_{\max} values of different mode I specimens	154
6.5	Computed normalized mode I SIF of different mode I specimens	155
6.6	Details of TML strain gage	159
6.7	Selected radial locations of strain gages for mode I experiments	164
6.8	Variation of experimental values of K_I and F_I at $r_1 = 10$ mm with the applied load in the 1 st test for $a/b=0.293$	168
6.9	Variation of experimental values of K_I and F_I at $r_2 = 30$ mm with the applied load in the 1 st test for $a/b=0.293$	169
6.10	Experimental values of F_I for three repeated tests for $a/b=0.293$	170
6.11	Experimental values of F_I for $a/b=0.293$ at different gage locations	170
6.12	Variation of experimental values of K_I and F_I at $r_1 = 17.5$ mm with the applied load in the 1 st test for $a/b=0.493$	175
6.13	Variation of experimental values of K_I and F_I at $r_2 = 35$ mm with the applied load in the 1 st test for $a/b=0.493$	175
6.14	Variation of experimental values of K_I and F_I at $r_3 = 50$ mm with the applied load in the 1 st test for $a/b=0.493$	176
6.15	Experimental values of F_I for three repeated tests for $a/b=0.493$	176
6.16	Experimental values of F_I for $a/b=0.493$ at different gage locations	177
6.17	Variation of experimental values of K_I and F_I at $r_1 = 7$ mm with the applied load in the 1 st test for $a/b=0.693$	180

6.18	Variation of experimental values of K_I and F_I at $r_2 = 27$ mm with the applied load in the 1 st test for $a/b=0.693$	180
6.19	Experimental values of F_I for three repeated tests for $a/b=0.693$	181
6.20	Comparison of experimental values of F_I for $a/b=0.693$ with the reference solutions	181
6.21	Selected radial locations of strain gages for SECP specimen	184
6.22	Different combinations of strain gages for determination of mixed mode SIFs	190
6.23	Experimental values of SIFs and normalized SIFs of all the schemes (1 st test at load=200N)	194
6.24	Experimental values of SIFs and normalized SIFs for the gage locations in scheme 1 (r_1, r_2, r_3) at different loads	195
6.25	Experimental values of F_I for all repeated tests corresponding to scheme 1	195
6.26	Comparison of experimental values of F_I and F_{II} with the reference solutions	196



Chapter 1

Introduction

This chapter briefly introduces the background of fracture mechanics, the importance of fracture mechanics based design and the significance of accurate determination of stress intensity factor (SIF) in design of engineering components. Strain gage based SIF measurements has been presented and finally, the importance of appropriate location of strain gage in accurate determination of SIF has been discussed in outlining the motivation of the present work.

1.1 Introduction to fracture mechanics

The industrial world experienced that man made structures built of metals did not always function satisfactorily and unexpected catastrophic failures like fracture often occurred. Fracture is one of the important structural failure modes such as buckling and excessive plastic deformation. Fracture of engineering structures is usually caused by a flaw or a crack. A crack can be visualized as a fine slit with the radius of curvature approaching zero at the crack tip. Due to repeated or sustained service loads a crack may start developing from a structural flaw or stress concentration zones and grows with time in size due to the service loading. Due to continual development of crack, the stiffness of the structure decreases. Once the crack reaches a critical condition, the strength becomes so low that the service loads can not be carried any more by the structure and fracture occurs. Fracture mechanics as an engineering discipline is a study of mechanics of deformable solid bodies containing crack-like singularities.

The theory of fracture mechanics, as it stands now, classifies fracture in general into two types viz.; brittle fracture and ductile fracture. Brittle fracture (also called cleavage fracture or elastic fracture) is one which is associated with either very little or no plastic deformation ahead of the crack tip preceding the fracture. On the other hand, large plastic deformation precedes the fracture in the case of ductile fracture (also known as fibrous fracture or dimpled rupture). Brittle fracture of

engineering structures is considered to be the most dangerous mode of failure compared to the ductile fracture as it does not give any prior warning and occurs suddenly at stresses considerably lower than the design stresses.

The industrialized world witnessed many unexpected and catastrophic brittle fractures which led to loss of capital investments and more importantly loss of many human lives. As a consequence, the discipline of fracture mechanics was started with the need to understand the brittle fracture. One of the most disastrous fractures which substantially influenced the development of fracture mechanics is the brittle fracture of several tankers and Liberty ships (built by the United States) during World War II using newly introduced welding technology. Shortly after these ships were commissioned several ships suffered from serious fractures and many of them fractured into two. All these fractures occurred, were at very low stress levels, sudden and accompanied by loud noise.

Another tragic accident due to fatigue fracture is the disintegration of pressurized cabins of the de Havilland comet jetliners in the mid air. These jetliners were the world's first pressurized passenger jetliners placed in service in 1952. Tragically three comets disintegrated or exploded in mid-air in a span of a few months in 1954 killing many people.

Another important catastrophic incident is the fracture (possibly due to fatigue crack growth) of a liquid natural gas storage tank that took place in Cleveland in 1944. Nearly 130 people were killed due to fire and explosions that accompanied fracture of the tank.

In 1962, the one year old Kings Bridge in Melbourne, Australia fractured after a span collapsed as a result of cracks which developed in the welded girder. After five years, in 1967 the Point Pleasant Bridge at Point Pleasant, West Virginia in US collapsed without warning, resulting in the loss of 46 lives. Apart from the above characteristic cases, large number of disasters involving failures of pipes, weapons, tanks, ships, railways and aerospace structures occurred throughout world.

The following general characteristics of brittle fracture were noticed from the examination and analysis of these structural disasters.

- 1 Most fractures were accompanied by very little plastic deformation, i.e., brittle fracture although they were made of materials which were ductile at ambient temperatures.
- 2 The stresses in the structures at failure were observed to be well below the yield stress of the material.
- 3 Many of these failures originated from structural discontinuities such as holes, notches, re-entrant corners and welding defects etc.
- 4 In most of these failures the origin was preexisting defects and flaws, such as cracks, accidentally introduced into the structure.
- 5 In all these cases of brittle fracture structures were mostly made of high-strength materials having low notch or fracture toughness (ability of the material to resist loads in the presence of notches or cracks).
- 6 In most of the cases, fractures usually propagated at high speeds.

These findings played vital role in the development of new structural design philosophy using fracture mechanics. The first significant work in the development of fracture mechanics was the work of Inglis [1] on stresses in the vicinity of a two dimensional (2D) elliptical hole in an isotropic plate. Using this work, the basic ideas leading to modern fracture mechanics were put forward by Griffith [2] in 1920 which led to the use of energy balance approach to study the fracture phenomenon in cracked bodies. This could be considered as the first solution to understand the effect of crack length on the strength of the structure using continuum mechanics based approach. However, the development of fracture mechanics as an engineering discipline was mainly due to contributions of Irwin and his co-workers [3] at the Naval Research Laboratory, Washington DC. In addition, the linear elastic analysis of cracked bodies in 2D by Westergaard [4] and Williams [5] were also important milestones in the development of modern fracture mechanics. Subsequently, the concepts of fracture mechanics were further developed and refined by large number of researchers in different universities, laboratories and aircraft and aerospace industries throughout the globe. Many concepts of fracture mechanics have now reached to a matured state and they can be applied confidently to the safe design of engineering components.

In 1982 the National Bureau of Standards (NBS), USA commissioned a study of the total direct and indirect costs of fracture in the economy of the United States. This study conducted by Duga et al. [6] considering direct loss and imputed costs associated with fracture related accidents of all kinds. The grand total was estimated to be some 120 billion dollars annually and the study revealed that more than 50% of the estimated cost could be saved by judicious use of fracture control technology that was known at that time. That showed the importance of the use of fracture mechanics in fracture prevention and the impact it had on the economy.

1.2 Importance of fracture mechanics approach to design

In the strength of materials approach of design or conventional strength based design approach of an engineering component, for a specific structural geometry (assumed to be free of crack-like flaws), a calculation is made to determine the relation between the load and the maximum stress that exists in the structure. An acceptable design is achieved when the computed maximum stress is less than the relevant strength of the material of the structure suitably reduced by a factor of safety. Due to their obvious limitations these conventional failure criteria can not answer the fracture of structures which occurs at stress levels much below the design stress due to presence of cracks or crack like flaws. A new design philosophy was therefore introduced by fracture mechanics to prevent and control the unfortunate fracture of engineering structures, due to the presence of such cracks. Experience from various fracture failures suggested that the existence of crack-like flaws could not be precluded in any engineering structure. Based on this fact, fracture mechanics studies the load bearing capacity of structures which are assumed to contain dominant cracks.

In fracture mechanics approach, in addition to the applied stress and structural geometry (which are also used in the strength of materials approach), an additional important structural variable known as the crack length also enters in strength calculations. By combination of these three variables the parameter that characterizes the crack (or driving force) can be determined. The critical value of crack driving force known as fracture toughness, which is the ability of the material to resist fracture

in presence of cracks and is considered to be a material property. By equating the crack driving force to the fracture toughness, a relationship between applied load, crack size, fracture toughness and structural geometry can be obtained which gives the necessary information for structural design. Fracture mechanics based design approach does not replace the conventional strength based design approach but indeed augments the conventional approach to prevent catastrophic failures due to brittle fracture. However, a designer has to make balance between both the design approaches as the high strength materials usually have low fracture toughness and low strength materials have high fracture toughness.

Fracture mechanics is not only limited to determining critical size and loading combinations for fracture instability in static conditions, but it also plays useful role in life prediction of components that are subjected to time-dependant crack growth mechanisms such as fatigue and stress corrosion cracking. As a consequence, fracture mechanics also introduced a new design philosophy known as damage tolerant design. As the name suggests, this philosophy allows subcritical flaws or cracks to remain in structure during their operation. An important component of this design philosophy is the nondestructive testing (NDT) of engineering components. In this design approach fracture mechanics analyses predict remaining life and specify inspection intervals using NDT for improving the health of the structures. Fracture mechanics design philosophy is now extensively used in industries such as aircraft, aerospace, and nuclear, industries, offshore platforms and locomotives, pressure vessels etc.

1.3 Methods of analysis: Linear elastic fracture mechanics

Fracture mechanics analyses have been broadly classified into two divisions viz. *linear elastic fracture mechanics* (LEFM) and *elastic plastic fracture mechanics* (EPFM). LEFM is based on the concept of *small scale yielding conditions* (SSY). In small scale yielding conditions, the plastic zone at the crack tip is sufficiently small compared to the crack length and other relevant geometric parameters. The stress-strain behavior and load- displacement behavior is linear in LEFM. In LEFM elastic analysis of cracked bodies is usually employed to determine the displacement and

stress field in the cracked body. Fracture criteria that are based on the LEFM are applicable for control and prevention of the brittle fracture as it involves very limited amount of plastic deformation ahead of the crack tip. Most of the engineering designs based on fracture mechanics approach are primarily on the brittle fracture. LEFM is well suited for applications which involve high strength materials (which have low fracture toughness) such as aluminum alloys used in aircraft structures. This theory is not valid when significant plastic deformation precedes the failure. This restriction severely limits the application of LEFM to ductile fracture.

1.4 Elastic plastic fracture mechanics

In cases where the extent of the plastic zone becomes large compared to the specimen thickness and crack length, the LEFM methodology breaks down and the linear conditions no longer exist due to large scale plasticity. Under such large scale plastic conditions or *large scale yielding conditions* (LSY), elastic-plastic fracture mechanics (EPFM) is employed to characterize the crack tip conditions. This situation generally is observed for highly ductile materials used in nuclear industry. This approach is mainly useful for ductile fracture. As compared to SSY conditions, fracture under LSY conditions absorb more amount of energy for fracture of components due to more plastic deformation. The severity of the crack in both LEFM and EPFM is characterized by certain fracture mechanics parameters. By comparing with their corresponding critical values of those parameters the severity of the existing crack could be predicted.

1.5 Fracture mechanics parameters

Depending on whether LEFM or EPFM is employed to characterize the crack, the following four fracture mechanics parameters are widely used to measure the potency of an existing crack in an engineering component.

- Energy release rate (G)
- Stress intensity factor (K)
- J -integral (J)

- Crack tip opening displacement (*CTOD*) or crack opening displacement (*COD*)

Depending upon the materials and crack tip conditions an appropriate parameter is chosen to analyze the given problem. The first two parameters G and K are used in LEFM analysis. However, in comparison to G , K is more widely employed by the engineers. On the other hand the J -integral and *CTOD* are widely employed in EPFM studies.

1.5.1 Strain energy release rate

The strain energy release rate G (in honor of Griffith) or simply energy release rate is based on the energy balance which establishes the necessary condition for fracture. The concept of energy release rate is introduced by Irwin [7] in an effort to extend the pioneering work of Griffith [2] to metals. G is a measure of the energy available for the crack growth. An unstable fracture occurs when G attains a critical value, G_c , which is a material property and represents materials resistance to crack growth.

1.5.2 Stress intensity factor

Stress intensity factor (SIF), K is the most important fracture mechanics parameter in LEFM (it is a grouped parameter like Reynolds number). SIF is the most widely used to characterize the crack under SSY (brittle or quasi brittle fracture conditions of metals). Unlike G , the SIF is derived from the stress based approach. The magnitude of K depends on the geometry of the cracked structure, crack length and applied load. Unlike the concept of stress concentration factor that determines the magnitude of the stress at a single point, the parameter K provides a complete description of the state of stress, strain and displacement in the vicinity of a crack tip known as the singularity dominated zone (SDZ). Further, the SIF represents the strength of the singularity in linear elastic conditions i.e. the rate at which the stresses approach infinity. Many important phenomena of fracture of metals that fall within the scope of LEFM can be explained with the help of the SIF approach. For example,

SIF approach could be used in determination of the safe operating loads for known sizes and locations of existing cracks and for determination of the largest crack size that can exist for given loads without fracture. Further, SIF approach could also be employed for remaining life prediction using the fatigue crack propagation laws such as Paris law and for prediction of crack growth rate for environmentally assisted cracking such as corrosion etc. Due to its practical importance, a collection of SIFs of various cracked configurations are made available in many handbooks [8,9]. By comparing the operating K with the critical K_c (or fracture toughness) it is possible to predict whether the existing crack grows or not. Thus it is clear that the knowledge of accurate values of SIFs of a configuration is essential for application of the above fracture criterion. The introduction of the SIF by Irwin and his co-workers did much to establish the basis of modern fracture mechanics.

1.5.3 J- integral

Rice [10,11] introduced the path-independent contour J -integral for applications of fracture mechanics where LEFM is no longer applicable and elastic-plastic deformation due to significant amount of plasticity at the crack tip is to be taken into account. It is one of the widely used parameter in EPFM studies of ductile materials. J -integral is like G based on the energy approach. In fact, there exists a relationship between J , K and G for SSY conditions.

1.5.4 Crack opening displacement

The crack opening displacement (COD) is an alternative to the J -integral for applications where the plastic deformation is significant as compared to dimensions of the cracked body and is introduced by Wells [12]. It is derived from a displacement based approach. Like J -integral COD is also widely employed in EPFM studies.

1.6 Stress intensity factors for different modes of loading

The stress intensity factor K is represented according to the mode of loading. Referring to Fig. 1.1, in mode I loading, the principal load is applied normal to the

crack plane, and tends to open the crack. Mode II corresponds to in-plane shear loading and tends to slide one crack face with respect to other. The displacement of the crack surfaces is in the plane of the crack and perpendicular to the leading edge of the crack. Mode III refers to out-of-plane shear. Crack surface displacements are in the plane of the crack and parallel to the leading edge of the crack. A cracked body can be loaded in any one of these modes, or a combination of two or three modes and thus leads to the mixed mode problems. The SIFs corresponding to mode I, mode II and mode III loading cases are designated as K_I , K_{II} and K_{III} respectively.

Referring to the crack-tip local coordinate system in Fig. 1.1 (origin is placed at the center of the crack front) the stress field ahead of a crack tip for the case of linear elastic, isotropic materials under modes I, II and III loading conditions can be written as.

$$\lim_{r \rightarrow 0} \sigma_{ij}^{(I)} = \frac{K_I}{\sqrt{2\pi r}} f_{ij}^I(\theta) \quad (1.1)$$

$$\lim_{r \rightarrow 0} \sigma_{ij}^{(II)} = \frac{K_{II}}{\sqrt{2\pi r}} f_{ij}^{II}(\theta) \quad (1.2)$$

$$\lim_{r \rightarrow 0} \sigma_{ij}^{(III)} = \frac{K_{III}}{\sqrt{2\pi r}} f_{ij}^{III}(\theta) \quad (1.3)$$

where r and θ are polar coordinates of a point as shown in Fig. 1.1, and f_{ij} are universal functions that only depend on θ .

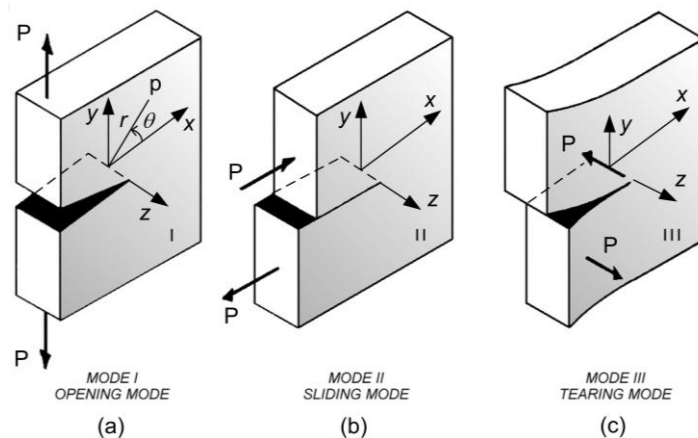


Figure 1.1 Three types of loading

It can be noticed from Eq. (1.1) that $1/\sqrt{r}$ singularity prevails in stress components. Since strain components are functions of stress components, therefore all strain components also tend to infinity in a $1/\sqrt{r}$ fashion while approaching the crack tip. Experience shows that the majorities of cracks are loaded in the opening mode compared to the other two modes (II and III) for isotropic materials but occur in a combined fashion only. In the mixed mode problems (i.e. when more than one loading mode are present), the individual contributions to a given stress component are additive i.e.,

$$\sigma_{ij}^{(total)} = \sigma_{ij}^{(I)} + \sigma_{ij}^{(II)} + \sigma_{ij}^{(III)} \quad (1.4)$$

In case of mixed mode (I / II) loading one needs to know both the values of K_I and K_{II} for complete description of crack tip conditions. Thus, the SIF defines the amplitude of the crack tip singularity and the stress near the crack tip increases in proportion to the SIFs. This single parameter description of crack tip conditions turned out to be one of the most important concepts in fracture mechanics. If K is accurately known, it is possible to solve for all components of stress, strain and displacement ahead of crack tip as a function of r and θ .

1.7 Methods for the determination of stress intensity factors

The SIF plays a vital role in the application of the principles of linear elastic fracture mechanics to practical problems in design and analysis. Determination of SIF for real life components with a crack is therefore very important for prediction of the crack condition. The SIFs can be determined through analytical, numerical and experimental methods.

1.7.1 Analytical methods

The analytical methods are mostly suitable for idealized geometries, loading and boundary conditions. There are number of techniques used in the solution of the SIFs of two-dimensional crack problems. Amongst, very notable methods are conformal mapping, Laurent series expansion, boundary collocation method, integral

transform method and weight function method. Theoretical methods are essential for two reasons. First, they provide the correct form of singularities and asymptotic solutions that are useful in analyzing and interpreting the experimental observations and in improving the accuracy of numerical solutions. Secondly, they provide accurate solutions for relatively simple geometries and for certain idealized material behavior and could be used as benchmark problems for validation of numerical methods and experimental methods.

1.7.2 Numerical methods

Numerical methods for determination of SIF are extremely useful in dealing with the complex configurations usually found in a great many practical problems. Finite element and boundary element methods are widely used for numerical estimations of SIFs. The SIFs can be estimated either by the displacement based methods or energy based methods. The use of numerical methods, particularly finite element methods, has vastly broadened the range of problems that can be solved by computational approaches. A major advantage is that engineers can easily calculate SIFs at their desks, using personal computers and large number of commercially available finite element codes.

1.7.3 Experimental methods

Experimental methods provide new alternatives and opportunities for solving fracture mechanics problems. Many factors make the experimental determination of the SIFs indispensable. Analytical methods for determination of the SIFs are usually based on simplifying assumptions which imply certain detachment from reality and those theories can be verified only by experimentation to convince whether such idealization has not resulted in an undue distortion of the essential features of the problem. The aim of all experimental methods is to extract the SIFs from the measurable data. Several experimental methods have been developed for the measurement of SIFs in the past and some of the widely used experimental methods are caustics, moiré interferometry, photoelasticity and strain gage techniques.

1.7.3.1 The method of caustics

The method of caustics or shadow spot method relies on the deflection of light rays due to stress field gradient. Caustics are three dimensional surfaces in space enclosing a dark region and along which a high intensity of light occurs [13,14]. When a uniform beam of light is incident on a reflective surface containing geometric nonlinearities, the beam is reflected in such a way that its intensity varies spatially to form the caustic. This occurs when light is reflected from the region around the crack tip in a polished specimen subjected to load. The caustic can be seen by placing a screen in the reflected light path. A thin ring of high intensity light the caustic, surrounding a dark spot will be observed. The size and shape of the ring, or caustic can be related to the magnitude of SIFs. The SIF is related to diameter of the caustic, specimen thickness, the distance between the reference plane and the specimen and also Young's modulus and Poisson's ratio of the specimen.

The advantage of caustics method is that it can be applied to both transparent and opaque materials. It has also been used with variety of materials such as isotropic, anisotropic and composite material for the determination of SIFs under static and dynamic loading condition. This method is also widely employed for the determination of mixed mode SIFs. However, the data produced were not as reliable as other methods such as moiré interferometry, photoelasticity and strain gage method [15].

1.7.3.2 Moire interferometry

The two basic principles that govern the formation of moiré interferometry fringes are the interference of light and the diffraction of light. It provides contour maps of the in-plane displacement field, from which small strains can be determined [13]. This technique is based on the interference of two regular gratings and widely employed in quasi-static and dynamic loading problems. Out of two gratings, first grating acts as reference which is undeformed. The second grating which is called active grating is affixed to the surface of the specimen and is deformed by the strains experienced in the specimen. Simultaneous viewing of the two gratings produces the fringes due to crossing of these. The order of fringe starts from known zero

displacement. Then, SIF is calculated by substitution of the order of fringe and the pitch of the reference grating in appropriate equation. This method is not consistent as compared to other optical method such as photoelasticity and is also more expensive [15].

1.7.3.3 Photoelasticity

Photoelasticity method is by far the most widely used whole-field technique for studying cracked bodies. It is an optical method of experimental stress analysis, which yields a whole field representation of principal stress difference [13]. The difference in the principal stresses is related to the fringe order, material fringe constant and the length of the light path. In this method the SIF can be determined by measuring the fringe order and position parameters on a fringe loop. This method has also been applied for determination of mixed mode SIFs. Many investigators used this technique to study crack tip stress field for both static and dynamic conditions.

In comparisons of optical analyses of crack tip stress field, the photoelastic results were the most consistent and in a fully equipped laboratory, photoelasticity would be the first choice to provide accurate, repeatable data [15]. Although the idea of using the photoelastic method of stress analysis to the solution of crack problems seems to be attractive, many difficulties are encountered during measurements due to high concentration of the isochromatic fringes near the crack tip which alter the real meaning of the isochromatic pattern of the corresponding problem of the cracked plate.

1.7.3.4 Electrical resistance strain gage

Of all of the techniques of experimental mechanics, by far the most commonly used techniques are those based on electrical resistance strain gage. Moreover, among the experimental techniques for the determination of SIFs strain gage based techniques are relatively simple, easy to use and inexpensive [13]. Electrical resistance strain gages are the most commonly used type of strain sensors and hereafter these gages are named as only strain gages for simple representation. The

change in resistance of a conductor with its change in length forms the basis for strain measurement using strain gages.

Strain gages are bonded to the surface of the body and forms a part of it. When the body deforms, the gage also subjected to the same deformation. As a result, resistance of the gage material changes due to changes in its length due to deformation. This resistance change due to deformation is measured in terms of voltage change using a Wheatstone bridge circuit. The output voltage of the Wheatstone bridge circuit can be calibrated to give the axial strain along the strain gage. The measured strain is then related to SIF by employing appropriate analytical equations, and the SIFs can be determined from those equations. Several static as well as dynamic studies of the cracked components have been reported by many investigators using the strain gage techniques. These techniques are also used for experimental determination of mixed mode SIFs. Strain gage methods are as powerful as photoelastic methods and are also cost effective measurements. Due to the minimal investment in measuring equipment, these techniques are particularly employed in the development of standard methods of measuring the dynamic initiation, propagation and arrest toughness.

1.8 Principle of operation of the electrical resistance strain gage

The electrical resistance strain gage is the most versatile of many devices to measure free surface strains of machine components and structural members. In 1856, Lord Kelvin reported that certain metal wires exhibited a change of electrical resistance with the change in strain. The resistance R of a uniform conductor with a length L , cross-sectional area A and specific resistance ρ is given by

$$R = \rho \frac{L}{A} \quad (1.5)$$

Thus when a conductor is pulled in the axial direction, a change in electrical resistance occurs due to the change in length of the conductor. This forms the basic principle of

working of electrical resistance strain gages. Usually the change in resistance is extremely small quantity. The amount of the resistance change in relation to change in length of the conductor is known as the strain sensitivity of the material of conductor. Since the change in resistance for a change in length of the conductor is so small that special bridge circuits such as Wheatstone bridge and potentiometer bridge circuits are widely employed in practice. The output voltage of bridge circuit is proportional to the change in resistance of strain gages and hence proportional to the axial strain. The most commonly used strain gages are foil gages.

1.9 Bonded metallic foil strain gages

Although, it is theoretically possible to measure strain with a single length of wire as the sensing element of the strain gage, in order to sense the strain in a robust way and accurately, modern strain gages are available in a form popularly known as bonded metal foil strain gages. These are most widely used for measurement of surface axial strains. A metallic foil strain gage consists of a very thin rolled foil arranged in a grid pattern. The grid pattern maximizes the amount of metallic wire subject to strain in the parallel direction. Figure 1.2 shows a typical foil strain gage.

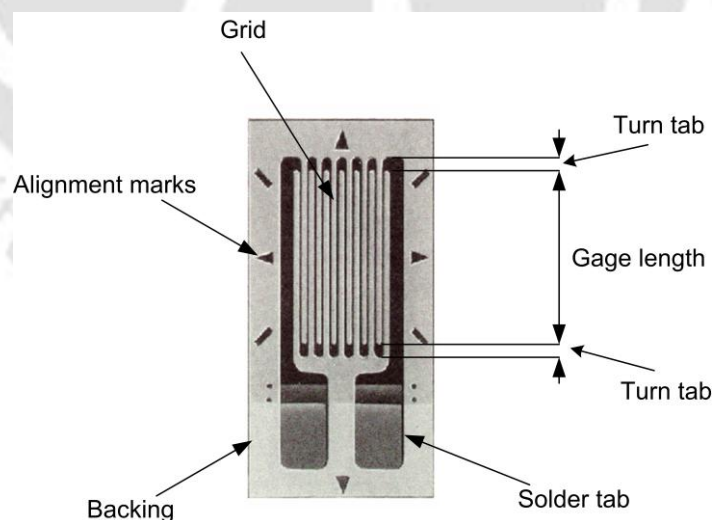


Figure 1.2 Typical foil strain gage

The dimension between the ends of the grid is the basic measuring length of a strain gage, and is called the *gage length*. Henceforth the word strain gage will be used to denote the bonded metallic foil gages. Most general purpose strain gages produced

today are fabricated from the copper-nickel alloy known as Advance or Constantan. The cross sectional area of the grid is minimized to reduce the effect of shear strain and Poisson's effect. The grid is bonded to a thin backing, called the carrier, which is attached directly to the test specimen. Therefore, the strain experienced by the test specimen is transferred directly to the strain gage, which responds with a linear change in electrical resistance.

A variety of strain gages such as single element gage, two and three element rosettes, shear gage, strip gage and stress gage, etc., are commercially available for use in various situations. As discussed earlier, the change in resistance is so small that a high sensitive circuits such as Wheatstone bridge circuit is widely employed along with the metallic foil gages to measure the strains. The output voltage of the bridge can be directly related to the surface strains. The overall output of strain sensor depends on gage resistance, lead wire resistance, type of lead wire connection, transverse sensitivity, thermal sensitivity, gage length, gage factor, type of strain gage and excitation voltage of bridge circuit. For accurate measurement of strain the above parameters should be optimized so that error in strain measurement can be reduced. In addition, it is very important to employ the proper adhesive and bonding procedures to achieve precise strain measurements. The most widely used commercially available strain gages are 120Ω , 350Ω and 1000Ω . Using commercially available dedicated strain gage data acquisition systems the accuracy of strain measurement can be further improved and can be made easier. Some of the basic requirements of strain gage are

- Linear strain sensitivity in the elastic range – for accuracy and repeatability.
- High resistivity – for smallest size.
- Low hysteresis – for repeatability and accuracy.
- High strain sensitivity –for maximum electrical output for a given strain.
- Low and controllable temperature coefficient of resistance – for good temperature compensation.
- Wide operating temperature range – for the widest range of applications.

- Good fatigue life – for dynamic measurements.

1.10 Motivation

As stated earlier the strain gage methods are cost-effective, accurate and easy to use in the determination of SIFs. They can be used on components made of both the metallic and non-metallic materials. In these methods of the determination of SIFs, a truncated series for a strain component in a desired directions is usually considered first. The SIFs are then determined using the measured strain(s) from the strain gage (s) and the selected truncated strain series equations. It is evident that in order to obtain accurate values of the SIFs, it is very important to decide the number of strain gages required, their angular location and orientation (defined by θ and α) with respect to the crack axis (Fig. 1.3) and radial location (r) from the crack tip to the center of the gage.

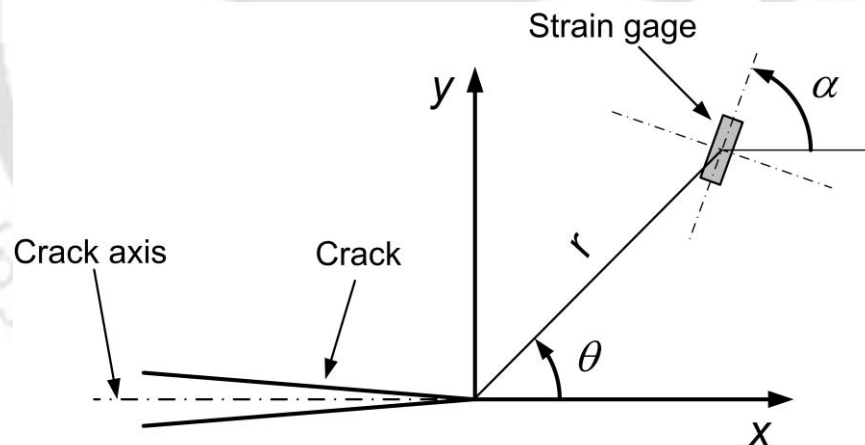


Figure 1.3 Location of strain gage from the crack tip

The number of strain gages required can be assessed from the number of unknown coefficients considered in the truncated strain field equation. The angular position of gages can also be easily obtained from the direction of the strain component given by the truncated series. However, the most difficult and challenging problem is in deciding the appropriate radial distance (r) for each of the selected number of strain gages. To the best of authors' knowledge no recommendation, or no methodology, or

no solution in any form is available to date for selection of valid radial locations (r) for strain gages and is an open problem [16] in the determination of SIFs using strain gage techniques. As a result researchers are forced to guess the radial locations of gages.

If the gages are pasted very close to the crack tip then the three dimensional (3D) effects, strain gradient effects and plasticity effects will induce erroneous strain measurements and hence errors in the SIF values. On the other hand, if the strain gages are pasted far from the crack tip then the measured strains could not be represented by the selected strain field equations at those locations. Therefore, it is evident that quantitative prediction of appropriate radial location (r) for the strain gages is extremely important for the accurate determination of SIFs. This forms the motivation for taking up the present study of quantitative determination of appropriate radial locations for strain gages and their experimental verification with an aim to provide some recommendations for different types of crack configurations which will ensure an accurate determination of SIFs.

1.11 Organization of the thesis

The present thesis has been organized as follows:

Chapter 1 introduces the importance of fracture mechanics and its importance in design of structures. A brief introduction of strain gage technique for determination of stress intensity factors is presented.

In order to understand the application of strain gage techniques for accurate determination of stress intensity factors in various cracked configurations, comprehensive literature review has been done and presented in chapter 2.

Details of problem formulation for radial location of strain gage in both opening mode and mixed mode have been presented in chapter 3 of the thesis.

Chapter 4 describes the development of a methodology for determination of valid or optimal radial locations of strain gages for accurate determination of mode I stress intensity factors. It also describes the application of this method to find out

valid strain gage locations for important single and double ended cracked configurations for accurate determination of mode I stress intensity factors.

Chapter 5 describes the development of a methodology for determination of valid radial locations of strain gages in mixed mode loading conditions and corresponding strain gage technique for determination of mixed mode stress intensity factors.

Experimental verification of proposed methodology for optimal radial location of strain gages in both mode I and mixed mode I/II is described in chapter 6 of the thesis.

Chapter 7 concludes the thesis outlining the important conclusions drawn from the present work and it also discusses the scope for the future work.



Chapter 2

Literature Review

In experimental fracture mechanics, electrical resistance strain gage techniques have been extensively used for measurement of various fracture mechanics parameters. Many researchers have used these techniques for measurement of static and dynamic stress intensity factors (SIFs) in various materials for different configurations. For the measurement of strain and, in turn, SIFs, researchers have used single strain gage, multiple strain gages and strain gage rosettes. In all these cases of strain gage based measurements, the radial location and orientation of strain gages with respect to crack tip are very important for accurate determination of SIFs. Considering the importance of location of strain gages on measurement of SIFs, the review of existing literature has been presented in three sections. The first section discusses literatures on the strain gage based determination of mode I SIF for static as well as dynamic loading conditions in isotropic and orthotropic materials. Second section presents the literature on the strain gage based determination of static mode II SIFs in isotropic materials. Literatures on strain gage based methods for mixed mode SIFs determination are presented in the third section. The summary of the literature review leading to the objectives of the present work have been given at the end of this chapter.

2.1 Strain gage techniques for determination of mode I SIF

The use of strain gage to determine SIFs near the crack tip was first suggested by Irwin [17] in 1957. However, practically feasible methods based on the strain gages were not realized for long time due to constraints such as measurement of strains at high strain gradients zones in the vicinity of crack tips using finite sized strain gages, local yielding and three-dimensional effects near the crack tip. As reported by Broek [18], a very early attempt to determine the mode I SIFs using strain gages were made by Bhandari and co-workers [19, 20]. They employed strain gage measurements at several points close to the crack tip and extrapolated the measured data to crack tip for determination of SIFs. Despite the above constraints, they

reported to obtain accurate values of SIFs [19, 20]. However, no strain gage radial locations were recommended for using the above extrapolation technique [18].

In the mean time, in an effort to establish the range of applicability of two dimensional near tip solutions, Rosakis and Ravi-Chandar [21] experimentally found the extent of three dimensionality of the crack tip stress fields using caustics. Polymethylmethacrylate (PMMA) plates of various thicknesses were considered. They showed that plane stress conditions prevail at distances greater than half the specimen thickness from the crack tip for mode I loading conditions and below this distance the state of stress is three dimensional.

At this point, it is beneficial to introduce different ways of representation of strain field around a crack tip and their extent of validity around the crack tip. The singularity dominated zone (or zone I) is one in which the strains can be accurately represented alone by the leading term or singular term of the infinite strain series. Such a representation is known as the single parameter representation. On the other hand, adding a few non-singular strain terms to the singular term forms what is known as multi-parameter representation of strain field. Using these multi-parameter equations, the strains can be accurately represented in zone that is significantly larger than the singularity dominated zone. Such a zone is represented as zone II.

To overcome the constraints in development of strain gage based methods (as mentioned above) Dally and Sanford [22] were first to propose a practically viable and theoretically well supported single strain gage technique for determination of the static mode I SIF in two dimensional bodies of isotropic materials. They employed a truncated strain series consisting of three unknown coefficients (multi-parameter strain series) for the representation of the strains in the experimental specimens. As a consequence, the strain gages could be placed at greater radial distances from the crack tip instead of placing in the vicinity of the crack tip. Further, by use of clever manipulation of the selected multi-parameter strain expressions, they devised a robust technique for experimental determination of the mode I SIF using only one strain gage.

Thus the major advantage of their technique is that a single strain gage located at radial distance sufficiently away from the crack tip is sufficient to determine the

mode I SIF of any configuration. For experimental validation of their method three single element strain gages were pasted on an aluminum CT (Compact Tension) specimen. These three gages were located at different radii from the crack tip. They noticed that the error in the measured SIF was more in the first and last strain gages as compared to the intermediate one indicating the importance of radial location of strain gage on determination of accurate values of SIFs. It can be noticed from their technique that the radial location of the single strain gage should be within the realm of applicability of the selected three parameter representation. Consequently, this technique requires prior knowledge regarding the extent of validity of the selected three parameter strain representation (which in turn provides valid or optimal gage locations) which is a function of the geometry of the specimen and applied loading. No suggestions were made by Dally and Sanford [22] on the valid or optimal gage locations. However, based on Rosakis and Ravi-Chandar work [21] they suggested that the strain gages should be placed at distances greater than half the thickness of the specimen from the crack tip in order to avoid three dimensional effects. Clearly this suggestion serves in identifying only the minimum radial distance for the strain gage. The Dally and Sanford [22] single strain gage technique is henceforth will be abbreviated as *DS technique* in the present investigation.

Subsequent to the DS technique many new techniques were proposed. Some of these new techniques were extension of the DS technique to other areas such as dynamic loading conditions, composites and mixed mode loading conditions etc.

Berger and Dally [23] developed an overdeterministic method for determination of mode I SIFs under elastostatic conditions. In their technique, they employed many single element strain gages as was employed by earlier researchers [19, 20] and increased the three term representation of strain series (as considered in DS technique) to more than those terms to accommodate many strain gages in relatively large field. The mode I SIFs were then obtained experimentally using the measured strains from many strain gages and solving the corresponding overdeterministic equations by least-square methods. Thus, in this technique no prior knowledge of radial location of strain gages is required due to the use of many strain

gages and the corrections due to the plasticity effects are not required as the gages are placed at greater distances from the crack tip. A CT specimen fabricated from Aluminum alloy was employed with three ten-element strip gages pasted at angles of 0° , 45° and 90° with the crack axis. They observed that error in determining opening mode SIFs using six parameter strain series equation was more compared to that using three parameter strain field equation. Clearly, a major limitation of this technique [23] is the use of many strain gages for determination of mode I SIF which could be determined by a single gage with the help of DS technique.

Another technique for determination of mode I SIF using single strain gage under static loading conditions is developed by Kuang and Chen [24]. They employed asymptotic strain expression for the representation of measured strains. They incorporated an integration scheme in the SIF calculations for minimization of the possible error caused by strain gradients across the gage length. For experimental verification of their work, three ten element strip gages were mounted on the CT specimen made of an Aluminum alloy at angles of 0° , 45° and 90° with the crack axis for the measurement of strains. They observed that the SIF determined by this method consistently underestimated the theoretical values, with gages located close to crack tip. Their technique was found to be stable only for radial measurement of strains along 0° and 45° rays. They suggested that gages could be placed at distances greater than half the thickness of the specimen from the crack tip in spite of the fact that at large distances the measured strains could not be accurately represented by asymptotic equations alone. As a consequence, their results indicated that normalized SIF was a function of the applied loads, the thickness of the specimen and the angular position θ from axis of the crack.

A two strain gage techniques for determination of mode I SIF under elastostatic conditions was developed by Wei and Zhao [25] based on two parameter representation of measured strains. The measured strains from the two strain gages were employed to solve a set of two linear equations for determination of SIF. A three point bend specimen (TPBS) of construction steel was tested to determine SIF. They suggested empirical relations for radial locations of the two gages. These relations

necessitate a priori knowledge about the plastic zone size which clearly depends on the unknown SIF. It was reported that for suitable location of two strain gages, errors of measurement of SIFs would be within 5%.

The strain gage techniques were also developed and employed to determine the dynamic SIFs in dynamic fracture problems. A single strain gage technique for measurement of mode I dynamic SIF for propagating crack was developed by Shukla et al. [26], in a similar way to that of DS technique. They considered a two parameter (neglecting the $r^{1/2}$ term) dynamic strain series for the representation of the strain field. A comparison of dynamic SIFs for a propagating crack obtained using their strain gage technique and photoelastic coating method was carried out on a single edge notch plate made of steel and aluminum. In order to determine dynamic SIFs, they mounted four strain gages with equal spacing in a row above the crack tip. It was reported that the dynamic SIFs obtained from strain gage method were in good agreement with the values obtained from the photoelastic coatings. The distance of strain gages from the crack tip was not reported and no suggestions on valid or optimal locations were also provided.

Another single strain gage technique for measurement of mode I dynamic SIF was also developed by Berger et al. [27], for propagating cracks in a similar way to that of DS technique. They considered a three parameter strain series and included the $r^{1/2}$ term in the selected dynamic strain series which was neglected by Shukla et al. [26], and demonstrated the importance of this term in measuring dynamic SIF. Further, they also developed a crack tip algorithm for precise location of crack tip with respect to the strain gages in a propagating crack. After the precise position of the crack tip was determined, the dynamic SIF was calculated from the strain sensed by the gages. Six strain gages were placed on the line below the crack axis of CT specimen made of alloy steel. No explanation was provided on selected radial locations of strain gages used for measurement of dynamic SIFs. They reported that the measured strains using this technique deviated 5% to 7% from the computed strains.

Dally and Sanford [28] proposed a strain gage technique for determination of mode I dynamic SIFs of a propagating crack. They also considered the same three parameter strain series for representation of dynamic strain field as in work of Berger et al. [27], but without any crack tip locating algorithm. In this technique six strain gages were mounted on a CT specimen made of hardened steel along the gage line at a distance of 10.5 mm from the crack axis and the uniform spacing between gages was 12.7mm. No explanation was provided to support whether the selected gage locations were valid ones or not. Furthermore, they realized from their results that some of the strain gages were not located within the realm of three parameter zone.

Using the strain gage technique developed by Berger et al. [27] and solving a overdetermined system of equations Berger and Dally [29] proposed a technique for determination of dynamic SIFs with improved accuracy. In spatially overdetermined analysis, a Newton-Rapheson iterative procedure with QR decomposition was used to solve resulting linear least squares problem. For experimentation a CT specimen made of alloy steel was used. Strains were measured from six strain gages which were pasted in a line with a constant distance below the crack axis. Criterion for the selected radial locations of strain gages was not reported. The result of dynamic stress intensity obtained by this method was reported to be within 5% when compared with the published results.

Apart from the development of new techniques for determination of mode I static and dynamic SIFs in isotropic materials as discussed above, strain gage techniques for determination of mode I SIFs for orthotropic materials were also proposed.

Shukla et al. [30] extended the DS technique to composite materials and developed a single strain gage technique for determination of static mode I SIF by employing orthotropic stress-strain relations. Their technique was verified by conducting experiments on a glass-epoxy single-edge-notched composite specimen. Although, it was realized that the selected radial locations should be according to the theoretical formulations, the radial location of strain gages for their experimental work were primarily based on minimizing the average errors due to the strain gradients. Based on the averaging error, two strain gages were pasted at distances of 5mm and 9mm from the crack tip. The SIF was measured corresponding two locations. The

result showed that the strain gage located at 9mm could produce good agreement with theoretical SIF. But the error in SIF using strain gage located at 5mm was about 18% and attributed this large error to the three dimensional effects etc.

Khanna and Shukla [31] extended the DS technique and developed a single strain gage technique for determination of mode I dynamic SIF for a moving crack at a constant speed in the orthotropic composite materials. Theoretical equations of the strain field around a crack moving at a constant velocity in an orthotropic composite material were developed. If the strain gages were within the realm of the selected strain expression, a procedure was developed to evaluate the optimum size, orientation and location of strain gage for minimizing the average errors. A single edge notch (SEN) fracture specimen made from unidirectional glass-epoxy composite laminate was used to determine the SIF for a crack propagating along the direction of fiber reinforcement. The radial location of strain gages on the experimental specimen was decided based on the experimental results on averaging error with the radial locations. No validity or explanation was provided as the selected locations are valid locations to satisfy the realm of the selected strain expression.

Khanna and Shukla [32] also investigated the effect of the position and gage orientation on determination of dynamic SIF using the technique developed by Khanna and Shukla [31]. Based on the maps of singularity dominated zone for certain configurations and experiments on a modified CT specimen made of three different materials they found that their technique [31] determined the dynamic SIFs close to the photoelastic values if the gages were pasted within the singularity dominated zone and oriented at obtuse angles. As stated earlier the plasticity, strain gradient and three dimensional effects clearly affect the measured strains in such small zones such as singularity dominated zones. Moreover, a complete map of singularity dominated zone for the experimental specimen is needed a priori for application of their technique.

Because of its simplicity and strong mathematical foundations, the DS technique was extensively employed in various studies of experimental fracture mechanics. Following is the review of literature wherein the DS technique was employed for determination of static and dynamic mode I SIFs in specimens made of isotropic and orthotropic materials.

In an attempt to verify a new technique for the measurement of dynamic initiation toughness (based on detonation of explosives), Dally and Barker [33] employed the DS technique for experimental determination of mode I dynamic SIF of a sharp stationary crack. The dynamic initiation toughness was measured for Homalite 100 using both DS technique and photoelastic method. A dog-bone specimen was used in their experiments. The dynamic loads were induced to the specimen by detonation of explosives. The strain gages were reported to be located within the singularity dominated zone but at a distance greater than half the thickness of the specimen to avoid the three dimensional effects. No further discussion was presented on the selected gage locations. They observed that strain gage method yielded better result as compared to photoelastic method even though it was based on static theory. They reported experimental error on determination of dynamic SIF was about 25 percent.

To study the effect of material composition and thickness of the specimen in determination of static mode I SIF using DS technique, Parnas et al. [34] conducted several experiments. They considered CT specimens made of steel and aluminum of different thicknesses. Strain gages were pasted at a radial distance from the crack tip greater than half the thickness of the CT specimen and no further discussion was available on radial location of strain gages. However, they suggested from their experimental results that the thickness of the specimen and the region of strain gage location should seriously be considered during the application of DS technique. The SIFs obtained were higher than theoretical and finite element values.

While studying the dimple fracture under shot pulse loading, Rizal and Homa [35] employed the DS technique for measuring the dynamic SIF. The material used in their experiment was aluminum alloy. For measurement of strain, a strain gage was mounted at a distance of 7mm from crack tip according to DS technique. No other discussion was made on the radial locations of the strain gages and the selected radial distance 7 mm was possibly based on their intuition/past experience. They observed that pulse duration was having significant effect on dynamic fracture toughness and reported that the with decrease in pulse duration to a particular limit there would be steep rise in dynamic fracture toughness.

Marur et al. [36] studied the influence of particle size and volume fraction on both the static and dynamic fracture toughness of a composite material. They

employed the DS technique for measuring the dynamic SIF. To measure dynamic strain and in turn, the SIF, a single strain gage was pasted at a distance of 0.6 times the thickness of the specimen from the crack tip to avoid the three dimensional effects. No investigation was conducted on whether the selected radial distance was within the realm of strain expressions employed in DS technique or not. Further, no discussion was also made on selection of radial locations for strain gages. It appears that the selected gage location was possibly based on their intuition/past experience. They reported that for a given volume fraction, smaller size particles reduce the dynamic fracture toughness.

Kirugulige and Tippur [37] studied mixed mode dynamic crack growth behavior in functionally graded glass filled epoxy sheets. In order to measure mode I crack initiation toughness of filler, they employed DS technique to obtain dynamic SIF histories. No explanation was made on the selected radial locations of the strain gages on the edge cracked beam specimen. It appears that the selected gage locations were based on their intuition/past experience. Experiments were conducted by alternating load on stiffer side and compliant side.

While studying the viscoelastic effect on the dynamic fracture toughness of a glass fiber reinforced polyester composite, Shirley and Homma [38] employed the DS technique for measurement of dynamic SIF under various loading rates. They pasted a strain gage at a distance of 7mm from the crack tip. No explanation/remarks were provided for the selected radial distance for the strain gage. They observed that the fracture toughness based on stress singularity is significantly affected by the loading rate and while one based on the strain singularity is less affected by the loading rate. They reported that to fully understand loading rate on the dynamic fracture toughness in addition to the fracture behavior for viscoelastic materials, interfacial bonding strength under different loading conditions must be considered.

To verify static mode I SIFs obtained from experimental method with the numerical method, Swamy et al. [39] used DS technique to various finite edge cracked configurations made of PMMA material. In all the specimens the strain gages were pasted at a constant distance of 10 mm from crack tip based on their previous

experience. No discussion on valid or optimal radial locations for strain gages was made. The mode I SIFs were determined for different height to crack length ratio. Reasonably good agreement between the results of mode I SIFs obtained using numerical and experimental investigations were reported.

Wadgaonkar and Parameswaran [40] employed the DS technique for measurement of mode I SIFs on epoxy side and glass bead side of a graded material system. Experiment was conducted on a single edge notch specimen subjected to four point bending. To determine SIFs, two strain gages were installed, one at epoxy rich surface and another at glass bead surface at a radial distance of $3/4^{\text{th}}$ of thickness of the plate from the crack tip to avoid three dimensional effects and strain gradients. No further information on radial locations was provided. It seems that the selected radial distance of strain gages may be based on their intuition/past experience. The results showed that the SIFs on the stiffer face of the plate were more than two times those on compliant face.

2.2 Strain gage techniques for determination of mode II SIFs

The strain gage technique was also successfully applied for determination of mode II SIFs. Kalthoff and Burgel [41] modified the DS technique for determination mode II SIF. They employed this technique while studying the influence of loading rate on shear fracture toughness of chromium steel and a high strength aluminum alloy. Though, they [41] completely realized the importance of radial locations of the strain gages to avoid plasticity effects and effects of higher order terms, the selected strain gage locations however were based on additional calibration experiments with the strain gages in a quasi-static pre-experiment. For determination of mode II SIF at the moment of fracture, two strain gages were mounted at distances of 10.5 and 15.5 mm. No further explanation on the radial locations was reported in their work. They observed that the loading rate significantly influences the shear fracture toughness of the material.

2.3 Strain gage techniques for determination of mixed mode I/II SIFs

Very limited amount of published work is available on applications of strain gage techniques for determination of mixed mode I/II SIFs for isotropic materials. The very first work in this direction was due to Dally and Berger [42] who extended DS technique to the mixed mode strain field for the determination of static SIFs K_I and K_{II} in isotropic materials. More number of parameters was employed in their method as compared to DS technique so that the strain gages could be placed at greater distances from the crack tip. Due to the use of multiparameter strain field representation, the region of strain field was increased substantially but at the same time more number of strain gages was required to find the unknown coefficients. Two ten element strip gages were pasted on both sides of crack axis in a slant edge cracked plate made of aluminum alloy at equal angle and at equal radius from crack tip to capture corresponding positive and negative strains. No guidelines or procedure was suggested on valid or optimal radial locations for strain gages. It appears that the placement of strip gages, from the crack tip was probably based on their intuition/past experience. It is clear that since they employed strip gages some of the gages may be at the optimal locations and others may be at unacceptable locations. The SIFs were obtained by graphical extrapolation technique. The SIFs obtained by experimental techniques were compared with both numerical result and published result. An error of about 16.4% in K_I and 29% in K_{II} were reported when they compared their experimental values with the published data. In the present investigation, henceforth, Dally and Berger [42] mixed mode technique is termed as *DB technique* throughout the present investigation.

Kondo et al. [43] proposed a strain gage method for determination of mixed mode SIFs of sharp notched strips. In this technique it was necessary to position the strain gage along more than two different directions for determination of mixed mode SIFs. They employed two strip gages containing five elements for measuring strain along two rays from the bisector angle of the notch. The radial locations of each strain gage were selected based on the theory given by Dally and Sanford [22] for minimizing the averaging errors in gages. No procedure was discussed for valid or

optimal radial locations of strain gages. The experimental results of mode I and mode II SIFs were consistently smaller than the theoretical results and within 10% difference for various notch angles and shapes.

Another strain gage technique for determination of mixed mode SIFs was proposed by Dorogoy and Rittel [44] using strain gage rosettes instead of single element gages. The procedure for obtaining the SIFs was presented using numerical studies on a slant edge cracked plate and no experimental results were reported. They observed from the numerical analysis that the radial location of rosette was an important factor in accurate measurement of SIFs. They recommended that the rosette should be placed as close as possible to the crack tip but out side the plastic zone and three dimensional effects which clearly demands knowledge of unknown SIFs. From the numerical example, they suggested the use of two strain gage rosettes at the same angle and linearly extrapolate their results for obtaining reasonably accurate mixed mode SIFs.

Multiphase material interfaces are found in many applications. The interface between the two materials is a plane of low strength. Fracture starts along the interface. The determination of fracture toughness of bimaterial interface is important in advanced material systems. It is represented by a complex SIF which is a combination of both tensile and shear effect that are intrinsically linked and therefore inseparable. Therefore, both mode I and mode II SIFs are required to represent the complex SIF. As a consequence some strain gage techniques have also been developed for bimaterial systems.

Ricci et al. [45] were first to apply the strain gage technique to determine complex SIFs in bimaterial system of PSM-1 and aluminum under quasi-static loading. Singular radial strain field equations were derived from stress field equations. In their technique mixed mode SIFs were determined using singular or leading strain field terms without considering subsequent higher order terms. As a consequence, the two SIFs were determined using only two strain gages which were necessarily to be placed within the singularity dominated zone. From a series of parametric studies they decided that the radial distance more than or equal to half the specimen thickness was sufficient to measure the strain accurately without affected by strain gradient,

plasticity and three dimensional effects. However, no explanation was provided as the selected radial distance was within the singularity dominated zone or not i.e., within the realm of selected strain terms. They reported that the mixed mode SIFs K_I and K_{II} obtained by strain gage method deviated from theoretical values by 11% and 4% respectively.

Marur and Tippur [46] developed a strain gage technique for determination of complex SIF in bimaterial systems. As in the case of Ricci et al. [45] technique, only singular strain terms were considered for representation of strain field ahead of the crack tip. Unlike Ricci et al. [45], Marur and Tippur [46] considered both the radial and hoop strains for the determination of mixed mode SIFs and therefore a strain rosette was employed for experimental determination of SIFs. They selected the radial distance for the strain gages from the parametric studies presented by Ricci et al. [45] and no explanation was provided as to whether the selected radial distances were within the singularity dominated zone or not. The angular position of the rosette was selected based on conditioning of the coefficient matrix and to maximize the sensitivity of the measurements. The results corresponding to static and dynamic loading conditions showed that the complex SIFs obtained by strain gage method were in agreement with the finite element estimations.

Ricci et al. [47] extended the strain gage technique developed by Ricci et al. [45] for subsonic dynamic loading conditions of isotropic-isotropic bimaterial systems. They selected the radial distance for the strain gages from the parametric studies presented by Ricci et al. [45] and no explanation was provided as to whether the selected radial distances were within the singularity dominated zone or not. The angular position was again based on the parametric study which maximized the sensitivity of strain measurement. Results obtained using their strain gage technique were in agreement with the photoelastic results.

Ricci et al. [48] extended their strain gage technique presented in Ref. [47] to isotropic- orthotropic bimaterial interface. Again they selected the radial distance for the strain gages from the parametric studies presented by Ricci et al. [45] and no explanation was provided as to whether the selected radial distances were within the

singularity dominated zone or not. As stated earlier, these locations were selected to avoid three dimensional and plasticity effects at the crack tips. For the experiments, four strain gages were mounted in a row. The orientation of strain gages were decided based on peak strain profile. Results showed that the complex SIF obtained by strain gage method was in agreement with results obtained by photoelasticity method.

To the best of author's knowledge the very early attempt on determination of optimal strain gage locations corresponding to the DS technique was proposed by Kaushik and Murthy [49]. Their estimation was based on the extent of applicability of assumed strain distribution in the DS technique. Although, the proposed technique was applicable for all configurations, it is observed that their approach resulted into highly inconsistent and over estimated values optimal gage locations. No experimental study was conducted for verification of the estimated gage locations. Due to erroneous estimations, many important results were obscured.

2.4 Summary of literature review and objectives

The extensive literature review could be surmised as follows.

- There has been number of works reported in the determination SIFs using strain gages.
- The DS technique has been observed to be very popular and is applied as it is in many investigations of static and dynamic loading conditions. Further it has been extended to other areas for determination of SIFs.
- The DS technique is very widely employed as compared to the other techniques due to the reason that only a single strain gage is sufficient to determine mode I SIF and this gage can be located at a radial distance far from crack tip where the effects of plasticity, three-dimensional state of stress and strain gradients are very minimal.
- No works are reported on use of existing strain gage techniques (on mixed mode SIFs) for experimental determination of mixed mode SIFs in two dimensional configurations.

- Although, DB technique for determination of mixed mode SIFs has not been employed for experimental determination of mixed mode SIFs by other researchers, but it is a well-known technique in fracture mechanics literature. This is due to the reason that this technique is an extension of well-known and theoretically sound DS technique to the mixed mode problems.
- Locations of strain gages play a vital role in accurate determination of SIFs and Dally and Sanford [22] and Dally and Berger [42] suggested that the strain gage should be placed in the region II in order to avoid strain gradient effect, plasticity effect and three-dimensional effect.
- Even though many papers reported strain gage based methods for determination of SIFs but none of these provided any useful recommendations or guidelines or any methodology to estimate the valid strain gage locations for accurate experimental determination of SIFs. This is especially true for DS and DB techniques despite their popularity. This may perhaps be the reason why these two techniques in spite of their popularity have not been extensively used for experimental verification of the analytically or numerically obtained SIFs. In contrast, validation has been carried out using other experimental techniques such as photoelastic technique and caustic technique. Such investigations only establish the existing techniques as useful tools in real design situations of great complexity.

Therefore, determination of valid or optimal strain gage locations for accurate determination of SIFs using DS and DB techniques is an important issue in experimental fracture mechanics which has not been addressed until now [16]. Clearly, successful development of such methodologies to provide a priori knowledge of valid strain gage locations for accurate determination of SIFs will be a significant contribution in the area of experimental fracture mechanics. Keeping this in mind, the objectives of the present thesis have been laid as:

- 1 To develop a methodology for deciding optimal radial location of strain gage for accurate determination of mode I SIF using DS technique in two

dimensional cracked configurations made of homogeneous and isotropic materials.

- 2 To determine optimal strain gage locations for important single and double ended cracked configurations for accurate determination of mode I SIFs.
- 3 To develop a modified DB technique using multiple strain gages for more reliable determination of mixed mode SIFs K_I and K_{II} .
- 4 To develop a methodology for deciding optimal radial locations of strain gages using modified DB technique for accurate determination of mixed mode SIFs in two dimensional cracked configurations made of homogeneous and isotropic materials.
- 5 To determine optimal strain gage locations for important single ended mixed mode cracked configurations for accurate determination of mixed mode SIFs.
- 6 To study the effect of crack length to width ratio on the maximum permissible radial location of strain gages in determining mode I and mixed mode SIFs.
- 7 To study the effect state of stress (plane stress or plane strain) of the cracked configuration on the maximum permissible radial location of strain gages in determining mode I and mixed mode SIFs.
- 8 To study the effect of Poisson's ratio on the maximum permissible radial location of strain gages.
- 9 To conduct experiments using strain gages (a) to determine mode I and mixed mode SIFs (b) to substantiate the importance of placing strain gages in optimal locations (obtained from the present methodologies) in accurate determination of SIFs (c) to verify the erroneous determination of SIFs when strain gages are placed in non-optimal locations (d) to verify the effect of crack length to width ratio on the maximum permissible radial location for strain gages.

Chapter 3

Theoretical Background and Formulations

This chapter describes the theoretical formulation supporting the estimation of valid radial locations for strain gages for accurate determination of stress intensity factors in mode I and mixed mode (I/II) cases. For numerical analyses, finite element method has been used in the present investigation. The finite element formulation for modeling the crack tip and discretization of the geometry of the cracked specimen has been discussed in brief.

3.1 The generalized Westergaard approach

The generalized Westergaard approach proposed by Sanford [50] is a generalization of the familiar Westergaard stress function approach [4] to include the finite bodies subjected to arbitrary surface tractions and containing a single ended crack and double ended crack (internal crack) with traction free crack faces. For the case of a single ended crack the method is functionally equivalent to the well-known Williams eigenfunction expansion method [5]. The generalized Westergaard formulation requires an additional analytic function $Y(z)$ in addition to the standard Westergaard stress function $Z(z)$. Accordingly, the modified Airy stress function for mode I (ϕ_I) and mode II (ϕ_{II}) are then given by [50],

$$\phi_I = \text{Re } \overline{\overline{Z}}_I(z) + y \text{Im } \overline{\overline{Z}}_I(z) + y \text{Im } \overline{\overline{Y}}_I(z) \quad (3.1)$$

$$\phi_{II} = -y \text{Re } \overline{\overline{Z}}_{II}(z) + \text{Im } \overline{\overline{Y}}_{II}(z) - y \text{Re } \overline{\overline{Y}}_{II}(z) \quad (3.2)$$

where

$$\frac{d\overline{\overline{Z}}_i}{dz} = \overline{\overline{Z}}_i, \quad \frac{d\overline{\overline{Z}}_i}{dz} = \overline{\overline{Z}}_i, \quad \frac{d\overline{\overline{Y}}_i}{dz} = \overline{\overline{Y}}_i \quad \text{where } i = I, II \quad (3.3)$$

The complex analytic functions for opening mode $Z_I(z)$, $Y_I(z)$ and those for shearing mode $Z_{II}(z)$, $Y_{II}(z)$ are defined as

$$Z_I(z) = \sum_{n=0}^{\infty} A_n z^{n-\frac{1}{2}} \quad \text{and} \quad Y_I(z) = \sum_{m=0}^{\infty} B_m z^m \quad (3.4)$$

$$Z_{II}(z) = \sum_{n=0}^{\infty} C_n z^{n-\frac{1}{2}} \quad \text{and} \quad Y_{II}(z) = \sum_{m=0}^{\infty} D_m z^m \quad (3.5)$$

These are series type functions in terms of complex variable $z = x + iy$ (refer Fig. 3.1) containing infinite number of real coefficients corresponding to opening mode ($A_0, A_1, \dots, A_{\infty}; B_0, B_1, \dots, B_{\infty}$)

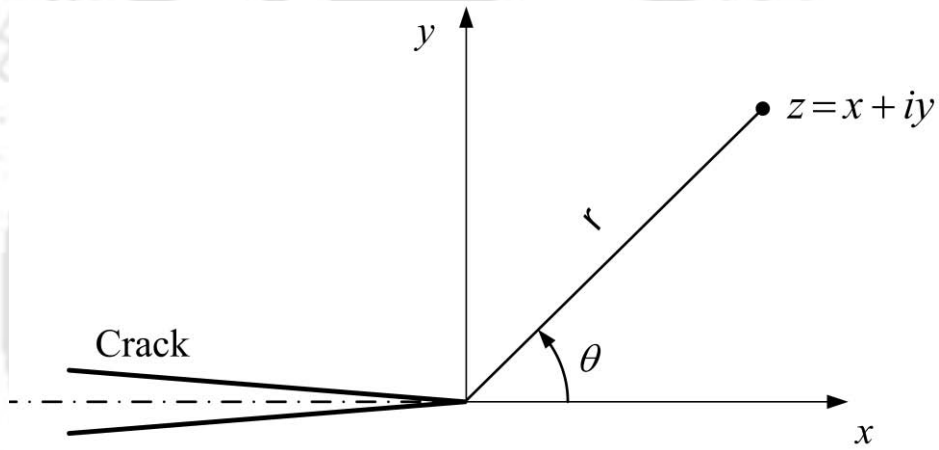


Figure 3.1 The complex plane at the crack tip

and shearing mode ($C_0, C_1, \dots, C_{\infty}; D_0, D_1, \dots, D_{\infty}$). These coefficients are functions of boundary conditions and geometry of the cracked configuration. It should be noted that the above approach is argued to be valid for any length of edge cracks (single ended) and only for sufficiently large double ended cracks (internal cracks) [13].

For a complex analytic function, such as $Z(z)$ the Cauchy-Riemann equations are given by

$$\begin{aligned} \frac{\partial \operatorname{Re} Z(z)}{\partial x} &= \operatorname{Re} Z' \quad \text{and} \quad \frac{\partial \operatorname{Im} Z(z)}{\partial x} = \operatorname{Im} Z' \\ \frac{\partial \operatorname{Re} Z(z)}{\partial y} &= -\operatorname{Im} Z' \quad \text{and} \quad \frac{\partial \operatorname{Im} Z(z)}{\partial y} = \operatorname{Re} Z' \end{aligned} \quad (3.6)$$

Using Cauchy-Riemann equations and Airy stress function approach, the stress components for mode I in the absence of body forces, then can be given as

$$\begin{aligned}\sigma_{xx} &= \frac{\partial^2 \phi_I}{\partial y^2} = \operatorname{Re} Z_I - y \operatorname{Im} Z'_I - y \operatorname{Im} Y'_I + 2 \operatorname{Re} Y_I \\ \sigma_{yy} &= \frac{\partial^2 \phi_I}{\partial x^2} = \operatorname{Re} Z_I + y \operatorname{Im} Z'_I + y \operatorname{Im} Y'_I \\ \tau_{xy} &= -\frac{\partial^2 \phi_I}{\partial x \partial y} = y \operatorname{Re} Z'_I - y \operatorname{Re} Y'_I - \operatorname{Im} Y_I\end{aligned}\quad (3.7)$$

and the stress components for the mode II can be obtained as

$$\begin{aligned}\sigma_{xx} &= \frac{\partial^2 \phi_{II}}{\partial y^2} = y \operatorname{Re} Z'_{II} + 2 \operatorname{Im} Z_{II} + y \operatorname{Re} Y'_{II} + \operatorname{Im} Y_{II} \\ \sigma_{yy} &= \frac{\partial^2 \phi_{II}}{\partial x^2} = -y \operatorname{Re} Z'_{II} - y \operatorname{Re} Y'_{II} + \operatorname{Im} Y_{II} \\ \tau_{xy} &= -\frac{\partial^2 \phi_{II}}{\partial x \partial y} = \operatorname{Re} Z_{II} - y \operatorname{Im} Z'_{II} - y \operatorname{Im} Y'_{II}\end{aligned}\quad (3.8)$$

Assuming plane stress conditions, the stress-strain relation for linear elastic and isotropic materials are given by

$$\begin{aligned}\varepsilon_{xx} &= \frac{1}{E} (\sigma_{xx} - \nu \sigma_{yy}) \\ \varepsilon_{yy} &= \frac{1}{E} (\sigma_{yy} - \nu \sigma_{xx}) \\ \gamma_{xy} &= \frac{\tau_{xy}}{G}\end{aligned}\quad (3.9)$$

Substituting Eq. (3.7) into Eq. (3.9) equations for strain field corresponding mode I can be obtained as

$$\begin{aligned}E \varepsilon_{xx} &= (1-\nu) \operatorname{Re} Z_I - (1+\nu) y \operatorname{Im} Z'_I - (1+\nu) y \operatorname{Im} Y'_I + 2 \operatorname{Re} Y_I \\ E \varepsilon_{yy} &= (1-\nu) \operatorname{Re} Z_I + (1+\nu) y \operatorname{Im} Z'_I + (1+\nu) y \operatorname{Im} Y'_I - 2\nu \operatorname{Re} Y_I \\ E \gamma_{xy} &= 2(1+\nu) (-y \operatorname{Re} Y'_I - \operatorname{Im} Y_I - y \operatorname{Re} Z'_I)\end{aligned}\quad (3.10)$$

Similarly substituting Eq. (3.8) into Eq. (3.9) the strain field corresponding to mode II can be obtained as

$$\begin{aligned} E \varepsilon_{xx} &= (1+\nu) y \operatorname{Re} Z'_{II} + 2 \operatorname{Im} Z_{II} + (1+\nu) y \operatorname{Re} Y'_{II} + (1-\nu) \operatorname{Im} Y_{II} \\ E \varepsilon_{yy} &= -(1+\nu) y \operatorname{Re} Z'_{II} - 2\nu \operatorname{Im} Z_{II} - (1+\nu) y \operatorname{Re} Y'_{II} + (1-\nu) \operatorname{Im} Y_{II} \quad (3.11) \\ E\gamma_{xy} &= 2(1+\nu)(-y \operatorname{Im} Y'_{II} - y \operatorname{Im} Z'_{II} + \operatorname{Re} Z_{II}) \end{aligned}$$

By integrating the strain components in Eq. (3.10) and neglecting rigid body modes of deformation, the displacement components for mode I can be obtained as

$$\begin{aligned} u &= \frac{1}{2G} \left[\frac{(1-\nu)}{(1+\nu)} \operatorname{Re} \bar{Z}_I - y \operatorname{Im} Z_I - y \operatorname{Im} Y_I + \frac{2}{(1+\nu)} 2 \operatorname{Re} \bar{Y}_I \right] \\ v &= \frac{1}{2G} \left[\frac{2}{(1+\nu)} \operatorname{Im} \bar{Z}_I - y \operatorname{Re} \bar{Z}_I - y \operatorname{Re} Y_I + \frac{(1-\nu)}{(1+\nu)} \operatorname{Im} \bar{Y}_I \right] \end{aligned} \quad (3.12)$$

and that for mode II (by integrating Eq. (3.11)) are obtained as

$$\begin{aligned} u &= \frac{1}{2G} \left[\frac{2}{(1+\nu)} \operatorname{Im} \bar{Z}_{II} + y \operatorname{Re} Z_{II} + \frac{(1-\nu)}{(1+\nu)} \operatorname{Im} \bar{Y}_{II} + y \operatorname{Re} \bar{Y}_{II} \right] \\ v &= \frac{1}{2G} \left[-y \operatorname{Im} Z_{II} + \frac{(\nu-1)}{(1+\nu)} \operatorname{Re} \bar{Z}_I - y \operatorname{Im} Y_{II} - \frac{2}{(1+\nu)} \operatorname{Re} \bar{Y}_{II} \right] \end{aligned} \quad (3.13)$$

Equations corresponding to plane strain can be obtained by replacing E by $E/(1-\nu^2)$ and ν by $\nu/(1-\nu)$ in Eqs. (3.10) – (3.13).

Substitution of series form of complex functions $Z_I(z)$, $Y_I(z)$, $Z_{II}(z)$ and $Y_{II}(z)$ from Eqs. (3.4) and (3.5) into Eqs. (3.7) and (3.8) and Eqs. (3.10) – (3.13) gives exact representation of stress, strain and displacement fields with infinite number of unknown coefficients A_n , B_m , C_n and D_m . The *first term* or the *leading term* in these series are extremely important in LEFM and play vital role in K -based fracture criterion. This term can be obtained by substituting $m = 0$, $n = 0$ and $r = \cos \theta + i \sin \theta$ in Eqs. (3.7) and (3.8) and Eqs. (3.10) – (3.13).

3.1.1 Leading terms for mode I loading

The expressions for leading term for stress and strain components corresponding to mode I loading are given by

$$\begin{aligned}\sigma_{xx} &= A_0 r^{-1/2} \cos \frac{\theta}{2} \left[1 - \sin \frac{\theta}{2} \sin \frac{3\theta}{2} \right] \\ \sigma_{yy} &= A_0 r^{-1/2} \cos \frac{\theta}{2} \left[1 + \sin \frac{\theta}{2} \sin \frac{3\theta}{2} \right] \\ \tau_{xy} &= A_0 r^{-1/2} \cos \frac{\theta}{2} \sin \frac{\theta}{2} \sin \frac{3\theta}{2} \\ \sigma_{zz} &= 0 \text{ for plane stress}\end{aligned}\quad (3.14)$$

and

$$\begin{aligned}E\varepsilon_{xx} &= A_0 r^{-1/2} \cos \frac{\theta}{2} \left[(1-\nu) - (1+\nu) \sin \frac{\theta}{2} \sin \frac{3\theta}{2} \right] \\ E\varepsilon_{yy} &= A_0 r^{-1/2} \cos \frac{\theta}{2} \left[(1-\nu) + (1+\nu) \sin \frac{\theta}{2} \sin \frac{3\theta}{2} \right] \\ 2G\gamma_{xy} &= A_0 r^{-1/2} \sin \theta \cos \frac{3\theta}{2}\end{aligned}\quad (3.15)$$

The displacement field near the crack tip under plane stress conditions can be obtained as

$$\begin{aligned}Gu &= A_0 r^{1/2} \cos \frac{\theta}{2} \left[\frac{(1-\nu)}{(1+\nu)} - \sin^2 \frac{\theta}{2} \right] \\ Gv &= A_0 r^{1/2} \sin \frac{\theta}{2} \left[\frac{2}{(1+\nu)} - \cos^2 \frac{\theta}{2} \right]\end{aligned}\quad (3.16)$$

It is clear from Eqs. (3.14) and (3.15) that each stress and strain component is inversely proportional to the square of the radial distance r of a point from the crack tip and they tend to infinity as r approaches to zero. Such solutions are also called as *singular solutions*. Unlike the stress and strain components the displacement equations do not contain singularity and are finite near the crack tip. This is a typical characteristic of LEFM. The stress intensity factor K_I is formally defined as

$$K_I = \lim_{r \rightarrow 0} \sqrt{2\pi r} \sigma_{yy} (r, \theta = 0^0) \quad (3.17)$$

which relates K_I to A_0 as

$$K_I = \sqrt{2\pi} A_0 \quad (3.18)$$

3.1.2 Leading terms for mode II loading

The expressions for leading term for the stress, strain and displacement components near the crack tip for plane stress conditions corresponding to mode II loading are given by

$$\begin{aligned} \sigma_{xx} &= -C_0 r^{-1/2} \sin \frac{\theta}{2} \left[2 + \cos \frac{\theta}{2} \cos \frac{3\theta}{2} \right] \\ \sigma_{yy} &= C_0 r^{-1/2} \sin \frac{\theta}{2} \cos \frac{\theta}{2} \cos \frac{3\theta}{2} \\ \tau_{xy} &= C_0 r^{-1/2} \cos \frac{\theta}{2} \left[1 - \sin \frac{\theta}{2} \sin \frac{3\theta}{2} \right] \\ \sigma_{zz} &= 0 \text{ for plane stress} \end{aligned} \quad (3.19)$$

and

$$\begin{aligned} E\varepsilon_{xx} &= -C_0 r^{-1/2} \sin \frac{\theta}{2} \left[2 + (1+\nu) \cos \frac{\theta}{2} \cos \frac{3\theta}{2} \right] \\ E\varepsilon_{yy} &= C_0 r^{-1/2} \sin \frac{\theta}{2} \left[2\nu + (1+\nu) \cos \frac{\theta}{2} \cos \frac{3\theta}{2} \right] \\ G\gamma_{xy} &= C_0 r^{-1/2} \cos \frac{\theta}{2} \left[1 - \sin \frac{\theta}{2} \sin \frac{3\theta}{2} \right] \end{aligned} \quad (3.20)$$

The displacement field near the crack tip under plane stress conditions can be obtained as

$$\begin{aligned} Gu &= C_0 r^{1/2} \sin \frac{\theta}{2} \left[\frac{2}{(1+\nu)} + \cos^2 \frac{\theta}{2} \right] \\ Gv &= C_0 r^{1/2} \cos \frac{\theta}{2} \left[-\frac{(1-\nu)}{(1+\nu)} + \sin^2 \frac{\theta}{2} \right] \end{aligned} \quad (3.21)$$

Once again the singular behavior in stress and strain components can also be noticed in mode II loading from Eqs. (3.19) and (3.20). The stress intensity factor K_{II} can be defined as

$$K_{II} = \lim_{r \rightarrow 0} \sqrt{2\pi r} \tau_{xy}(r, \theta = 0^0) \quad (3.22)$$

which leads to the relationship between K_{II} and C_0 as

$$K_{II} = \sqrt{2\pi} C_0 \quad (3.23)$$

Thus the coefficients A_0 and C_0 are related to the SIFs K_I and K_{II} respectively.

3.2 Dally and Sanford [22] technique for the determination of K_I

Irwin [17] was the first to suggest the use of strain gages for experimental determination of SIFs. However, difficulties such as three dimensional effect, local yielding or plasticity effect and strain gradient effect were observed in application of this strain gage methods for long time. Due to the development in strain gage technology, the strain gradient effects were greatly minimized due to the use of small strain gages. However, three dimensional effect and plasticity effects significantly influence the strain gage readings. Dally and Sanford [22] single strain gage technique (DS technique) was the first successful technique proposed to minimize significantly the effect of strain gradient, 3D and plasticity effects by allowing the placement of gages far away from the crack tip. It is a highly practically feasible technique and is based on the strong theoretical foundations. This technique has been most widely employed for the determination of K_I using strain gages.

A major benefit of their technique is that only a single strain gage is sufficient to measure the K_I and which can be placed considerably away from the crack tip in order to avoid strain gradient, plasticity and 3D effects. An important feature of DS technique is the identification of an appropriate zone around the crack tip for strain measurements which may not be influenced by aforesaid effects. SIFs are then

determined by equating the measured strains with the theoretical strain series that is valid within the measurement zone. In DS technique, the region around a crack tip is divided into three zones viz. *zone I*, *zone II* and *zone III* as shown in Fig. 3.2 in order to identify the suitable zone for strain measurements. Zone I is close to the crack tip and first term of the strain series (singular strain term) in Eq. (3.15) is sufficient to represent the strains within this zone. However, it is not a valid zone for accurate measurement of strains as the stress state in this region could be three dimensional [22] and the measured strains will be severely affected by plasticity, 3D and strain gradient effects.

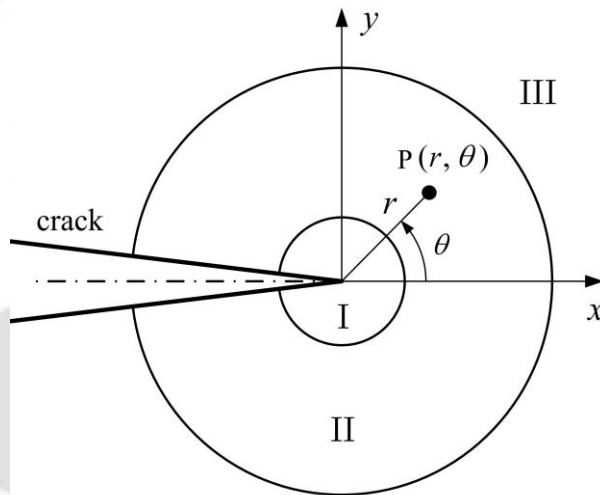


Figure 3.2 Different zones at the crack tip [22]

Zone III is again not suitable for collection of strain data as a very large number of terms in the strain series is required to yield accurate results. Therefore, the intermediate region or zone II is favorable and optimum zone for accurate measurement of the surface strains. This is defined as a zone in which a singular term plus a small number of higher order terms would accurately describe the strain field within this zone. It is assumed that the strain field for the mode I in the zone II can be sufficiently represented by the three parameter series with unknown parameters or coefficients A_0 , A_1 and B_0 [22] as opposed to infinite number of coefficients in the strain series (Eq. 3.10). The three term representation of strain field or the truncated strain series in this zone can therefore be written as

$$\begin{aligned}
 2G\varepsilon_{xx} &= A_0 r^{-1/2} \cos \frac{\theta}{2} \left[\kappa - \sin \frac{\theta}{2} \sin \frac{3\theta}{2} \right] + \frac{2B_0}{(1+\nu)} + A_1 r^{1/2} \cos \frac{\theta}{2} \left[\kappa + \sin^2 \frac{\theta}{2} \right] \\
 2G\varepsilon_{yy} &= A_0 r^{-1/2} \cos \frac{\theta}{2} \left[\kappa + \sin \frac{\theta}{2} \sin \frac{3\theta}{2} \right] - \frac{2\nu B_0}{(1+\nu)} + A_1 r^{1/2} \cos \frac{\theta}{2} \left[\kappa - \sin^2 \frac{\theta}{2} \right] \quad (3.24)
 \end{aligned}$$

$$2G\gamma_{xy} = A_0 r^{-1/2} \left[\sin \theta \cos \frac{3\theta}{2} \right] - A_1 r^{1/2} \left[\sin \theta \cos \frac{\theta}{2} \right]$$

where $\kappa = (1-\nu)/(1+\nu)$ for plane stress and A_0 , A_1 and B_0 are unknown coefficients which can be determined using geometry of the specimen and loading conditions and are independent of state of stress. Thus by measuring A_0 one can determine K_I using Eq. (3.18). The normal strain component ε_{aa} defined by an angle α with the crack axis (positive to crack axis) at a point P located by r and θ (Fig. 3.3) can be obtained using strain transformation laws as

$$\begin{aligned}
 2G\varepsilon_{aa} &= A_0 r^{-1/2} \left[\kappa \cos \frac{\theta}{2} - \frac{1}{2} \sin \theta \sin \frac{3\theta}{2} \cos 2\alpha + \frac{1}{2} \sin \theta \cos \frac{3\theta}{2} \sin 2\alpha \right] \\
 &+ A_1 r^{1/2} \cos \frac{\theta}{2} \left[\kappa + \sin^2 \frac{\theta}{2} \cos 2\alpha - \frac{1}{2} \sin \theta \sin 2\alpha \right] + B_0 (\kappa + \cos 2\alpha) \quad (3.25)
 \end{aligned}$$

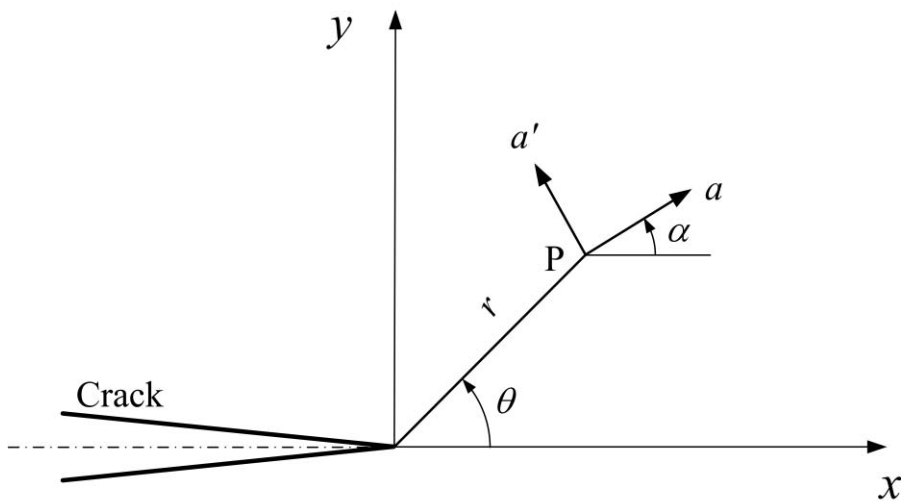


Figure 3.3 Strain gage location and orientation

The coefficient of B_0 term in Eq. (3.25) can be eliminated by selecting the angle α such that

$$\cos 2\alpha = -\kappa = -\frac{1-\nu}{1+\nu} \quad (3.26)$$

Similarly coefficient of A_1 can also be made zero if the angle θ (Fig. 3.3) is selected as

$$\tan \frac{\theta}{2} = -\cot 2\alpha \quad (3.27)$$

Thus by placing a single strain gage (Fig. 3.4) on the radial line OS defined by θ (Eq. (3.27)) at an appropriate radial distance r from the crack tip and orienting the gage at an angle α (according Eq. (3.26)), the strain ε_{aa} can be measured and which in turn is related to K_I by

$$2G\varepsilon_{aa} = \frac{K_I}{\sqrt{2\pi r}} \left[\kappa \cos \frac{\theta}{2} - \frac{1}{2} \sin \theta \sin \frac{3\theta}{2} \cos 2\alpha + \frac{1}{2} \sin \theta \cos \frac{3\theta}{2} \sin 2\alpha \right] \quad (3.28)$$

Thus, from the selected values of Poisson's ratio ν and radial distance r , K_I can be determined from the measured strain ε_{aa} . It may be noted from Eqs. (3.26) and (3.27) that K_I can also be determined by placing a strain gage on the line OT which makes an angle of $-\theta$ with respect to the crack axis. In such case the orientation angle of the gage should be $-\alpha$ as shown in Fig. 3.4.

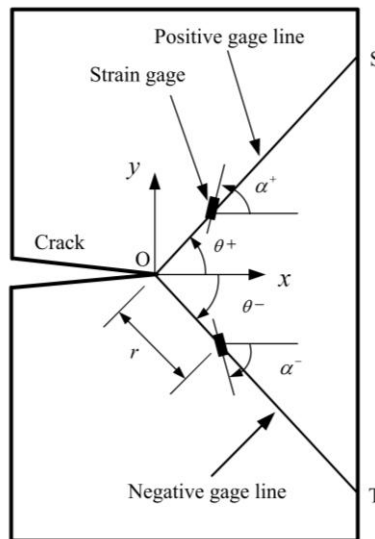


Figure 3.4 Gage lines and strain gage location for mode I

It may be observed from the description of DS technique that while analytical expressions are available for deciding angular placements α and θ (Eqs. (3.26) and (3.27)) for locating the single strain gage but no means are available for deciding or selecting radial location r for the strain gage. As shown Fig. 3.4 the line OS and OT defined by positive θ and negative θ (Eq. (3.27)) respectively are termed in the present investigation as the *positive gage line* and *negative gage line* respectively. Thus these are the radial lines on either of which a strain gage is to be pasted according to DS technique, for the determination of K_I . The gage lines start at the crack tip and terminate at the outer boundaries of the cracked plate.

3.3 Proposed approach for the determination of optimal radial locations for strain gage for the determination of K_I

As noted earlier, although the angular positions for the strain gages such as α and θ are very well defined for a particular material but the radial distance r at which the gage needs to be placed to avoid 3D effects, plasticity effects and strain gradient effects is not available. It is also evident from Eq. (3.28) that prior knowledge of valid gage location or radial distance is extremely important for use of the Eq. (3.28) in determination of accurate values of K_I according to DS technique.

As described earlier, if the gages are located very close to the crack tip (due to lack of prior values of the valid radial distance for gage) then the strain measurements may be affected by strain gradients, 3D and plasticity effects. On the other hand if the gages are located significantly far away from the crack tip then the Eq. (3.28) may not be applicable for strain measurements although the aforesaid effects can be avoided at such locations. This is because the measured strain at such a large distance may also have contribution due to the coefficients other than A_0 , A_1 and B_0 . Therefore prior knowledge of valid radial location or distance for strain gage is essential to take the complete advantage of DS technique for the accurate determination of K_I .

Several experimental and numerical studies have established that 3D effects prevailed up to a radial distance equal to half the thickness of the plate from the crack

tip [21]. It was reported that the state of stress is neither plane stress nor plane strain within this distance [21]. Therefore, the minimum radial distance r_{\min} for strain measurements on the free surface (which are under plane stress conditions) should be greater than half the thickness of the plate [21]. As a consequence, the optimal or valid radial location r for strain gage in DS technique can now be given as

$$r_{\min} (= \frac{1}{2}\text{thickness of plate}) \leq r \leq r_{\max} \quad (3.29)$$

where r_{\max} is defined as the maximum radial distance from the crack tip or the upper bound for the valid radial location for the strain gage. As described above, Eq. (3.28) is valid only upto a certain radial distance from the crack tip and beyond that radial distance more number of coefficients or parameters other than A_0 , A_1 and B_0 are needed to represent the strain field. The r_{\max} , thus conversely can be defined as the extent of validity of Eq. (3.28) or extent of three parameter representations along the radial line defined by θ (Eq. (3.27)). Further, r_{\max} can also be interpreted as the extent of zone II. Thus determination of the r_{\max} is the solution to the problem of determination of optimal radial location for strain gage. The proposed theoretical basis for the determination of r_{\max} is described in the following.

Eq. (3.28) can be rewritten as

$$\varepsilon_{aa} = \frac{1}{\sqrt{r}} \left[\frac{K_I}{G\sqrt{8\pi}} \left(\kappa \cos \frac{\theta}{2} - \frac{1}{2} \sin \theta \sin \frac{3\theta}{2} \cos 2\alpha + \frac{1}{2} \sin \theta \cos \frac{3\theta}{2} \sin 2\alpha \right) \right] \quad (3.30)$$

Thus, for a given configuration, applied load, Young's modulus E and Poisson's ratio ν the expression within the square bracket on the right hand side of Eq. (3.30) is a constant. Therefore,

$$\varepsilon_{aa} = \frac{C}{\sqrt{r}} \quad (3.31)$$

where C is a constant. Taking logarithm on both sides of Eq. (3.31)

$$\ln(\varepsilon_{aa}) = -\frac{1}{2} \ln(r) + \ln(C) \quad (3.32)$$

Clearly Eq. (3.32) is valid along the line given by Eq. (3.27) for $r \leq r_{\max}$. Thus a plot of Eq. (3.32) ($\ln(\varepsilon_{aa})$ versus $\ln(r)$) depicts a straight line of slope equals to -0.5 , with an intercept of $\ln(C)$. Theoretically, the straight line property will break beyond $r > r_{\max}$ as more than three parameters (A_0 , A_1 and B_0) are needed in Eq. (3.25) or Eq. (3.28) to estimate the ε_{aa} . Using the straight line property exhibited by Eq. (3.32), the value of r_{\max} can be accurately estimated from the plots of $\ln(\varepsilon_{aa})$ and $\ln(r)$. The forgoing discussion indicates that the graph of the $\ln(\varepsilon_{aa})$ versus $\ln(r)$ should have a initial straight line portion of slope equals to -0.5 followed by a non-linear portion as shown in Fig. 3.5(a). This nonlinear portion is due to the domination of parameters or coefficients other than A_0 , A_1 and B_0 in Eq. (3.28). Evidently, the r_{\max} is then the radial distance at which the straight line portion terminates and nonlinear portion begins (Fig. 3.5(b)). The extent of straight line portion is clearly a function of A_0 , A_1 and B_0 . Therefore, the r_{\max} is in turn a function of geometry of the given cracked body and boundary conditions.

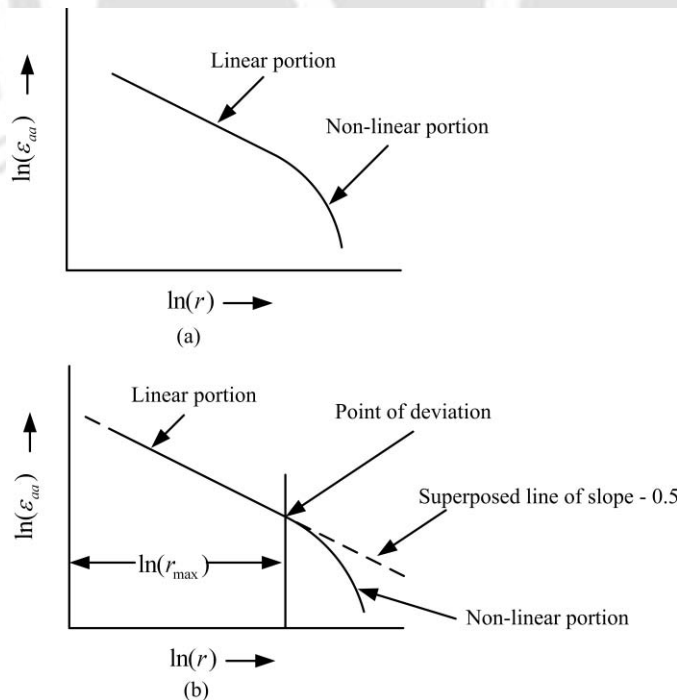


Figure 3.5 (a) Plot of $\ln(\varepsilon_{aa})$ versus $\ln(r)$ (b) linear and non-linear variation of $\ln(\varepsilon_{aa})$ and $\ln(r)$ along the gage line

Once the r_{\max} value of a cracked configuration is determined, then valid or optimal strain gage location that will ensure correct measurement of strains according to Eq. (3.28) can be easily obtained using Eq. (3.29). In order to take full advantage of DS technique for avoiding strain gradient, plasticity and 3D effects, Eq. (3.32) indicates that the strain gage can be pasted very close to r_{\max} (but not beyond r_{\max}) yet the gage readings can be expected to obey Eq. (3.30). Thus experimentalist can easily decide valid gage locations using Eq. (3.29) depending on material of the specimen.

In the present investigation a finite element based approach is proposed for the first time for accurate determination of r_{\max} value of a given cracked configuration. In this approach, the strain ε_{aa} at a large number of points along the positive gage line (OS in Fig. 3.4) is computed using finite element analysis (FEA) of the cracked domain. In fact, negative gage line (instead of positive gage line) and any other appropriate numerical method (instead of FEA) can also be chosen for computations of the strain defined by α and θ given by Eq. (3.26) and Eq. (3.27) respectively. If the proposed theoretical basis presented in this section are correct then a graph similar to that shown in Fig. 3.5(a) can be obtained on the log-log scale with a distinct linear and non-linear portions.

Because of logarithmic plot a reliable procedure is needed for accurate identification of end point of the straight line portion. For this purpose the following procedure is devised in the present investigation.

- (a) First a line of slope -0.5 is superposed on to the plots of $\ln(\varepsilon_{aa})$ versus $\ln(r)$ as shown in Fig. 3.5(b).
- (b) This line is considered as the exact solution and absolute percent relative error in computed values of $\ln(\varepsilon_{aa})$ is then determined at all values of radius in the plot. The error can be expected to be very large in the non-linear portion and gradually diminishes as one approaches toward the points corresponding to the line in Eq. (3.32).

- (c) Finally, the r_{\max} or the point of deviation on the log-log plot from the superposed line is evaluated as the value of the radius at which the error reaches a value $\leq 0.5\%$ (as one observes from right to left in Fig. 3.5(b)).

3.4 Dally and Berger [51] strain gage technique for determination of mixed mode SIFs K_I and K_{II}

Frequently, mixed mode conditions are produced due to the orientation of the crack with respect to the loading. In 2D solutions, mixed mode loading indicates simultaneous occurrence of the opening mode (mode I) and shearing mode (mode II) for which both K_I and K_{II} are needed to describe the conditions near the crack tip. Dally and Berger [42, 51] were the first to extend the Dally and Sanford [22] strain gage technique for the determination of K_I and K_{II} in 2D cracked bodies. The strain field at any point within the cracked body for mixed mode I/II loading can be found by simply superposing strain fields for mode I (Eq. (3.10)) and that of mode II (Eq. (3.11)).

Referring to Fig. 3.2, the region around a crack tip is again divided into three zones viz. *zone I*, *zone II* and *zone III* in a similar way as that of DS technique. Again, the zone I is not considered suitable for strain measurements as it is prone to plasticity, strain gradient and 3D effects. Further, zone III is also not suitable due to the requirement of large number of unknown coefficients in strain representation. Therefore, zone II is again suitable for strain measurements and is assumed to be composed of the leading term and a few higher order terms.

In Dally and Berger [42, 51] technique, it was assumed that the mixed mode strain field in the zone II can be represented accurately by four parameter strain series containing mode I coefficients A_0, A_1, B_0, B_1 and mode II coefficients C_0, C_1, D_0, D_1 . Accordingly, the rectangular strain components $\varepsilon_{xx}, \varepsilon_{yy}$ and γ_{xy} (in terms of both mode I and mode II coefficients) at any point within the zone II for plane stress conditions can be obtained using Eqs. (3.10) and (3.11) as

$$\begin{aligned}
 E\varepsilon_{xx} = & A_0 r^{-1/2} \cos \frac{\theta}{2} \left[(1-\nu) - (1+\nu) \sin \frac{\theta}{2} \sin \frac{3\theta}{2} \right] + A_1 r^{1/2} \cos \frac{\theta}{2} \\
 & \left[(1-\nu) + (1+\nu) \sin^2 \frac{\theta}{2} \right] + 2B_0 + 2B_1 r \cos \theta - C_0 r^{-1/2} \sin \frac{\theta}{2} \\
 & \left[(1+\nu) \cos \frac{\theta}{2} \cos \frac{3\theta}{2} + 2 \right] + C_1 r^{1/2} \sin \frac{\theta}{2} \left[2 + (1+\nu) \cos^2 \frac{\theta}{2} \right] \\
 & + 2D_1 r \sin \theta
 \end{aligned} \tag{3.33}$$

$$\begin{aligned}
 E\varepsilon_{yy} = & A_0 r^{-1/2} \cos \frac{\theta}{2} \left[(1-\nu) + (1+\nu) \sin \frac{\theta}{2} \sin \frac{3\theta}{2} \right] + A_1 r^{1/2} \cos \frac{\theta}{2} \\
 & \left[(1-\nu) - (1+\nu) \sin^2 \frac{\theta}{2} \right] - 2\nu B_0 - 2\nu B_1 r \cos \theta + C_0 r^{-1/2} \sin \frac{\theta}{2} \\
 & \left[2\nu + (1+\nu) \cos \frac{\theta}{2} \cos \frac{3\theta}{2} \right] - C_1 r^{1/2} \sin \frac{\theta}{2} \left[2\nu + (1+\nu) \cos^2 \frac{\theta}{2} \right] \\
 & + 2D_1 r \nu \sin \theta
 \end{aligned} \tag{3.34}$$

and

$$\begin{aligned}
 G\gamma_{xy} = & \frac{1}{2} A_0 r^{-1/2} \left(\sin \theta \cos \frac{3\theta}{2} \right) - \frac{1}{2} A_1 r^{1/2} \left(\sin \theta \cos \frac{\theta}{2} \right) - 2B_1 r \sin \theta \\
 & + C_0 r^{-1/2} \cos \frac{\theta}{2} \left[1 - \sin \frac{\theta}{2} \sin \frac{3\theta}{2} \right] + C_1 r^{1/2} \cos \frac{\theta}{2} \left[\sin^2 \frac{\theta}{2} + 1 \right]
 \end{aligned} \tag{3.35}$$

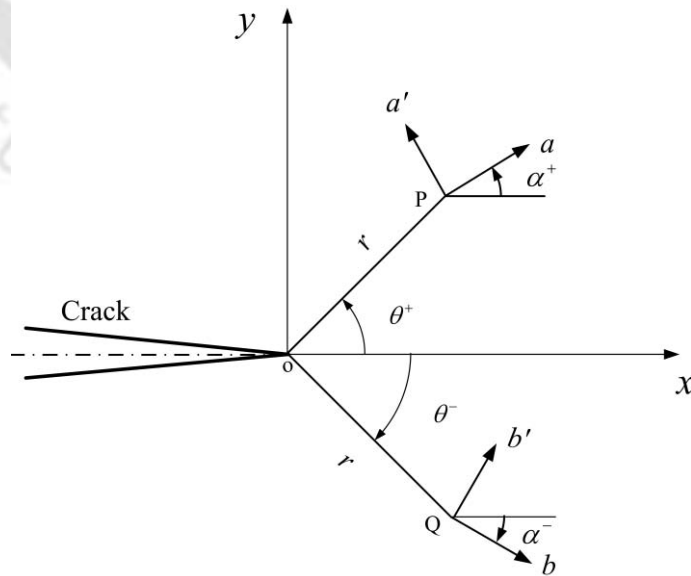


Figure 3.6 Strain gage location and orientation for mixed mode

Referring to Fig. 3.6, the strain in the direction of a (i.e., ε_{aa}) defined by an arbitrary angle α with respect to crack axis at any point within the zone II is given by

$$\begin{aligned}
 E\varepsilon_{aa} = & A_0 r^{-1/2} \left\{ \cos \frac{\theta}{2} \left[(1-\nu) - (1+\nu) \sin \frac{\theta}{2} \sin \frac{3\theta}{2} \right] \cos^2 \alpha \right. \\
 & + \cos \frac{\theta}{2} \left[(1-\nu) + (1+\nu) \sin \frac{\theta}{2} \sin \frac{3\theta}{2} \right] \sin^2 \alpha \\
 & \left. + (1+\nu) \sin \theta \sin \frac{3\theta}{2} \sin \alpha \cos \alpha \right\} + 2B_0 (\cos^2 \alpha - \nu \sin^2 \alpha) \\
 & + A_1 r^{1/2} \left\{ \cos \frac{\theta}{2} \left[(1-\nu) + (1+\nu) \sin^2 \frac{\theta}{2} \right] \cos^2 \alpha + \cos \frac{\theta}{2} \left[(1-\nu) + (1+\nu) \sin^2 \frac{\theta}{2} \right] \right. \\
 & \left. \sin^2 \alpha - (1+\nu) \sin \theta \cos \frac{\theta}{2} \sin \alpha \cos \alpha \right\} \\
 & + 2B_1 r \left\{ \cos \theta (\cos^2 \alpha - \nu \cos \theta \sin^2 \alpha) - 2(1+\nu) \sin \theta \sin \alpha \cos \alpha \right\} \quad (3.36) \\
 & + C_0 r^{-1/2} \left\{ \sin \frac{\theta}{2} \left[(1+\nu) \cos \frac{\theta}{2} \cos \frac{3\theta}{2} + 2\nu \right] \sin^2 \alpha - \sin \frac{\theta}{2} \right. \\
 & \left. \left[(1+\nu) \cos \frac{\theta}{2} \cos \frac{3\theta}{2} + 2 \right] \cos^2 \alpha + 2(1+\nu) \cos \frac{\theta}{2} \left[1 - \sin \frac{\theta}{2} \cos \frac{3\theta}{2} \right] \sin \alpha \cos \alpha \right\} \\
 & + C_1 r^{1/2} \left\{ \sin \frac{\theta}{2} \left[(1+\nu) \cos^2 \frac{\theta}{2} + 2 \right] \cos^2 \alpha - \sin \frac{\theta}{2} \left[(1+\nu) \cos^2 \frac{\theta}{2} + 2\nu \right] \sin^2 \alpha \right. \\
 & \left. + 2(1+\nu) \cos \frac{\theta}{2} \left[1 + \sin^2 \frac{\theta}{2} \right] \sin \alpha \cos \alpha \right\} \\
 & + 2D_1 r \sin \theta (\cos^2 \alpha - \nu \sin^2 \alpha)
 \end{aligned}$$

Again if

$$\cos 2\alpha = -\kappa = -\frac{1-\nu}{1+\nu} \quad (3.37)$$

the coefficients of B_0 and D_1 term in Eq. (3.36) vanish. Further, if

$$\tan \frac{\theta}{2} = -\cot 2\alpha \quad (3.38)$$

the coefficient of the A_1 term vanishes. Thus the angles α and θ which permit these simplification are exactly same as in the case of determination of K_I . Thus for

positive values of θ and α (Fig. 3.6) given by Eqs. (3.37) and (3.38) respectively the strain component ε_{aa} is simplified

$$\begin{aligned}
 E\varepsilon_{aa} = & A_0 r^{-1/2} \left\{ (1-\nu) \cos \frac{\theta}{2} - \frac{1}{2} (1+\nu) \sin \theta \left(\cos 2\alpha \sin \frac{3\theta}{2} - \sin 2\alpha \cos \frac{3\theta}{2} \right) \right\} \\
 & + 2B_1 r \left\{ \cos \theta (\cos^2 \alpha - \nu \cos \theta \sin^2 \alpha) - (1+\nu) \sin \theta \sin 2\alpha \right\} \\
 & + C_0 r^{-1/2} \left\{ 2 \sin \frac{\theta}{2} (\nu \sin^2 \alpha - \cos^2 \alpha) + (1+\nu) \cos \frac{\theta}{2} \sin 2\alpha \right. \\
 & \left. - \frac{1}{2} (1+\nu) \sin \theta \left(\cos \frac{3\theta}{2} \cos 2\alpha + \sin \frac{3\theta}{2} \sin 2\alpha \right) \right\} \\
 & + C_1 r^{1/2} \left\{ \cos \frac{\theta}{2} (1+\nu) \left[\sin \frac{\theta}{2} \cos \frac{\theta}{2} \cos 2\alpha + \left(1 + \sin^2 \frac{\theta}{2} \right) \sin 2\alpha \right] \right. \\
 & \left. + 2 \sin \frac{\theta}{2} \cos^2 \alpha - 2\nu \sin \frac{\theta}{2} \sin^2 \alpha \right\}
 \end{aligned} \tag{3.39}$$

It can be noticed that the term D_0 is absent in the Eq. (3.39). Since for negative value of θ , the angle α is also negative, the strain component ε_{bb} defined by $-\theta$ and $-\alpha$ as shown in Fig. 3.6 can be obtained from Eq. (3.39) as

$$\begin{aligned}
 E\varepsilon_{bb} = & A_0 r^{-1/2} \left\{ (1-\nu) \cos \frac{\theta}{2} - \frac{1}{2} (1+\nu) \sin \theta \left(\cos 2\alpha \sin \frac{3\theta}{2} - \sin 2\alpha \cos \frac{3\theta}{2} \right) \right\} \\
 & + 2B_1 r \left\{ \cos \theta (\cos^2 \alpha - \nu \sin^2 \alpha) - (1+\nu) \sin \theta \sin 2\alpha \right\} - C_0 r^{-1/2} \left\{ 2 \sin \frac{\theta}{2} (\nu \sin^2 \alpha \right. \\
 & \left. - \cos^2 \alpha) + (1+\nu) \cos \frac{\theta}{2} \sin 2\alpha - \frac{1}{2} (1+\nu) \sin \theta \left(\cos \frac{3\theta}{2} \cos 2\alpha + \sin \frac{3\theta}{2} \sin 2\alpha \right) \right\} \\
 & - C_1 r^{1/2} \left\{ \cos \frac{\theta}{2} (1+\nu) \left[\sin \frac{\theta}{2} \cos \frac{\theta}{2} \cos 2\alpha + \left(1 + \sin^2 \frac{\theta}{2} \right) \sin 2\alpha \right] + 2 \sin \frac{\theta}{2} \cos^2 \alpha \right. \\
 & \left. - 2\nu \sin \frac{\theta}{2} \sin^2 \alpha \right\}
 \end{aligned} \tag{3.40}$$

Thus if the strain gages are pasted along the positive gage line (line OP) along the $+\alpha$ direction and along the negative gage line (line OQ) along the $-\alpha$ direction, then the measured strains would be according to the Eq. (3.39) and Eq. (3.40) respectively,

provided that the gages are located within the zone II or the extent of applicability of these equations. Eq. (3.39) and Eq. (3.40) are added and multiplied by \sqrt{r} resulting

$$E(\varepsilon_{aa} + \varepsilon_{bb})\sqrt{r} = 2A_0 \left\{ (1-\nu) \cos \frac{\theta}{2} - \frac{1}{2}(1+\nu) \sin \theta \left(\cos 2\alpha \sin \frac{3\theta}{2} - \sin 2\alpha \cos \frac{3\theta}{2} \right) \right\} + 4B_1 r^{3/2} \left\{ \cos \theta (\cos^2 \alpha - \nu \sin^2 \alpha) - (1+\nu) \sin \theta \sin 2\alpha \right\} \quad (3.41)$$

Subtracting Eq. (3.40) from Eq. (3.39) and multiplying with \sqrt{r} leads to

$$E(\varepsilon_{aa} - \varepsilon_{bb})\sqrt{r} = 2C_0 \left\{ 2 \sin \frac{\theta}{2} (\nu \sin^2 \alpha - \cos^2 \alpha) + (1+\nu) \cos \frac{\theta}{2} \sin 2\alpha - \frac{1}{2}(1+\nu) \sin \theta \left(\cos \frac{3\theta}{2} \cos 2\alpha + \sin \frac{3\theta}{2} \sin 2\alpha \right) \right\} + 2C_1 r \left\{ \cos \frac{\theta}{2} (1+\nu) \left[\sin \frac{\theta}{2} \cos \frac{\theta}{2} \cos 2\alpha + \left(1 + \sin^2 \frac{\theta}{2} \right) \sin 2\alpha \right] + 2 \sin \frac{\theta}{2} \cos^2 \alpha - 2\nu \sin \frac{\theta}{2} \sin^2 \alpha \right\} \quad (3.42)$$

Eqs. (3.41) and (3.42) contain only coefficients of mode I and mode II respectively.

Denoting the coefficient of A_0 in Eq. (3.41) as

$$I_1 = 2 \left\{ (1-\nu) \cos \frac{\theta}{2} - \frac{1}{2}(1+\nu) \sin \theta \left(\cos 2\alpha \sin \frac{3\theta}{2} - \sin 2\alpha \cos \frac{3\theta}{2} \right) \right\} \quad (3.43)$$

and denoting the coefficient of C_0 in Eq. (3.42) as

$$I_2 = 2 \left\{ 2 \sin \frac{\theta}{2} (\nu \sin^2 \alpha - \cos^2 \alpha) + (1+\nu) \cos \frac{\theta}{2} \sin 2\alpha - \frac{1}{2}(1+\nu) \sin \theta \left(\cos \frac{3\theta}{2} \cos 2\alpha + \sin \frac{3\theta}{2} \sin 2\alpha \right) \right\} \quad (3.44)$$

Then Eq. (3.41) and Eq. (3.42) can be rewritten as

$$\frac{E(\varepsilon_{aa} + \varepsilon_{bb})\sqrt{r}}{I_1} = A_0 + \frac{4B_1 r^{3/2}}{I_1} \left\{ \cos \theta (\cos^2 \alpha - \nu \sin^2 \alpha) - (1+\nu) \sin \theta \sin 2\alpha \right\} \quad (3.45)$$

and

$$\frac{E(\varepsilon_{aa} - \varepsilon_{bb})\sqrt{r}}{I_2} = C_0 + \frac{2C_1 r}{I_2} \left\{ \cos \frac{\theta}{2} (1 + \nu) \left[\sin \frac{\theta}{2} \cos \frac{\theta}{2} \cos 2\alpha + \left(1 + \sin^2 \frac{\theta}{2} \right) \sin 2\alpha \right] + 2 \sin \frac{\theta}{2} \cos^2 \alpha - 2\nu \sin \frac{\theta}{2} \sin^2 \alpha \right\} \quad (3.46)$$

Clearly, the quantities of left hand side (LHS) of Eqs. (3.45) and (3.46) yields A_0 and C_0 respectively as $r \rightarrow 0$. It is also evident from Eqs. (3.45) and (3.46) that at least two strain gages each at an angle of α with the crack axis are to be deployed along the positive and negative gage lines (as shown in Fig. 3.7) for the determination of K_I and K_{II} . Further, the corresponding gages on the gage line should be placed at the same radial distance from the crack tip as shown in Fig. 3.7.

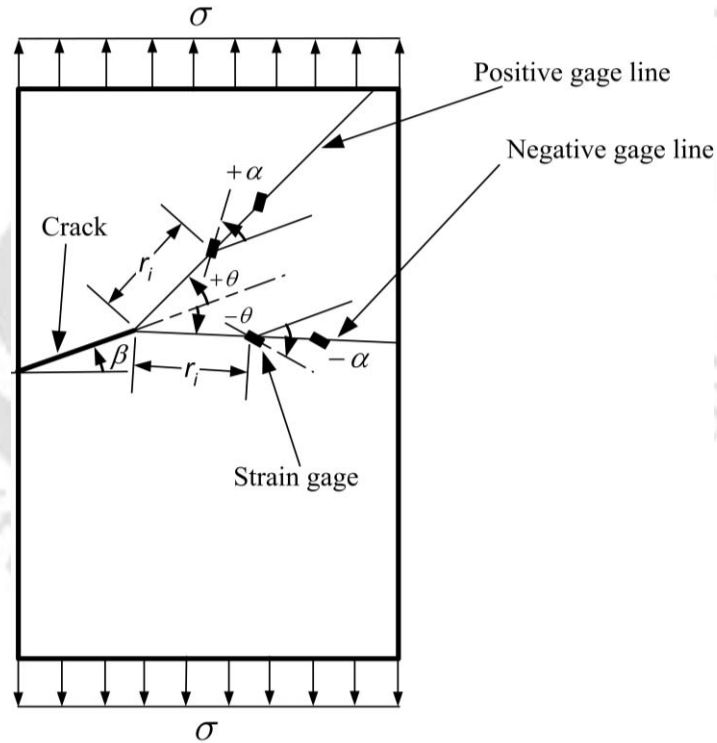


Figure 3.7 Gage lines and strain gage locations for mixed mode

To determine A_0 and C_0 a graphical procedure is suggested by Dally and Berger [42, 51]. In this approach a graph of the measured quantity say $\frac{E(\varepsilon_{aa} + \varepsilon_{bb})\sqrt{r}}{I_1}$ is to be plotted as function of r . Then the extrapolation of the graph back to the crack tip i.e.,

$r = 0$ gives the unknown coefficient A_0 as shown in Fig. 3.8. Similarly C_0 can be obtained by considering measured values of LHS of Eq. (3.46) as shown in Fig. 3.8. Finally K_r and K_{II} can be determined from A_0 and C_0 using Eqs. (3.18) and (3.23) respectively.

It may be observed from the description of Dally and Berger [42, 51] technique that while very precise prescriptions of angular parameters α and θ (Eq. (3.37) and Eq. (3.38)) are available but no prescriptions/approach for selection of appropriate radial location r for each of the strain gages is put forward by researchers till date.

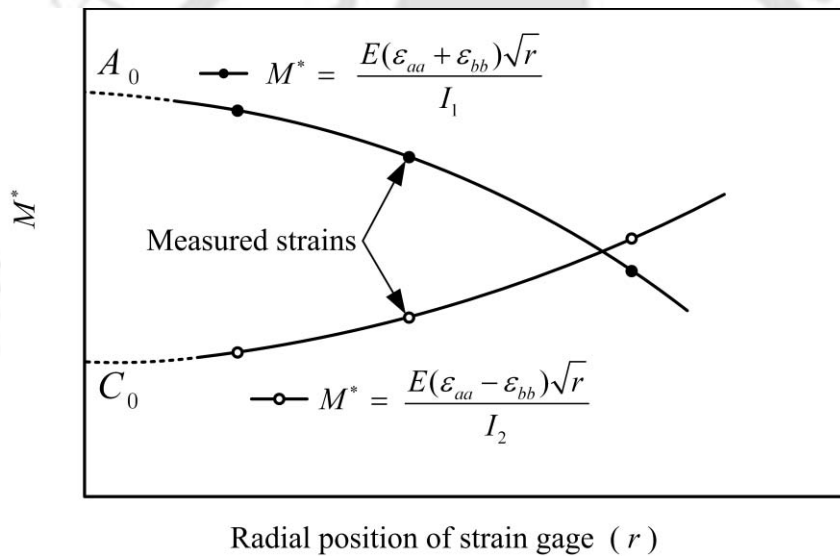


Figure 3.8 Extrapolation technique for determination of A_0 and C_0

3.5 Proposed modified Dally and Berger technique

In the present investigation Dally and Berger [51] strain gage technique (Section 3.4) is modified primarily to render the determination of the optimal radial locations definitively and consistently. A major difference between the present modified technique and that of original technique [51] is the inclusion of additional coefficients A_2 and C_2 in Eqs. (3.33)-(3.35) which makes a five parameter strain series containing mode I coefficients A_0, A_1, A_2, B_0, B_1 and shearing mode coefficients C_0, C_1, C_2, D_0, D_1 . It is assumed that these five parameter

representation can accurately describe the strain field within the zone II. With this, the rectangular strain components at any point within the zone II are given by

$$\begin{aligned}
 E\varepsilon_{xx} = & A_0 r^{-1/2} \cos \frac{\theta}{2} \left[(1-\nu) - (1+\nu) \sin \frac{\theta}{2} \sin \frac{3\theta}{2} \right] + A_1 r^{1/2} \cos \frac{\theta}{2} \\
 & \left[(1-\nu) + (1+\nu) \sin^2 \frac{\theta}{2} \right] + \frac{1}{2} A_2 r^{3/2} \left[2(1-\nu) \cos \frac{3\theta}{2} - 3(1+\nu) \sin \theta \sin \frac{3\theta}{2} \right] \\
 & 2B_0 + 2B_1 r \cos \theta - C_0 r^{-1/2} \sin \frac{\theta}{2} \left[(1+\nu) \cos \frac{\theta}{2} \cos \frac{3\theta}{2} + 2 \right] + \\
 & C_1 r^{1/2} \sin \frac{\theta}{2} \left[2 + (1+\nu) \cos^2 \frac{\theta}{2} \right] + C_2 r^{3/2} \left[2 \sin \frac{3\theta}{2} + \frac{3}{2} (1+\nu) \sin \theta \cos \frac{\theta}{2} \right] \\
 & + 2D_1 r \sin \theta
 \end{aligned} \tag{3.47}$$

$$\begin{aligned}
 E\varepsilon_{yy} = & A_0 r^{-1/2} \cos \frac{\theta}{2} \left[(1-\nu) + (1+\nu) \sin \frac{\theta}{2} \sin \frac{3\theta}{2} \right] + A_1 r^{1/2} \cos \frac{\theta}{2} \\
 & \left[(1-\nu) - (1+\nu) \sin^2 \frac{\theta}{2} \right] + \frac{1}{2} A_2 r^{3/2} \left[2(1-\nu) \cos \frac{3\theta}{2} + 3(1+\nu) \sin \theta \sin \frac{\theta}{2} \right] \\
 & - 2\nu B_0 - 2\nu B_1 r \cos \theta + C_0 r^{-1/2} \sin \frac{\theta}{2} \left[2\nu + (1+\nu) \cos \frac{\theta}{2} \cos \frac{3\theta}{2} \right] \\
 & - C_1 r^{1/2} \sin \frac{\theta}{2} \left[2\nu + (1+\nu) \cos^2 \frac{\theta}{2} \right] - C_2 r^{3/2} \left[2\nu \sin \frac{3\theta}{2} \right. \\
 & \left. + \frac{3}{2} (1+\nu) \sin \theta \cos \frac{\theta}{2} \right] + 2D_1 r \nu \sin \theta
 \end{aligned} \tag{3.48}$$

and

$$\begin{aligned}
 G\gamma_{xy} = & \frac{1}{2} A_0 r^{-1/2} \left(\sin \theta \cos \frac{3\theta}{2} \right) - \frac{1}{2} A_1 r^{1/2} \left(\sin \theta \cos \frac{\theta}{2} \right) - \frac{3}{2} A_2 r^{3/2} \left(\sin \theta \cos \frac{\theta}{2} \right) \\
 & - 2B_1 r \sin \theta + C_0 r^{-1/2} \cos \frac{\theta}{2} \left[1 - \sin \frac{\theta}{2} \sin \frac{3\theta}{2} \right] + C_1 r^{1/2} \cos \frac{\theta}{2} \left[\sin^2 \frac{\theta}{2} + 1 \right] \\
 & + C_2 r^{3/2} \left[\cos \frac{3\theta}{2} - \frac{3}{2} \sin \theta \sin \frac{\theta}{2} \right]
 \end{aligned} \tag{3.49}$$

Once again referring to Fig. 3.6, the normal strain $\varepsilon_{\alpha\alpha}$ in the direction of an arbitrary angle α with respect to crack axis is thus given by

$$\begin{aligned}
 E\varepsilon_{aa} = & A_0 r^{-1/2} \left\{ (1-\nu) \cos \frac{\theta}{2} - \frac{1}{2} (1+\nu) \sin \theta \left(\cos 2\alpha \sin \frac{3\theta}{2} - \sin 2\alpha \cos \frac{3\theta}{2} \right) \right\} \\
 & + A_1 r^{1/2} \left\{ \cos \frac{\theta}{2} \left[(1-\nu) + \sin^2 \frac{\theta}{2} (1+\nu) \cos 2\alpha - \frac{1}{2} (1+\nu) \sin \theta \sin 2\alpha \right] \right\} \\
 & + A_2 r^{3/2} \left\{ \cos \frac{3\theta}{2} (1-\nu) - \frac{3}{2} (1+\nu) \sin \theta \left[\sin \frac{\theta}{2} \cos 2\alpha + \cos \frac{\theta}{2} \sin 2\alpha \right] \right\} \\
 & + 2B_0 (\cos^2 \alpha - \nu \sin^2 \alpha) + 2B_1 r \left\{ \cos \theta (\cos^2 \alpha - \nu \cos \theta \sin^2 \alpha) \right. \\
 & \left. - (1+\nu) \sin \theta \sin 2\alpha \right\} + C_0 r^{-1/2} \left\{ 2 \sin \frac{\theta}{2} (\nu \sin^2 \alpha - \cos^2 \alpha) + \right. \\
 & \left. + (1+\nu) \cos \frac{\theta}{2} \sin 2\alpha - \frac{1}{2} (1+\nu) \sin \theta \left(\cos \frac{3\theta}{2} \cos 2\alpha + \sin \frac{3\theta}{2} \sin 2\alpha \right) \right\} \\
 & + C_1 r^{1/2} \left\{ \cos \frac{\theta}{2} (1+\nu) \left[\sin \frac{\theta}{2} \cos \frac{\theta}{2} \cos 2\alpha + \left(1 + \sin^2 \frac{\theta}{2} \right) \sin 2\alpha \right] \right. \\
 & \left. + 2 \sin \frac{\theta}{2} \cos^2 \alpha - 2\nu \sin \frac{\theta}{2} \sin^2 \alpha \right\} \\
 & + C_2 r^{3/2} \left\{ 2 \sin^2 \frac{\theta}{2} (\cos^2 \alpha - \nu \sin^2 \alpha) + \frac{3}{2} (1+\nu) \sin \theta \cos \frac{\theta}{2} \cos 2\alpha \right. \\
 & \left. + (1+\nu) \left(\cos \frac{3\theta}{2} - \frac{3}{2} \sin \theta \sin \frac{\theta}{2} \right) \sin 2\alpha \right\} + 2D_1 r (\cos^2 \alpha - \nu \sin^2 \alpha)
 \end{aligned} \tag{3.50}$$

It could be noted that the coefficient D_0 is absent in the mixed mode strain field equation (3.50).

For

$$\cos 2\alpha = -\kappa = -\frac{1-\nu}{1+\nu} \tag{3.51}$$

the coefficients of B_0 and D_1 terms in Eq. (3.50) can be eliminated and if

$$\tan \frac{\theta}{2} = -\cot 2\alpha \tag{3.52}$$

then, the coefficient of the A_1 term also vanishes.

Referring to Fig. 3.6 for positive values of α and θ , the strain component ε_{aa} and for negative values of both α and θ (since for negative value of θ , the angle α is also negative) the strain ε_{bb} can be obtained respectively as

$$\begin{aligned}
 E\varepsilon_{aa} = & A_0 r^{-1/2} \left\{ (1-\nu) \cos \frac{\theta}{2} - \frac{1}{2} (1+\nu) \sin \theta \left(\cos 2\alpha \sin \frac{3\theta}{2} - \sin 2\alpha \cos \frac{3\theta}{2} \right) \right\} \\
 & + A_2 r^{3/2} \left\{ \cos \frac{3\theta}{2} (1-\nu) - \frac{3}{2} (1+\nu) \sin \theta \left[\sin \frac{\theta}{2} \cos 2\alpha + \cos \frac{\theta}{2} \sin 2\alpha \right] \right\} \\
 & + 2B_1 r \left\{ \cos \theta (\cos^2 \alpha - \nu \cos \theta \sin^2 \alpha) - (1+\nu) \sin \theta \sin 2\alpha \right\} \\
 & + C_0 r^{-1/2} \left\{ 2 \sin \frac{\theta}{2} (\nu \sin^2 \alpha - \cos^2 \alpha) + (1+\nu) \cos \frac{\theta}{2} \sin 2\alpha \right. \\
 & \left. - \frac{1}{2} (1+\nu) \sin \theta \left(\cos \frac{3\theta}{2} \cos 2\alpha + \sin \frac{3\theta}{2} \sin 2\alpha \right) \right\} \\
 & + C_1 r^{1/2} \left\{ \cos \frac{\theta}{2} (1+\nu) \left[\sin \frac{\theta}{2} \cos \frac{\theta}{2} \cos 2\alpha + \left(1 + \sin^2 \frac{\theta}{2} \right) \sin 2\alpha \right] \right. \\
 & \left. + 2 \sin \frac{\theta}{2} \cos^2 \alpha - 2\nu \sin \frac{\theta}{2} \sin^2 \alpha \right\} + C_2 r^{3/2} \left\{ 2 \sin^2 \frac{\theta}{2} (\cos^2 \alpha - \nu \sin^2 \alpha) \right. \\
 & \left. + \frac{3}{2} (1+\nu) \sin \theta \cos \frac{\theta}{2} \cos 2\alpha + (1+\nu) \left(\cos \frac{3\theta}{2} - \frac{3}{2} \sin \theta \sin \frac{\theta}{2} \right) \sin 2\alpha \right\}
 \end{aligned} \tag{3.53}$$

and

$$\begin{aligned}
 E\varepsilon_{bb} = & A_0 r^{-1/2} \left\{ (1-\nu) \cos \frac{\theta}{2} - \frac{1}{2} (1+\nu) \sin \theta \left(\cos 2\alpha \sin \frac{3\theta}{2} - \sin 2\alpha \cos \frac{3\theta}{2} \right) \right\} \\
 & + A_2 r^{3/2} \left\{ \cos \frac{3\theta}{2} (1-\nu) - \frac{3}{2} (1+\nu) \sin \theta \left[\sin \frac{\theta}{2} \cos 2\alpha + \cos \frac{\theta}{2} \sin 2\alpha \right] \right\} \\
 & + 2B_1 r \left\{ \cos \theta (\cos^2 \alpha - \nu \sin^2 \alpha) - (1+\nu) \sin \theta \sin 2\alpha \right\} \\
 & - C_0 r^{-1/2} \left\{ 2 \sin \frac{\theta}{2} (\nu \sin^2 \alpha - \cos^2 \alpha) + (1+\nu) \cos \frac{\theta}{2} \sin 2\alpha \right. \\
 & \left. - \frac{1}{2} (1+\nu) \sin \theta \left(\cos \frac{3\theta}{2} \cos 2\alpha + \sin \frac{3\theta}{2} \sin 2\alpha \right) \right\} \\
 & - C_1 r^{1/2} \left\{ \cos \frac{\theta}{2} (1+\nu) \left[\sin \frac{\theta}{2} \cos \frac{\theta}{2} \cos 2\alpha + \left(1 + \sin^2 \frac{\theta}{2} \right) \sin 2\alpha \right] \right. \\
 & \left. + 2 \sin \frac{\theta}{2} \cos^2 \alpha - 2\nu \sin \frac{\theta}{2} \sin^2 \alpha \right\} - C_2 r^{3/2} \left\{ 2 \sin^2 \frac{\theta}{2} (\cos^2 \alpha - \nu \sin^2 \alpha) \right. \\
 & \left. + \frac{3}{2} (1+\nu) \sin \theta \cos \frac{\theta}{2} \cos 2\alpha + (1+\nu) \left(\cos \frac{3\theta}{2} - \frac{3}{2} \sin \theta \sin \frac{\theta}{2} \right) \sin 2\alpha \right\}
 \end{aligned} \tag{3.54}$$

Thus if a strain gage is placed at a radial distance r from the crack tip on a line making an angle of θ (Eq. (3.52)) and gage orientation of α (Eq. (3.51)) with the crack axis then the measured strains contain only the terms A_0 , A_2 , B_1 , C_0 , C_1 , C_2 .

Adding Eqs. (3.53) and (3.54) and multiplying with \sqrt{r} results to

$$\begin{aligned}
 E(\varepsilon_{aa} + \varepsilon_{bb})\sqrt{r} = & 2A_0 \left\{ (1-\nu) \cos \frac{\theta}{2} - \frac{1}{2}(1+\nu) \sin \theta \left(\cos 2\alpha \sin \frac{3\theta}{2} \right. \right. \\
 & \left. \left. - \sin 2\alpha \cos \frac{3\theta}{2} \right) \right\} + 2A_2 r^2 \left\{ \cos \frac{3\theta}{2} (1-\nu) \right. \\
 & \left. - \frac{3}{2}(1+\nu) \sin \theta \left[\sin \frac{\theta}{2} \cos 2\alpha + \cos \frac{\theta}{2} \sin 2\alpha \right] \right\} \\
 & + 4B_1 r^{3/2} \left\{ \cos \theta (\cos^2 \alpha - \nu \sin^2 \alpha) - (1+\nu) \sin \theta \sin 2\alpha \right\}
 \end{aligned} \tag{3.55}$$

which contains only coefficients of mode I loading. Similarly subtraction of Eq. (3.54) from Eq. (3.53) and multiplying \sqrt{r} results to

$$\begin{aligned}
 E(\varepsilon_{aa} - \varepsilon_{bb})\sqrt{r} = & 2C_0 \left\{ 2 \sin \frac{\theta}{2} (\nu \sin^2 \alpha - \cos^2 \alpha) + (1+\nu) \cos \frac{\theta}{2} \sin 2\alpha \right. \\
 & \left. - \frac{1}{2}(1+\nu) \sin \theta \left(\cos \frac{3\theta}{2} \cos 2\alpha + \sin \frac{3\theta}{2} \sin 2\alpha \right) \right\} \\
 & + 2C_1 r \left\{ \cos \frac{\theta}{2} (1+\nu) \left[\sin \frac{\theta}{2} \cos \frac{\theta}{2} \cos 2\alpha \right. \right. \\
 & \left. \left. + \left(1 + \sin^2 \frac{\theta}{2} \right) \sin 2\alpha \right] + 2 \sin \frac{\theta}{2} \cos^2 \alpha - 2\nu \sin \frac{\theta}{2} \sin^2 \alpha \right\} \\
 & + 2C_2 r^2 \left\{ 2 \sin^2 \frac{\theta}{2} (\cos^2 \alpha - \nu \sin^2 \alpha) + \frac{3}{2}(1+\nu) \sin \theta \right. \\
 & \left. \cos \frac{\theta}{2} \cos 2\alpha + (1+\nu) \left(\cos \frac{3\theta}{2} - \frac{3}{2} \sin \theta \sin \frac{\theta}{2} \right) \sin 2\alpha \right\}
 \end{aligned} \tag{3.56}$$

which now contains only coefficients of mode II loading.

Let the coefficient of A_0 in Eq. (3.55)

$$2 \left\{ (1-\nu) \cos \frac{\theta}{2} - \frac{1}{2}(1+\nu) \sin \theta \left(\cos 2\alpha \sin \frac{3\theta}{2} - \sin 2\alpha \cos \frac{3\theta}{2} \right) \right\} = I_1 \text{ (say)} \tag{3.57}$$

and the coefficient of C_0 in Eq. (3.56) is

$$2 \left\{ 2 \sin \frac{\theta}{2} (\nu \sin^2 \alpha - \cos^2 \alpha) + (1 + \nu) \cos \frac{\theta}{2} \sin 2\alpha - \frac{1}{2} (1 + \nu) \sin \theta \left(\cos \frac{3\theta}{2} \cos 2\alpha + \sin \frac{3\theta}{2} \sin 2\alpha \right) \right\} = I_2 \quad (\text{say}) \quad (3.58)$$

Eqs. (3.55) and (3.56) can now be rewritten as

$$\begin{aligned} \frac{E(\varepsilon_{aa} + \varepsilon_{bb})\sqrt{r}}{I_1} &= A_0 + \frac{2A_2r^2}{I_1} \left\{ \cos \frac{3\theta}{2} (1 - \nu) \right. \\ &\quad \left. - \frac{3}{2} (1 + \nu) \sin \theta \left[\sin \frac{\theta}{2} \cos 2\alpha + \cos \frac{\theta}{2} \sin 2\alpha \right] \right\} \\ &\quad + \frac{4B_1r^{3/2}}{I_1} \left\{ \cos \theta (\cos^2 \alpha - \nu \sin^2 \alpha) - (1 + \nu) \sin \theta \sin 2\alpha \right\} \end{aligned} \quad (3.59)$$

$$\begin{aligned} \frac{E(\varepsilon_{aa} - \varepsilon_{bb})\sqrt{r}}{I_2} &= C_0 + \frac{2C_1r}{I_2} \left\{ \cos \frac{\theta}{2} (1 + \nu) \left[\sin \frac{\theta}{2} \cos \frac{\theta}{2} \cos 2\alpha \right. \right. \\ &\quad \left. \left. + \left(1 + \sin^2 \frac{\theta}{2} \right) \sin 2\alpha \right] + 2 \sin \frac{\theta}{2} \cos^2 \alpha - 2\nu \sin \frac{\theta}{2} \sin^2 \alpha \right\} \\ &\quad + \frac{2C_2r^2}{I_2} \left\{ 2 \sin^2 \frac{\theta}{2} (\cos^2 \alpha - \nu \sin^2 \alpha) + \frac{3}{2} (1 + \nu) \sin \theta \cos \frac{\theta}{2} \cos 2\alpha \right. \\ &\quad \left. + (1 + \nu) \left[\cos \frac{3\theta}{2} - \frac{3}{2} \sin \theta \sin \frac{\theta}{2} \right] \sin^2 2\alpha \right\} \end{aligned} \quad (3.60)$$

Thus as $r \rightarrow 0$ the LHS quantities of Eqs. (3.59) and (3.60) yield A_0 and C_0 respectively. Eqs. (3.59) and (3.60) can be rewritten in a simplified form as

$$\frac{E(\varepsilon_{aa} + \varepsilon_{bb})\sqrt{r}}{I_1} = A_0 + \beta_1 A_2 r^2 + \beta_2 B_1 r^{3/2} \quad (3.61)$$

and

$$\frac{E(\varepsilon_{aa} - \varepsilon_{bb})\sqrt{r}}{I_2} = C_0 + \delta_1 C_1 r + \delta_2 C_2 r^2 \quad (3.62)$$

where, β_1 , β_2 , δ_1 and δ_2 are constants for a given Poisson's ratio ν and are given by

$$\beta_1 = \frac{2 \left\{ \cos \frac{3\theta}{2} (1-\nu) - \frac{3}{2} (1+\nu) \sin \theta \left[\sin \frac{\theta}{2} \cos 2\alpha + \cos \frac{\theta}{2} \sin 2\alpha \right] \right\}}{I_1}$$

$$\beta_2 = \frac{4 \left\{ \cos \theta (\cos^2 \alpha - \nu \sin^2 \alpha) - (1+\nu) \sin \theta \sin 2\alpha \right\}}{I_1}$$

$$\delta_1 = \frac{2}{I_2} \left\{ \cos \frac{\theta}{2} (1+\nu) \left[\sin \frac{\theta}{2} \cos \frac{\theta}{2} \cos 2\alpha + \left(1 + \sin^2 \frac{\theta}{2} \right) \sin 2\alpha \right] \right. \\ \left. + 2 \sin \frac{\theta}{2} \cos^2 \alpha - 2\nu \sin \frac{\theta}{2} \sin^2 \alpha \right\} \quad (3.63)$$

$$\delta_2 = \frac{2}{I_2} \left\{ 2 \sin^2 \frac{\theta}{2} (\cos^2 \alpha - \nu \sin^2 \alpha) + \frac{3}{2} (1+\nu) \sin \theta \cos \frac{\theta}{2} \cos 2\alpha \right. \\ \left. + (1+\nu) \left[\cos \frac{3\theta}{2} - \frac{3}{2} \sin \theta \sin \frac{\theta}{2} \right] \sin^2 2\alpha \right\}$$

It is clear from Eqs. (3.59) and (3.60) that, the quantities on the LHS of these equations are to be measured on a cracked specimen using a minimum of three strain gages located at different radii on both the positive and negative gage lines as shown in Fig. 3.9 to determine all the six coefficients.

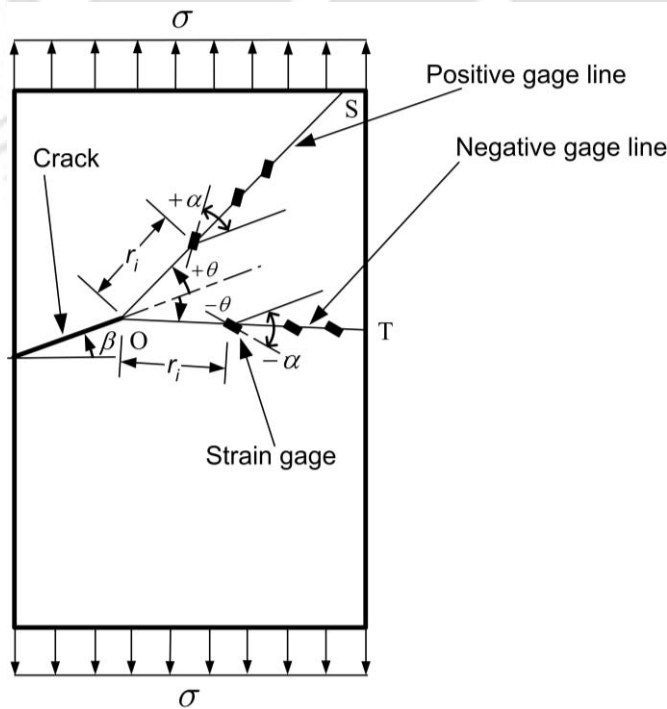


Figure 3.9 Proposed gage locations for a mixed mode cracked body

It should be noted that the radial distance from the crack tip to the corresponding strain gages on the positive and negative gage lines should be same (Fig. 3.9) for calculation of the LHS quantities of Eqs. (3.59) and (3.60).

In contrast to Dally and Berger [51] original approach, the present investigation proposes to determine the coefficients A_0 and C_0 by taking best-fit of the measured quantities of $\frac{E(\varepsilon_{aa} + \varepsilon_{bb})\sqrt{r}}{I_1}$ and $\frac{E(\varepsilon_{aa} - \varepsilon_{bb})\sqrt{r}}{I_2}$ to the curves of the form on the right hand sides (RHS) of Eqs. (3.61) and (3.62) respectively. Using the values of coefficients A_0 and C_0 from the best-fit regression, the mixed mode SIFs K_I and K_{II} can be respectively determined as

$$K_I = \sqrt{2\pi} A_0 \quad \text{and} \quad K_{II} = \sqrt{2\pi} C_0 \quad (3.64)$$

It is to be noted that equations corresponding to plane strain conditions can be obtained by replacing E by $E/(1-\nu^2)$ and ν by $\nu/(1-\nu)$ in Eqs. (3.47)–(3.62). It should be noted that for the same Poisson's ratio, plane stress and plane strain conditions will have different values of α and hence θ . Considering $\nu = 1/3$ for which $\alpha = \pm 60^\circ$, Eqs. (3.53) and (3.54) and Eqs. (3.61) and (3.62) can be simplified to

$$E\varepsilon_{aa} = \left(\frac{\sqrt{3}}{2}\right) A_0 r^{-1/2} - \left(\frac{\sqrt{3}}{2}\right) A_2 r^{3/2} - 2B_1 r + \left(\frac{1}{2}\right) C_0 r^{-1/2} + C_1 r^{1/2} - \left(\frac{3}{2}\right) C_2 r^{3/2} \quad (3.65)$$

$$E\varepsilon_{bb} = \left(\frac{\sqrt{3}}{2}\right) A_0 r^{-1/2} - \left(\frac{\sqrt{3}}{2}\right) A_2 r^{3/2} - 2B_1 r - \left(\frac{1}{2}\right) C_0 r^{-1/2} - C_1 r^{1/2} + \left(\frac{3}{2}\right) C_2 r^{3/2} \quad (3.66)$$

$$E(\varepsilon_{aa} + \varepsilon_{bb}) \left(\sqrt{\frac{r}{3}}\right) = A_0 - A_2 r^2 - \left(\frac{4}{\sqrt{3}}\right) B_1 r^{3/2} \quad (3.67)$$

$$E(\varepsilon_{aa} - \varepsilon_{bb}) \sqrt{r} = C_0 + 2C_1 r - 3C_2 r^2 \quad (3.68)$$

Eqs. (3.65)–(3.68) are extensively used in numerical examples of the present investigation and are also useful in understanding the subsequent discussions in the

present work. As can be observed from the description of the proposed modified DB technique, although the angular positions for all the strain gages such as α and θ are clearly defined and easily determined but the approach for the optimal radial distances r_i ($i = 1, 2, 3 \dots$) for each of the three strain gages along both the gage lines which are necessarily to be placed is not available. In case of all or some of the strain gages are located very close to the crack tip, the strain measurements will be affected by strain gradients, 3D effects and plasticity effects. Though these effects can be avoided by pasting the gages quite away from the crack tip, but then Eqs. (3.53) and (3.54) may not be applicable for strain measurements at such locations. This is due to the reason that, the measured strain at such a large distances may also have contribution due to the coefficients other than $A_0, A_1, A_2, B_0, B_1, C_0, C_1, C_2, D_0,$ and D_1 . It is clear that all strain gages should be located within the zone of domination of the above coefficients i.e. zone II and at the same time should not be located very close to the crack tip. It should be noted that the size of zone II for mixed mode is significantly larger than that in case of mode I due to the use of more number of parameters or coefficients in the strain field. As a consequence, more number of strain gages could be accommodated. This is a significant advantage of the proposed modified DB technique which justifies the increased number of gages. Therefore, prior knowledge of valid radial locations for strain gages is essential for successful application of the modified Dally and Berger technique for the accurate determination of K_I and K_{II} .

Similar to the case of determination of K_I , the minimum radial distance r_{\min} for strain measurements is governed by the presence of 3D state of stress near the crack tip. Accordingly, the r_{\min} is given by [22]

$$r_{\min} = \frac{\text{thickness of the specimen}}{2} \quad (3.69)$$

Defining r_{\max} as the maximum radial distance from the crack tip or the upper bound for the valid radial locations for all the strain gages, clearly, r_{\max} is also the extent of

validity of five parameter strain series represented by Eqs. (3.53) and (3.54) on positive and negative gage lines respectively. Conversely, Eqs. (3.53) and (3.54) can represent the strain field accurately along the positive and negative gage lines respectively upto a radial distance r_{\max} . However, the extent of validity of Eq. (3.53) on positive gage line, say r_{\max}^+ need not necessarily be equal to the extent of validity of Eq. (3.54) on negative gage line say r_{\max}^- . In order to take into account of Eqs. (3.53) and (3.54), the maximum permissible (or upper bound) radial location or the extent of validity of both the Eqs. (3.53) and (3.54) (r_{\max}), for a given specimen will then be

$$r_{\max} = \text{minimum} \left[r_{\max}^+, r_{\max}^- \right] \quad (3.70)$$

Consequently, the optimal or valid radial locations r_i ($i = 1, 2, 3, \dots$) for all strain gages both the gage lines in the proposed modified Dally and Berger technique can now be given as

$$r_{\min} \leq r_i \leq r_{\max} \quad (3.71)$$

3.6 Determination of maximum permissible radial location r_{\max} in mixed mode (I/II)

A straight forward extension of the procedure for the determination of r_{\max} for mode I problems (Section 3.2) is not possible for problems of mixed mode (I/II) loading due to the presences of large number of unknown coefficients in Eqs. (3.53) and (3.54) and due to the requirement of more than one strain gage in the proposed technique. Therefore, application of curve fitting based on the linear regression models is proposed for the first time in the present investigation and is described as follows.

In the present investigation a FE based approach is proposed for the accurate determination of r_{\max} value for a given mixed mode cracked specimen. In this approach, the parameters $E\varepsilon_{aa}$ and $E\varepsilon_{bb}$ are computed at large number of points

along the positive and negative gage lines (OS and OT in Fig. 3.9) using FEA of a given cracked configuration. The quantities on the LHS of Eqs. (3.61) and (3.62) i.e.

$$\frac{E(\varepsilon_{aa} + \varepsilon_{bb})\sqrt{r}}{I_1} \quad \text{and} \quad \frac{E(\varepsilon_{aa} - \varepsilon_{bb})\sqrt{r}}{I_2}$$

are then computed at those points using the FE solutions. It should be noted that, the radial distances from the crack tip to the corresponding points on the positive and negative gage lines should be same for computation of the LHS quantities of Eqs.(3.61) and (3.62) and meshes for FEA should be designed accordingly.

Using linear regression models, a curve of the form $A_0 + \beta_1 A_2 r^2 + \beta_2 B_1 r^{3/2}$ (RHS of Eq. (3.61)) is fitted to the computed values of $\frac{E(\varepsilon_{aa} + \varepsilon_{bb})\sqrt{r}}{I_1}$ at all the points on the positive gage line. Initially the fit will not be good due to the fact that the form $A_0 + \beta_1 A_2 r^2 + \beta_2 B_1 r^{3/2}$ (with only three parameters) could accurately represent the quantity $\frac{E(\varepsilon_{aa} + \varepsilon_{bb})\sqrt{r}}{I_1}$ only up to a certain radial distance from the crack-tip. Since this radial distance is unknown, the computed values of $\frac{E(\varepsilon_{aa} + \varepsilon_{bb})\sqrt{r}}{I_1}$ at larger values of r are then to be deleted gradually and continuously from the data set until a best-fit curve is obtained. The value of coefficients A_0, A_2 and B_1 for the best-fit regression is noted. The same procedure is repeated with Eq. (3.62) in order to obtain the best-fit coefficients C_0, C_1 and C_2 .

Consistent and accurate values of the above six unknown coefficients can be obtained by ensuring that

- (a) the corresponding plots of LHS (obtained using FEA) and RHS quantities (obtained using best-fit coefficients) of Eqs. (3.61) and (3.62) should be congruent to each other to *the maximum possible radial distance* from the crack tip

- (b) the percentage relative error between the LHS and RHS quantities of Eqs.(3.61) and (3.62) should be $\leq 0.5\%$ within the maximum possible radial distance and
- (c) the quality of fit defined by the coefficient of determination R^2 should be very close to 1.

Using the best-fit regression values of A_0, A_2, B_1, C_0, C_1 and C_2 and FE values of $E\varepsilon_{aa}$ and $E\varepsilon_{bb}$, the LHS and RHS of quantities of Eqs. (3.53) and (3.54) can be compared graphically with respect to the radial distance from the crack-tip for all points on the positive and negative gage line respectively. It is clear that the RHS quantities of Eqs. (3.53) and (3.54) can only accurately represent the LHS quantities (i.e. $E\varepsilon_{aa}$ and $E\varepsilon_{bb}$ obtained using FEA) up to a certain radial distance because of a few number of coefficients (or parameters) A_0, A_2, B_1, C_0, C_1 and C_2 are present in RHS quantities. The point of deviation of the RHS of Eq. (3.53) from the finite element values of $E\varepsilon_{aa}$ indicates the r_{\max}^+ value for the given configuration. Percent relative error between the LHS and RHS of Eq. (3.53) can be employed for computation of the r_{\max}^+ . In the present investigation an error 0.5% (as given in mode I) is employed for obtaining the r_{\max}^+ or the point of deviation in the above graphical analysis. Similarly the r_{\max}^- can be obtained from the graphical comparison of LHS and RHS quantities of Eq. (3.54) and using the error criterion as mentioned above.

Thus, the maximum permissible radial location for the strain gages (r_{\max}) for a given configuration, given state of stress and a given Poisson's ratio is the minimum of r_{\max}^+ and r_{\max}^- (Eq. 3.70), which satisfies both Eqs. (3.53) and (3.54). Thus, three strain gages are to be pasted on each gage line for the determination of K_I and K_{II} using the proposed technique such that the radial distance of each gage should be greater than half the thickness of the plate (to avoid 3D effects [21, 22]) and less than the r_{\max} value (as it is the maximum permissible distance) of a given configuration. In order to avoid errors due to the crack tip complications such as strain gradient,

plasticity and 3D effects it is recommended in the present investigation to paste the strain gages as far as possible from the crack tip but not beyond the r_{\max} .

It is worth mentioning that apart from the effect of mesh gradation, the consistency and accuracy of evaluation of the r_{\max} (and hence unknown coefficients A_0, A_2, B_1, C_0, C_1 and C_2) also depend on how the best-fit process is carried out and the field variables that are employed in the best-fit process. It has been noticed from extensive numerical investigation that highly erroneous and inconsistent coefficients and hence r_{\max} are obtained if Eq. (3.53) or Eq. (3.54) is directly used for the best-fit process instead of using Eqs. (3.61) and (3.62) as suggested in the present investigation. The above observation is also noticed even in the case of highly refined finite element meshes.

The first and important advantage of using Eqs. (3.61) and (3.62) is that they contain less number of unknown coefficients as compared to Eqs. (3.53) and (3.54). Further, Eq. (3.62) needs only a quadratic best-fit and Eq. (3.61) needs a nearly quadratic fit which can be easily and efficiently carried out using commercially available software.

3.7 Finite element formulation

As described in Section 3.6, a finite element based approach has been suggested for determination of optimal radial locations for the determination of K_I in opening mode problems and K_I and K_{II} for mixed mode problems. In the present investigation, linear elastic finite element analysis of various cracked configurations has been carried out using displacement based FE method. For this purpose commercial software ANSYS 11 has been utilized for numerical analyses.

In the present investigation, PLANE183 element embodied in ANSYS is used for discretization of the cracked domains. PLANE183 is a higher order 2D, eight noded isoparametric quadrilateral element (Q8). These elements are well suited for both plane stress and plane strain conditions. At the crack tip, the elements have been modeled using quarter point elements (QPEs) obtained by using PLANE 183 to

incorporate square root singularity which arises in LEFM [52]. The details of these elements including the FE formulation have been presented in the following sections.

In the present investigation, the FE method has been employed for two purposes viz. (a) for computation of the SIFs of experimental specimens and (b) for computation of the r_{\max} values of various cracked configurations.

3.7.1 Eight noded quadrilateral element

The eight noded isoparametric quadrilateral element (Q8) is generally used to solve fracture mechanics problems and also permits modeling of complicated shapes. The Q8 is shown in Fig. 3.10. Being isoparametric element, the geometric variables are expressed in a similar way as field variable. Thus, in Q8

$$x = \sum_{i=1}^8 N_i x_i \quad (3.72)$$

$$y = \sum_{i=1}^8 N_i y_i \quad (3.73)$$

Similarly, the field variables are also represented as

$$u = \sum_{i=1}^8 N_i u_i \quad (3.74)$$

$$v = \sum_{i=1}^8 N_i v_i \quad (3.75)$$

where the $N_i (i=1,2,\dots,8)$ are shape functions, (x_i, y_i) are nodal coordinates and (u_i, v_i) are nodal displacements

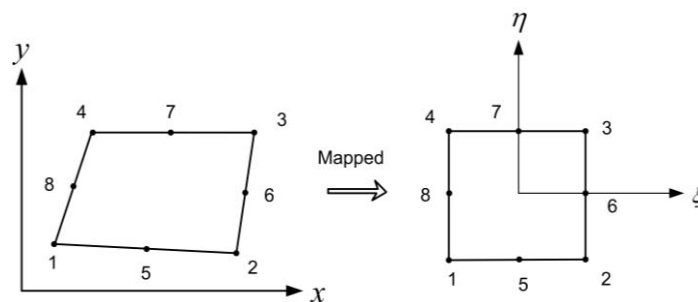


Figure 3.10 Eight noded quadrilateral isoparametric element represented in natural coordinates

Shape function must be expressed in a natural co-ordinate system for numerical integration. Natural coordinate (ξ, η) systems are dimensionless and have a maximum absolute magnitude of one. They are defined with reference to the element rather than with reference to the global co-ordinate system in which the element resides (Fig. 3.10). The shape functions for a Q8 element are expressed in natural coordinates as

$$\begin{aligned} N_1 &= \frac{1}{4}(1+\xi)(1-\eta) - \frac{1}{2}(N_8 + N_5) & N_5 &= \frac{1}{2}(1-\xi^2)(1-\eta) \\ N_2 &= \frac{1}{4}(1-\xi)(1+\eta) - \frac{1}{2}(N_5 + N_6) & N_6 &= \frac{1}{2}(1+\xi)(1-\eta^2) \\ N_3 &= \frac{1}{4}(1-\xi)(1-\eta) - \frac{1}{2}(N_6 + N_7) & N_7 &= \frac{1}{2}(1-\xi^2)(1-\eta) \\ N_4 &= \frac{1}{4}(1+\xi)(1-\eta) - \frac{1}{2}(N_7 + N_8) & N_8 &= \frac{1}{2}(1+\xi)(1-\eta^2) \end{aligned} \quad (3.76)$$

The displacements within the element in terms of nodal displacements can be expressed as

$$\{U\} = \begin{Bmatrix} u \\ v \end{Bmatrix} = [N]\{X\}_e \quad (3.77)$$

where $\{U\}$ is the displacement vector of an element, with the shape function matrix

$$[N] = \begin{bmatrix} N_1 & 0 & N_2 & 0 & N_3 & 0 & N_4 & 0 & N_5 & 0 & N_6 & 0 & N_7 & 0 & N_8 & 0 \\ 0 & N_1 & 0 & N_2 & 0 & N_3 & 0 & N_4 & 0 & N_5 & 0 & N_6 & 0 & N_7 & 0 & N_8 \end{bmatrix} \quad (3.78)$$

and nodal displacement

$$\{X\}_e^T = \{u_1 \ v_1 \ u_2 \ v_2 \ u_3 \ v_3 \ u_4 \ v_4 \ u_5 \ v_5 \ u_6 \ v_6 \ u_7 \ v_7 \ u_8 \ v_8\} \quad (3.79)$$

The governing equations of equilibrium for the plane elastostatic problems are given by

$$\frac{\partial \sigma_{xx}}{\partial x} + \frac{\partial \tau_{xy}}{\partial y} + f_x = 0 \quad (3.80)$$

$$\frac{\partial \tau_{xy}}{\partial x} + \frac{\partial \sigma_{yy}}{\partial y} + f_y = 0 \quad (3.81)$$

where f_x and f_y denote the body force per unit volume along the x and y direction; σ_{xx} and σ_{yy} are the normal stresses and τ_{xy} is the in-plane shear stress. The strain matrix associated with the plane stress and plane strain problems in terms of nodal displacement vector is then given by

$$\{\varepsilon\} = \begin{Bmatrix} \varepsilon_{xx} \\ \varepsilon_{yy} \\ \gamma_{xy} \end{Bmatrix} = \begin{Bmatrix} \frac{\partial u}{\partial x} \\ \frac{\partial v}{\partial y} \\ \frac{\partial u}{\partial y} + \frac{\partial v}{\partial x} \end{Bmatrix} = \begin{bmatrix} \frac{\partial}{\partial x} & 0 \\ 0 & \frac{\partial}{\partial y} \\ \frac{\partial}{\partial y} & \frac{\partial}{\partial x} \end{bmatrix} \begin{Bmatrix} u \\ v \end{Bmatrix} = \begin{bmatrix} \frac{\partial}{\partial x} & 0 \\ 0 & \frac{\partial}{\partial y} \\ \frac{\partial}{\partial y} & \frac{\partial}{\partial x} \end{bmatrix} [N] \{X\}_e \quad (3.82)$$

According to the standard notation the strain matrix is

$$\{\varepsilon\} = [B] \{X\}_e \quad (3.83)$$

The matrix $[B]$ is also called strain gradient matrix and can be represented as

$$[B] = \begin{bmatrix} \frac{\partial}{\partial x} & 0 \\ 0 & \frac{\partial}{\partial y} \\ \frac{\partial}{\partial y} & \frac{\partial}{\partial x} \end{bmatrix} [N] \quad (3.84)$$

Then the stress-strain relationship for an element is given by

$$\{\sigma\} = \begin{Bmatrix} \sigma_{xx} \\ \sigma_{yy} \\ \tau_{xy} \end{Bmatrix} = [D] \{\varepsilon\} = [D][B] \{X\}_e \quad (3.85)$$

where $[D]$ is the elasticity matrix and is given for plane stress and plane strain problems for isotropic material as

$$[D]_{Plane-Stress} = \frac{E}{1-\nu^2} \begin{bmatrix} 1 & \nu & 0 \\ \nu & 1 & 0 \\ 0 & 0 & \frac{1-\nu}{2} \end{bmatrix} \quad (3.86)$$

and

$$[D]_{Plane-Strain} = \frac{E(1-\nu)}{(1-2\nu)(1+\nu)} \begin{bmatrix} 1 & \frac{\nu}{1-\nu} & 0 \\ \frac{\nu}{1-\nu} & 1 & 0 \\ 0 & 0 & \frac{1-2\nu}{2(1-\nu)} \end{bmatrix} \quad (3.87)$$

Here, E and ν are Young's modulus and Poisson's ratio respectively. The displacements, derivatives of displacements, strains and stresses at any point within the element can be easily computed once $\{X\}_e$ of an element is known.

The element stiffness matrix which relates the unknown nodal displacements to the applied forces on an element can be given as

$$[K]_e = t \int_A [B]^T [D] [B] dx dy \quad (3.88)$$

where $[D]$ is the elasticity matrix consisting of element material constants. The matrix $[B]$, which relates strains and displacements, is a function of (x, y) and t is thickness of the element (assumed constant). The differential area $dx dy$ can be replaced by

$$dx dy = |J| d\xi d\eta \quad (3.89)$$

where $|J|$ is the determinant of the Jacobian matrix and is given by

$$|J| = \frac{\partial x}{\partial \xi} \frac{\partial y}{\partial \eta} - \frac{\partial x}{\partial \eta} \frac{\partial y}{\partial \xi} \quad (3.90)$$

Then Eq. (3.88) becomes

$$[K]_e = t \int_A [B]^T [D] [B] |J| d\xi d\eta \quad (3.91)$$

The above equation is now entirely a function of local co-ordinates (ξ, η) . Numerical integration is required to be employed over the area for the evaluation of element stiffness matrix $[K]_e$.

3.7.2 Quarter point elements (QPEs)

Quarter point elements are extensively used in LEFM for modeling of inverse square root singularity at the crack tip. A large number of conventional elements are required to model the same singularity at the crack tip. Barsoum [52] and Hanshell and Shaw [53] were first to discover the quarter point elements which can be easily generated from any conventional elements containing mid-side nodes. The singularity in the QPE is achieved by shifting the mid-side nodes on edges that are connected to the crack tip by an amount of quarter of length of the edge towards the crack tip. Such a simple and bodily movement of nodes ensures accurate estimation of the SIFs and modeling of $\frac{1}{\sqrt{r}}$ singularity with less number of elements around the crack tip. In the present investigation the mid-side nodes of selected Q8 element are shifted to quarter points, to generate QPEs around the crack tip. The conventional Q8 elements are first collapsed to six noded triangular elements and arranged in a standard *spider-web pattern* around the crack tip. Finally, the mid-side nodes are shifted to build the QPEs. All these steps are carried out by ANSYS automatically using its in built command KSCON. The proof for ability to represent $\frac{1}{\sqrt{r}}$ singularity by the Q8 element used in the present investigation is presented in the following section.

3.7.3 Collapsed six-noded triangle quarter point elements

Fig. 3.11 shows a collapsed Q8 crack-tip element, in which nodes 1, 4 and 8 are collapsed at the crack tip. This triangle is generated by collapsing the side 1-4 of

the quadrilateral in Fig. 3.10. In this case the singularity is investigated along the x – axis (i.e., $\eta = 0$) using

$$x = N_1x_1 + N_2x_2 + N_3x_3 + N_4x_4 + N_5x_5 + N_6x_6 + N_7x_7 + N_8x_8 \quad (3.92)$$

the x - coordinate along the x – axis is given by

$$x = -\frac{1}{4}(1+\xi)(1-\xi)l_1 - \frac{1}{4}(1+\xi)(1-\xi)l_1 + \frac{1}{2}(1-\xi^2)\frac{l_1}{4} + \frac{1}{2}(1+\xi)l_1 + \frac{1}{2}(1-\xi^2)\frac{l_1}{4} \quad (3.93)$$

which simplifies to

$$x = (\xi^2 + 2\xi + 1)\frac{l_1}{4} \quad (3.94)$$

Therefore, ξ in terms of x can be given as

$$\xi = \left[-1 + 2\sqrt{\frac{x}{l_1}} \right] \quad (3.95)$$

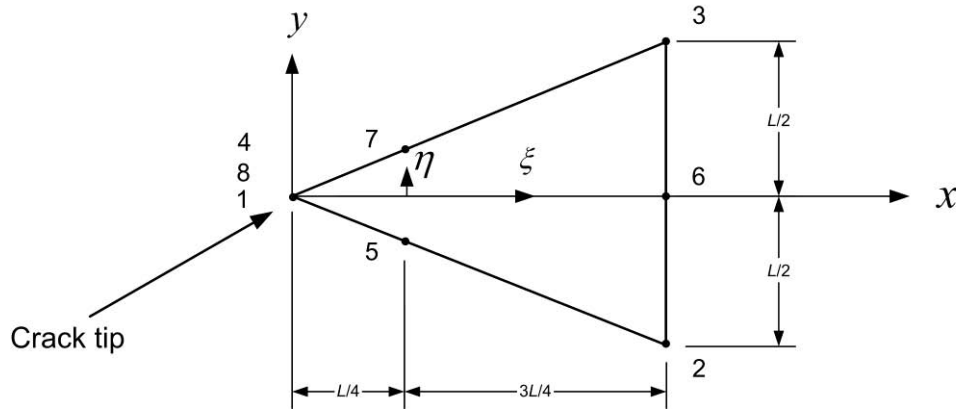


Figure 3.11 Six noded quadrilateral isoparametric element with mid-side nodes at the quarter point [52]

The displacement u along x – axis is given by

$$u = N_1u_1 + N_2u_2 + N_3u_3 + N_4u_4 + N_5u_5 + N_6u_6 + N_7u_7 + N_8u_8 \quad (3.96)$$

Substituting shape functions and Eq. (3.95) into Eq. (3.96) and differentiating w.r.t x , the strain in the x -direction using along x -axis is then

$$\varepsilon_{xx} = \frac{\partial u}{\partial x} = -\frac{1}{2} \left[\frac{1}{\sqrt{(xL)}} - \frac{2}{L} \right] u_2 + \frac{1}{2} \left[-\frac{1}{\sqrt{(xL)}} + \frac{2}{L} \right] u_3 + \left(\frac{1}{\sqrt{(xL)}} - \frac{2}{L} \right) u_7 + \frac{1}{2} \left[\frac{1}{\sqrt{(xL)}} \right] u_6 + \left[\frac{1}{\sqrt{(xL)}} - \frac{2}{L} \right] u_5 \quad (3.97)$$

Thus, Eq. (3.97) shows that the strain singularity along the x – axis is $\frac{1}{\sqrt{x}}$ as $x \rightarrow 0$.

3.8 Summary

In this chapter, development of the detailed formulation of the method for determination of optimal radial location of strain gages for accurate determination of SIFs has been presented. Starting with Westergaard approach and DS technique and using finite element analysis, the theoretical basis of a proposed method is developed for determination of optimal radial location for accurate determination of K_I . Similarly, detailed formulation and methodology have been developed where by extending DB technique and using FEA optimal radial locations of strain gages could be estimated for accurate determination of mixed mode SIFs K_I and K_{II} .

Chapter 4

Determination of r_{\max} for Mode I Cases

This chapter mainly focuses on estimation of r_{\max} value of two dimensional benchmark mode I configurations. Finite element analyses in all the examples are carried out using ANSYS 11. Eight noded isoparametric quadrilateral elements (Q8) are employed throughout this work (Section 3.7.1). In order to model the square root singularity at the crack tips, Q8 elements are collapsed to triangles and mid-side nodes are shifted to quarter points. These collapsed Q8 QPEs (Section 3.7.3) are employed in a standard spider web pattern in all the examples. Effect of crack length, net ligament length, state of stress and Poisson's ratio on the estimated values of r_{\max} has also been studied in this chapter. Finally, whether the selected strain gage locations in DS technique [22] employed by various earlier researchers (based on guess work or past experience) are valid locations or not is also verified and presented in the present chapter. As explained in section 3.1, determination of r_{\max} is the solution for deciding optimal strain gage locations for experimental determination of mode I SIF K_I using DS technique [22]. The procedure described in Section 3.1 is employed here for estimation of r_{\max} using FEA. Different types of cracked configurations such as edge cracked plate, center cracked plate, double edge cracked plate and eccentric cracked plate have been considered in this chapter.

4.1 Determination and convergence of r_{\max} for the center cracked plates

This example illustrates the general procedure for the determination of r_{\max} for cracked bodies using FE method. The procedure is described by considering a center cracked plate subjected to uniform tensile stress as shown in Fig. 4.1(a). The geometric and material properties are presented in Table 4.1. Due to symmetry, only one quarter of the plate is modeled with symmetric boundary conditions as shown in

Fig. 4.1(b). For evaluating the influence of the mesh refinement on r_{\max} values, three meshes of increasing mesh density for each of the plates with $a/b = 0.2$ and 0.5 are considered for the convergence study as shown Figs. 4.2 and 4.3 respectively. The number of elements (NE) and number of nodes (NN) are also mentioned in Figs. 4.2 and 4.3.

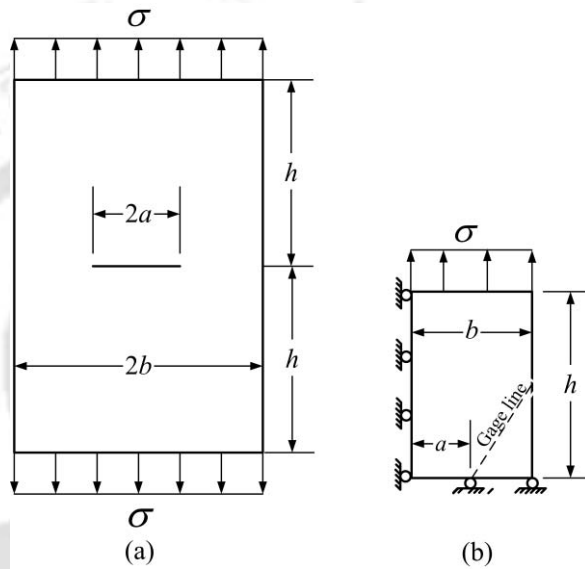


Figure 4.1 (a) center cracked plate; (b) solution domain for the center cracked plate

Table 4.1 Geometric and material parameters of center cracked plates

Section	State of stress	b (mm)	a/b	h/b	ν	E (GPa)	σ (MPa)
4.1	Plane stress	150	0.2 and 0.5	2	1/3	200	100
4.2	Plane stress	150	0.2-0.8	2	1/3	200	100
4.3	Plane stress	1200, 60, 42.857	0.0125, 0.025, 0.05, 0.5, 0.7	2	1/3	200	100
4.4	Plane stress	150	0.5	2	0.25, 0.3, 1/3	200	100

The meshes (Fig. 4.2 and Fig. 4.3) are designed such that nodes of several elements are made to lie along the gauge line (Fig. 4.1(b)) which makes an angle of θ with the axis of the crack (Eq. (3.27)). As explained in section 3.2 this gauge line begins at the crack-tip and terminates at the outer boundaries of the cracked plate. According to DS

technique, a single strain gage is required to be placed at an appropriate location on this line in the direction of α (Eq. (3.26)) in order to measure the linear strain ε_{aa} (Fig. 3.3). The computed strains in the global coordinates along the gage line are then transformed to the linear strain ε_{aa} in the direction defined by α . The radial distances (r) of each of the nodes on the gage line from the crack tip are then computed.

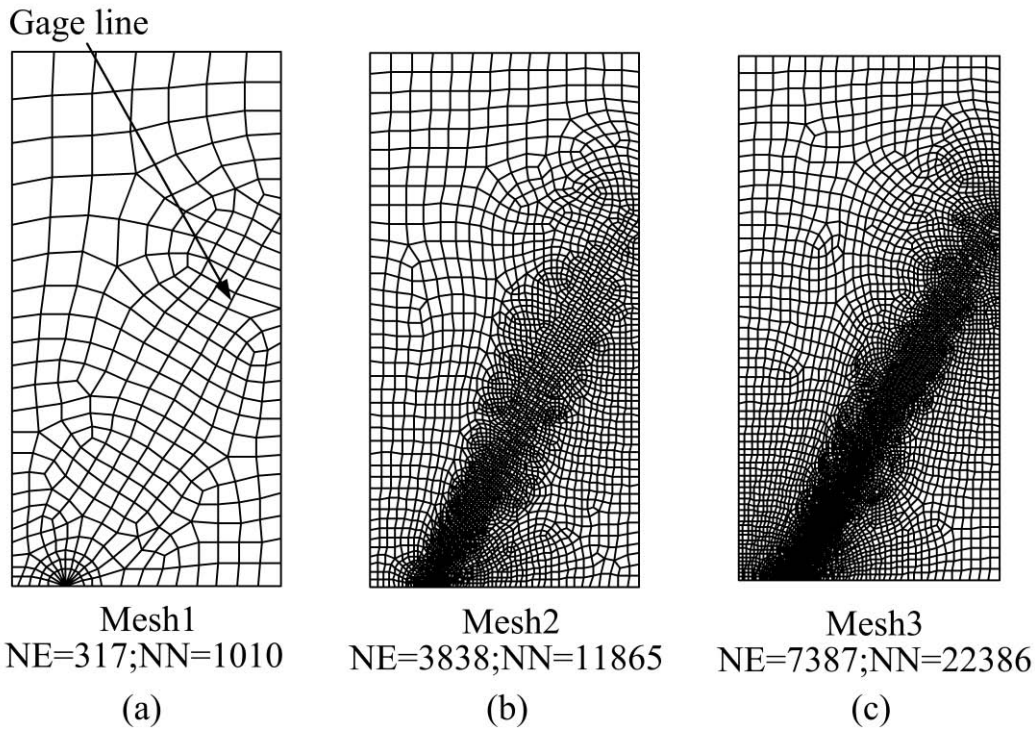


Figure 4.2 Different finite element meshes used for the convergence study of r_{\max} of the center cracked specimen with $a/b = 0.2$.

Plots of $\ln(\varepsilon_{aa})$ versus $\ln(r)$ for each of the three meshes of $a/b = 0.2$ and 0.5 are shown in Figs. 4.4 and 4.5 respectively. Crack tip point is not plotted as the radius of this point is zero. It is interesting to notice in Figs. 4.4 and 4.5 that, each plot of $a/b = 0.2$ and 0.5 consists of distinguishable linear portion followed by nonlinear portion (in logarithmic scale) as predicted by theory in the section 3.3. The linear trend distinctly exists up to a certain radial distance and thereafter gradually turns to the nonlinear portion. The extent of the straight line portion of the plots is observed to have gradually increased as the meshes are refined and can be seen more prominently in fine meshes than in coarse meshes due to less number of elements.

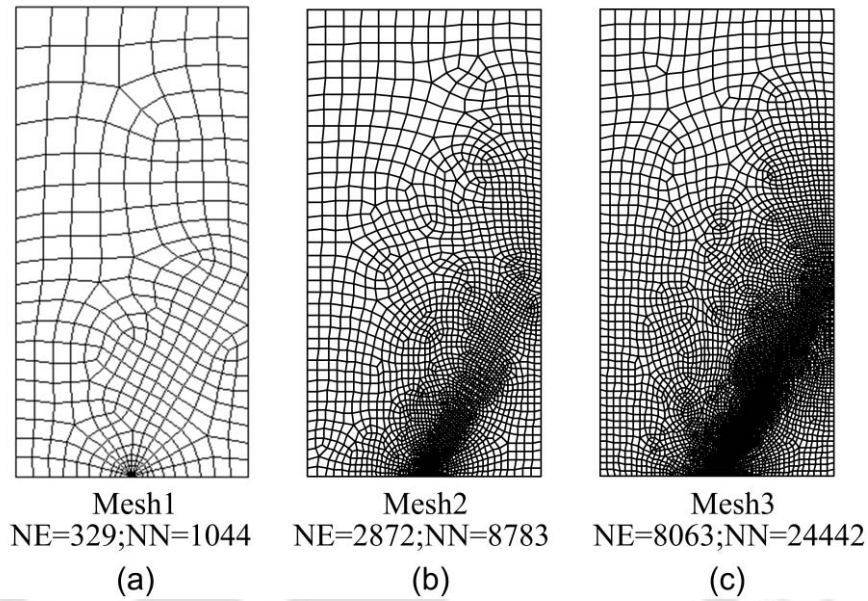


Figure 4.3 Different finite element meshes used for the convergence study of r_{\max} of the center cracked specimen with $a/b = 0.5$

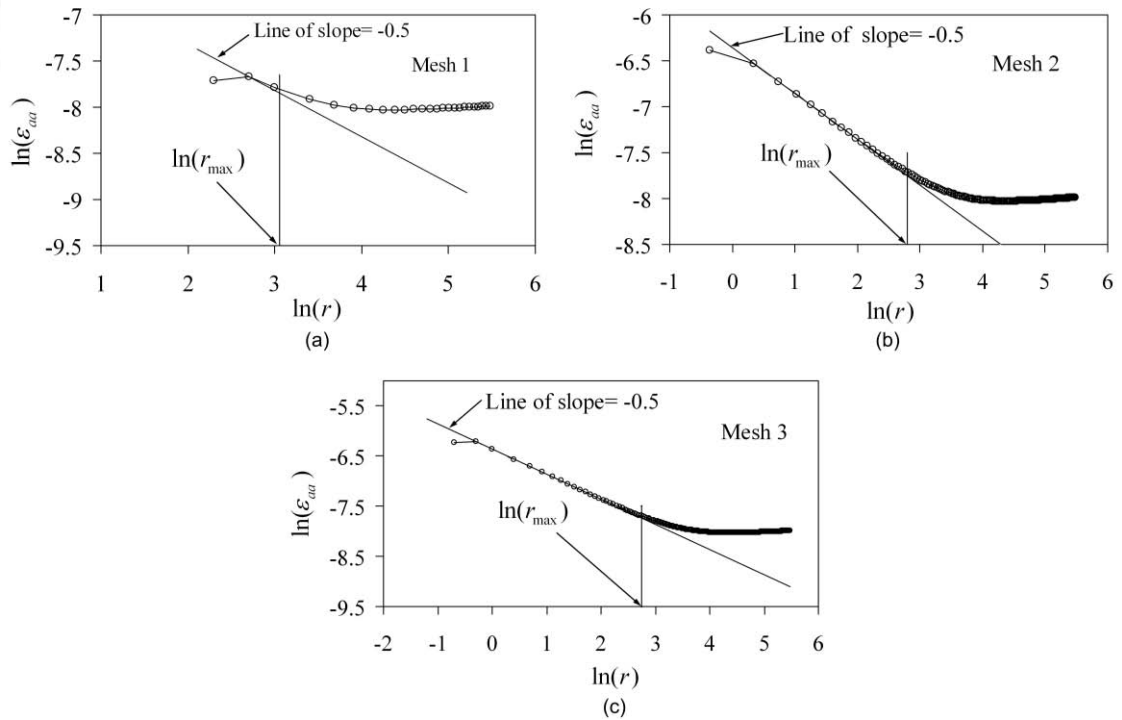


Figure 4.4 Linear and nonlinear variation of $\ln(\varepsilon_{aa})$ with $\ln(r)$ along the gage line for the sequence of meshes of center cracked plate with $a/b = 0.2$.

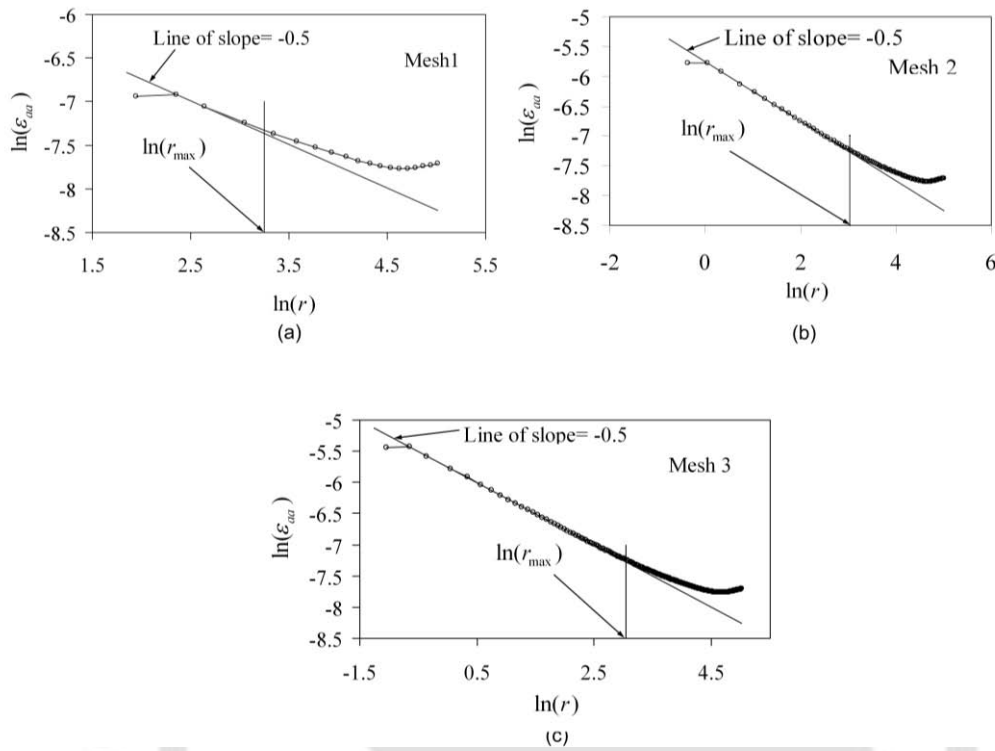


Figure 4.5 Linear and nonlinear variation of $\ln(\epsilon_{aa})$ with $\ln(r)$ along the gage line for the sequence of meshes of center cracked plate with $a/b = 0.5$

As discussed in section 3.3, the initial linear part is due to the dominance of the three parameters (Eq. (3.25)) and nonlinear part is due to the presence of more than three parameters in the expression for ϵ_{aa} . The end point of the linear portion of the plots in these figures clearly indicates the extent of the three parameter strain series (Eq. (3.25)) or the upper bound r_{\max} for radial location of strain gage in accordance with DS technique. The first point in all the plots of Figs. 4.4 and 4.5 is the strain value at the corner node of the quarter point element. The deviation of this point from the straight line portion may be due to the effect of the constant strain term (Eq. (3.97)) of the quarter point elements [54]. Similar trend has been noticed in all examples of the present investigation.

In order to determine the terminal point of the initial straight line portion, following procedure described in section 3.3, a line having a slope of -0.5 is superposed onto the plots of $\ln(\epsilon_{aa})$ versus $\ln(r)$. This line is considered as the

exact solution and absolute percent relative error in computed values of $\ln(\varepsilon_{aa})$ is then determined at all values of r in the plot. The error will be large in the non-linear portion and gradually diminishes as one approaches toward the points corresponding to the line in Eq. (3.32). Finally, the r_{\max} or the point of deviation of the log-log plot from the superposed line is evaluated as the value of the r at which the error reaches 0.5% (as one observes from right to left).

Following the above procedure, straight lines having slope of -0.5 are superposed on to the plots of $\ln(\varepsilon_{aa})$ versus $\ln(r)$ in Figs. 4.4 and 4.5. It is interesting to notice from Figs. 4.4 and 4.5 that both the initial straight line portion of the plots and superposed lines are congruent to each other up to a certain radial distance and the numerical results deviate from the superposed line thereafter due to the dominance of coefficients other than A_0 , A_1 and B_0 in Eq. (3.25). Fig. 4.6 shows the percent relative errors between the superposed line and that of the FE results of $\ln(\varepsilon_{aa})$ at different radii for $a/b = 0.2$ and 0.5 .

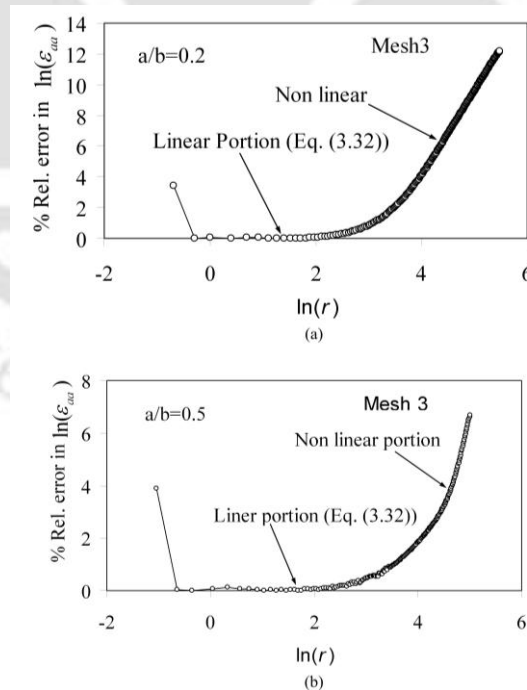


Figure 4.6 Percent relative error in computed values of $\ln(\varepsilon_{aa})$ for the center cracked configurations (a) $a/b = 0.2$ and (b) $a/b = 0.5$

These graphs are plotted using the FE results of the Mesh3 in Figs. 4.2 (c) and 4.3 (c) respectively. It can be seen from Fig. 4.6 that in both the cases the error decreases monotonically from the nonlinear to linear portion on the left. The r_{\max} is the radial distance in Fig. 4.6 at which the % relative error reaches 0.5% as one observes from right to left. These estimated values of r_{\max} or the extent of validity of the three parameter zone are marked in Figs. 4.4 and 4.5 for different meshes. The corresponding numerical values of the r_{\max} are presented in Table 4.2. It can be noticed from the results of Table 4.2 that as the meshes are refined r_{\max} values converge. No improvement is noticed when the meshes in Figs. 4.2 (c) and 4.3 (c) are further refined.

Table 4.2 Convergence of the r_{\max} with the mesh refinement for the center cracked plate with $a/b = 0.2$ and 0.5 .

Mesh	r_{\max} (mm)	
	$a/b = 0.2$	$a/b = 0.5$
Mesh1	21.33	25.72
Mesh2	16.51	20.90
Mesh3	15.66	20.94

4.2 Effect of a/b ratio on r_{\max}

In order to understand the effect of a/b on r_{\max} for center cracked plate, plates with different $a/b = 0.3$ to 0.8 in steps of 0.1 are considered. As the solutions for the center cracked plates with $a/b = 0.2$ and 0.5 are already obtained in previous section, therefore r_{\max} values of $a/b = 0.3, 0.4, 0.6, 0.7$ and 0.8 have been computed in this section. The other details of these configurations are presented in Table 4.1. Fine meshes of these ($a/b = 0.3, 0.4, 0.6, 0.7, 0.8$) configurations for the FEA are shown in Fig. 4.7. It can be observed from Fig. 4.7 that a large number of elements are made to fall on the gage lines for accurate prediction of strain ϵ_{aa} of

these configurations. The plots of $\ln(\varepsilon_{aa})$ versus $\ln(r)$ corresponding to $a/b = 0.2-0.8$ are shown in Fig. 4.8.

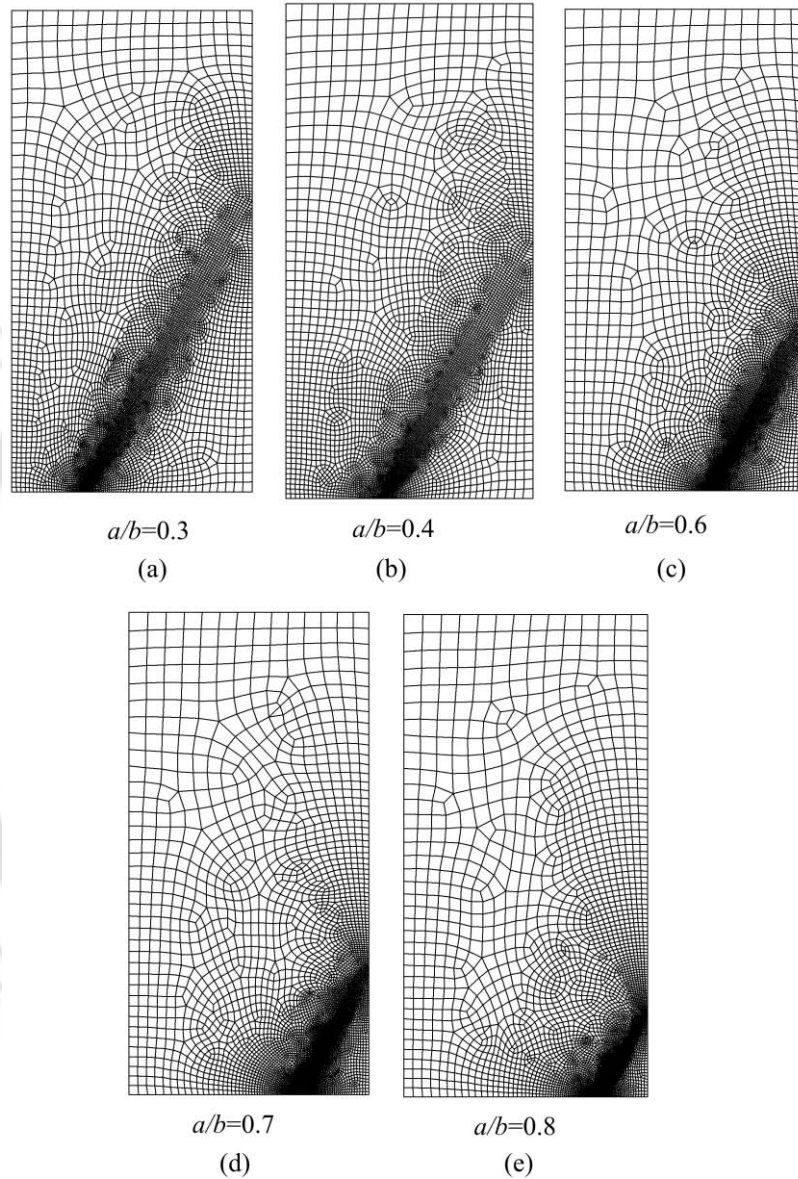


Figure 4.7 Finite element meshes for the center cracked plate employed to study the effect of a/b on r_{\max}

The estimated values of r_{\max} corresponding to each of these configurations are presented in Table 4.3. Variation of the r_{\max} as a function of a/b is presented in Fig. 4.9 to observe the effect of a/b on r_{\max} . It can be seen from Fig. 4.9 that as a/b increases the r_{\max} value increases initially and then decreases giving rise to a bell

shaped trend curve. Similar to the present investigation, Chona et al. [55] investigated the extent of the singular term or singularity dominated zone (SDZ) of various cracked configurations. The decrease of size of the SDZ with the increase of a/b at higher values of a/b was also observed by them. However, no mention of increase of size of the SDZ with a/b is reported in their work.

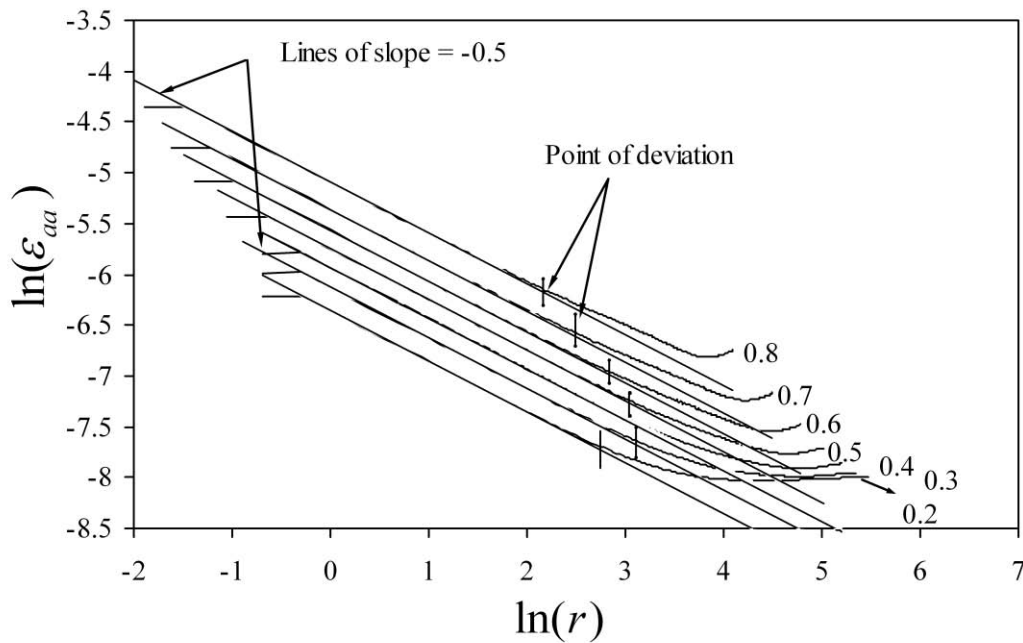


Figure 4.8 Variation of $\ln(\epsilon_{aa})$ with $\ln(r)$ along the gage-line for the center cracked plates with different values of a/b

Table 4.3 Variation of the r_{\max} with a/b of the center cracked plate ($b = 150\text{mm}$)

a/b	r_{\max} (mm)	r_{\max}/a	$r_{\max}/(b-a)$	$r_{\max}/2b$
0.2	15.66	0.5220	0.1305	0.0522
0.3	22.45	0.4988	0.2138	0.0748
0.5	20.94	0.2792	0.2792	0.0698
0.6	17.02	0.1891	0.2837	0.0567
0.7	12	0.1142	0.2700	0.0400
0.8	8.65	0.0721	0.2883	0.0288

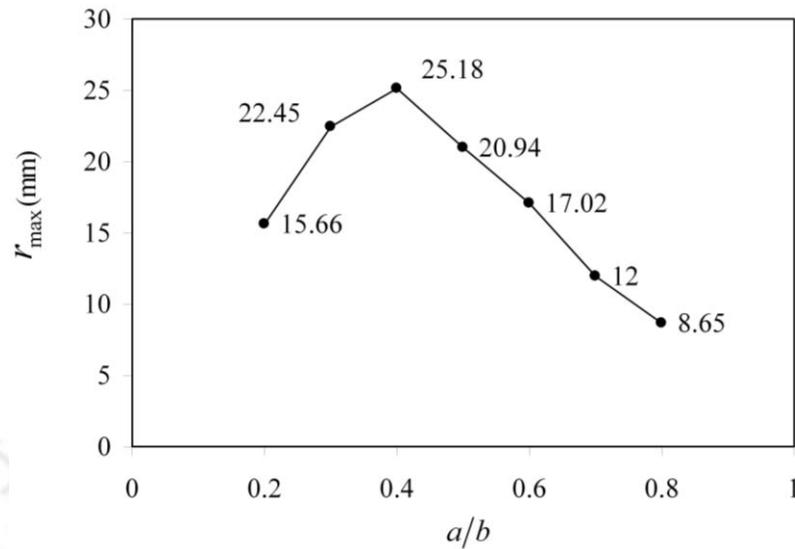


Figure 4.9 Graph of the r_{\max} as a function of a/b for the center cracked plate

4.3 An in-depth investigation on dependence of r_{\max} on a/b of center cracked plates

To further understand the reason for variation of r_{\max} with a/b in a bell shaped manner (Fig. 4.9), two aspects are studied. First, the effect of crack length alone is studied on r_{\max} by isolating the boundary effects. Second, the effect of proximity of the boundary (i.e., decreasing net ligament length $(b-a)$) on the r_{\max} is studied by keeping the crack length constant. To investigate the effect of crack length, the problem of center cracked plate having $h/b=2$ and $b=1200$ mm subjected to uniform tensile stresses (Fig. 4.1(a)) is chosen. Three different crack lengths of $a=15, 30$ and 60 mm are considered in this study. Since the corresponding a/b values are very small (0.0125, 0.025 and 0.05 respectively) it can be assumed that the boundaries have no effect while the crack length is increased. Other parameters of the present example can be found in Table 4.1. Fig. 4.10 shows the FE discretization for the configurations $a/b=0.0125, 0.025$ and 0.05 with sufficient mesh density to obtain accurate field variables.

Fig. 4.11 shows the variation of $\ln(\varepsilon_{aa})$ with $\ln(r)$ on the gage line of the above configurations along with the point of deviation ($\ln(r_{\max})$) of the straight line portions.

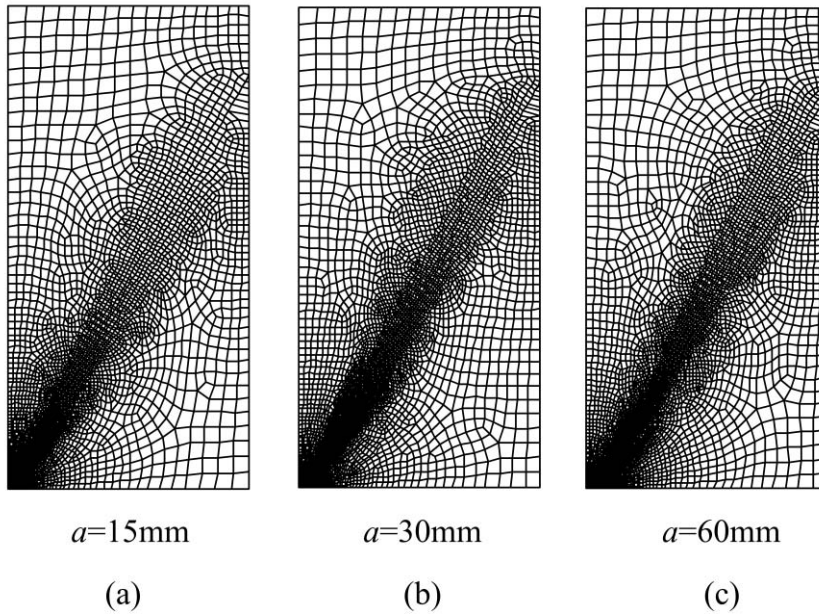


Figure 4.10 Finite element meshes for the center cracked plates used to study the effect of the crack length a on the r_{\max}

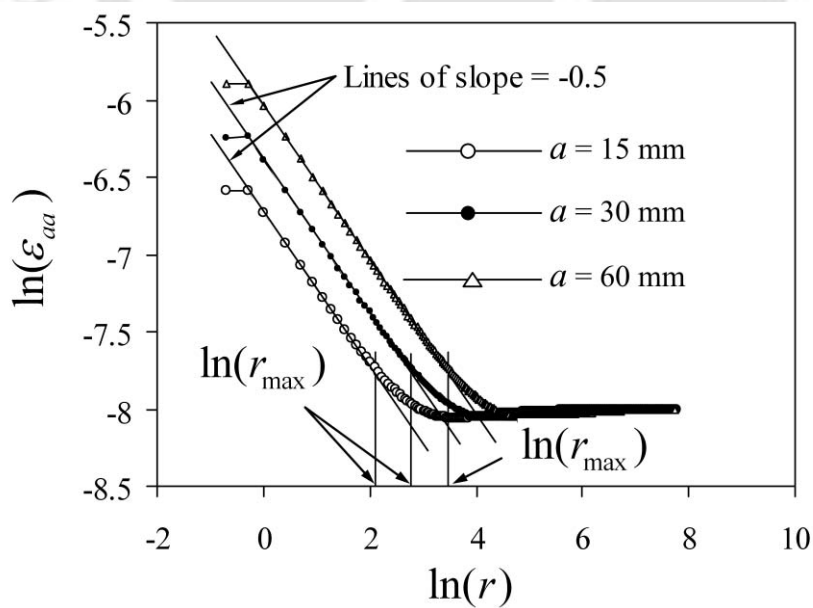


Figure 4.11 Graph of $\ln(\varepsilon_{aa})$ versus $\ln(r)$ showing variation of the r_{\max} with the crack length when the boundary effects are absent

The trends of all these plots are similar to those obtained in the previous example and are as per the theoretical predictions of chapter 3 (Section 3.3). The r_{\max} values are obtained following the procedure described earlier and are presented in Table 4.4. It can be seen from Table 4.4 that the r_{\max} increases with the increase in crack length if the boundaries are at larger distances from the crack tip. The results of Table 4.4 clearly show that in the absence of boundary effects, the length of the crack, a is the controlling parameter for changes in the r_{\max} . Approximately identical values of the ratio r_{\max}/a in Table 4.4 further support the above conclusion.

Table 4.4 Variation of the r_{\max} with the crack length a for the center cracked plate

a (mm)	a/b	r_{\max} (mm)	r_{\max}/a
15	0.0125	8.27	0.5513
30	.025	16.03	0.5343
60	.05	32.67	0.5445

To study the effect of remaining net ligament length ($b-a$) or effect of boundary alone on the r_{\max} , three center cracked plates having the same crack length $a = 30$ mm and widths of $b = 1200, 60, 42.86$ mm ($b-a = 1170, 30$ and 12.86 mm) are considered. It is shown in previous paragraph that the boundary has no effect on r_{\max} for the configuration with $a = 30$ and $b = 1200$ mm due to the large net ligament length. Fig. 4.12 shows FE discretizations of the configurations having $b = 60$ and 42.86 mm for determination of ε_{aa} along the respective gage lines. Fig. 4.13 shows the variation of ε_{aa} with the radial distance r along the gage line on logarithmic scale for all of these three configurations and Table 4.5 shows results of the r_{\max} values obtained from these figures.

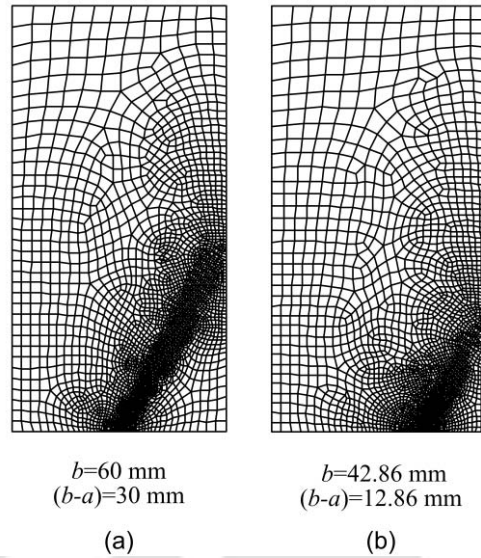


Figure 4.12 Finite element meshes for the center cracked plates employed to study the effect of net ligament length on r_{\max}

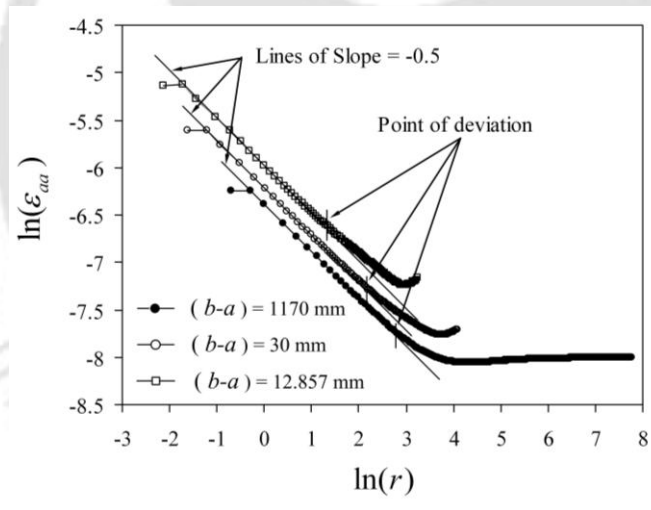


Figure 4.13 Graph of $\ln(\varepsilon_{aa})$ versus $\ln(r)$ showing variation of the r_{\max} with the net ligament length $(b-a)$

Table 4.5 Variation of the r_{\max} with the net ligament length $(b-a)$ for the center cracked plate

a (mm)	b (mm)	a/b	r_{\max} (mm)	$r_{\max}/(b-a)$	$r_{\max}/2b$
30	1200	0.025	16.03	0.0137	0.0067
30	60	0.5	8.78	0.2927	0.0732
30	42.857	0.7	3.78	0.2940	0.0441

Table 4.5 shows that the r_{\max} value decreases with the increase of a/b values that are having small net ligament length ($a/b = 0.5$ and 0.7). This implies that, in the cases of the small net ligament or higher a/b values, the net ligament length ($b - a$) is the controlling parameter for change in the r_{\max} values. To support this observation further, approximately identical values of the ratio $r_{\max}/(b - a)$ for $a/b = 0.5$ and 0.7 can be noticed in Table 4.5. These observations are in agreement with the results reported by Chona and co-workers [55] for singularity dominated zone.

The explanation for the bell shaped trend of the r_{\max} with a/b in Fig. 4.9 can now be given as follows. Initially, at low values of a/b , the r_{\max} value increases with the increase in a/b as the crack length is the controlling parameter due to the insignificance/absence of boundary effect on the r_{\max} . As a/b is further increased, the net ligament length becomes small and a point is reached at which the controlling parameter is shifted from the crack length, a to the net ligament length ($b - a$) due to the boundary effects. As a result, the r_{\max} value decreases as the a/b value is further increased. The results in last two columns of Table 4.3 provide further substantiation to the above conclusion. The values of r_{\max}/a corresponding to $a/b = 0.2$ and 0.3 are almost identical and are significantly different from other values of a/b , indicating the influence of the crack length, a . On the other hand, the values of $r_{\max}/(b - a)$ are nearly identical for a/b from 0.5 to 0.8 , indicating the influence of boundary effects.

4.4 Effect of Poisson's ratio on r_{\max}

To study the effect of Poisson's ratio on values of r_{\max} , three center cracked plates having $a/b = 0.5$ and different Poisson's ratios $\nu = 0.25, 0.3$ and $1/3$ are considered. Other parameters of the problem domains can be found in Table 4.1. Finite element meshes are designed for the center cracked plate with $\nu = 0.25$ and 0.3 in a similar way as that of $a/b = 0.5$ and $\nu = 1/3$ (see Fig. 4.3(c)). Fig. 4.14 shows the variation of $\ln(\varepsilon_{aa})$ with $\ln(r)$ along the gage line of the above configurations

along with the superposed lines of slope equals to -0.5. Fig. 4.14 also shows the point of deviation and the corresponding r_{\max} values computed using the proposed approach. The r_{\max}/a values corresponding to different value of ν are also presented in the Fig. 4.14 which shows that the Poisson's ratio does not have significant effect on r_{\max} values.

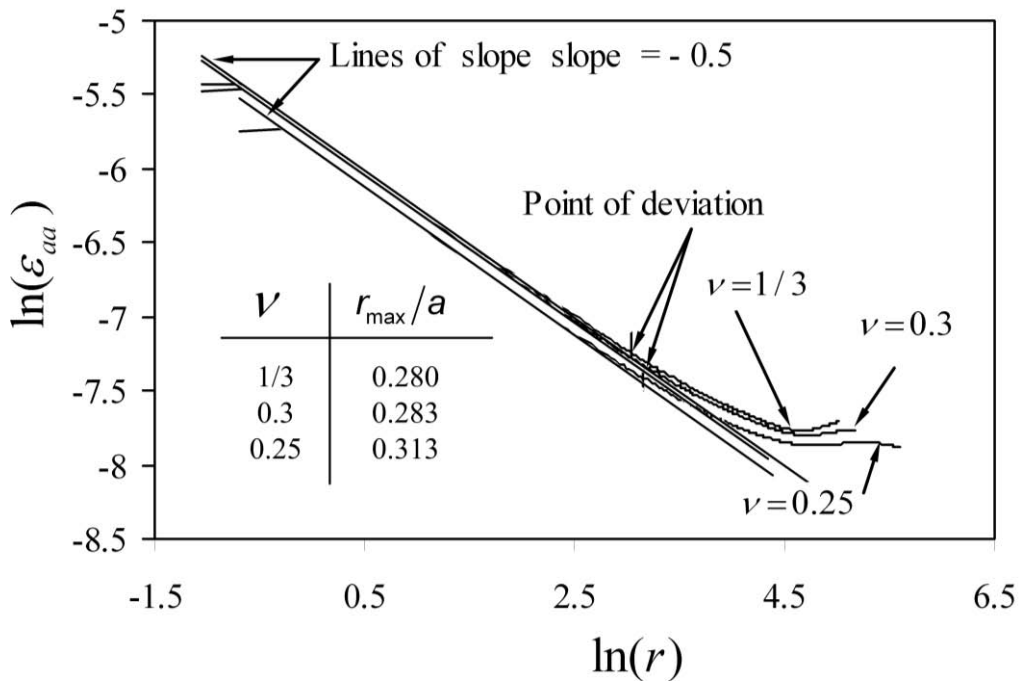


Figure 4.14 Graph of $\ln(\epsilon_{aa})$ versus $\ln(r)$ showing variation of the r_{\max} with the Poisson's ratio ν

4.5 Determination of r_{\max} for edge cracked plates

This example is intended for determination of r_{\max} values for edge cracked configurations under plane stress conditions subjected to uniform tensile stress as shown in Fig. 4.15(a). Different values of the crack length to width ratio (a/b) ranging from 0.1 to 0.8 in steps of 0.05 are considered. Material properties and other geometrical parameters used in this example are listed in Table 4.6. Due to symmetry only half of the domain as shown in Fig. 4.15(b) is employed for FEA. A typical finite element mesh for one half of the plate that is employed for determination of the r_{\max} is shown in Fig. 4.16(a).

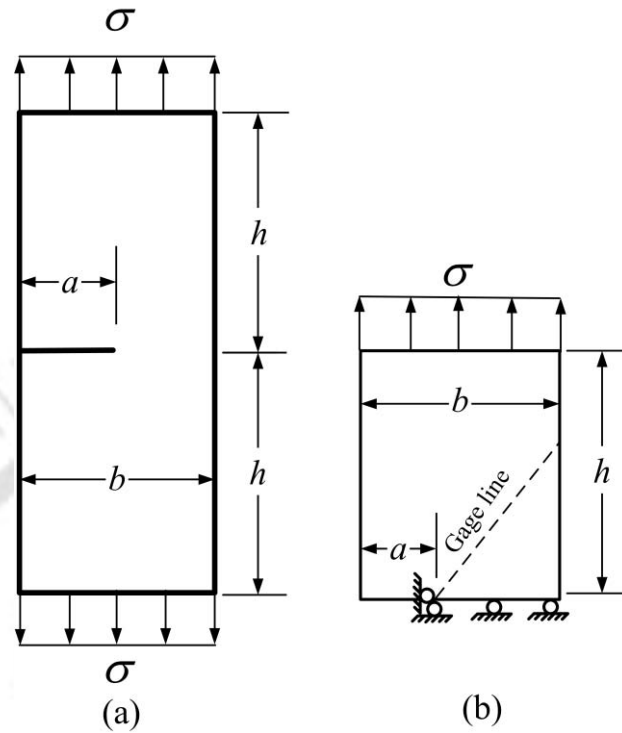


Figure 4.15 (a) A typical edge cracked plate (b) solution domain for edge cracked plate

Table 4.6 Geometric and material parameters of the edge cracked plate

Example	State of stress	b (mm)	a/b	h/b	ν	E (GPa)	σ (MPa)
4.5	Plane stress	1200	0.1-0.8	3	1/3	200	100
4.6	Plane stress	1200	0.00625, 0.0125, 0.025, 0.05	3	1/3	200	100
4.7	Plane stress and plane strain	1200	0.3-0.8	3	1/3	200	100

The mesh (Fig. 4.16(a)) is so designed that nodes of several elements are made to lie along the positive gage line which makes an angle of θ with the axis of crack (Eq. (3.27)). In all the meshes, this line begins at the crack tip and terminates at the outer boundaries of the cracked plate. According to DS technique, a single strain gage is required to be placed at an appropriate location on the gage line in the direction of α (Eq. (3.26)) in order to measure the linear strain ε_{aa} (Fig. 3.4). The strains calculated

in global coordinate along the gage line are then transformed into linear strain $\varepsilon_{\alpha\alpha}$ in the direction α . The radial distances (r) of each of the nodes on the gage line from the crack tip are then computed.

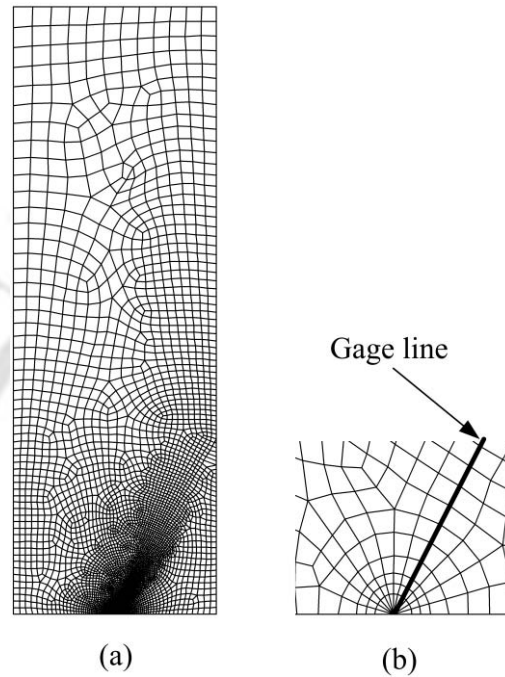


Figure 4.16 (a) Typical mesh used for edge cracked plate (b) enlarged view at the crack tip corresponding mesh

Following the procedure described in section 3.3, plot of $\ln(\varepsilon_{\alpha\alpha})$ versus $\ln(r)$ for all values of a/b is shown in Fig. 4.17. Crack tip point is not plotted as the radius of this point is zero. It is interesting to notice from Fig. 4.17 that, each plot consists of distinguishable linear portion followed by nonlinear portion (in logarithmic scale) as predicted by theory (section 3.3) and as observed in previous examples. The linear trend distinctly exists up to a certain radial distance and thereafter gradually turns to the nonlinear portion. This can be observed in plots for all values of a/b of edge cracked plate.

As discussed earlier, the initial linear part is due to the dominance of the three parameters (Eq. (3.25)) and nonlinear part is due to the presence of more than three parameters in the expression for $\varepsilon_{\alpha\alpha}$. The end point of the linear portion of the plots in these figures clearly indicates the extent of the three parameter strain series which is

the upper bound for strain gage locations i.e. r_{\max} according to the proposed theory. The first point in all the plots of Fig. 4.17 is the strain value at the corner node of the quarter point element. The deviation of this point from the straight line portion may be due to the effect of the constant strain term of the QPEs [54].

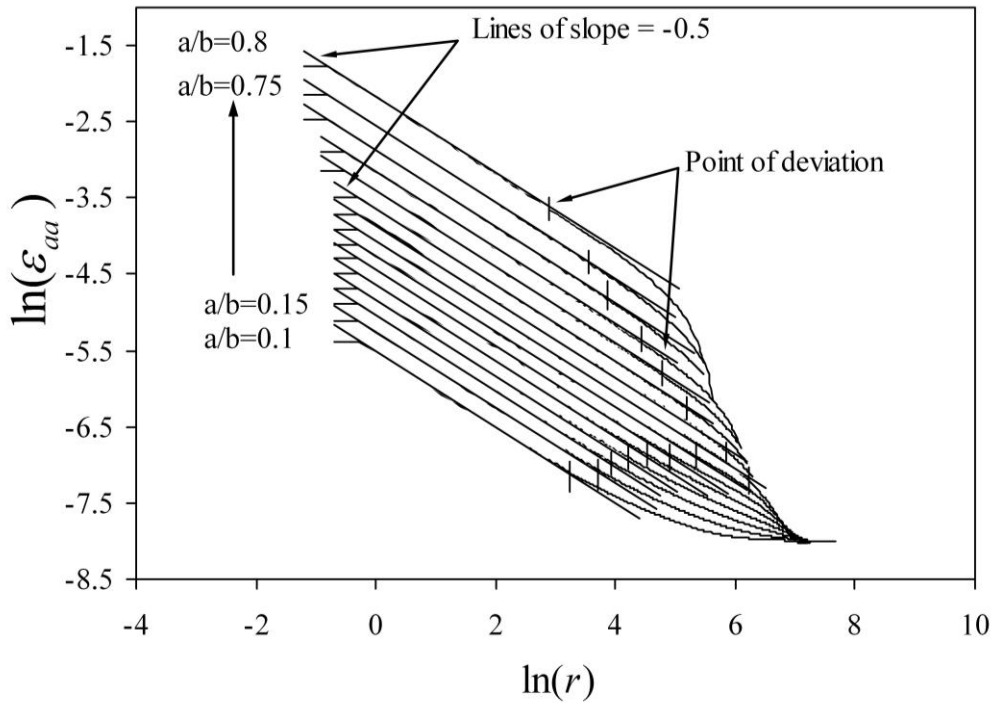


Figure 4.17 Variation of $\ln(\varepsilon_{aa})$ with $\ln(r)$ along the gage line for the edge cracked plates

Following the proposed procedure in section 3.3 for determination of r_{\max} , straight lines having slope of -0.5 are superposed onto the all plots of $\ln(\varepsilon_{aa})$ versus $\ln(r)$ in Fig. 4.17. It is interesting to notice from Fig. 4.17 that both the initial straight line portion of the plots and superposed lines are congruent to each other up to a certain radial distance for all a/b values and the numerical results deviate from the superposed line thereafter due to the dominance of coefficients other than A_0 , A_1 and B_0 in Eq. (3.25). The estimated values of r_{\max} or the extent of validity of the three parameter zone are marked in Fig. 4.17 as per the procedure described in section 3.3. The corresponding numerical values of the r_{\max} are presented in Table 4.7. A plot of variation of r_{\max} with a/b is presented in Fig. 4.18.

It can be seen from the results of Table 4.7 and Fig. 4.18 that as the crack length is increased, the value of r_{\max} increases initially until it reaches a maximum value at $a/b = 0.45$ ($r_{\max} = 505.34$ mm) and thereafter it decreases with the increase of the crack length. A similar trend has also been observed for center cracked plate in previous example. Similar to the previous example, an explanation to this behavior of the r_{\max} with a/b is investigated in the next section for edge cracked plate.

Table 4.7 Variation of the r_{\max} with crack length a of the edge cracked plate under plane stress condition ($b = 1200$ mm and $h/b = 3$)

a/b	a (mm)	r_{\max} (mm)	r_{\max}/a	$r_{\max}/(b-a)$	r_{\max}/b
0.00625	7.5	1.89	0.252	0.002	0.001
0.0125	15	3.97	0.265	0.005	0.003
0.025	30	7.51	0.250	0.006	0.006
0.05	60	13.55	0.226	0.012	0.011
0.1	120	25.73	0.214	0.024	0.021
0.15	180	41.16	0.229	0.040	0.034
0.2	240	51.34	0.214	0.053	0.043
0.25	300	67.64	0.225	0.075	0.056
0.3	360	91.82	0.255	0.109	0.077
0.35	420	136.80	0.326	0.175	0.114
0.4	480	208.96	0.435	0.290	0.174
0.45	540	505.34	0.936	0.766	0.421
0.5	600	347.51	0.579	0.579	0.290
0.55	660	178.98	0.271	0.331	0.149
0.6	720	120.71	0.168	0.251	0.101
0.65	780	83.63	0.107	0.199	0.070
0.7	840	47.85	0.057	0.133	0.040
0.75	900	34.42	0.038	0.115	0.029
0.8	960	17.75	0.018	0.074	0.015

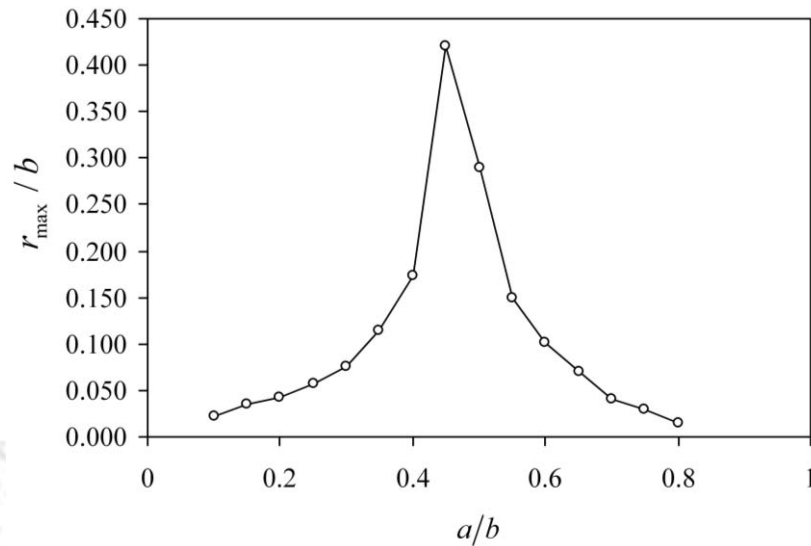


Figure 4.18 Graph of the r_{\max} as a function of a/b (0.1-0.8) for the edge cracked plate.

4.6 Effect of the crack length and proximity of boundary on the r_{\max}

As a/b is increased, the crack length increases and at the same time the crack tip approaches the boundary. In the present investigation, the proximity of the right boundary is measured by the net ligament length $(b-a)$. In order to understand the trend of the r_{\max} with a/b , the effect of increase in crack length alone is studied by keeping the boundary at a large distance from the crack tip. To achieve this, same edge cracked plate as in section 4.5, but with $b = 1200$ mm and $h/b = 3$ is again considered here. Four values of crack length $a = 7.5, 15, 30$ and 60 mm are considered leading to very small values of $a/b = 0.00625, 0.0125, 0.025$ and 0.05 . Since the corresponding a/b values are very small, it can be assumed that the right boundary of the edge cracked plate has no effect while the crack length is increased from 7.5 to 60 mm. Other parameters for the present analysis can be found in Table 4.6. Finite element meshes for the above configurations have been designed in a similar pattern as shown in Fig. 4.16(a). Fig. 4.19 shows the plots of $\ln(\varepsilon_{aa})$ versus $\ln(r)$ for $a/b = 0.00625, 0.0125, 0.025$ and 0.05 . The r_{\max} values for these configurations have been obtained as described earlier in section 3.3 and are presented in Table 4.7.

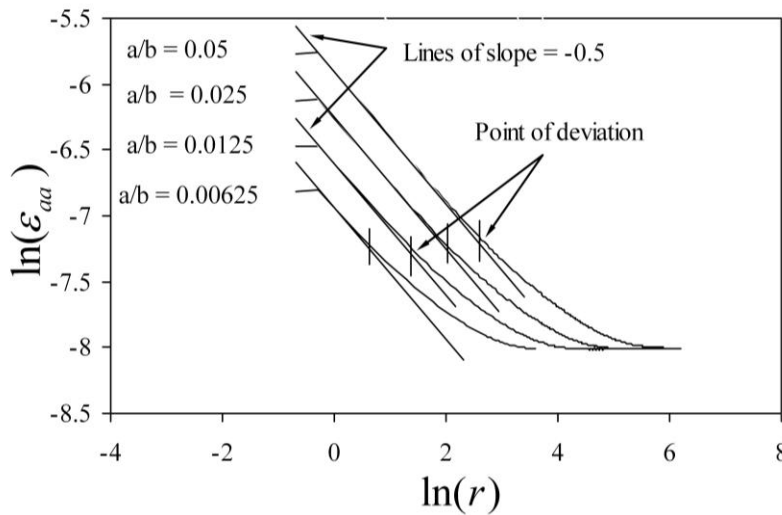


Figure 4.19 Variation of $\ln(\varepsilon_{aa})$ with $\ln(r)$ along the gage line for the edge cracked plates under plane stress condition with $a/b = 0.00625$ to 0.05

It can be observed from the results of Table 4.7 that, when the right boundary is remotely located from the crack tip, the r_{\max} values are significantly influenced by the crack length such that the r_{\max} increases with the increase in crack length. An exactly same trend has also been noticed for center cracked plates in the previous examples. Fig. 4.20 shows variation of the r_{\max}/a and $r_{\max}/(b-a)$ with a/b ratios considered in this example (Table 4.7).

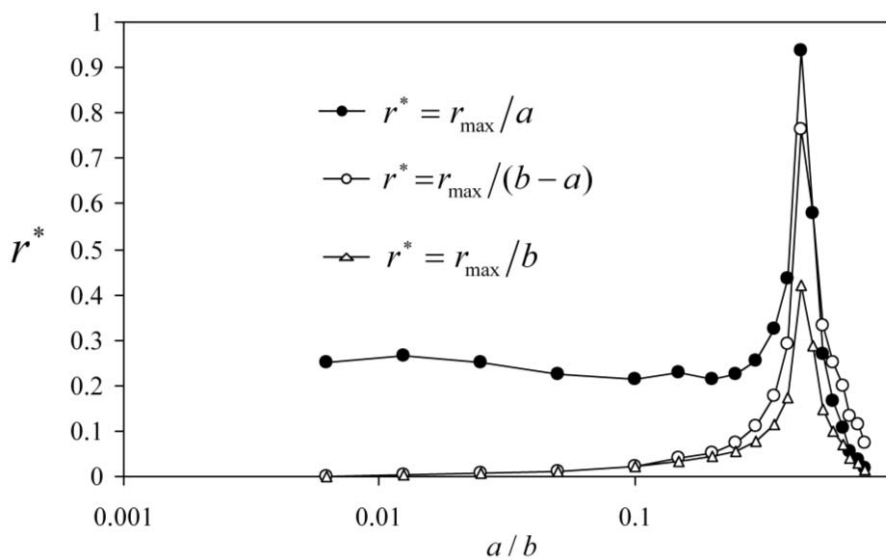


Figure 4.20 Variation of r_{\max} with a/b (0.00625 to 0.8) for edge cracked plates under plane stress condition

It can be noticed from Fig. 4.20 that for very small values of a/b , the r_{\max}/a values are almost constant and finite. On the other hand, the $r_{\max}/(b-a)$ values tend to zero for small values of a/b indicating the crack length is the controlling parameter in determining the r_{\max} . As a/b is further increased, the increase and decrease in r_{\max} values could be due to the predominant effect of crack length a and the net ligament length $(b-a)$, respectively as is evident in Fig. 4.20.

The influence of the right boundary might have initiated from $a/b = 0.3$. As the crack length increases from $a/b = 0.35$ to 0.45 , the r_{\max} continues to increase due to more influence of crack length as compared to the boundary effects (Table 4.7 and Fig. 4.20). After reaching a maximum value of $r_{\max} = 505.34$ mm at $a/b = 0.45$, the r_{\max} value starts decreasing with further increasing of a/b value indicating the increased influence of the proximity of right boundary or simply the boundary effect. The effect of boundary can be more clearly seen for $a/b = 0.7, 0.75$ and 0.8 for which approximately similar order of values of the ratio $r_{\max}/(b-a)$ can be noticed from Table 4.7. On the other hand, insignificant order of values of the ratio r_{\max}/a can be seen from Table 4.7 for $a/b = 0.7, 0.75$ and 0.8 . The range of $a/b = 0.35$ to 0.65 could be considered as a transition region. These observations are in agreement with the results obtained for the center cracked plate presented in section 4.3.

Thus, the above observations can be summarized as: (a) the r_{\max} increases with the increase in crack length as long as the effect of the boundary is either absent or insignificant which usually occurs at relatively low values of a/b and (b) r_{\max} decreases with the increase in a/b due to the domination of the boundary effects which occurs at relatively larger values of a/b . Similar to the present investigation, Chona et al. [55] investigated the extent of the singular term or singularity dominated zone (SDZ) of various cracked configurations and reported the decrease of size of the SDZ with the increase of a/b .

Another justification for the observed variation of the r_{\max} with a/b ratio can be explained as follows. The longitudinal strain ε_{aa} as defined by Eq. (3.28) for the entire gage line is a function of coefficients $A_0, A_1, A_2, A_3, \dots, B_0, B_1, B_2, B_3, \dots$, the radial distance from the crack tip, material properties (E, ν), angular parameters θ, α and the state of stress (κ). Referring to Fig. 4.17, the r_{\max} is computed at the end point of the singular term (A_0) dominance zone (i.e. end of the straight line portion) or beginning of the dominance zone of the nonsingular terms $A_1, A_2, A_3, \dots, B_0, B_1, B_2, B_3, \dots$ (i.e. beginning of nonlinear portion in Fig. 4.17). Thus, it is evident that the extent of nonlinear portion and hence the r_{\max} value is a function of the magnitude of the nonsingular terms, relative to the singular term A_0 . Conversely, relative increase in magnitude of the A_0 has a tendency to increase the r_{\max} , while increase in magnitude of the nonsingular terms (relative to the A_0) decreases r_{\max} value.

An experimental evidence to this increasing trend of the nonsingular terms with a/b was noticed by Chona et al. [55] using the photoelasticity technique. They showed that, magnitude of all the coefficients (singular and nonsingular) increased gradually and after a certain value of a/b , the magnitude of nonsingular terms sharply increased with increase in a/b values. Referring to Fig. 4.17, as a/b is increased, the magnitude of the singular term A_0 has dominated over the magnitudes of nonsingular terms. As a result, the r_{\max} value increases (due to the increase in linear portion as compared to nonlinear portion) with increase in a/b ratio. For subsequent increase in a/b , the magnitude of nonsingular terms have dominated over the singular term, due to which the nonlinear portions increases and hence r_{\max} decreases. Thus, relative increase in magnitude of the A_0 leads to increase in the r_{\max} value, while increase in magnitude of the nonsingular terms results in decrease in the r_{\max} .

4.7 Effect of state of stress on r_{\max}

This section demonstrates the influence of the state of stress (i.e., plane stress or plane strain conditions) on the r_{\max} values for a given a/b ratio. For this purpose, an edge cracked (Fig. 4.15) plate of different a/b ratios ranging from 0.3 to 0.8 in steps of 0.1 has been analyzed under plane strain conditions. Material properties, loading and other geometrical parameters for this configuration can be found in Table 4.6. Angles α and θ are computed using Eqs. (3.26) and (3.27) by replacing ν by $\nu/(1-\nu)$. Fig. 4.21 shows variation of $\ln(\varepsilon_{aa})$ versus $\ln(r)$ for different a/b ratios under plane strain conditions.

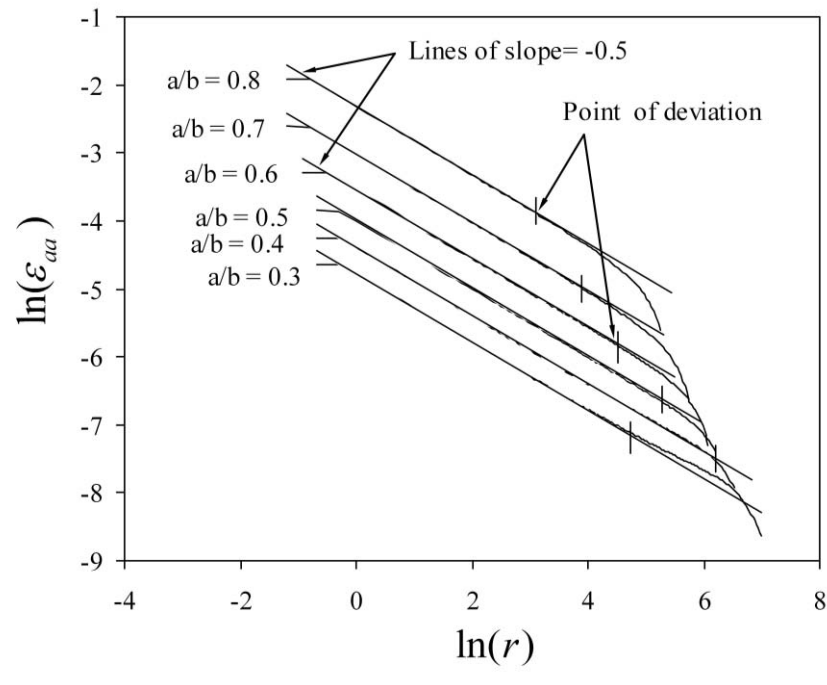


Figure 4.21 Variation of $\ln(\varepsilon_{aa})$ with $\ln(r)$ along the gage line for the edge cracked plates with under plane strain conditions

Fig. 4.22 shows comparison between r_{\max} values obtained using plane stress and plane strain conditions. It can be observed from Fig. 4.22 that for smaller values of a/b the value of r_{\max} in plane strain conditions is larger than that in plane stress conditions. Insignificant difference between the r_{\max} values can be noticed at larger a/b .

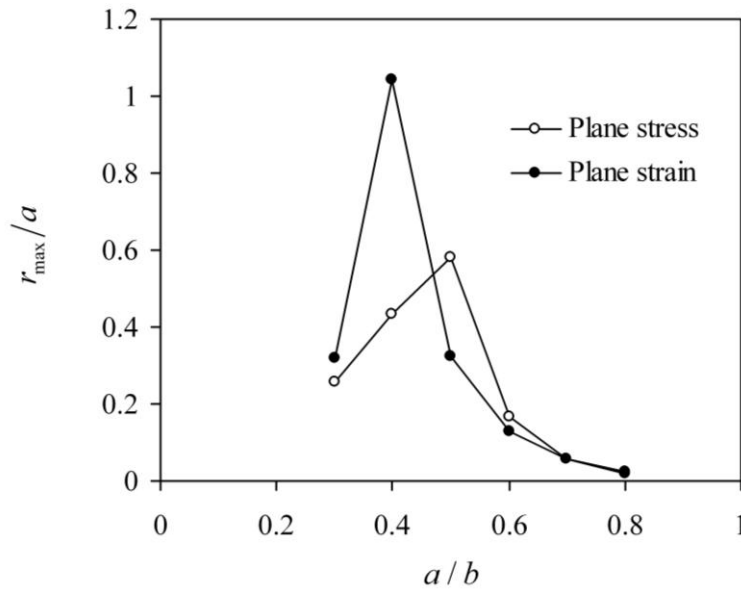


Figure 4.22 Comparison of plane stress and plane strain r_{\max} values for the edge cracked plate

The observed difference in r_{\max} values between the plane stress and plane strain condition (Fig. 4.22) can be explained with the help of discussion made in the previous section. It is well known that the magnitude of singular (A_0) and nonsingular coefficients ($A_1, A_2, A_3, \dots, B_0, B_1, B_2, \dots$) in the expression for ε_{aa} (Eq. (3.25)) along the entire gage line remain same for both plane stress and plane strain conditions as they are functions of the geometry and boundary conditions of the cracked body. Thus, ε_{aa} along the entire gage line for plane stress differs from the plane strain conditions mainly due to the change in terms that are associated with material properties (E and ν).

For a given geometry and boundary conditions, the increase in magnitude of the singular and nonsingular terms with the increase in a/b remains same for both the plane stress and plane strain states. Consequently, bell shaped variation of the r_{\max} with a/b can be noticed in Fig. 4.22 for both plane stress and plane strain cases. The difference in r_{\max} values, therefore, is mainly due to the material property dependant terms which assume different values in plane stress and plane strain conditions.

4.8 Determination of r_{\max} for double edge cracked plates

In this example, the r_{\max} values of double edge cracked plates are presented. For this purpose, a double edge cracked plate as shown in Fig. 4.23(a) with $a/b = 0.2$ to 0.7 in steps 0.1 , $b = 150$ mm, $h/b = 2$ and subjected to uniform tensile stress is considered. Applied stress 100 MPa, and Young's modulus $E = 200$ GPa and Poisson's ratio $\nu = 1/3$ have been considered. Plane stress conditions are assumed. Due to symmetry only a quarter portion of the domain as shown in Fig. 4.23(b) is employed for FE analysis.

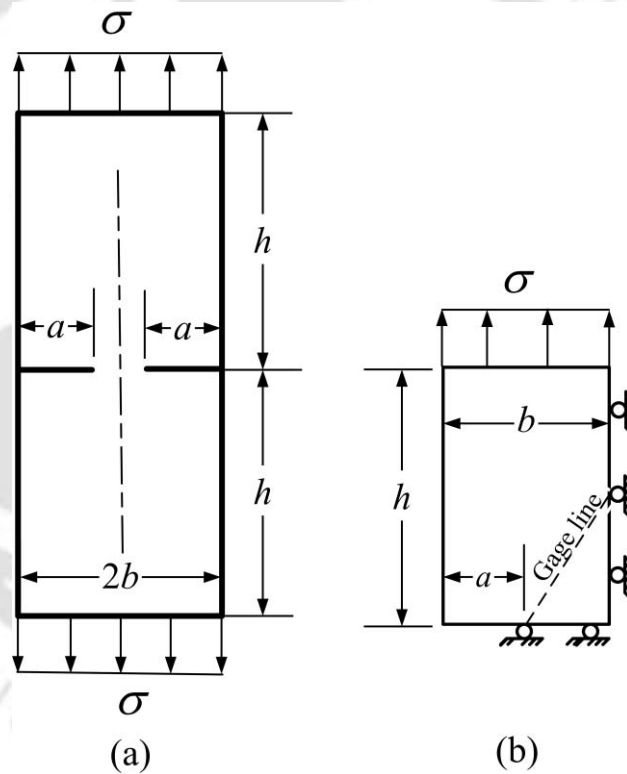


Figure 4.23 (a) Double edge cracked plate (b) solution domain for the double edge cracked plate

Fig. 4.24(a) shows a typical mesh employed in the FE analysis for all a/b values and Fig. 4.24(b) shows enlarged view at the crack tips. Following the procedure described in the section 3.3, ε_{aa} values of double edge cracked plate with $a/b = 0.2$ to 0.7 have been computed. Fig. 4.25 shows the variation of $\ln(\varepsilon_{aa})$ versus $\ln(r)$ for

different a/b ratios. It could be seen from Fig. 4.25 that in each case, there is a definite linear portion followed by non-linear portion as predicted by the theory.

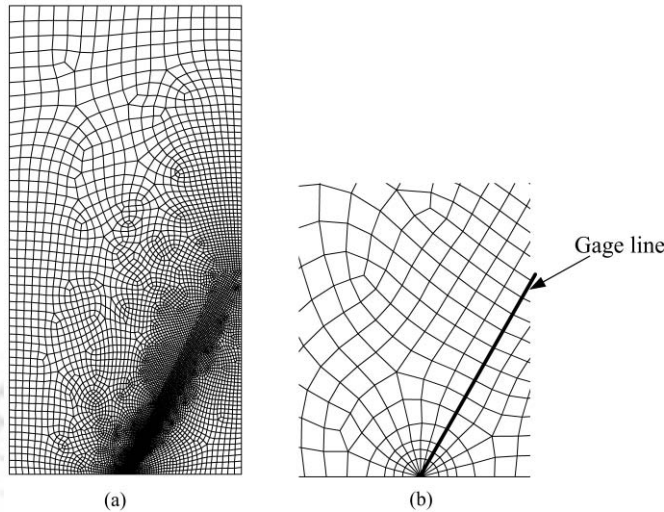


Figure 4.24(a) Typical mesh used for double edge cracked plate (b) enlarged view at the crack tip corresponding mesh

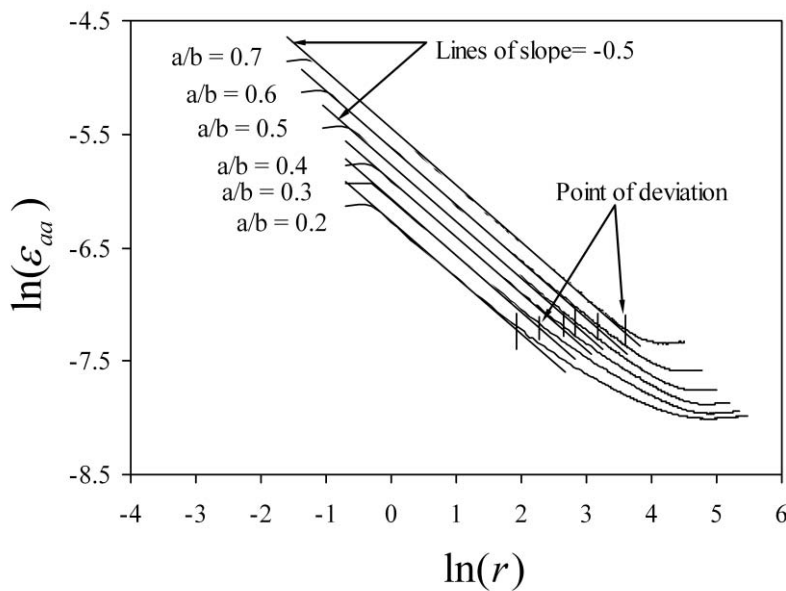


Figure 4.25 Variation of $\ln(\varepsilon_{aa})$ with $\ln(r)$ along the gage line for the double edge cracked plates with $a/b = 0.2$ to 0.7

Using the same procedure as described in section 3.3, the r_{\max} values are extracted and are tabulated in Table 4.8. It should be noted that each crack on either side of this plate can be increased to maximum length of b . It is interesting to observe from the

results of Table 4.8 that the r_{\max} value increases with the increase in a/b . In fact, this could be anticipated because, as a/b increases, in contrast to previous examples, the crack tips in this configuration moves away from their respective boundaries. Therefore, the crack length is the controlling parameter for changes in r_{\max} values. As a consequence, the r_{\max} values increased with the increase in a/b ratio. This explanation is clearly based on the investigations carried out on effect of crack length and proximity of boundaries in the previous examples.

Table 4.8 Variation of the r_{\max} with a/b for the double edge cracked plate subjected to uniform tensile stress ($b = 150\text{ mm}$ and $h/b = 2$)

a/b	r_{\max} (mm)	r_{\max} / a
0.2	6.90	0.230
0.3	9.82	0.218
0.4	14.02	0.234
0.5	16.74	0.223
0.6	24.20	0.269
0.7	36.56	0.348

4.9 Eccentric center cracked plate subjected to uniform tensile stress

The objective of this example is to determine the r_{\max} values for more complicated configuration like the eccentric center cracked plate subjected to uniform tensile stress as shown in Fig. 4.26(a). In this example, only the eccentricity ratio (e/b) is varied keeping the total length of the crack and width of the plate constant. In this way the crack tips can be made to occupy close to and away from a boundary, so that the effect of boundary on r_{\max} once again can be substantiated. Different eccentricity ratios ranging from 2.5% to 15% in steps of 2.5% have been considered in this example. Material properties and other geometrical parameters used in this example are listed in Table 4.9. Fig. 4.27(a) shows a typical mesh used for

determination of the r_{\max} values using the present approach and Fig. 4.27(b) shows enlarged view at the crack tip.

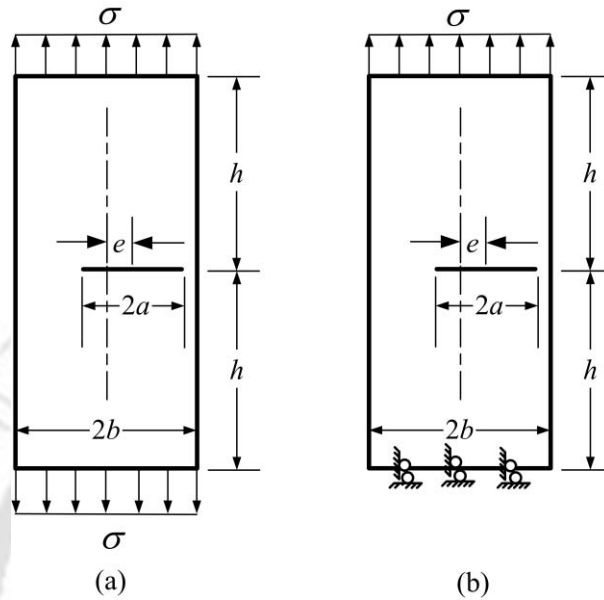


Figure 4.26 (a) Eccentric cracked plate; (b) solution domain for eccentric cracked plate

Table 4.9 Geometric and material properties of eccentric center cracked plate

Eccentricity (%) (e/b)*100	b (mm)	a/b	$h/b = 2$	ν	E (GPa)	σ (MPa)
2.5-15	75	0.5	2	1/3	200	100

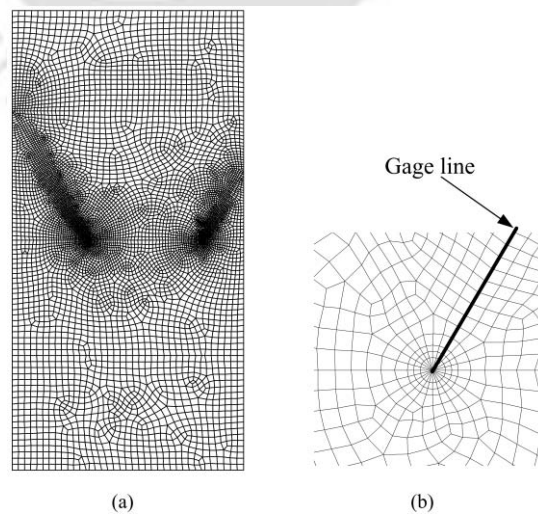


Figure 4.27(a) Typical mesh used for eccentric cracked plate (b) enlarged view at the crack tip corresponding mesh

Fig. 4.28(a) shows plots of $\ln(\varepsilon_{aa})$ versus $\ln(r)$ obtained using the values at the right crack tip for an eccentricity ratio 15%. Similarly, Fig. 4.29 shows plots of $\ln(\varepsilon_{aa})$ versus $\ln(r)$ at the left crack tips, for a typical eccentricity 15%. Similar trend has been observed at both the right and left crack tip for all the above values of eccentricity ratios. Once again it could be noticed from Figs. 4.28 and 4.29 that there is a definite linear portion followed by non-linear portion as predicted by theory.

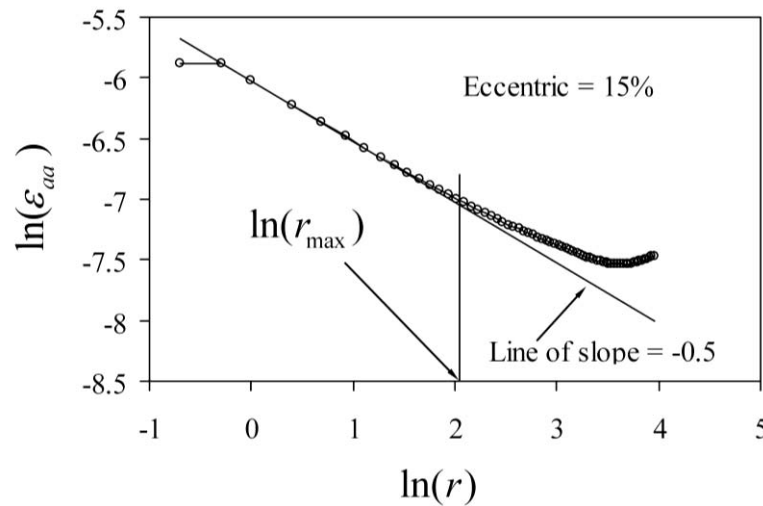


Figure 4.28 Variation of $\ln(\varepsilon_{aa})$ with $\ln(r)$ along the right gage line for 15% eccentricity ratio

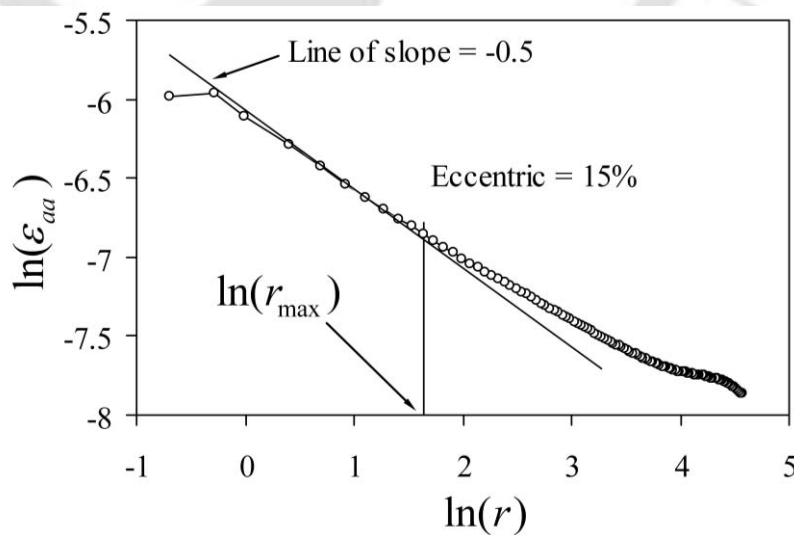


Figure 4.29 Variation of $\ln(\varepsilon_{aa})$ with $\ln(r)$ along the left gage line for 15% eccentricity ratio

The r_{\max} values are obtained at both the right tip and left tip using the proposed procedure as described earlier and are presented in Table 4.10.

Table 4.10 Variation of the r_{\max} with % eccentricity of center cracked plate

Eccentricity (%)	Left gage line r_{\max} (mm)	Right gage line r_{\max} (mm)
2.5	3.74	12.43
5.0	4.92	10.49
7.5	4.29	10
10.0	5.7	10.13
12.5	5.06	8.79
15.0	5.35	7.77

It is interesting to notice from results of Table 4.10 that with the increase in eccentricity ratio the r_{\max} values showed a continuous decreasing trend in the case of right crack tip while for the left crack tip it showed an increasing trend. It should be noted that the selected $a/b = 0.5$ is sufficiently large enough to interact with the boundaries. Thus, as the eccentricity ratio is increased the right crack tip is shifted more close to the right boundary while the left crack tip is moved away from the left boundary. Since the right crack tip is moved close to the boundary, the r_{\max} values decreases due to the boundary effects as demonstrated in the previous sections. On the other hand, since the left crack tip is moving away from the boundary, the r_{\max} values obtained at this tip are increasing as expected. This example clearly reinforces the observations made in the present investigation made on the effect of crack length and boundary on the r_{\max} .

4.10 Verification of gage locations used by earlier researchers [22, 33, 35, 39, 56]

As mentioned earlier, a large number of researchers have employed DS technique in which the gage locations were selected based on their past experience/guess work. The purpose of this example is to compare the used gage locations by the earlier workers with the r_{\max} values of their corresponding cracked specimens obtained using the present method. Five cracked configurations are considered for this purpose viz., (a) Compact tension (CT) specimen used by Dally and Sanford [22], (b) Dog bone specimen employed by Dally and Barker [33], (c) three point bend specimen considered by Rizal and Homma [35] (d) edge cracked plate specimen with $h/b = 1.0$ employed by Swamy et al. [39] and (e) the three point bend specimen (TPB) used by Maleski et al. [56]. Fig. 4.30 shows geometry of experimental mode I specimens employed by the above researchers.

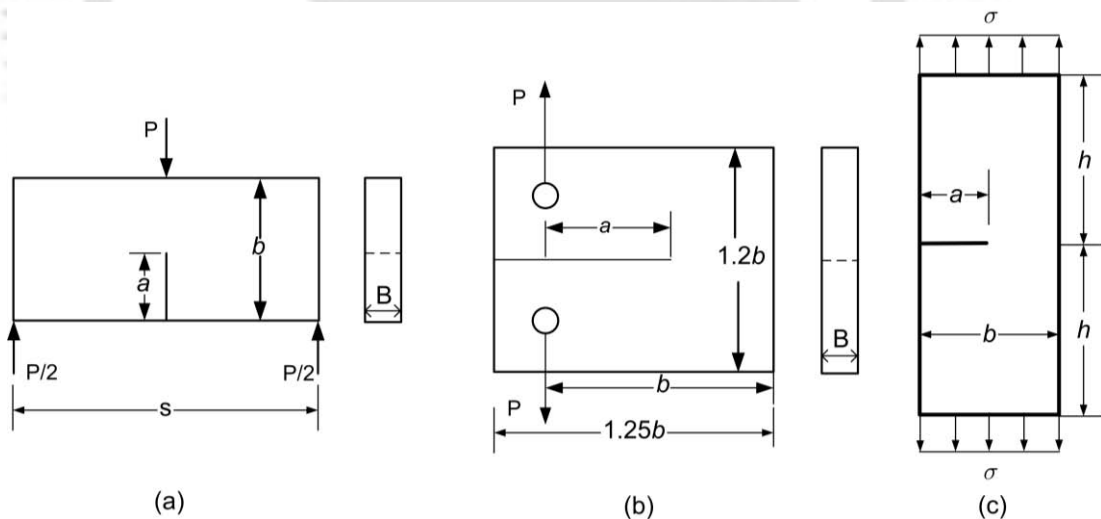


Figure 4.30 Geometry of mode I specimens (a) TPB (b) CT (c) Edge/Dog bone specimen

Table 4.11 shows other information about geometry, material properties, loading and state of stress considered by the above researchers. Fig. 4.31 shows FE meshes for the determination of r_{\max} for various configurations.

Table 4.11 Specimens and material properties used by various researchers			
Specimen	Dimensions in mm	ν	E (GPa)
CT [22]	$b=305, B=6.35, a/b=0.5$	0.33	70
Dog bone [33]	$a=18, b=50, 2h =200,$ $B=9.4, a/b=0.36$	0.33	3.45
TPB [35]	$a=20, b=40, s=180, B=10, a/b=0.5$	0.33	71.1
EC [39]	$a=75, b= 150 h =100, a/b=0.5, B=6$	0.37	2.3
TPB [56]	$a=10, b=50 s=200, B=8.8, a/b=0.2$	0.35	3.2

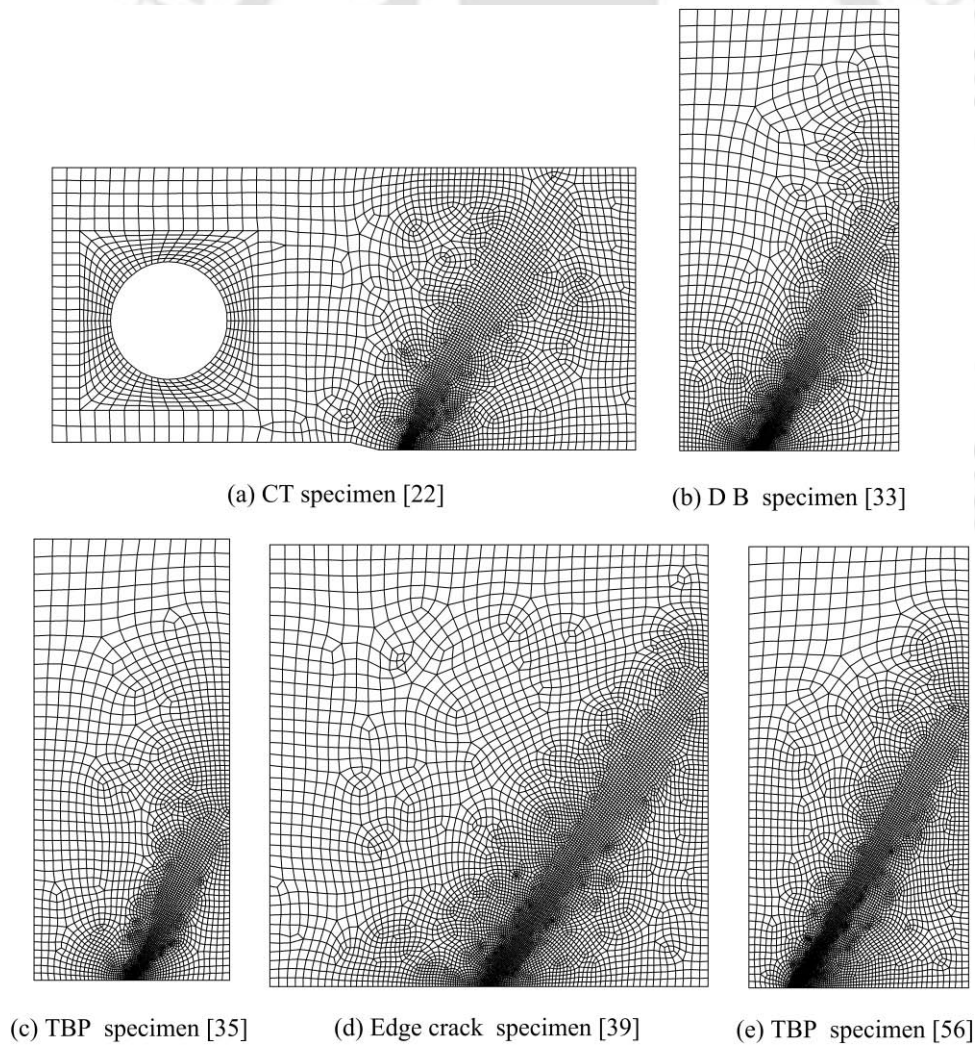


Figure 4.31 Finite element meshes for numerical analysis

Fig. 4.32 shows plots of $\ln(\varepsilon_{aa})$ versus $\ln(r)$ for the above five configurations along with terminal point of the straight line portion. Fig. 4.32 shows upper bound for the strain gage locations i.e. r_{\max} values along with the actual gage locations used by the earlier workers [22, 33, 35, 39, 56] for their corresponding specimen.

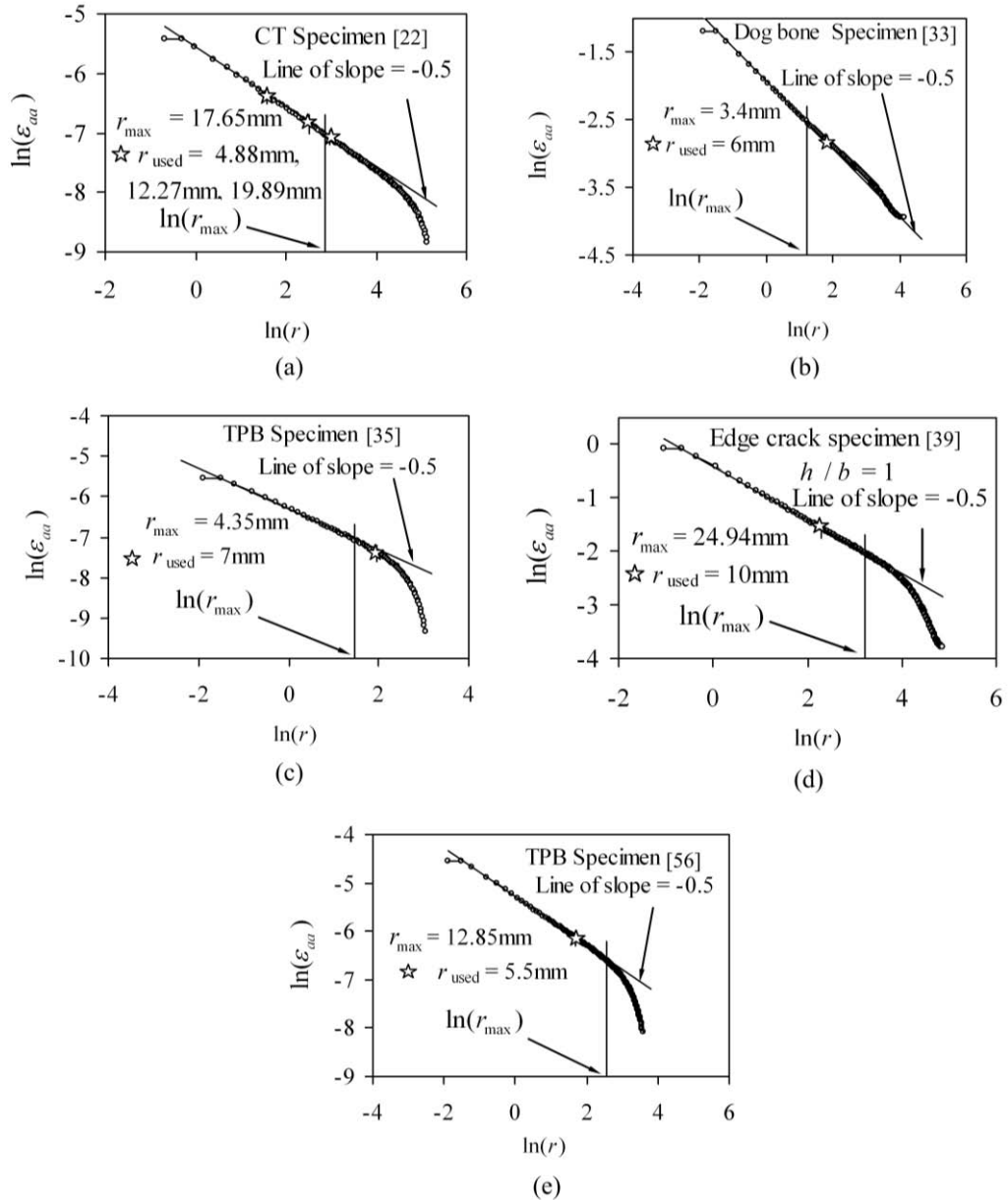


Figure 4.32 Plots showing the used strain gage locations by the earlier workers and their corresponding r_{\max} values for (a) CT specimen in Ref. [22] (b) Dog bone specimen in Ref. [33] (c) TPB specimen in Ref. [35] (d) Edge cracked plate specimen in Ref. [39] and (e) TPB specimen in Ref. [56]

It can be notice from all plots in Fig. 4.32 that, even for these configurations also, a distinct straight line and non-linear portion can be clearly observed. Except Rizal and Homma [35] and Dally and Barker [33] all other selected radial locations are well within the corresponding r_{\max} values. However, a value of $r = 19.89$ mm used by Dally and Sanford [22] is slightly greater than the corresponding $r_{\max} = 17.65$ mm. The strain gage location at $r = 4.88$ mm by Dally and Sanford [22] could be considered to be very close to the crack tip in comparison to their corresponding r_{\max} value.

As discussed earlier the measured strain also involves contribution due to the higher order nonsingular terms if a gage is located sufficiently beyond the r_{\max} . Thus, the strain measurements made at the gage locations employed by Rizal and Homma [35] and Dally and Barker [33], would not be the same as predicted by Eq. (3.25) and hence the measured SIF could be erroneous. On the other hand, the locations employed by Dally and Sanford [22], Maleski et al. [56] and Swamy et al. [39] could be considered as optimal or valid gage locations and it can be expected that strain measurements will be close to the theoretical prediction given by Eq. (3.25). Consequently, if all other experimental errors are minimized, the SIFs obtained from the above measurements [22, 39, 56] are expected to be very accurate.

4.11 Summary

Using the developed methodology r_{\max} values have been obtained for various mode I configurations. Variations of $\ln(\varepsilon_{aa})$ with $\ln(r)$ follows the expected trend supported by the theoretical formulations. Results obtained for mode I cases show that there is a strong dependence of r_{\max} value on the a/b ratio. It is observed that as a/b ratio increases the r_{\max} value increases up to a certain value of a/b and then with increase in a/b ratio the r_{\max} value decreases. Therefore, at large net ligament length i.e. small a/b , the crack length, a is the controlling parameter for r_{\max} as the boundary effects are negligible. But at small net ligament length i.e. at large a/b ,

boundary effects comes into picture and the net ligament length $(b-a)$ is the controlling parameter for r_{\max} . This trend of r_{\max} versus a/b is also in agreement with experimental results of Chona et al. [55]. It is observed that Poisson's ratio does not have significant effect on r_{\max} values. However, loading condition (plane stress and plane strain) affects r_{\max} values especially at lower value of a/b .



Chapter 5

Determination of r_{\max} for Mixed mode Cases

This chapter describes a general methodology for estimation of maximum permissible radial location for accurate measurement of mixed mode stress intensity factors (K_I and K_{II}) based on the theoretical formulations presented in sections 3.5 and 3.6 for mixed mode problems. The present chapter also investigates the performance of proposed modified DB technique for experimental determination of mixed mode SIFs in which the computed maximum permissible radial location is employed to locate the optimal gage locations. The effect of crack length to width ratio and the state of stress on optimal strain gage locations has also been investigated in this chapter. Accuracy of the proposed method in determination of coefficients of strain series expansion is substantiated and presented in this chapter by comparing the results from the present method with those of Xiao and Karihaloo [57] .

5.1 Problem Definition

In order to demonstrate the above aspects, a slant edge cracked plate (SECP) subjected uniform tensile stress as shown in Fig. 5.1(a) is considered in all the numerical examples. The proposed procedure for determination of the r_{\max} as discussed in section 3.6 is used in all the examples. Finite element analyses for all the examples considered are carried out using ANSYS. Eight noded isoparametric quadrilateral elements (Q8) embodied in ANSYS are employed for FE analysis of all the problems. In order to model the square root singularity at the crack tips, Q8 elements are collapsed to triangles and mid-side nodes are shifted to quarter points [52]. These collapsed Q8 quarter point elements (QPEs) are employed in a standard spider web pattern as shown in Fig. 5.1(c). Using ANSYS built-in KSCON command, these QPEs have been created by shifting mid-side nodes of the collapsed Q8 elements at the crack tip to the quarter position towards crack tip.

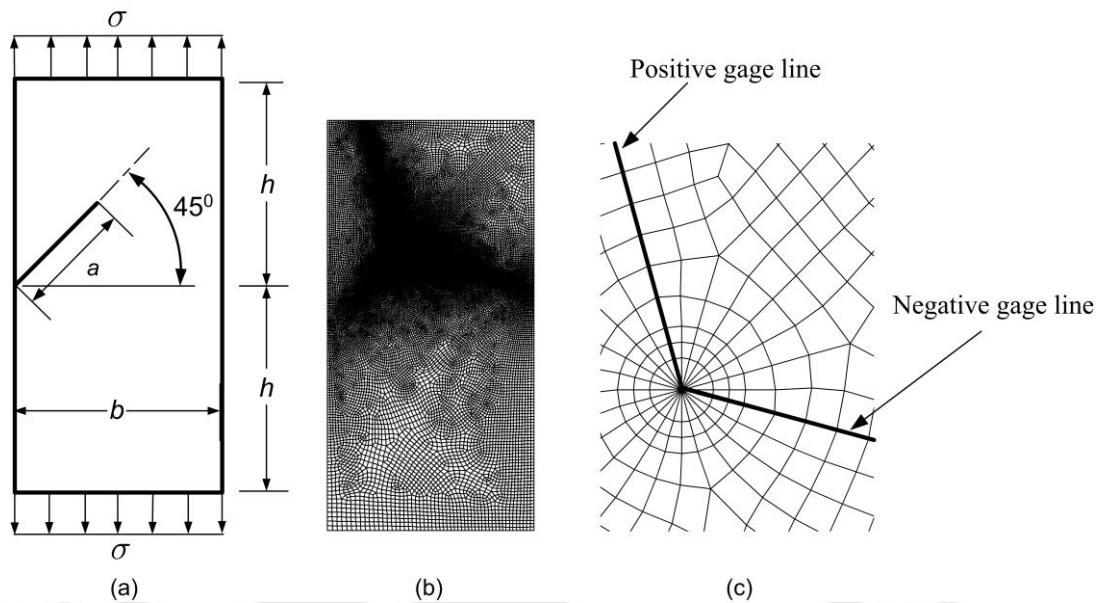


Figure 5.1 (a) Geometry of SECP subjected to uniform tension (b) typical mesh used in the present investigation for FEA (c) enlarge view at the crack tip region with the gage lines.

Fig. 5.1(b) shows a typical FE mesh along with the enlarged view at the crack-tip mesh (Fig. 5.1(c)) that is employed in all the examples of the present study for the FEA. In all the examples, plane stress conditions are assumed. The FE mesh is so designed that nodes of several elements are made to lie along the positive and negative gage lines (as shown in Fig. 5.1(c)) ensuring that the consecutive nodes from the crack-tip on both the gage lines will have same radial distance from the crack-tip. The bottom edge of the plate is completely restrained for displacements and uniform tensile stress is applied on the top edge of the plate. Mesh refinement has been done starting with a coarse mesh having 526 number of elements to the final refined mesh of 46720 elements till the convergence is obtained.

5.2 Determination of the r_{\max} for slant edge cracked plate

This example is intended to demonstrate the general procedure for determination of r_{\max} for a given 2D mixed mode configuration. For this purpose a SECP (Fig. 5.1(a)) with material, geometric and loading specifications as shown in Table 5.1 is considered.

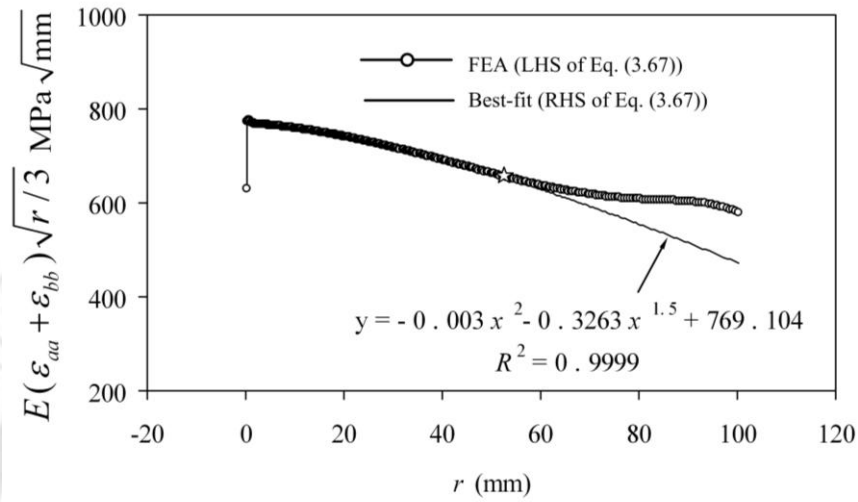
Table 5.1 Geometric and material parameters of the numerical examples of the present work.

Section	b (mm)	a/b	h/b	ν	E (GPa)	σ (MPa)	State of stress
5.2, 5.4	150	0.5	1	1/3	200	100	Plane stress
5.5	150	0.2-0.8	1	1/3	200	100	Plane stress
5.6	150	0.2-0.8	1	1/3	200	100	Plane stress and Plane strain

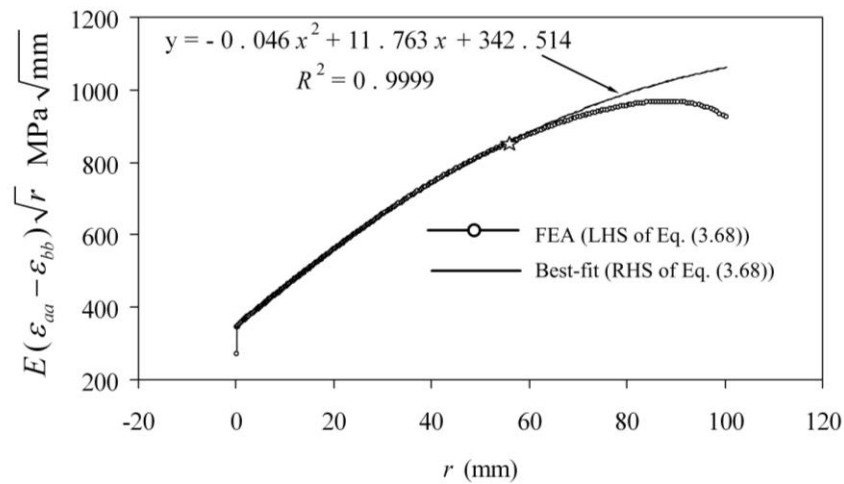
Following the procedure discussed in section 3.6 and from the present FEA, the values of $E\varepsilon_{aa}$ and $E\varepsilon_{bb}$ are computed at all the corner nodes of Q8 elements lying along the positive and negative gage lines respectively. Fig. 5.2(a) and Fig. 5.2(b) show the plots of FE values of $E(\varepsilon_{aa} + \varepsilon_{bb})\sqrt{r/3}$ and $E(\varepsilon_{aa} - \varepsilon_{bb})\sqrt{r}$ versus radial distance r respectively. Since $\nu = 1/3$ for this example, following Eq. (3.67) and Eq. (3.68), curves of the form $A_0 - A_2r^2 - \left(\frac{4}{\sqrt{3}}\right)B_1r^{3/2}$ and $C_0 + 2C_1r - 3C_2r^2$ are best-fitted to the computed data $E(\varepsilon_{aa} + \varepsilon_{bb})\sqrt{r/3}$ and $E(\varepsilon_{aa} - \varepsilon_{bb})\sqrt{r}$ in Fig. 5.2(a) and Fig. 5.2(b) respectively. These best-fits along with the values of coefficients A_0, A_2, B_1, C_0, C_1 and C_2 for best-fit regression and the corresponding correlation coefficient R^2 are also shown in Fig. 5.2(a) and Fig. 5.2(b).

It could be observed from Fig. 5.2(a) that the start marked point of graph of $E(\varepsilon_{aa} + \varepsilon_{bb})\sqrt{r/3}$ (obtained from FEA) indicates that beyond this point, correct representation of $(\varepsilon_{aa} + \varepsilon_{bb})$ requires more number of coefficients than A_0, A_2, B_1 (Eq. (3.67)). Similar arguments could be put forward for $E(\varepsilon_{aa} - \varepsilon_{bb})\sqrt{r}$ as shown in Fig. 5.2(b) using Eq. (3.68). Conversely, these start marked points (Fig. 5.2) also indicate that these are the maximum radial distances from the crack-tip upto which the best-fit can be obtained by satisfying all the three requirements as mentioned in Section 3.6. Using these values of best-fit coefficients A_0, A_2, B_1, C_0, C_1 and C_2 , the strains ε_{aa} and ε_{bb} can be calculated at any point along the positive gage line and negative gage line

by employing Eq. (3.65) and Eq. (3.66) respectively. At the same time ε_{aa} and ε_{bb} can also be obtained directly from the present FE solution at any point along the positive and negative gage lines respectively.



(a)



(b)

Figure 5.2 SECP with $a/b = 0.5$: (a) determination of A_0, A_2 and B_1 using the best-fit linear regression (b) determination of C_0, C_1 and C_2 using the best-fit linear regression

Fig. 5.3(a) shows comparison of values of $E\varepsilon_{aa}$ obtained from FEA with the value of $E\varepsilon_{aa}$ obtained by substitution of best-fit coefficients A_0, A_2, B_1, C_0, C_1 and C_2 , in RHS of Eq. (3.65) at all corner nodes lying on the entire positive gage line.

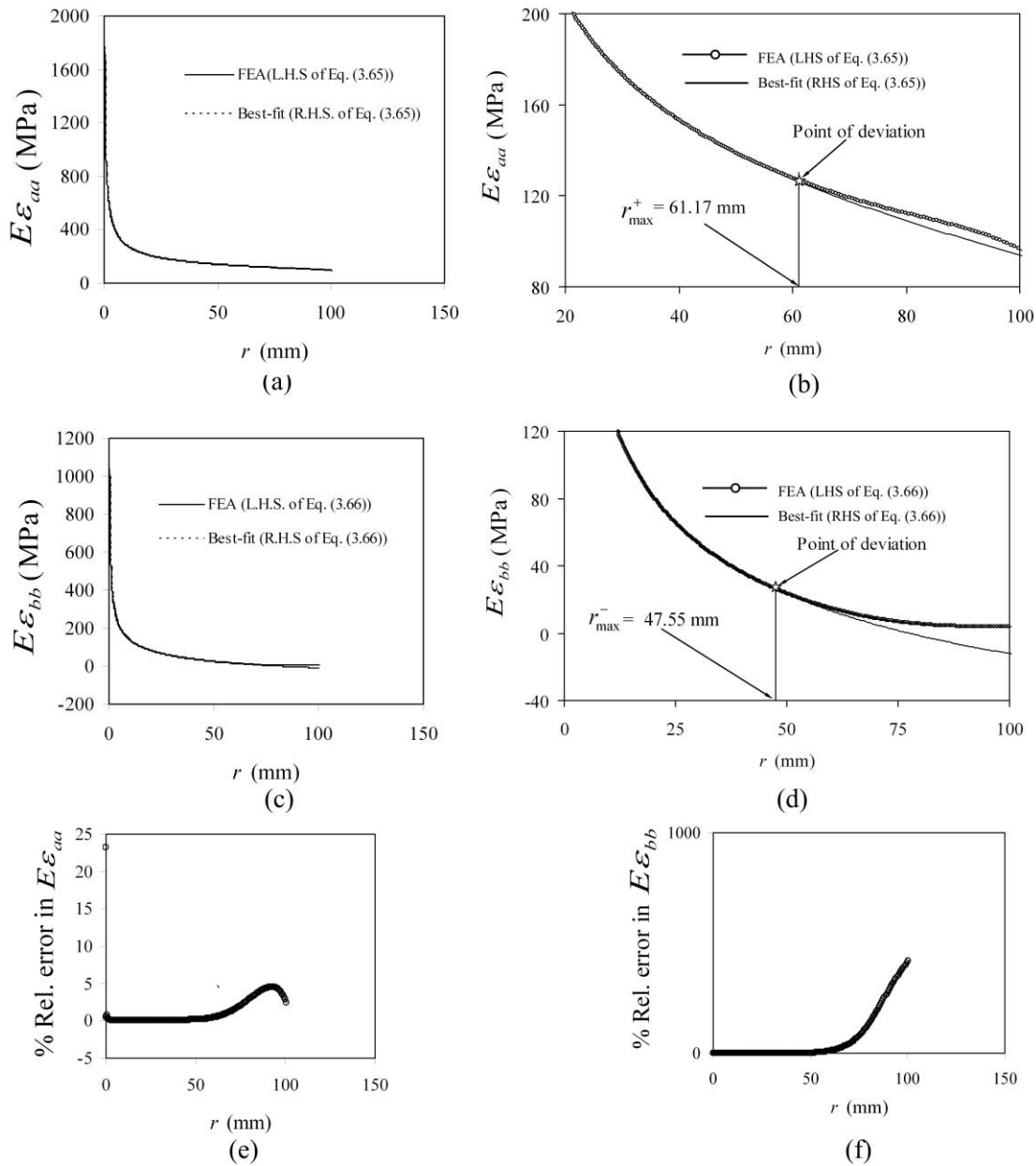


Figure 5.3 SECP with $a/b = 0.5$: (a) Plot of $E\varepsilon_{aa}$ versus r on the positive gage line (b) determination of r_{\max}^+ for the positive gage line (c) Plot of $E\varepsilon_{bb}$ versus r on the negative gage line (d) determination of r_{\max}^- for the negative gage line (e) % relative error in FE solutions of $E\varepsilon_{aa}$ and (f) % relative error in FE solutions of $E\varepsilon_{bb}$

Similarly Fig. 5.3(c) shows comparison of values of $E\varepsilon_{bb}$ obtained directly from FEA with those obtained using Eq. (3.66) on the negative gage line. As explained in Section 3.6, the RHS of Eqs. (3.65) and (3.66) cannot represent the strain field

accurately for the entire gage length of the positive and negative gage lines respectively as they contain only a few coefficients. As a consequence, they deviate from their corresponding FE solutions of the LHS of Eqs. (3.65) and (3.66) after certain radial distance. However, it is difficult to see clearly their points of deviation in both the plots of Figs. 5.3(a) and 5.3(c). To clearly visualize the points of deviation, only a part of the graph in Figs. 5.3(a) and 5.3(c) nearer to the point of deviation has been presented in Figs. 5.3(b) and 5.3(d) for the quantities $E\varepsilon_{aa}$ and $E\varepsilon_{bb}$ respectively. It can be noticed from Figs. 5.3(a) and 5.3(b) that the graph of $E\varepsilon_{aa}$ obtained by substitution of best-fit coefficients in Eq. (3.65) is congruent to the graph of $E\varepsilon_{aa}$ obtained using FEA up to the point of deviation. Similar observations can also be made in Figs. 5.3(c) and 5.3(d) corresponding to $E\varepsilon_{bb}$ on the negative gage line.

Identical trends similar to that in Figs. 5.3(a) and 5.3(c) has been obtained in all the examples of the present chapter. As consequence, similar problem of identification of point of deviation has also been observed in all examples of the present chapter. Therefore, scaled graphs similar to those shown in Figs. 5.3(b) and 5.3(d) which will clearly show the point of deviation in plots of $E\varepsilon_{aa}$ and $E\varepsilon_{bb}$ (i.e., r_{\max}^+ and r_{\max}^-) respectively, will be presented henceforth in the subsequent sections instead of full scale graphs such as shown in Figs. 5.3(a) and 5.3(c).

The radii corresponding to the points of deviation (star marked point) in Fig. 5.3(b) (i.e. $r_{\max}^+ = 61.17 \text{ mm}$) and that in Fig. 5.3(d) (i.e. $r_{\max}^- = 47.55 \text{ mm}$) clearly represent the extent of validity of five parameter strain field representation or the extent of zone II for the quantities ε_{aa} and ε_{bb} on the positive and negative gage lines respectively. Thus, as expected, these extents (i.e. r_{\max}^+ and r_{\max}^-) are different for the positive and negative gage lines.

As stated in section 3.6, the point of deviation in Fig. 5.3(b) i.e. r_{\max}^+ is the radial distance at which the percent relative error (between the values of $E\varepsilon_{aa}$ obtained using FEA and that using Eq. (3.65)) is less than or equal to 0.5% if one

moves from the right to the left in Fig. 5.3(a). In other words, it is the maximum radial distance from the crack tip within which the percentage relative error is $\leq 0.5\%$. Fig. 5.3(e) shows the percentage relative error of $E\varepsilon_{aa}$ (considering LHS of Eq. (3.65) as exact) at all the nodes lying on the entire positive gage line. As stated above, one can notice from Fig. 5.3(e) that % relative error decreases as one moves from right to left in Fig. 5.3(a) or Fig. 5.3(b). In a similar manner the point of deviation r_{\max}^- is obtained for the negative gage line as shown in Fig. 5.3(d) using the percent relative error calculated at all the nodes lying on the negative gage line. Fig. 5.3(f) shows the percent relative error in FE solutions of $E\varepsilon_{bb}$ (considering LHS of Eq. (3.66) as exact) at all the nodes lying on the entire negative gage line.

As the r_{\max}^+ and r_{\max}^- for positive and negative gage lines are different, therefore the radial distance corresponding to the points of deviation in Fig. 5.2(a) and Fig. 5.2(b) are expected to lie between the r_{\max}^+ and r_{\max}^- . Similar trend has been noticed in all the examples of the present investigation. Evidently, the minimum of r_{\max}^+ and r_{\max}^- (i.e. 47.55mm) is the r_{\max} which is the maximum permissible radial distance for placing the strain gages on both the positive and negative gage line as all the four Eqs. (3.65)-(3.68) are valid (for $\nu = 1/3$) within this r_{\max} value. Thus, the r_{\max} value of the selected configuration in this example i.e. $a/b = 0.5$ and $h/b = 1$ (Fig. 5.1(a)) is 47.55 mm.

In cases of Poisson's ratios other than 1/3, Eqs. (3.53)-(3.63) should be employed for the similar analysis. It can be observed that the quality of best-fits obtained in Fig. 5.2 and excellent congruence of plots in Fig. 5.3(a) or 5.3(b) and Fig. 5.3(c) or 5.3(d) up to the points of deviation are as per the theoretical basis presented in sections 3.5 and 3.6.

The results of this section are presented with the help of a highly refined FE mesh as shown in Fig. 5.4(c) (Number of elements=46720 and nodes=140945), which has been arrived at by conducting a convergence study for r_{\max} considering three levels of mesh refinement (coarse mesh with 636 elements, medium mesh with 5711

elements and fine mesh with 46720 elements) as shown in Fig. 5.4 similar to that for mode I loading.

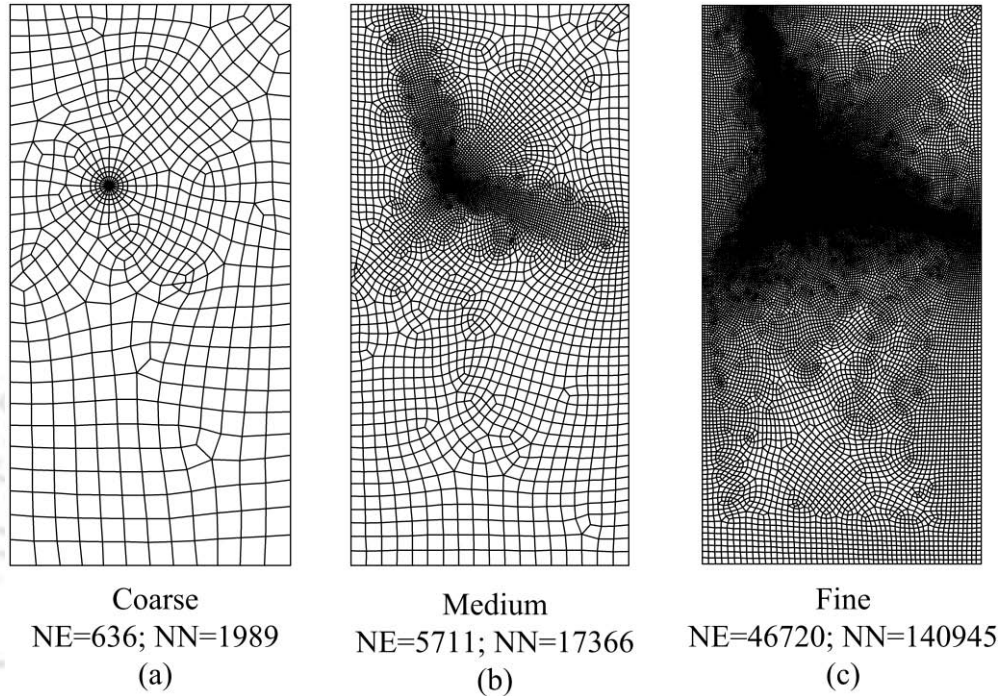
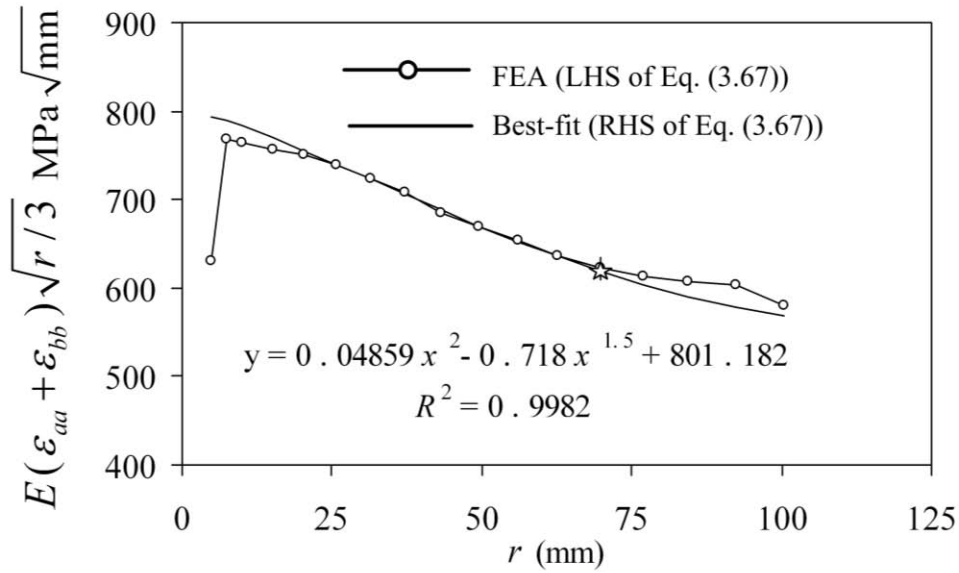
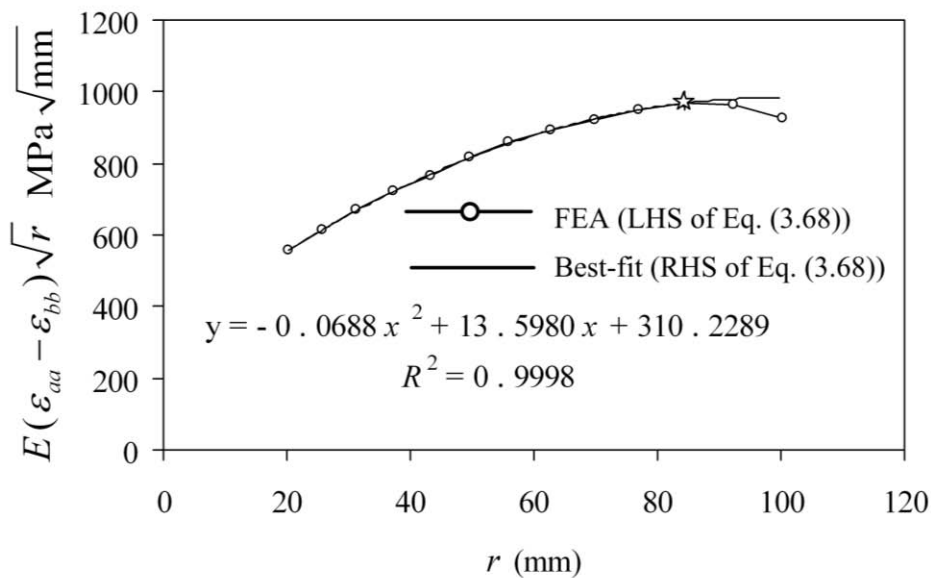


Figure 5.4 Different finite element meshes used for the convergence study of r_{\max} of SECP specimen with $a/b = 0.5$

Fig. 5.5(a) and Fig. 5.5(b) show the plots of finite element values of $E(\varepsilon_{aa} + \varepsilon_{bb})\sqrt{r/3}$ and $E(\varepsilon_{aa} - \varepsilon_{bb})\sqrt{r}$ versus radial distance r for coarse mesh. Fig. 5.6(a) and 5.6(b) show comparison of values of $E\varepsilon_{aa}$ and $E\varepsilon_{bb}$ obtained directly from FEA with those obtained using LHS of Eq. (3.65) and Eq. (3.66) on the positive and negative gage line respectively. Similarly, Fig. 5.7(a) and Fig. 5.7(b) show the plots of finite element values of $E(\varepsilon_{aa} + \varepsilon_{bb})\sqrt{r/3}$ and $E(\varepsilon_{aa} - \varepsilon_{bb})\sqrt{r}$ versus radial distance r for medium mesh. Fig. 5.8(a) and 5.8(b) show comparison of values of $E\varepsilon_{aa}$ and $E\varepsilon_{bb}$ obtained directly from FEA with those obtained using Eq. (3.65) and Eq. (3.66) on the positive and negative gage line respectively for medium mesh. The corresponding numerical values of r_{\max} are presented in Table 5.2. It can be observed from the Table 5.2 that as the meshes are refined r_{\max} values converge. No improvement is noticed when the meshes are further refined.

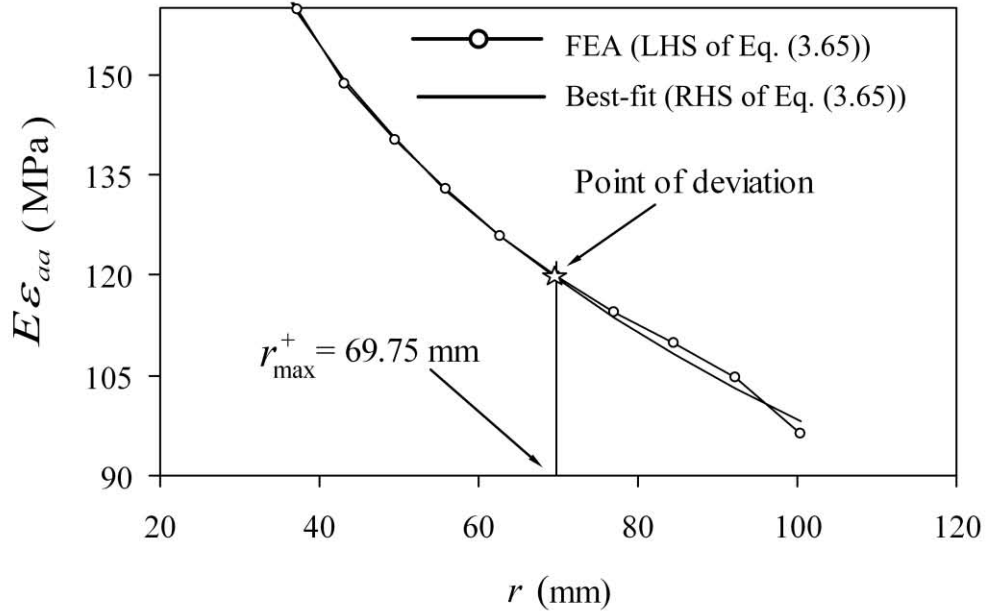


(a)

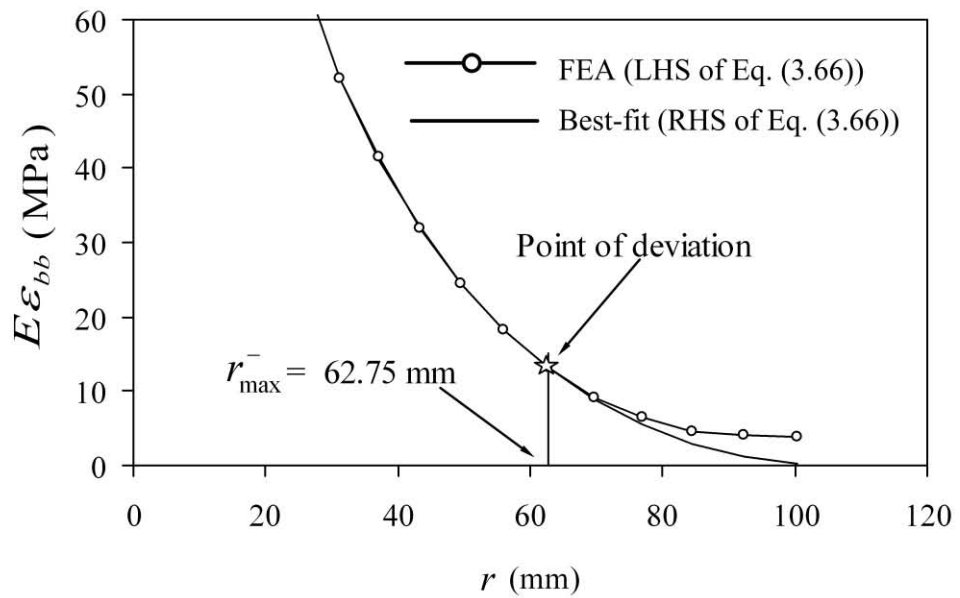


(b)

Figure 5.5 SECP with $a/b=0.5$ coarse mesh (a) determination of A_0, A_2 and B_1 using the best-fit linear regression (b) determination of C_0, C_1 and C_2 using the best-fit linear regression.



(a)



(b)

Figure 5.6 SECP with $a/b = 0.5$ coarse mesh (a) determination of r_{\max}^+ for the positive gage line (b) determination of r_{\max}^- for the negative gage line.

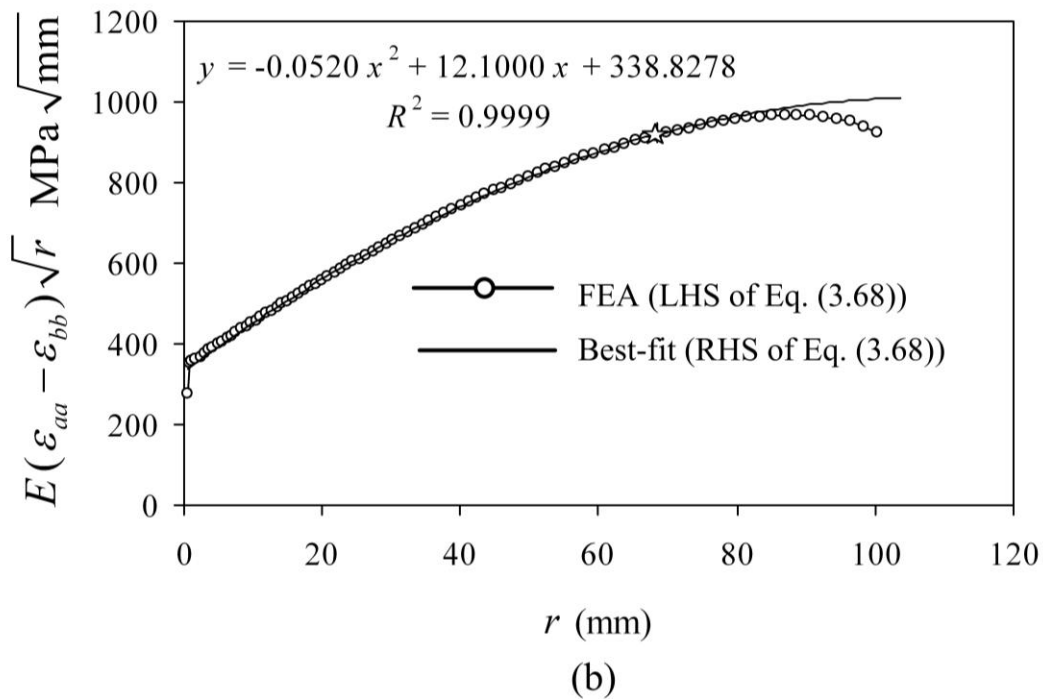
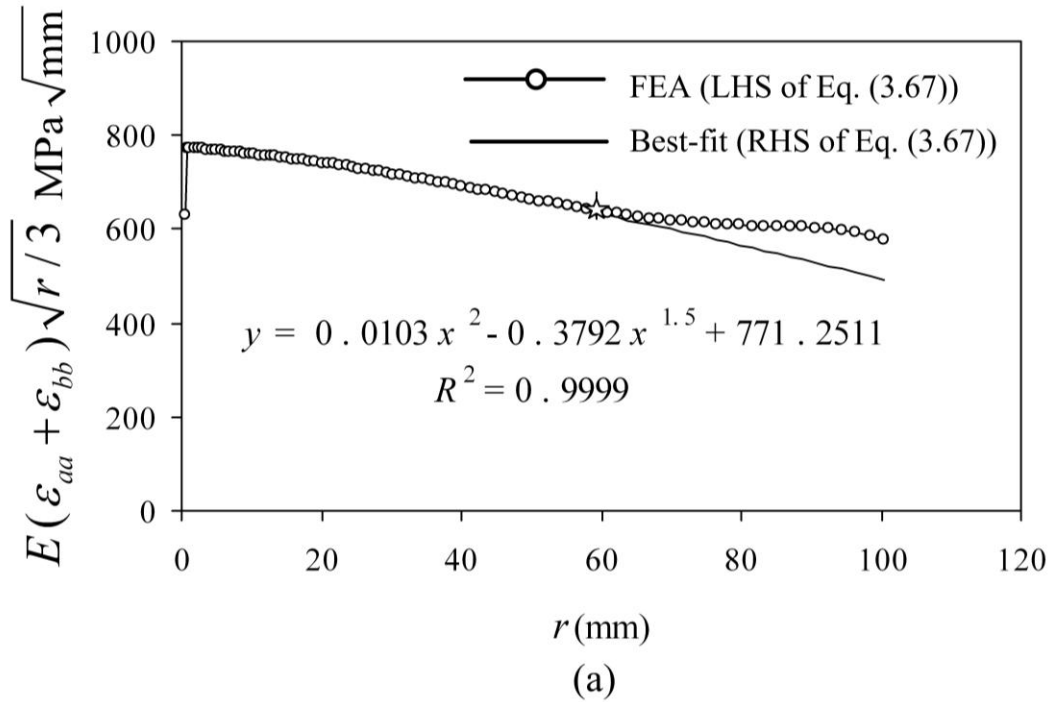


Figure 5.7 SECP with $a/b = 0.5$ medium mesh (a) determination of A_0, A_2 and B_1 using the best-fit linear regression (b) determination of C_0, C_1 and C_2 using the best-fit linear regression

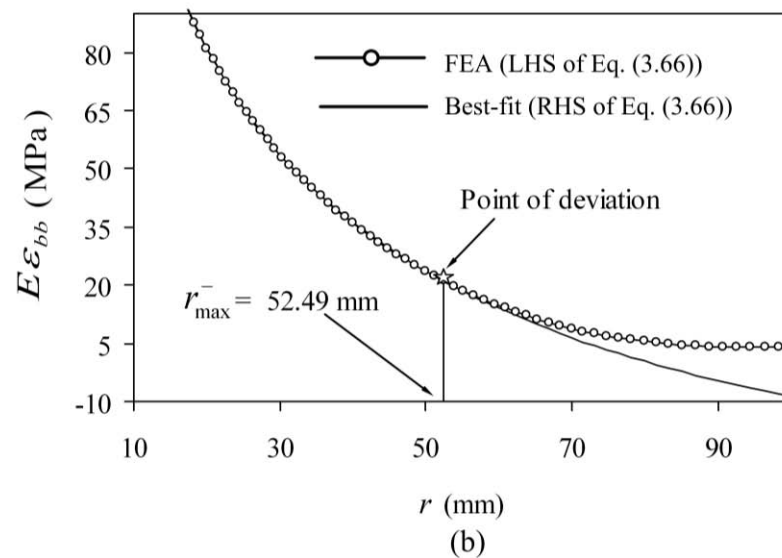
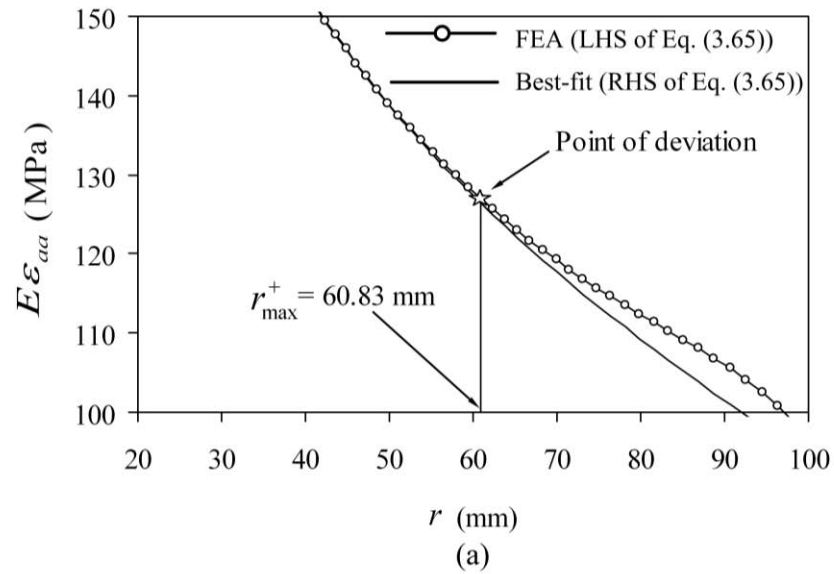


Figure 5.8 SECP with $a/b = 0.5$ medium mesh (a) determination of r_{\max}^+ for the positive gage line
(b) determination of r_{\max}^- for the negative gage line

Table 5.2 Convergence of the r_{\max} with the mesh refinement for SECP $a/b = 0.5$ under plane stress condition

Mesh	r_{\max} (mm)
Coarse	62.75
Medium	52.49
Fine	47.55

5.3 Validation of the present approach for determination of coefficients

It is evident that accuracy of r_{\max} depends on the accuracy of coefficients A_0, A_2, B_1, C_0, C_1 and C_2 obtained from the best-fit process. This section is intended to validate the coefficients obtained using the present approach with the coefficients obtained by Xiao and Karihaloo [57] using XFEM coupled with hybrid crack element (HCE). Here, a SECP configuration subjected to uniaxial tension as considered in the Xiao and Karihaloo's work [57] is studied for the purpose of validation. The geometrical parameters of SECP are [57]: $a/b=0.6$, $b=h=1$, Young's modulus $E=1$, Poisson's ratio $\nu=1/3$, orientation of crack with horizontal= 30° and the tensile stress $\sigma=1$ as shown in Fig. 5.9(a) and a state of plane stress is assumed.

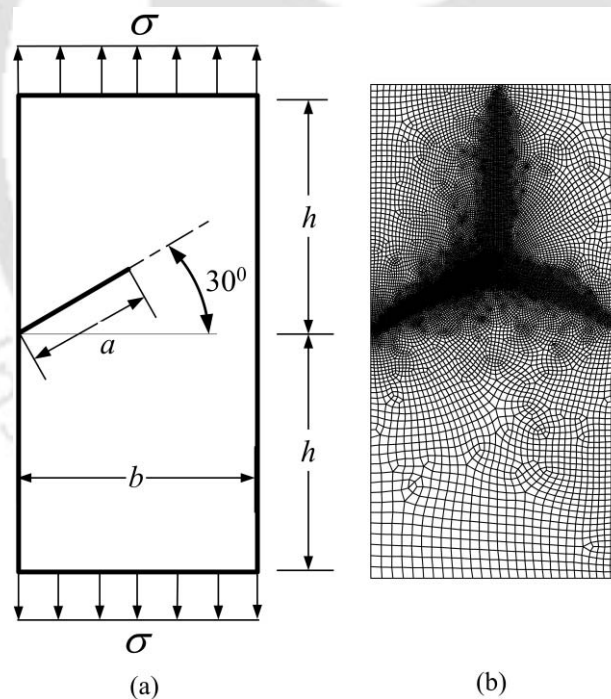


Figure 5.9 (a) Geometry of SECP subjected to uniform tension (b) mesh used for FEA

Figure 5.9 (b) shows mesh employed for FEA. The units are self-consistent. It should be noted that the coefficients A_0, A_2, B_1, C_0, C_1 and C_2 are independent of Young's modulus and Poisson's ratio. Since Poisson's ratio $\nu=1/3$, therefore Eqs. (3.65)-(3.68) have been again employed in this section. Following the best-fit procedure as

described in section 3.6 and as demonstrated in previous section, the values of coefficients A_0, A_2, B_1, C_0, C_1 and C_2 for the above SECP configuration have been determined. Fig. 5.10 shows best-fit of finite element solutions of $E(\varepsilon_{aa} + \varepsilon_{bb})\sqrt{r/3}$ and $E(\varepsilon_{aa} - \varepsilon_{bb})\sqrt{r}$ with RHS of Eqs. (3.67) and (3.68) respectively which are used for determination of above coefficients.

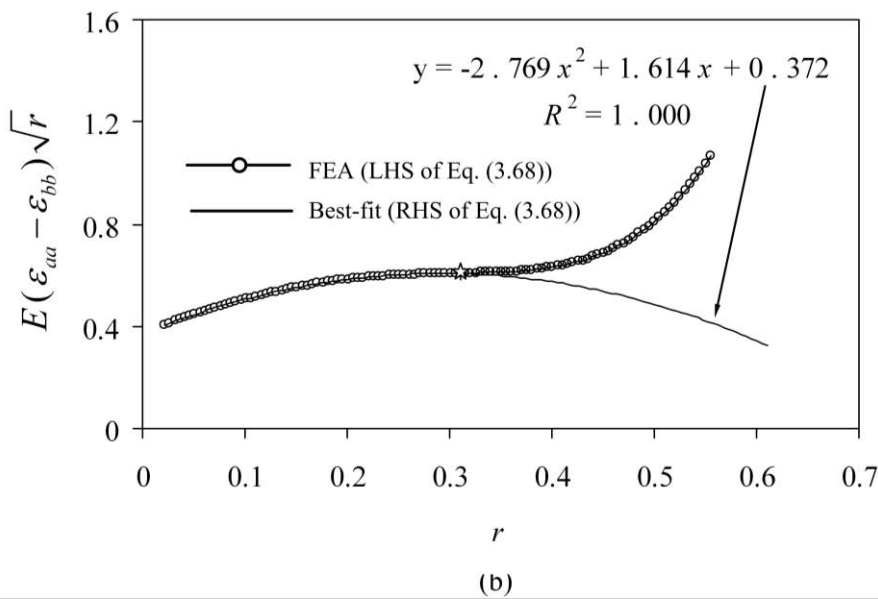
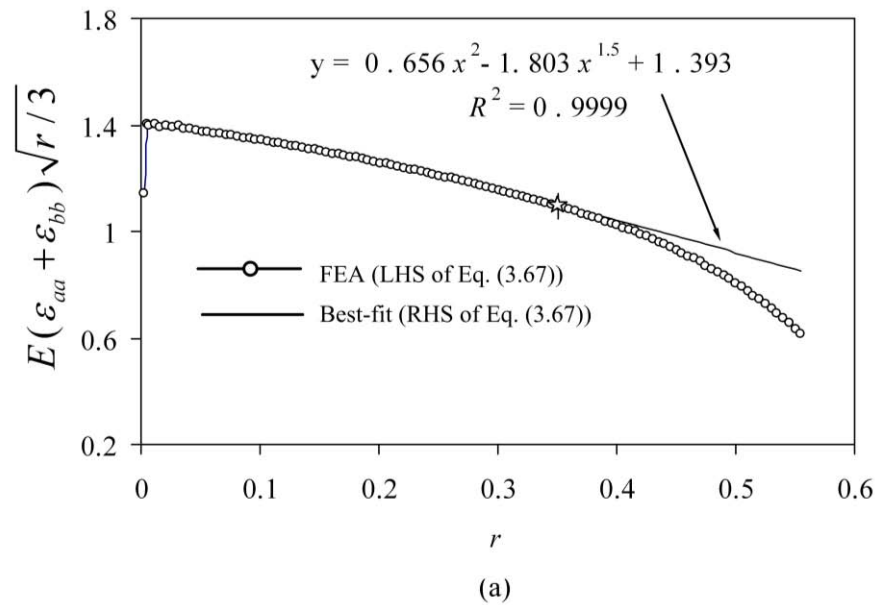


Figure 5.10 (a) determination of A_0, A_2 and B_1 using the best-fit linear regression (b) determination of C_0, C_1 and C_2 using the best-fit linear regression

Table 5.3 compares the results of the above coefficients obtained using the present approach and those reported by Xiao and Karihaloo [57]. Table 5.3 also shows values of coefficients A_0 and C_0 obtained using the displacement extrapolation technique in ANSYS [58]. It can be noticed from the results of Table 5.3 that there is an excellent agreement in values of coefficients A_0 and C_0 between all the methods. However, a significant difference can be noticed in values of the coefficients A_2, B_1, C_1 and C_2 obtained using the present approach and those reported by Xiao and Karihaloo [57].

Table 5.3 Comparison of coefficients.

Coefficient	Present	Xiao and Karihaloo [57]	ANSYS [58]
A_0	1.3933	1.3881	1.3956
A_2	-0.6558	-2.6740	-----
B_1	0.7806	1.0460	-----
C_0	0.3715	0.3775	0.3775
C_1	0.8071	0.6406	-----
C_2	0.9231	-1.0446	-----

Fig. 5.11(a) shows comparison of $E\varepsilon_{aa}$ values obtained using FEA, RHS of Eq. (3.65) with the coefficients reported by Xiao and Karihaloo [57] and RHS of Eq. (3.65) by substituting the coefficients obtained from the present approach along the entire positive gage line. Similarly Fig. 5.11(b) shows comparison of $E\varepsilon_{bb}$ values along the entire negative gage line. Due to significant variation in coefficients a large difference in trends of the strains obtained from both the approaches with that of FE solution can be noticed from Fig. 5.11. Considering strains obtained from FEA as exact strains, Fig. 5.12(a) and Fig. 5.12(b) show percentage relative error in the predicted values of $E\varepsilon_{aa}$ and $E\varepsilon_{bb}$ by using the coefficients from the present approach and those reported by Xiao and Karihaloo [57].

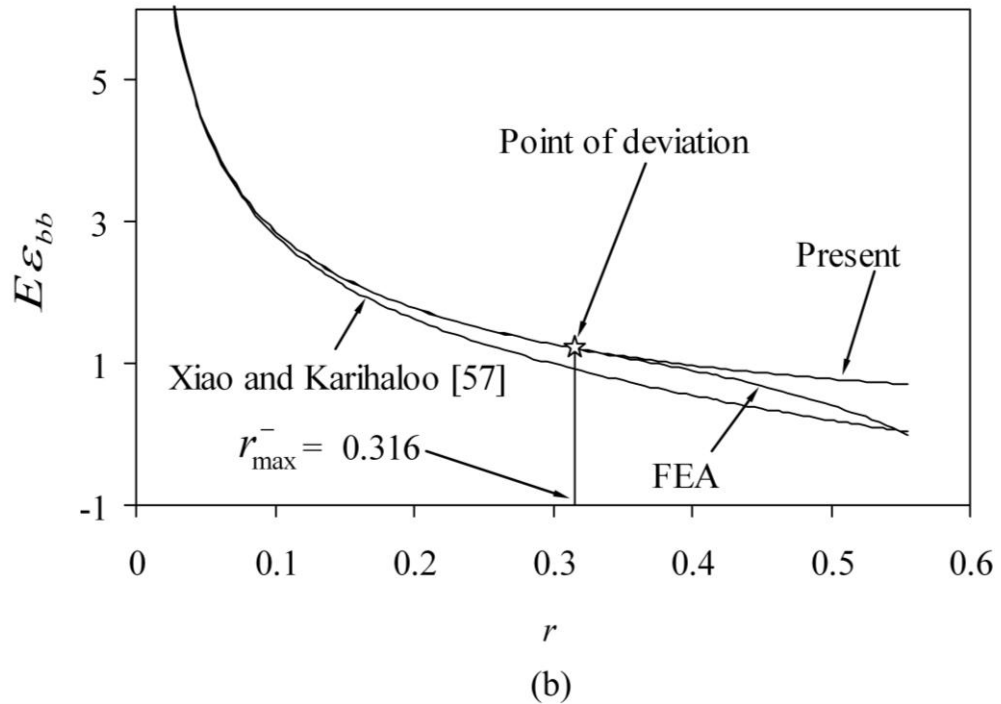
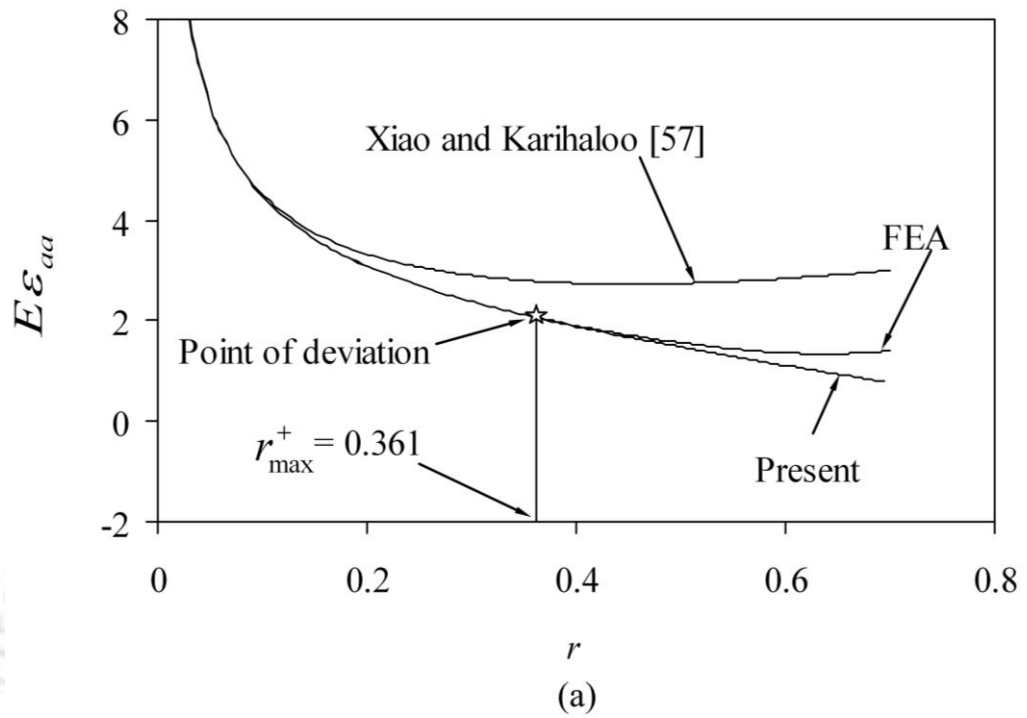


Figure 5.11 Validation of the present approach for determination of coefficients: (a) comparison of ε_{aa} along the positive gage line (b) comparison of ε_{bb} along the negative gage line

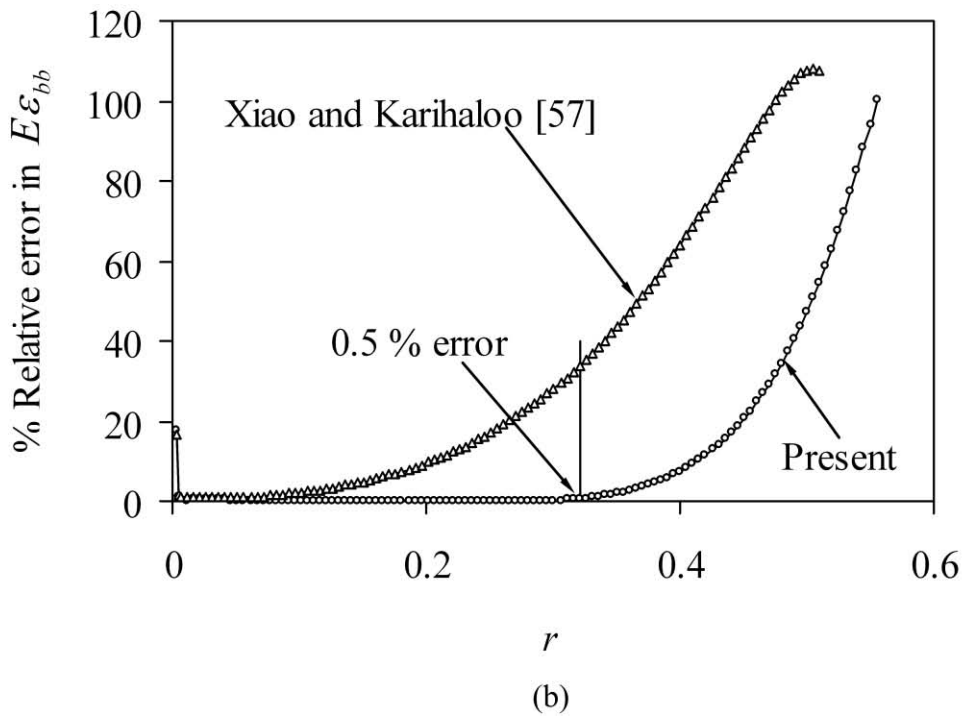
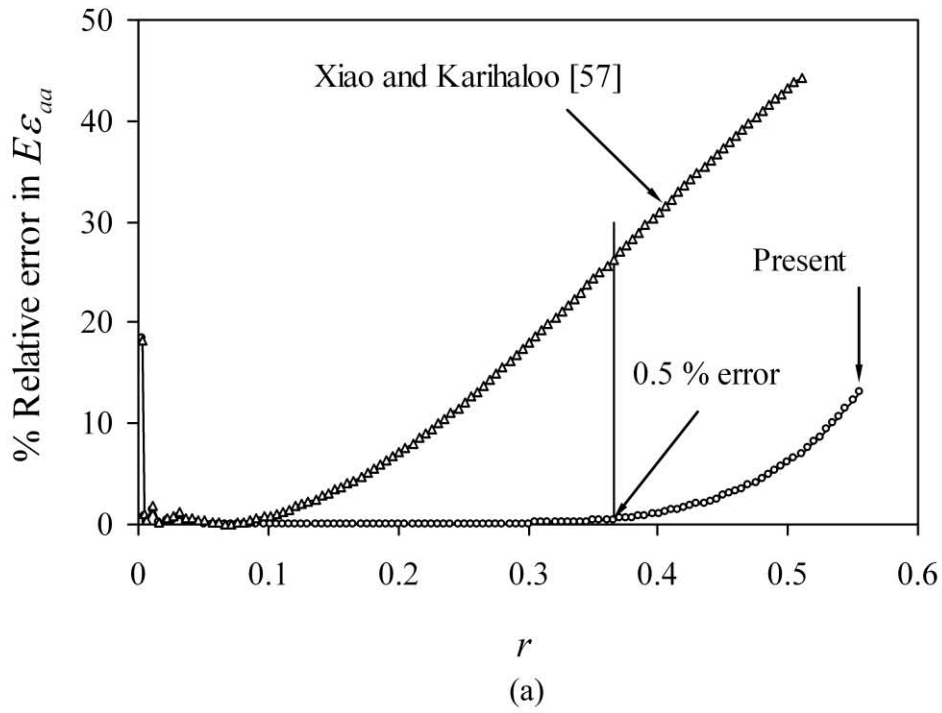


Figure 5.12 Comparison of errors due to the coefficients: (a) percentage relative error in ε_{aa} along the positive gage line (b) percentage relative error in ε_{bb} along the negative gage line

It is interesting to observe from Fig. 5.11 and Fig. 5.12 that the coefficients from the present approach could predict the FE values of strains within an error of 0.5% up to a larger radial distance from the crack tip as compared that predicted by the coefficients in [57]. A large error in predicted values by the coefficients of Xiao and Karihaloo [57] may be noticed (Fig. 5.12) even at small radial distances from the crack tip. Results presented in Fig. 5.11 and Fig. 5.12 clearly demonstrate that the present approach estimates more accurate values of unknown coefficients A_0, A_2, B_1, C_0, C_1 and C_2 and hence the r_{\max} value for a given 2D mixed mode configuration.

5.4 Numerical validation of modified DB technique

This example demonstrates the numerical simulation of the proposed modified DB technique for determination of mixed mode SIFs K_I and K_{II} for the SECP configuration that is considered in Section 5.1. Finite element values of ε_{aa} and ε_{bb} are computed at three arbitrarily selected strain gage locations on the positive and negative gage lines respectively. These three locations are selected within the r_{\max} (=47.55 mm) of the SECP configuration obtained using the present method (section 5.1). Fig. 5.13(a) and Fig. 5.13(b) show the LHS quantities of Eq. (3.67) and Eq. (3.68) at those three locations respectively. Curves of the form as appeared on the RHS of Eqs. (3.67) and (3.68) are then fitted to the above data at those simulated strain gage locations in Fig. 5.13(a) and Fig. 5.13(b) respectively.

As shown in Fig. 5.13, for the above hypothetical strain gage readings the best-fit values of A_0 and C_0 are 768.86 MPa $\sqrt{\text{mm}}$ and 343.40 MPa $\sqrt{\text{mm}}$ respectively. Using ANSYS's built-in displacement extrapolation technique [58] the values of coefficients A_0 and C_0 are found to be equal to 768.56 MPa $\sqrt{\text{mm}}$ and 346.63 MPa $\sqrt{\text{mm}}$ respectively, which are very close to the above simulated values. This numerical test assures that accurate values of K_I and K_{II} can be obtained using

the present modified DB technique with the proposed method of placing the strain gages within the computed r_{max} value for a given configuration.

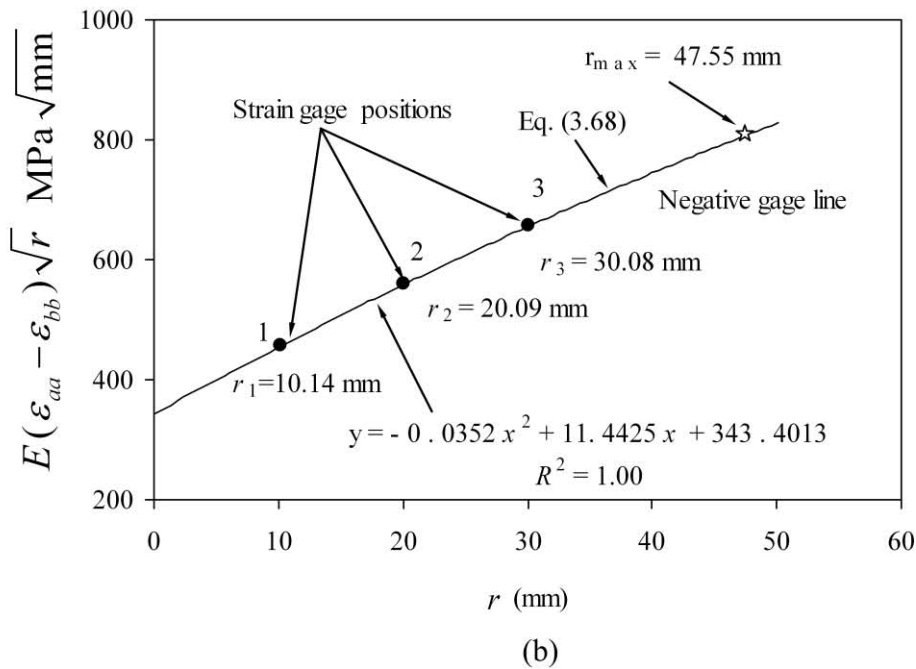
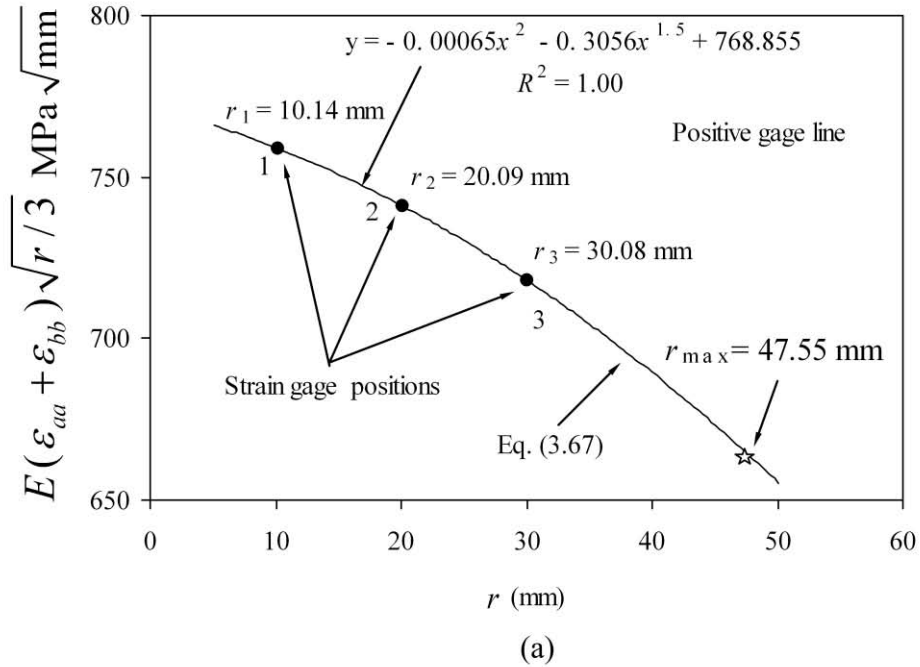


Figure 5.13 Simulation of the proposed modified Dally and Berger's method for SECP with $a/b = 0.5$: (a) best-fit to the simulated data along the positive gage line (b) best-fit plot to the simulated data along the negative gage line

5.5 Influence of a/b ratio on the r_{\max}

This example is intended to study the effect of a/b ratio on the r_{\max} value of a mixed mode cracked configuration. For this purpose a SECP subjected to uniform tension with $a/b = 0.2$ to 0.8 in steps of 0.1 and $h/b = 1.0$ is considered. Other parameters of the cracked plate are shown in Table 5.1. Since the Poisson's ratio $\nu = 1/3$, Eqs. (3.65)-(3.68) are again employed in all the calculations for all values of a/b . Following the procedure described in section 3.6 and in the previous examples, the value of r_{\max} for all values of a/b is determined. For example, Fig. 5.14(a) and Fig. 5.14(b) show best-fit of curves on the RHS of Eq. (3.67) and Eq. (3.68) to the FE values of the LHS of Eqs. (3.67) and (3.68) for $a/b = 0.3$. Fig. 5.14(a) and Fig. 5.14(b) also show the values of coefficients A_0, A_2, B_1, C_0, C_1 and C_2 corresponding to the best-fit linear regression. Fig. 5.14(c) and Fig. 5.14(d) show comparison of the values of $E\varepsilon_{aa}$ and $E\varepsilon_{bb}$ obtained from FEA with that of $E\varepsilon_{aa}$ and $E\varepsilon_{bb}$ obtained using RHS of Eq. (3.65) and Eq. (3.66) respectively. Fig. 5.14(c) and Fig. 5.14(d) also show the extent of five parameter zone (i.e., r_{\max}^+ and r_{\max}^-) for $a/b = 0.3$ on the positive and negative gage lines respectively.

Similarly Figs. 5.15–5.19 show the result corresponding to $a/b = 0.2, 0.4, 0.6, 0.7$ and 0.8 respectively. It should be noted that the r_{\max} value corresponding to $a/b = 0.5$ has already been computed in section 5.2. Table 5.4 shows results for r_{\max} (minimum of r_{\max}^+ and r_{\max}^-) values of SECP for different values of a/b corresponding to plane stress condition. Figure 5.20 shows the variation of r_{\max}/b with a/b which shows a bell shaped trend. Interestingly, it can be noticed that a very similar bell-shaped trend was also obtained for mode I problems and the detailed explanation (Chapter 4) given therein for such a trend is also applicable for the present example. It can be shown that the bell shaped trend is due to the variation of coefficients A_0, A_2, B_1, C_0, C_1 and C_2 with change in a/b values.

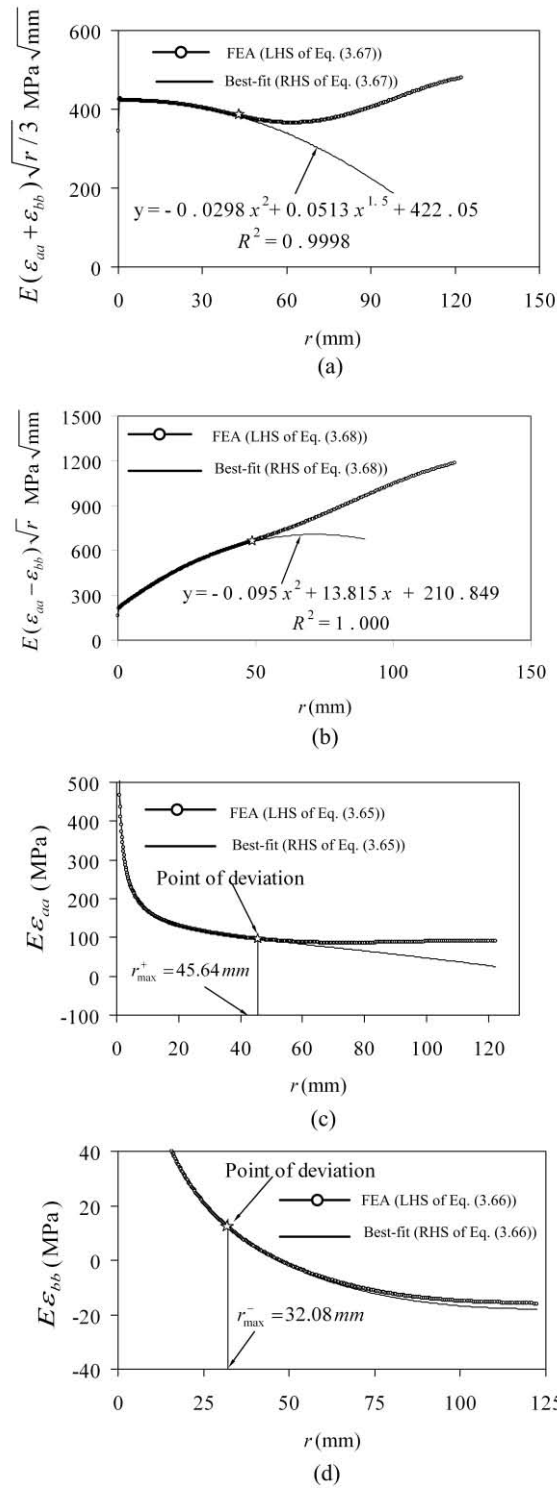


Figure 5.14 Results for determination of the r_{\max} for SECP with $a/b = 0.3$: (a) determination of A_0, A_2 and B_1 (b) determination of C_0, C_1 and C_2 (c) determination of r_{\max}^+ for the positive gage line (d) determination of r_{\max}^- for the negative gage line

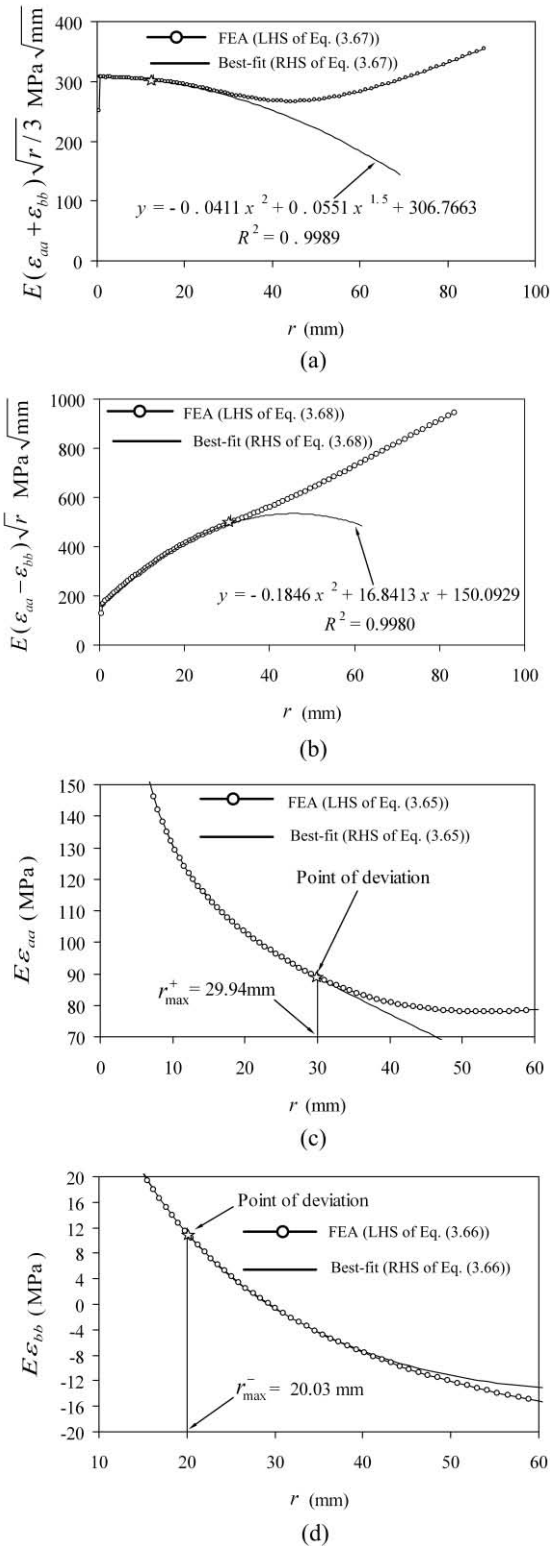


Figure 5.15 SECP with $a/b = 0.2$ (a) determination of A_0, A_2 and B_1 (b) determination of C_0, C_1 and C_2 (c) determination of r_{\max}^+ for the positive gage line (d) determination of r_{\max}^- for the negative gage line

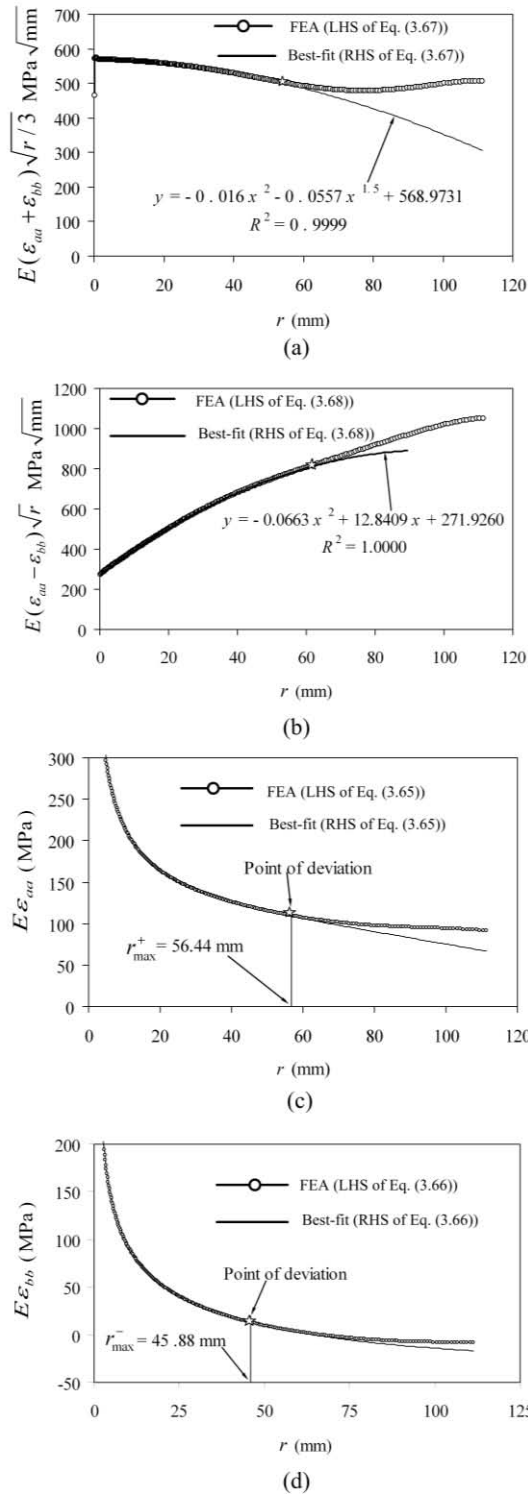


Figure 5.16 SECP with $a/b = 0.4$ (a) determination of A_0, A_2 and B_1 (b) determination of C_0, C_1 and C_2 (c) determination of r_{\max}^+ for the positive gage line (d) determination of r_{\max}^- for the negative gage line

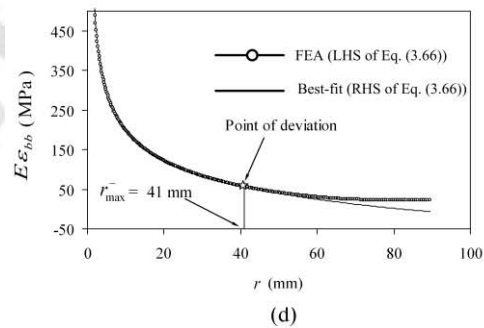
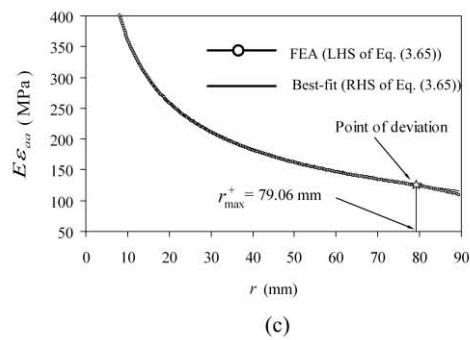
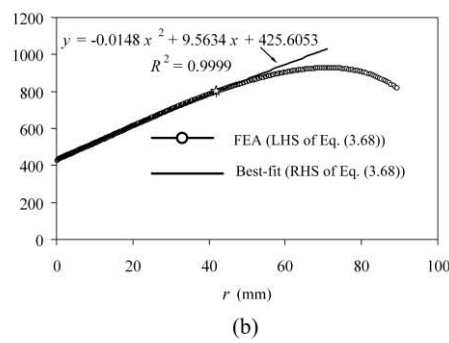
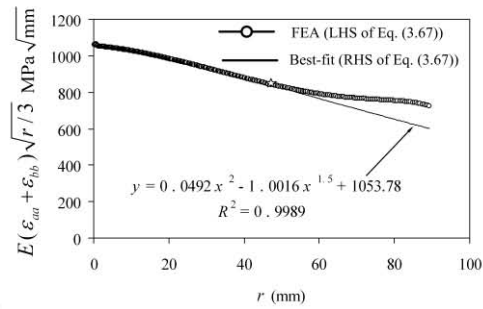
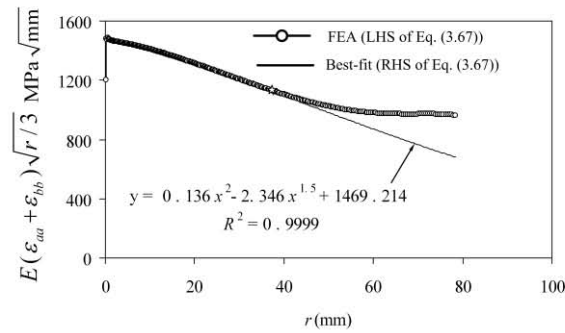
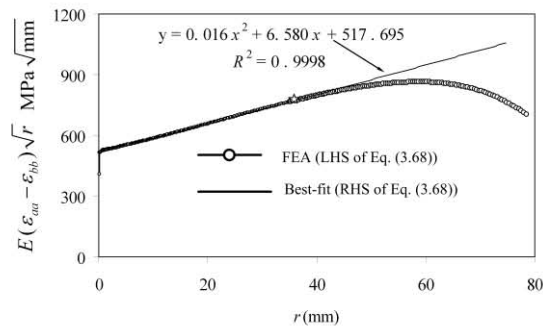


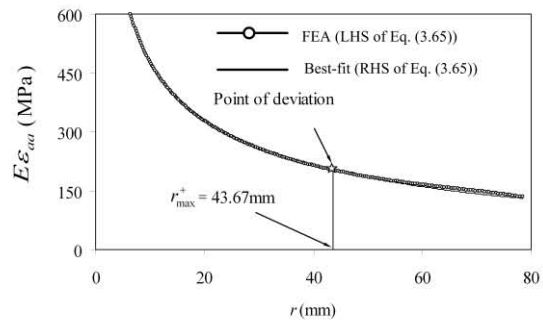
Figure 5.17 SECP with $a/b = 0.6$ (a) determination of A_0, A_2 and B_1 (b) determination of C_0, C_1 and C_2 (c) determination of r_{\max}^+ for the positive gage line (d) determination of r_{\max}^- for the negative gage line



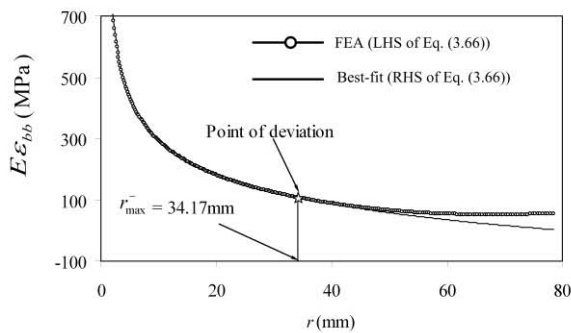
(a)



(b)

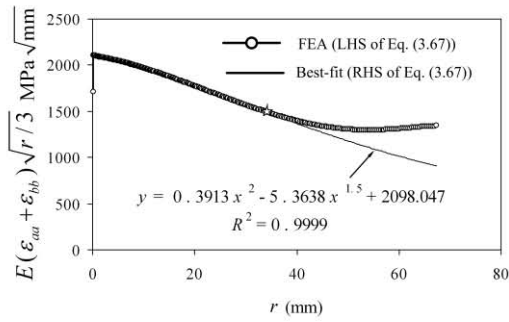


(c)

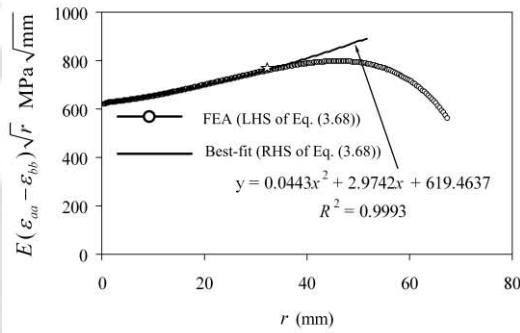


(d)

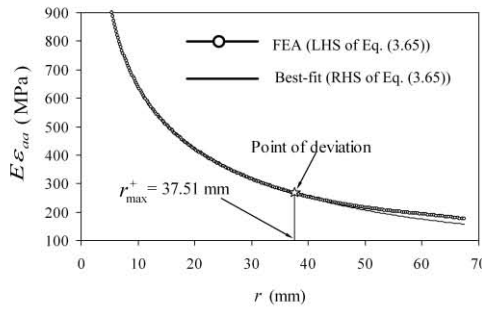
Figure 5.18 Results for determination of the r_{\max} for SECP with $a/b = 0.7$: (a) determination of A_0, A_2 and B_1 (b) determination of C_0, C_1 and C_2 (c) determination of r_{\max}^+ for the positive gage line (d) determination of r_{\max}^- for the negative gage line



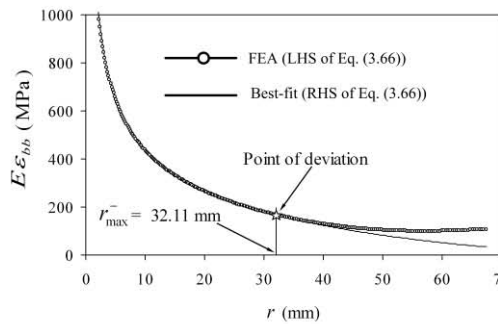
(a)



(b)



(c)

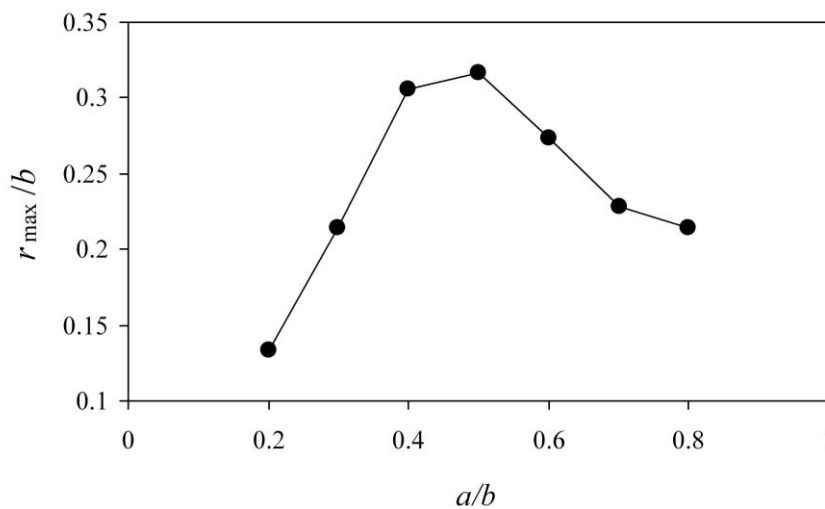


(d)

Figure 5.19 SECP with $a/b = 0.8$ (a) determination of A_0, A_2 and B_1 (b) determination of C_0, C_1 and C_2 (c) determination of r_{\max}^+ for the positive gage line (d) determination of r_{\max}^- for the negative gage line

Table 5.4 Variation of the r_{\max} with a/b of SECP under plane stress condition.

a/b	r_{\max} (mm)	r_{\max} / a
0.2	20.03	0.668
0.3	32.08	0.713
0.4	45.88	0.765
0.5	47.55	0.634
0.6	41.00	0.456
0.7	34.17	0.325
0.8	32.11	0.268

**Figure 5.20 Plot of the r_{\max} / b as a function of a/b for plane stress condition.**

5.6 Effect of state of stress on r_{\max}

In order to understand the effect of state of stress on the r_{\max} , the SECP as shown in Fig. 5.1(a) is analyzed for both the plane stress and plane strain conditions for the same Poisson's ratio $\nu = 1/3$. Different configurations of SECP with $a/b = 0.2$ to 0.8 in steps of 0.1 and $h/b = 1.0$ are considered in this study. Other parameters of these configurations are shown in Table 5.1.

Figure 5.21 shows the variation of the r_{\max} (minimum of r_{\max}^+ and r_{\max}^-) as a function of a/b corresponding to both the plane stress and plane strain conditions.

The solution corresponding to the plane stress conditions of the previous example in section 5.5 are considered in this example for the purpose of comparison with the result for plane strain conditions. It should be noted that though the Poisson's ratio $\nu = 1/3$ is same for the plane stress and plane strain conditions, the angle α and θ (as given by Eq. (3.51) and Eq. (3.52)) will be different for these two states. As a consequence, different r_{\max} values can be seen in Fig. 5.21. It can be noticed from Fig. 5.21 that for smaller values of a/b the r_{\max} in plane strain conditions is larger than that in plane stress conditions. Less difference between the r_{\max} values can be noticed at larger values of a/b . Similar trend has also been observed in mode I problems in section 4.7.

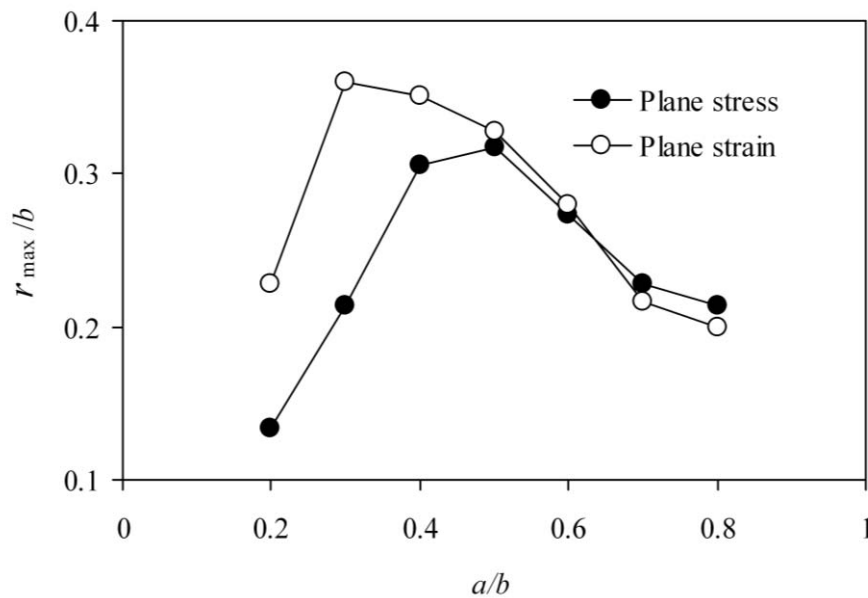


Figure 5.21 Comparison of the r_{\max}/b between plane stress and plane strain conditions as a function of a/b

As in case of mode I problems, the observed difference between the plane stress and plane strain values of the r_{\max} can be explained as follows. It is known that the magnitude of the coefficients A_0, A_2, B_1, C_0, C_1 and C_2 in the expressions for ε_{aa} (Eq.(3.65)) and ε_{bb} (Eq.(3.66)) remain same for both plane stress and plane strain conditions as they are functions of the geometry and boundary conditions of the cracked body only. Thus, the strains ε_{aa} and ε_{bb} along the positive and negative gage

line, respectively, will be different for plane stress and plane strain conditions mainly due to the change in magnitude of the terms that are associated with the Poisson's ratio ν in the Eq. (3.65) and Eq. (3.66). Further, as expected, a bell shaped trend of r_{\max} with increase of a/b is also exhibited in plane strain conditions. As stated in the previous example, a reason for bell shaped trend is due to the variation of the coefficients A_0, A_2, B_1, C_0, C_1 and C_2 with a/b and which remains same for both the plane stress and plane strain conditions. Thus the difference in the r_{\max} values is mainly due to the terms associated with Poisson's ratio.

5.7 Summary

Based on the proposed methodology, the upper bound on strain gage locations i.e., r_{\max} (minimum of r_{\max}^+ and r_{\max}^-) has been determined for different mixed mode SECP specimens. Variation of strains at different radial locations shows the expected trend supported by the present theoretical formulations. It has been demonstrated that accurate values of unknown coefficients in strain series can be obtained with the help of the proposed approach. The r_{\max} values have been determined for different a/b and the dependence of r_{\max} on a/b is observed. It is observed that for mixed mode also as a/b increases the r_{\max} value increases up to a certain value of a/b and then with further increase in a/b the r_{\max} value decreases. Therefore, at large net ligament length i.e. small a/b , the crack length ' a ' is the controlling parameter for r_{\max} as the boundary effects are negligible similar to opening mode. But at small net ligament length i.e. at large a/b , boundary effect comes into the picture and the net ligament length $(b-a)$ is the controlling parameter for variation in r_{\max} . Loading condition (plane stress and plane strain) affects r_{\max} values especially at lower value of a/b .

Chapter 6

Experimental Verification

Present chapter describes experimental verification for determination of optimal radial locations of strain gages using the proposed procedures described in previous chapters for mode-I and mixed mode I/II loading conditions. Experiments have been conducted with mode I as well as mixed mode-I/II loading and SIFs have been determined based on strain gage readings. Strain gages have been placed within r_{\max} and outside r_{\max} in order to study the importance of radial strain gage location on accuracy of SIFs determined using strain gage technique. The experimental investigation in this chapter also demonstrates accurate determination mixed-mode SIFs K_I and K_{II} using the proposed modified DB technique with the optimum gage locations. The following equations are employed for determination of normalized SIFs K_I and K_{II}

$$F_{I \text{ or } II} = \frac{K_{I \text{ or } II}}{\sigma \sqrt{\pi a}} \quad (6.1)$$

and the % relative error in F_I and F_{II} is computed as

$$\% \text{ Rel. error} = \left(\frac{F_{I \text{ or } II}^{\text{reference solution}} - F_{I \text{ or } II}^{\text{experimental}}}{F_{I \text{ or } II}^{\text{reference solution}}} \right) \times 100 \quad (6.2)$$

6.1 Description of the test specimen

In the present experimental investigation commercially available polymethylmethacrylate (PMMA) has been used as the material for all the test specimens. It is well known that PMMA is a homogeneous, isotropic and brittle material at room temperature [59]. This material has long been used in studies of many aspects of LEFM [60, 61]. A major advantage of this material is that it is relatively easier to introduce sharp cracks with the help of razor blades, jewelry saws etc. PMMA is an inexpensive material and easy to fabricate complex cracked configurations making it an excellent model material in experimental fracture

mechanics [59]. Historical account of PMMA in experimental fracture mechanics is reported in [59]. Specimens have been made of PMMA for conducting experiments corresponding to mode-I as well as mixed mode (I/II) loading conditions. The test specimens considered in the present investigation for verification of the optimal strain gage locations obtained by the proposed numerical techniques (described in chapters 4 and 5) are straight edge cracked plates and slant edge cracked plates subjected to tensile loading as shown in Fig. 6.1. The test specimen shown in Fig. 6.1(a) is employed for mode-I loading experiments and that in Fig. 6.1(b) is employed for mixed mode (I/II) experiments. The details of geometry and that of pre-crack are also shown in Fig. 6.1.

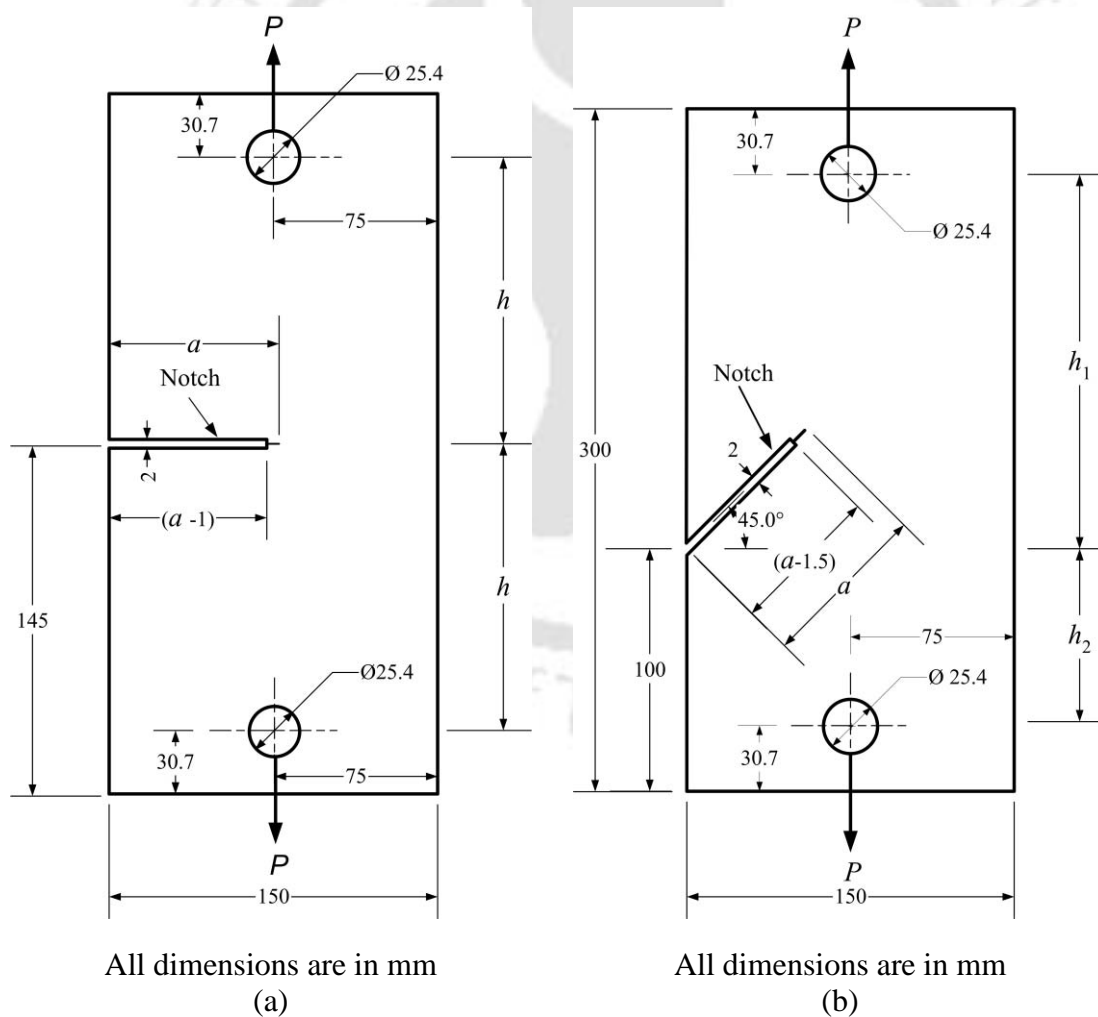


Figure 6.1 (a) A typical mode I specimen (b) mixed mode specimen

In all experiments of the present investigation, the width b of the test specimens is 150 mm and the thickness is 5.6 mm. The loading holes at the ends of the specimen are intended to load the specimen under tensile loading using clevis grips and pins. The location of these loading holes relative to the free ends are decided by the clearances available in the clevis grips.

To imitate sharp crack in the specimens, first a notch of width 2 mm has been introduced with the help of end milling cutter for a length of $(a-1)$ mm (Fig. 6.1(a)) for opening mode and a notch of length $(a-1.5)$ mm for mixed mode (Fig. 6.1(b)). Then a sharp crack of length 1 mm for opening mode and of length 1.5 mm for mixed mode has been introduced with the help of a jewelry saw of thickness 0.22 mm. In this way a very sharp pre-crack of root radius of 0.224 mm has been achieved. Fig. 6.2(a) shows the photograph of optical microscope setup and Fig. 6.2(b) shows the image obtained through optical microscope for the crack tip of a typical specimen. This procedure has been adopted for all test specimens for mode-I and mixed I/II mode experiments.

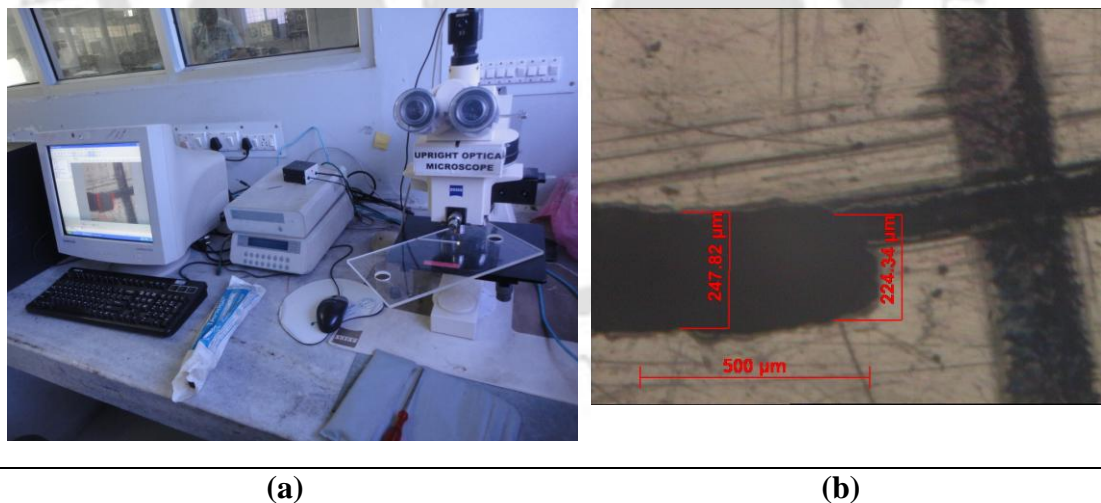


Figure 6.2 (a) Optical microscope setup (b) enlarged view at crack tip

In the present investigation it was intended to carry out tests for different values of a/b i.e., 0.3, 0.5 and 0.7. However, while creating the sharp crack using jewelry saw, it was experienced that the perfect alignment of the axis of the sharp crack with that of

the notch could not be maintained beyond 1.5 mm. Therefore, the sharp crack length was limited to 1 mm to 1.5 mm for all the specimens used in the present investigations. This resulted in the actual a/b ratios of the specimen as $a/b = 0.293$, $a/b = 0.493$, $a/b = 0.693$ i.e. $a = 44$ mm, $a = 74$ mm and $a = 104$ mm for mode I and $a/b = 0.497$ i.e., $a = 74.55$ mm for mixed mode experiments. These dimensions have been verified using the profile projector. Dimensions and loading conditions in all the test specimens have been chosen so as to ensure that plane stress conditions prevail during the experiments.

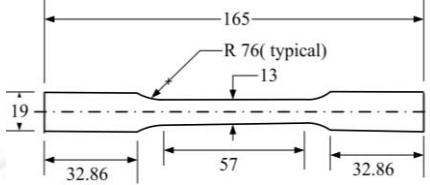
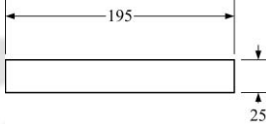
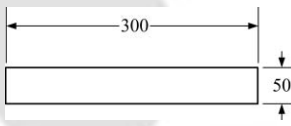
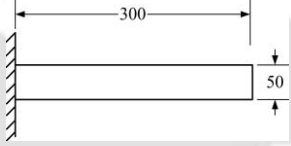
6.2 Experimental determination of material properties of PMMA

In order to experimentally verify the optimum strain gage locations for the selected PMMA specimens (Fig. 6.1), it is first required to determine the maximum permissible radial location (r_{\max}) of the strain gages using the proposed numerical approach. Referring to Eqs.3.26, 3.27, 3.51 and 3.52, it requires accurate values of Young's modulus, E and Poisson's ratio, ν to be input in the present finite element based approach to obtain accurate values of r_{\max} . Even in conducting the experiments for determination of SIFs using strain gages, accurate values of E and ν are required. Therefore, in the present investigation, utmost care has been taken to experimentally determine the values of E and ν for PMMA by different ways so as to ensure the accuracy of the measured values.

To arrive at accurate values of E and ν for the PMMA four different types of specimen as shown in Table 6.1, have been tested and a total of ten tests have been carried out. All these specimens have been fabricated from the same PMMA sheet which is used for preparing mode-I and mixed mode specimen for verification of optimum strain gage locations.

In all the cases of tensile tests (first-three cases), the specimen have been monotonically loaded in a closed loop servo hydraulic INSTRON 8801 machine (100KN capacity) under displacement control with a strain rate of 0.1mm/min.

Table 6.1 Details of test specimens for determination of E and ν of PMMA

Case	Test	Specimen type	Specimen geometry (All dimensions are in mm)	Number of specimens tested	Strain measurement
1	Tensile	ASTM D638		3	Extensometer
2	Tensile	Rectangular specimen		3	Strain gage
3	Tensile	Rectangular specimen		3	Strain gage
4	Bending	Rectangular specimen		1	Strain gage

In the first case, three specimens conforming to ASTM D638 have been loaded and the longitudinal as well as transverse strains have been measured using extensometers. Fig. 6.3 shows the photograph of the test setup for the first case.

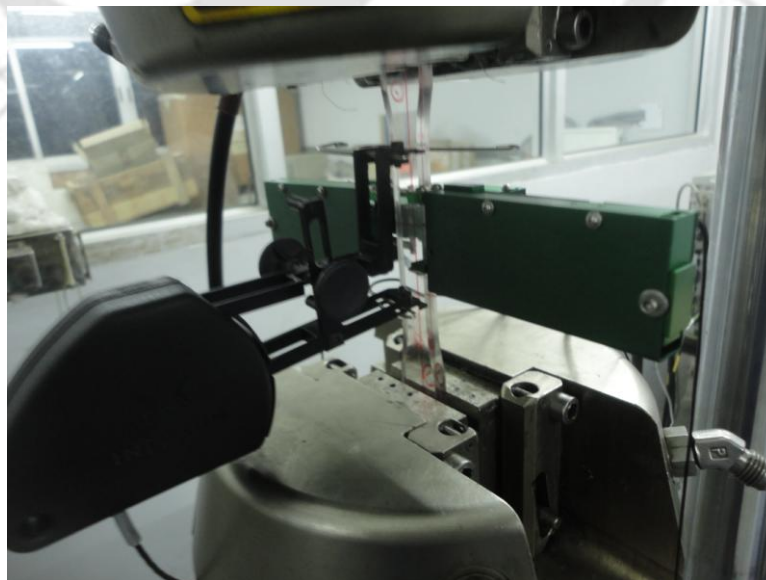
**Figure 6.3 ASTM D638 specimen with extensometer setup**



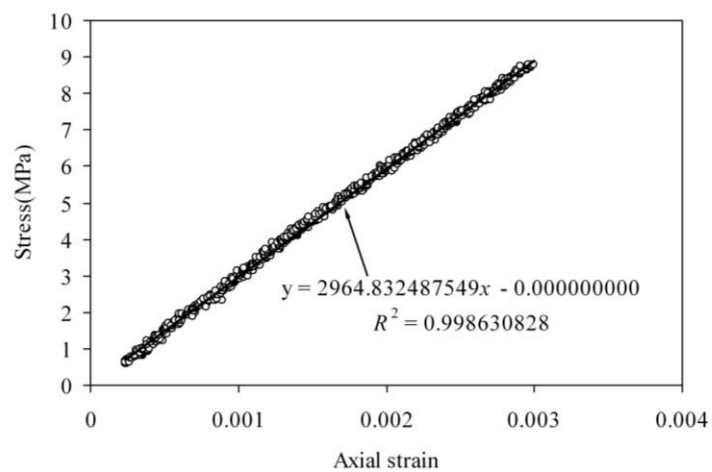
Figure 6.4 Rectangular specimens pasted with strain gages

In the third case (Table 6.1) similar specimens as in the second case but with larger dimensions have been used. The loading rate and strain gages are same as those in the second case. In the fourth case, one of the rectangular specimens of the third case is loaded as a cantilever beam as shown Fig. 6.5. A point load of 4.9 N was employed at the free end and strain gages on the specimen have been employed for measurement of strains in axial as well as in the transverse direction on the top face of the beam. Load has been applied using dead weights.

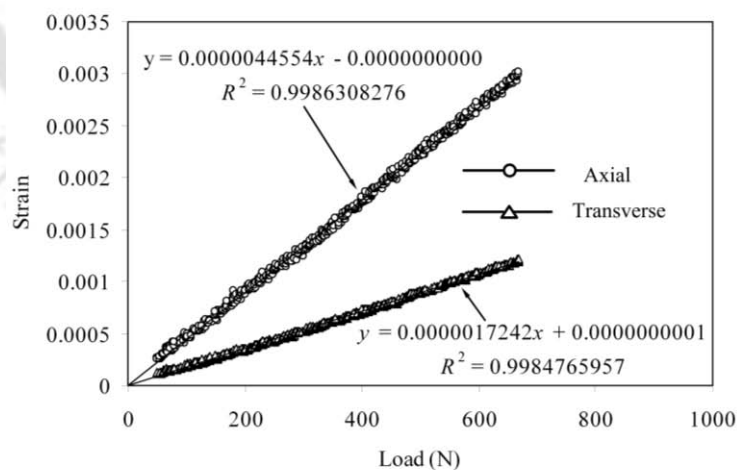


Figure 6.5 Cantilever beam testing setup

In all these cases (cases 2, 3 and 4), the measured strains have been stored, digitized and processed with the help of cDAQ-9178 data acquisition system of National Instruments (NI) along with LabVIEW™ 2009 software. Fig. 6.6 shows the raw data obtained from the tensile tests and the best-fitted lines to these raw data corresponding to a typical specimen of the first case in Table 6.1. Fig. 6.6 (a) shows the engineering stress-strain diagram for determination of Young's modulus. The slope of the best-fit line in Fig. 6.6(a) is the Young's modulus.



(a)



(b)

Figure 6.6 Tensile testing data of case 1 specimen (ASTM D638 specimen)

Fig. 6.6 (b) shows the load versus axial strain as well as load versus transverse strain for the measurement of Poisson's ratio. According to ASTM E132-04, Poisson's ratio

is defined as ratio of slope of line of transverse strain to the slope of line of axial strain in Fig. 6.6(b).

Fig. 6.7 shows the raw data corresponding to a typical specimen of the second case in Table 6.1 obtained from the tensile tests and the corresponding best-fit lines. Analogous to the first-case, here also Young's modulus and Poisson's ratio have been measured from the slopes of these best-fit lines.

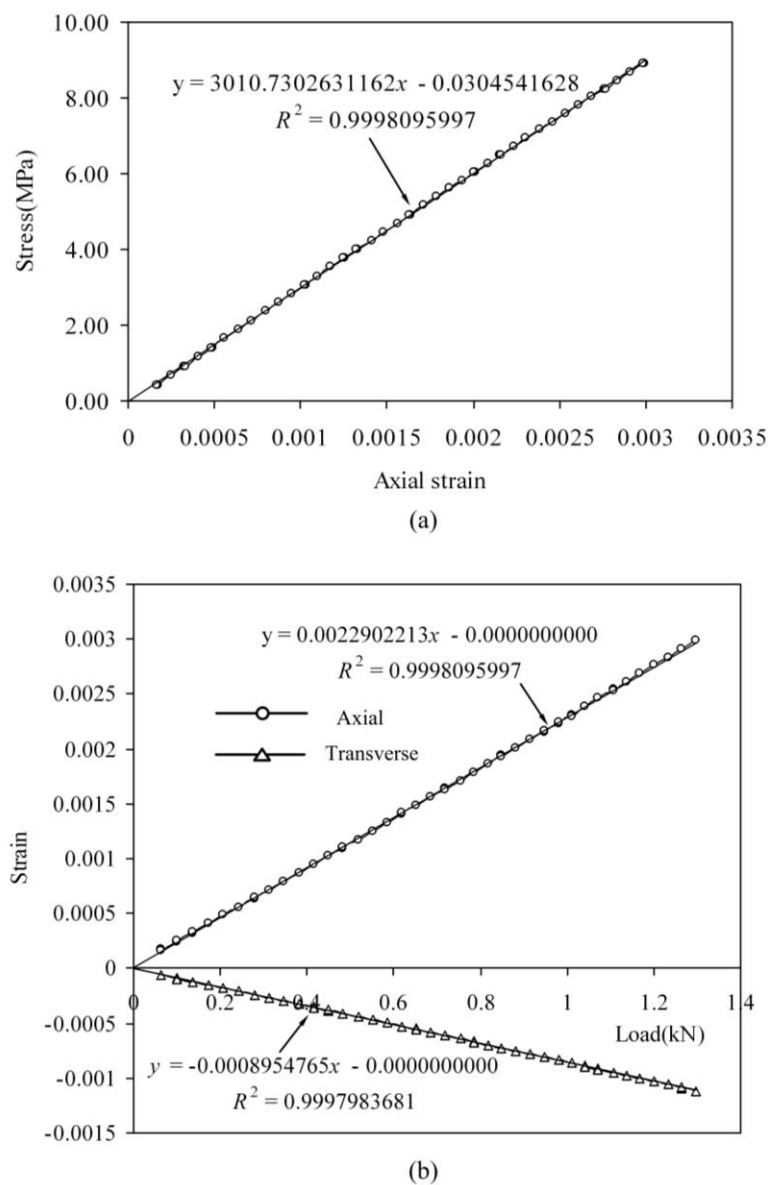


Figure 6.7 Tensile testing data of case 2 specimen (rectangular specimen)

Fig. 6.8 shows the raw data and the corresponding best-fit lines corresponding to a typical specimen of the third case in Table 6.1. Young's modulus and the Poisson's ratio have been obtained from the best-fit lines in a similar way as that in first and second cases.

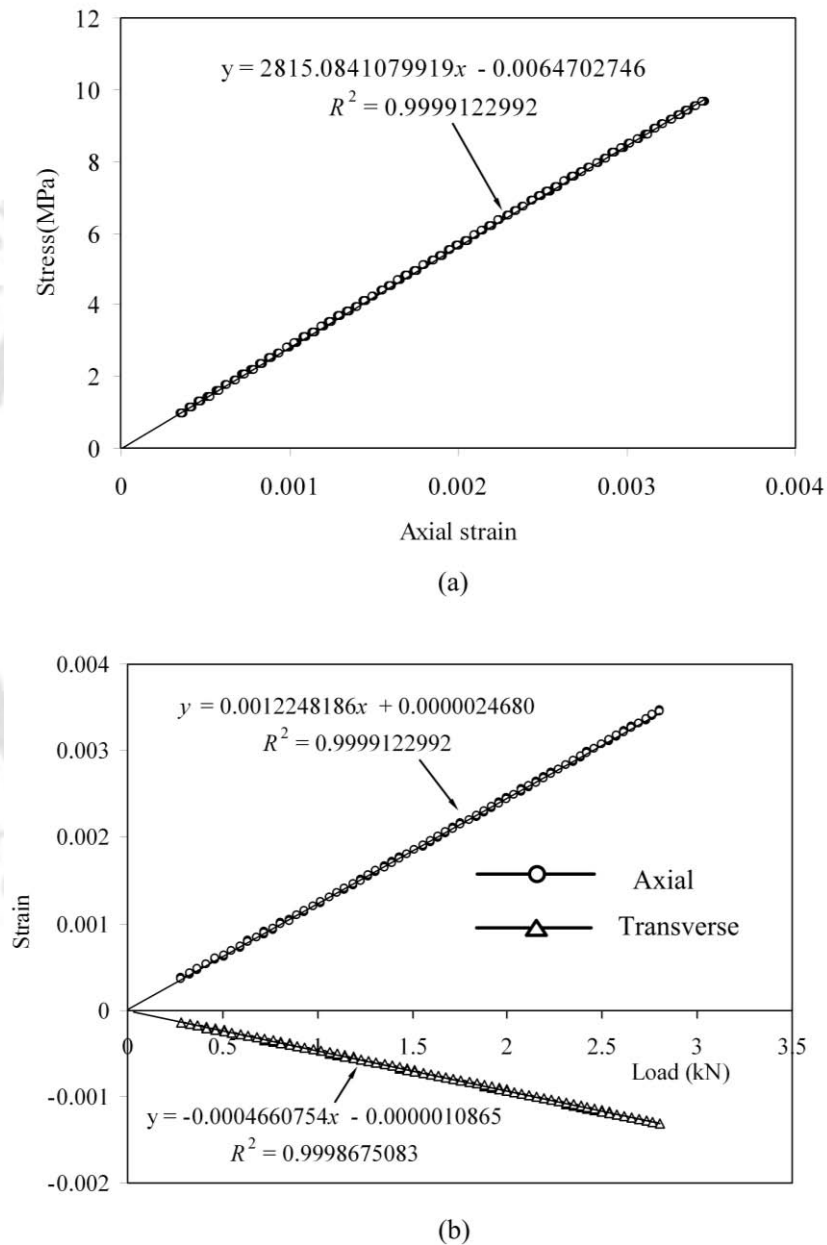


Figure 6.8 Tensile testing data of case 3 specimen (rectangular specimen)

In the fourth case the strain gage readings at the top face have been obtained for both the axial strain as well as transverse strain. Young's modulus and Poisson's ratio are

then calculated using these strain readings using pure bending formulae. Table 6.2 shows the values of Young's modulus values and Poisson's ratios obtained for all the ten tests carried out. Table 6.2 also shows the mean and standard deviation of these data. The mean value of $E = 2917$ MPa and mean value of $\nu = 0.382$ are then taken as the material properties of the chosen PMMA sheet and these values are employed for all the calculations in this chapter.

Table 6.2 Experimental results of material properties

Case	Specimen	E (MPa)	ν
1	SP1-A	2964.83	0.387
	SP2-A	2933.00	0.379
	SP3-A	2876.00	0.372
2	SP1-S	3010.73	0.391
	SP2-S	3065.70	0.391
	SP3-S	2927.70	0.373
3	SP1-L	2815.09	0.381
	SP2-L	2801.00	0.382
	SP3-L	2849.00	0.383
4	SP1-L	2926.00	----
Mean		2916.91	0.382
Std. Dev.		84.18	0.00691

6.3 Experimental verification of optimal strain gage locations

After obtaining the material properties for the PMMA, these properties have been used to evaluate the r_{\max} values using the proposed numerical approaches for the

selected mode I and mixed mode experimental specimens (Fig. 6.1). Based on the r_{\max} values of these configurations, optimum strain gage locations have been identified (based on Eq. (3.29)) and strain gages have been pasted at those selected locations. Strain gages have also been pasted outside the r_{\max} i.e. non-optimum locations in order to substantiate the importance of optimal locations of strain gages in accurate determination of SIFs. Table 6.3 shows the number of test specimens (Fig. 6.1) used for the mode I and mixed mode experiments and their dimensions.

Table 6.3 Details of experimental specimens for mode I and mixed mode loading

Loading	a/b	a (mm)	b (mm)	h (mm)
Mode I	0.293	44	150	114.3
	0.493	74	150	114.3
	0.693	104	150	114.3
Mixed mode I/II	0.497	74.5	150	$h_1=169.3$ $h_2=69.3$

It could be seen from Table 6.3 that three different specimens having $a/b = 0.293$, $a/b = 0.493$ and $a/b = 0.693$ have been used in mode I experiments in order to experimentally verify the general dependency of r_{\max} on a/b (as discussed in section 4.6) and to establish the validity of the proposed method over a wide range of a/b . However, only specimen with $a/b = 0.497$ has been used for mixed mode experiments.

6.3.1 Numerical evaluation of r_{\max} for mode I experimental specimen

Following the proposed methodology as described in section 3.3, r_{\max} values of all the three mode I experimental specimens have been obtained. Fig. 6.9 shows the boundary conditions of a typical specimen used for the FEA. Fig. 6.10 shows the FE

meshes for all the three configurations. Same Q8 elements and the corresponding QPEs (section 3.7.3) have also been employed here. In order to compute r_{\max} values for these configurations, the averaged material properties obtained experimentally (Table 6.2) for the PMMA have been used. Material properties for the material of the specimen as determined from experiments are $E=2917$ MPa and $\nu = 0.382$ (Table 6.2). Corresponding to this value of $\nu = 0.382$ the orientation of the gage line $\theta = 53.13^\circ$ (Eq. (3.27)) and the orientation of the gage $\alpha = 58.28^\circ$ (Eq. (3.26)).

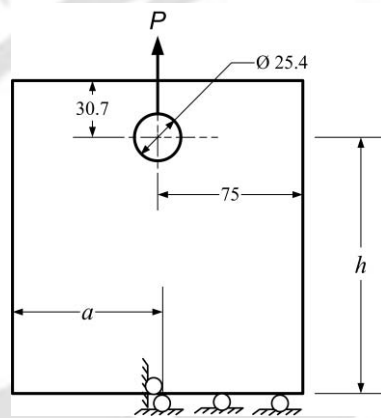


Figure 6.9 Symmetric boundary conditions for mode I specimens

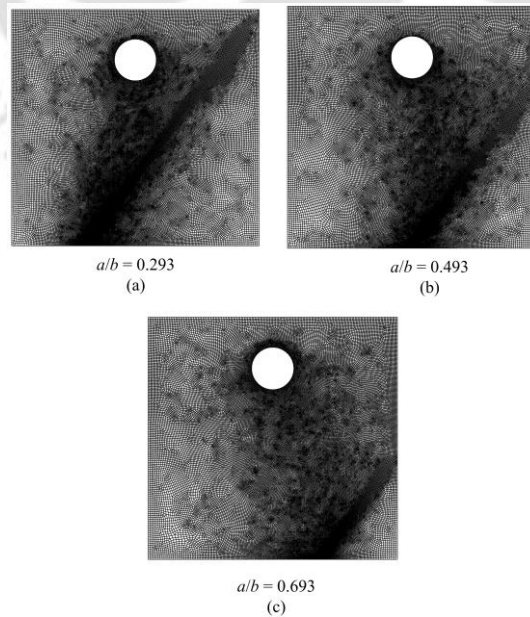


Figure 6.10 Finite element meshes of different mode I specimens

Fig. 6.11 shows the $\ln(\varepsilon_{aa})$ versus $\ln(r)$ obtained from the FEA along the gage lines for $a/b = 0.293$, $a/b = 0.493$, and $a/b = 0.693$ respectively. Following the detailed procedure (section 3.3), the r_{\max} values for all these three configurations have been evaluated from the graph of $\ln(\varepsilon_{aa})$ versus $\ln(r)$ as shown in Fig. 6.11.

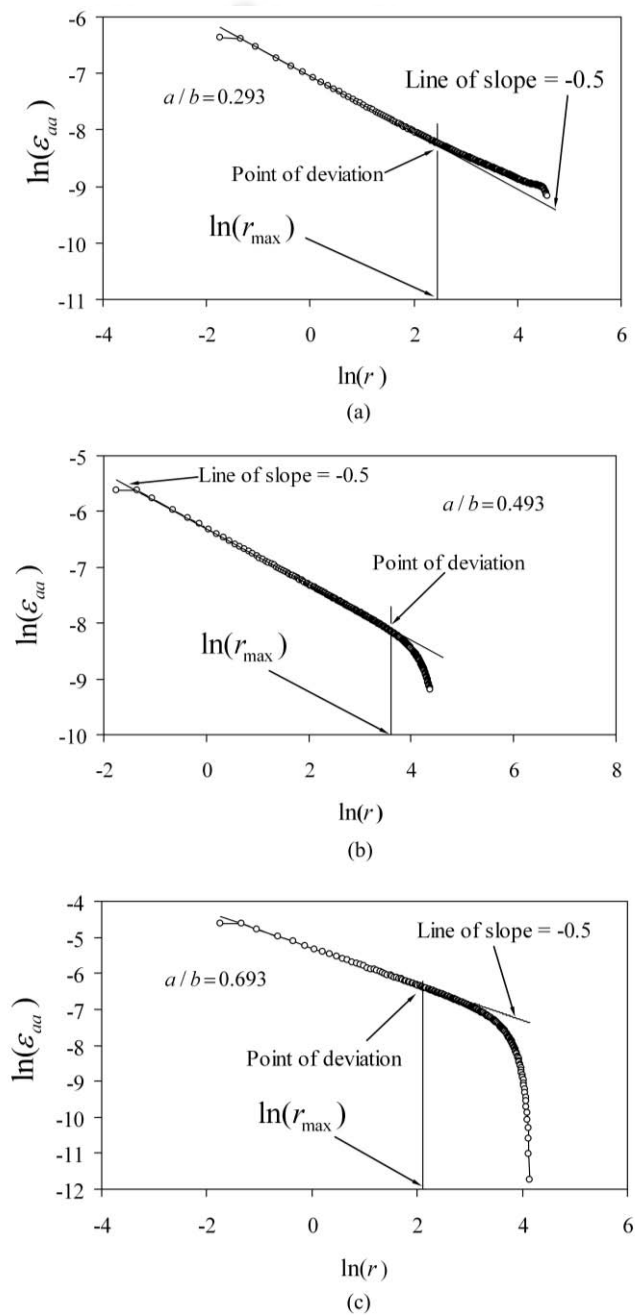


Figure 6.11 Plot of $\ln(\varepsilon_{aa})$ versus $\ln(r)$ for different mode I specimens

From Fig 6.11, it could be once again observed that each plot consists of a distinguishable linear portion followed by a non-linear portion (in logarithmic scale) as predicted by the theory. The linear trend distinctly exists up to a certain radial distance and there after gradually turns to the non-linear portion. As discussed earlier, the r_{\max} values are obtained at the point of deviation of the $(\ln(\varepsilon_{aa})$ versus $\ln(r))$ plot from a superposed line having a slope of -0.5 with an error $\leq -0.5\%$. Fig. 6.11 also shows the superposed lines along with the corresponding points of deviation for all values of a/b . Table 6.4 shows the r_{\max} values obtained in the present study for all the configurations in mode I. Fig. 6.12 shows the variation of r_{\max} of mode I specimens with a/b . As expected an initially increasing and then decreasing trend of r_{\max} with a/b has been obtained.

Table 6.4 r_{\max} values of different mode I specimens

a/b	r_{\max} (mm)
0.293	11.6
0.493	37.0
0.693	8.25

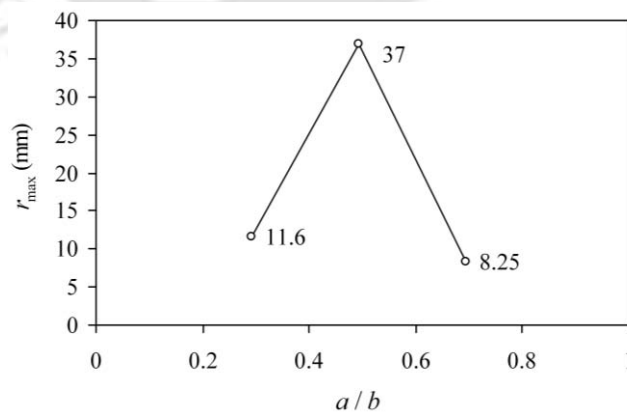


Figure 6.12 Variation of r_{\max} as a function of a/b

Employing the FE meshes shown in Fig. 6.9, for all the three configurations, Mode I SIFs, K_I have been computed using the built in displacement extrapolation technique

in ANSYS. Results of normalized SIFs F_I thus computed are shown in Table 6.5. These results has been used for experimental verification of optimal strain gage locations as discussed in later sections. The FE meshes shown in Fig. 6.9 are actually the final refined meshes beyond which no further improvement in r_{\max} and K_I values have been noticed. This is true for all the configurations.

Table 6.5 Computed normalized mode I SIF of different mode I specimens

a/b	F_I
0.293	1.650022
0.493	2.777738
0.693	6.140603

6.3.2 Numerical evaluation of r_{\max} for mixed mode experimental specimen

As stated earlier only one specimen with $a/b = 0.497$ has been employed in mixed mode experiments. Fig. 6.13(a) shows the mixed mode test specimen with boundary conditions for FEA and Fig. 6.13(b) shows the finite element discretization of the test specimen. Material properties for the material of the specimen as determined from experiments are $E=2917$ MPa, and $\nu = 0.382$ (Table 6.2). Corresponding to this value of $\nu = 0.382$ the orientation of the gage line $\theta = 53.13^\circ$ (Eq. (3.27)) and the orientation of the gage $\alpha = 58.28^\circ$ (Eq. (3.26)). Finite element analysis has been carried out using ANSYS for the mixed mode test specimen and the material properties determined experimentally for the PMMA (Table 6.2) have been used. Same Q8 elements and their corresponding QPEs have been used here in FE discretization. In order to determine r_{\max} value of this test specimen, following the procedure described in section 3.6, $E\varepsilon_{aa}$ and $E\varepsilon_{bb}$ are computed at all the corner nodes of Q8 elements lying on the positive and negative gage lines respectively using FEA. It should be noted that Eq. (3.53), Eq. (3.54), Eq. (3.61) and Eq. (3.62) should be used for determination of r_{\max} as the Poisson's ratio of PMMA is not equal to 1/3.

Fig. 6.14(a) shows the plot of $0.5653E(\varepsilon_{aa} + \varepsilon_{bb})\sqrt{r}$ versus radial distance r and Fig. 6.14(b) shows the plot of $0.7533E(\varepsilon_{aa} - \varepsilon_{bb})\sqrt{r}$ versus radial distance r as obtained from FEA.

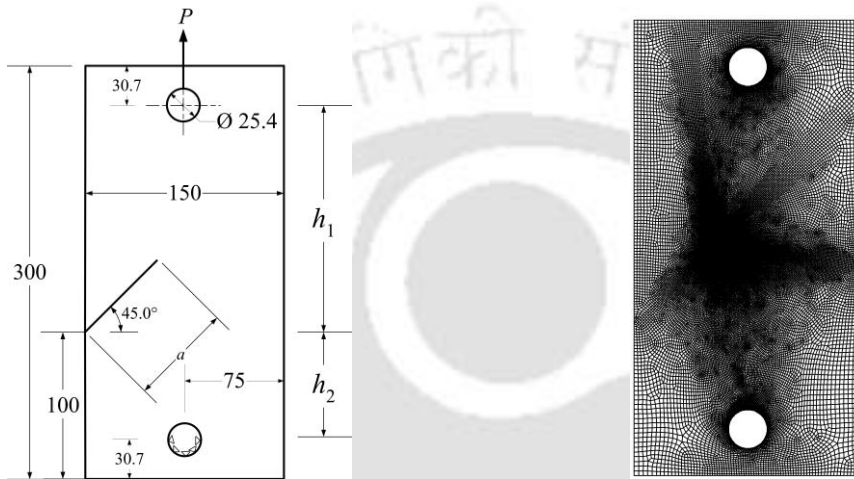


Figure 6.13 (a) Analysis domain for SECP specimen with boundary conditions and (b) Finite element discretization of the mixed mode specimen

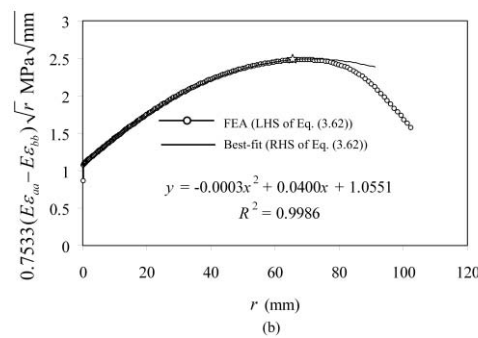
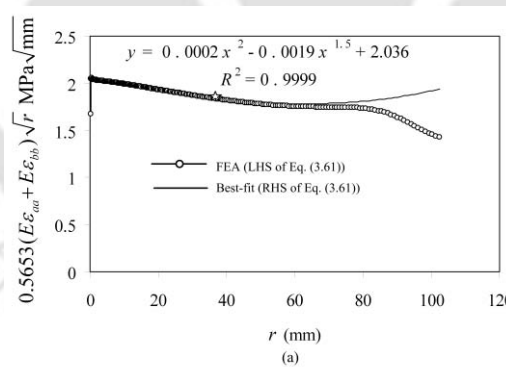


Figure 6.14 SECP with $a/b = 0.497$ (a) determination of A_0, A_2 and B_1 using the best-fit linear regression (b) determination of C_0, C_1 and C_2 using the best-fit linear regression

These figures (Figs. 6.14(a) and (b)) also show best-fits along with the values of coefficients A_0, A_2, B_1, C_0, C_1 and C_2 for best-fit regression and the corresponding correlation coefficient R^2 . Using the values of best-fit coefficients A_0, A_2, B_1, C_0, C_1 and C_2 , the strains ε_{aa} and ε_{bb} have been calculated at all the points along the positive and negative gage lines (Eqs. (3.53) and (3.54)). Fig. 6.15(a) shows comparison of values of $E\varepsilon_{aa}$ obtained using the best-fit coefficients at all the corner nodes along the positive gage line. Similarly Fig. 6.15(b) shows the comparison of values of $E\varepsilon_{bb}$ obtained from FEA with those obtained using the best-fit coefficients at all corner nodes along the negative gage line.

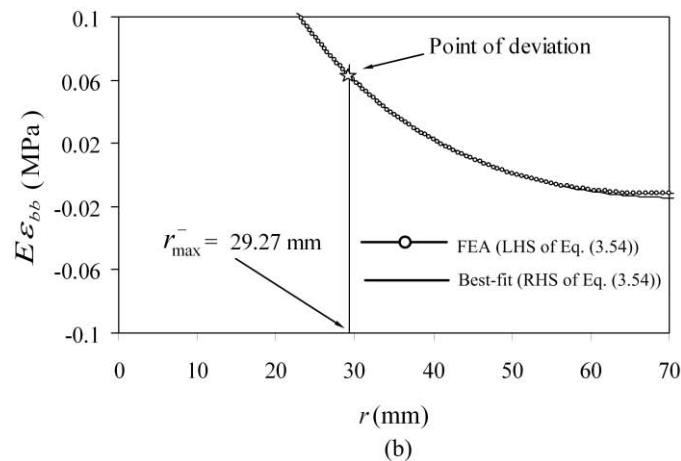
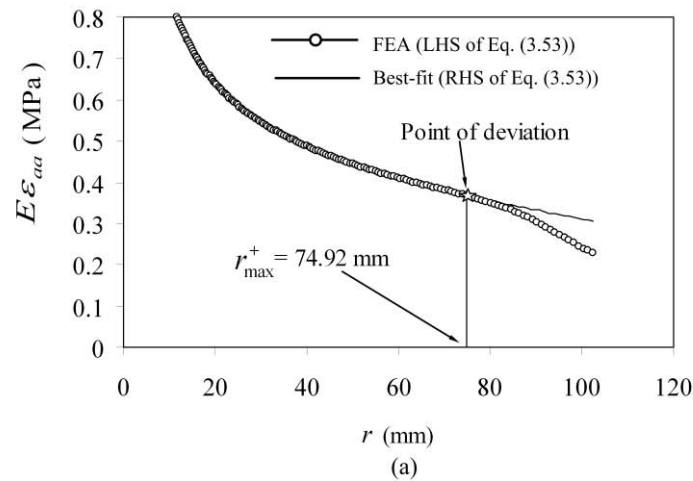


Figure 6.15 SECP with $a/b = 0.497$ (a) determination of r_{\max}^+ for the positive gage line (b) determination of r_{\max}^- for the negative gage line

From Fig. 6.15(a) r_{\max}^+ value has been obtained at the point where the graph of $E\varepsilon_{aa}$ obtained from FEA deviates from the graph of $E\varepsilon_{aa}$ obtained from the best-fit (with an error $\leq 0.5\%$). Similarly r_{\max}^- value is obtained from Fig. 6.15(b). Therefore, r_{\max} for the selected mixed mode experimental specimen is the minimum of r_{\max}^+ and r_{\max}^- . In this case as could be seen from Fig. 6.15, $r_{\max} = \min(r_{\max}^+ \text{ and } r_{\max}^-) = 29.27 \text{ mm}$ is obtained from present approach. Using the same FE mesh, mixed mode SIFs (K_I and K_{II}) have been computed using displacement extrapolation technique built in ANSYS. The FE mesh shown in Fig. 6.13 is the final refined mesh beyond which no further improvement in r_{\max} and K_I and K_{II} have been observed. The computed normalized SIFs of this configuration are found to be

$$\begin{aligned} F_I &= 1.1307 \\ F_{II} &= 0.5951 \end{aligned} \quad (6.3)$$

6.3.3 Details of experiments

In the present investigation, the experimental verification of optimal strain gage locations (determined by the present approach) has been demonstrated using experimental values of SIFs under mode I and mixed mode loading conditions. In order to determine mode I and mixed mode SIFs experiments have been conducted with mode I and mixed mode (I/II) test specimens made of PMMA with different configurations as shown in Fig. 6.1 and Table 6.3. The specimens have been made from the same PMMA sheet which was used for determination of material properties of PMMA.

All the specimens of mode I and mixed mode have been loaded with a closed loop servo hydraulic INSTRON 8801 machine with 100 kN capacity under the displacement control with an actuator speed 0.1 mm/min. Clevis grips have been used for transferring the tensile load from the machine to the specimen.

Strain measurements on all the loaded specimens have been carried out using the electrical resistance strain gages of type FLA-1-11-3LT, Make: TML Japan.

Details of the specification of strain gages used are given in Table 6.6. Fig. 6.16 shows the photograph of a typical strain gage. Utmost care has been taken while pasting the strain gages on the test specimens, to ensure perfect and defect free bonding following the standard procedures for strain gage pasting.

Table 6.6 Details of TML strain gage

Parameter	Specifications
Type	: FLA-1-11-3LT
Gage length	: 1 mm
Gage factor	: $2.12 \pm 1\%$
Gage resistance	: 119.5 ± 0.5
Transverse sensitivity	: 0.9%
Lead wires	: 10 / 0.12 3W pre-wired 3 m long
Test condition	: $23\text{ }^{\circ}\text{C}$ 50%RH



Figure 6.16 A typical 1 mm gage length, pre-wired TML strain gage

Number of strain gages (depending upon mode I and mixed mode) have been pasted very carefully at specific selected locations along the gage lines (at angle θ and α). The radial position and orientation of the strain gages have been maintained while pasting and have been cross-checked using a profile projector. Fig. 6.17 shows the picture of a profile projector showing clearly the orientation of a typical strain gage pasted on to the specimen.



Figure 6.17 Profile projector for verification of orientation and location of a strain gage

The measured strains have been acquired, digitized and processed using NI Data Acquisition System comprising of cDAQ9178 chassis. A universal analog input module (NI 9219 having 4 channels 24 Bit) has been used for the measurement of force from INSTRON machine in terms of voltage signals. This has been achieved by connecting BNC cable between the load cell of the INSTRON and the NI 9219 module. In this way the load has been measured simultaneously along with the strains. Strain measurements have been carried out using four number of NI 9237 (4 channels 24 Bit, half-full bridge analog input module).

In the present investigation, in all the experiments, quarter bridge Wheatstone bridge circuit has been employed for the measurement of strains. For this purpose, NI 9944(Quarter bridge completion accessories) has been added to the NI 9237 strain gage module. The sampling rate for data in all of these modules has been set to 100 Hz. LabVIEW 9 has been used to interface the DAQ System with the digital computer and this software is also used for processing and storing of experimental data. In all the experiments, offset-nulling and shunt calibration of strain gages has been done before the actual data acquisition during loading. An excitation voltage of 2.5V is set in all the experiments.

Fig. 6.18 shows the snap shot of a typical virtual instrumentation using DAQ assistant used in one of the experiments. Once the instrumentation part required for data acquisition is ready, the specimen with the strain gages pasted on it is put into the clevis grips of INSTRON machine using pins. In order to avoid bending of the specimen during tensile loading and to ensure that the specimen is subjected to only axial tensile loads, spacer blocks are employed in both the top and bottom clevis as shown in Fig. 6.19.

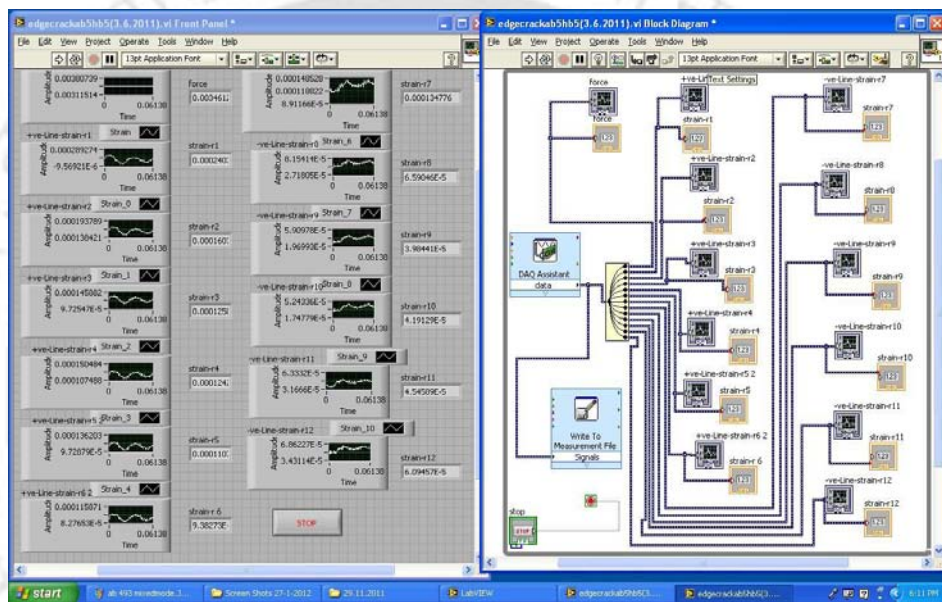


Figure 6.18 DAQ assistant of LabVIEW programming for a typical experiment

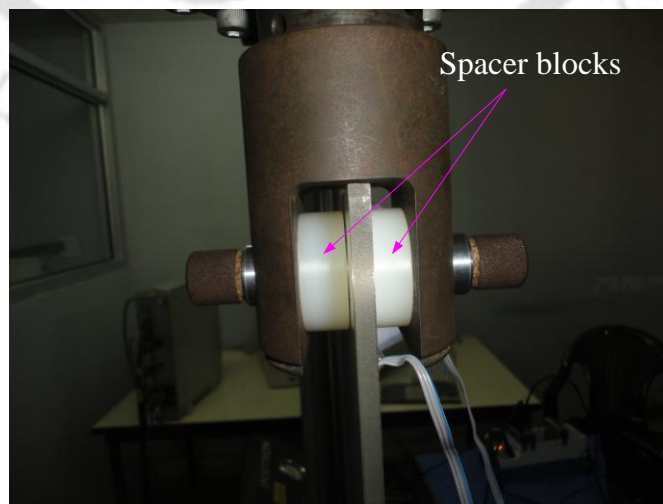


Figure 6.19 Specimen with the spacer blocks in clevis

The dimensions of the spacer blocks are machined so as to provide perfect alignment of the specimen. The alignment of the specimen is also checked using a plumb before loading as shown in Fig. 6.20. During loading both force and strain data have been simultaneously stored in the computer for further processing. Fig. 6.21 shows the photograph of the complete experimental setup highlighting all the individual elements as described in this section.



Figure 6.20 Checking of alignment of a specimen using plumb

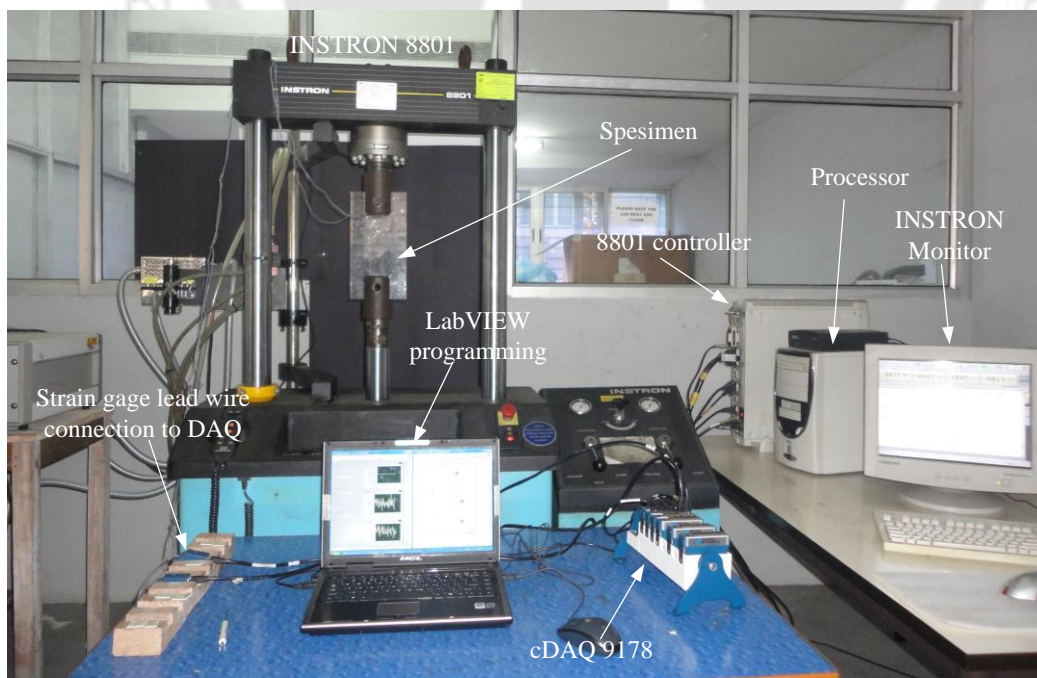


Figure 6.21 Photograph of complete experimental setup

As stated earlier, appropriate radial locations of strain gages are not only important for accurate determination of SIFs but also desirable to eliminate erroneous strain measurements due to the three dimensional effects, strain gradient effects and plasticity effects. In general, all these effects can be greatly minimized by placing strain gages as far as possible from the crack-tip. The three dimensional effects can be eliminated by placing the gages beyond $t/2$ [21]. In the present experimental study all the gage locations have been selected to satisfy the above condition in both mode I and mixed mode loading conditions.

The plasticity effects is avoided in the present investigation by choosing PMMA as the specimen material which is a linear elastic and brittle material at room temperature. The measurement errors due to the strain gradients can be drastically reduced by selecting strain gages with very small gage length and width [62, 63, 64]. In the present investigation very small gages of 1 mm gage length have been employed for strain measurements. In addition, the analysis of errors due to the strain gradients on the determination of mode I SIF by Dally and Sanford [22] clearly showed that these errors could be drastically reduced if the ratio of radial distance of center of a strain gage to the length of the gage is more than four. All the gage locations for both mode I and mixed mode experiments in the present experimental study are selected to satisfy the above requirement for avoiding the strain gradient effects.

6.3.4 Experimental results for verification of optimal strain gage locations in mode I

Here mode I SIFs have been determined using single strain gage DS technique in order to verify the optimal strain gage locations in mode I specimens. Fig. 6.22 shows the photograph of the three different specimens made of PMMA (along with strain gages pasted) which have been used in the present experiments. Material properties for the material of the specimen as determined from experiments are $E = 2917$ MPa, and $\nu = 0.382$ (Table 6.2). Corresponding to this value of $\nu = 0.382$ the

orientation of the gage line $\theta = 53.13^\circ$ (Eq. (3.27)) and the orientation of the gage $\alpha = 58.28^\circ$. (Eq. (3.26)).

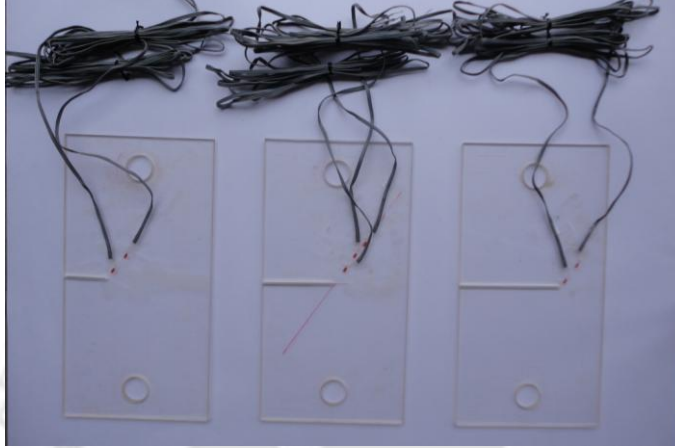


Figure 6.22 Photograph of different mode I specimens

As shown in Fig. 6.22, all the strain gages have been pasted along the gage line (θ) maintaining the proper orientation (α). According to the proposed approach, for optimal locations for the strain gages should be in the range $t/2 \leq r \leq r_{\max}$ in order to obtain the accurate value of SIF. Strain gages located beyond the r_{\max} will result in inaccurate SIF, K_I and thus are non-optimal locations as per the proposed approach. Based on these, strain gage locations have been decided in the present experiments for all the three configurations as shown in Table 6.7.

Table 6.7 Selected radial locations of strain gages for mode I experiments

a/b	r_1 (mm)	r_2 (mm)	r_3 (mm)	r_{\max} (mm)
0.293	10	30	----	11.6
0.493	17.5	35	50	37.0
0.693	7	27	-----	8.25

For $a/b = 0.293$, the value of r_{\max} obtained from the proposed approach is 11.6 mm. Therefore, one strain gage is pasted at $r = 10$ mm ($< r_{\max}$) and another strain gage is pasted beyond r_{\max} at $r = 30$ mm. Locations of strain gages one at optimal and the

other at non-optimal location are intentionally chosen to verify the importance of optimal strain gage location in terms of experimentally evaluated value of K_I . For $a/b = 0.493$, the $r_{\max} = 37$ mm has been obtained from the present numerical method. Therefore, for the experiment, two strain gages at $r = 17.5$ mm and $r = 35$ mm have been pasted within the r_{\max} while another strain gage has been pasted at $r = 50$ mm i.e. beyond r_{\max} . These locations have been selected to compare the experimentally determined value of K_I to emphasize the importance of optimal strain gage locations.

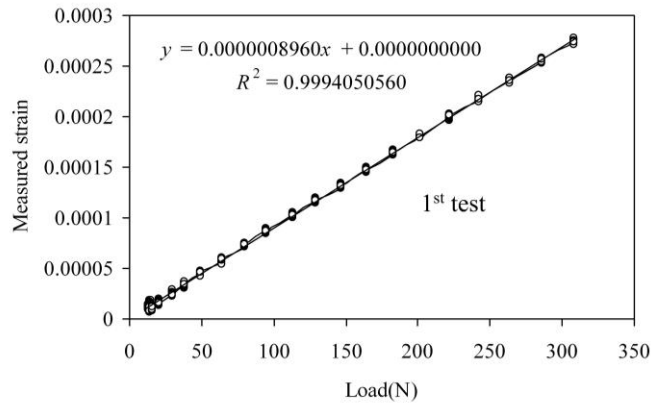
Similarly, for $a/b = 0.693$, the estimated value of $r_{\max} = 8.25$ mm and two strain gages one at $r = 7$ mm (within r_{\max}) and other at $r = 27$ mm (beyond r_{\max}) have been pasted for verification of the importance of optimal strain gage locations.

After pasting the strain gages, their locations and orientations have been verified using the profile projector (Fig. 6.17). It should be noted that in all experiments of all these specimens the magnitude of load applied to the specimens is kept well below the critical load for fracture. This critical load for a particular configuration has been estimated using the approximate value of $K_{IC} = 1 \text{ MPa} \sqrt{\text{m}}$ for PMMA. It should also be noted that in the present investigation, for all the configurations, experiments have been repeated three times to ensure the repeatability of the results. In all the experimental data, foot corrections have been done by subtracting the strain value corresponding to zero load from all the measured strain gage readings.

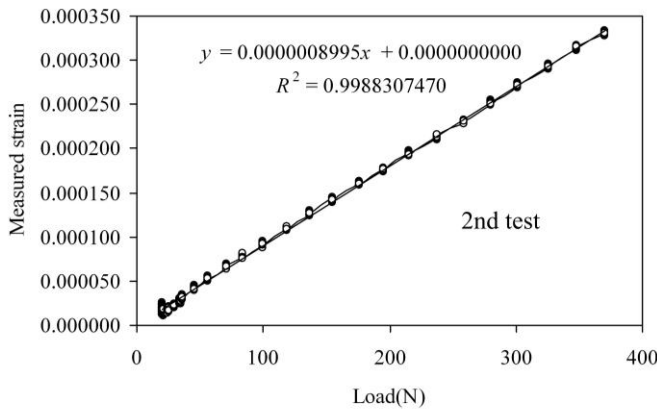
6.3.4.1 Results for $a/b = 0.293$

Fig. 6.23 shows the raw data of measured strain ε_{aa} by the strain gage (circled data points) at $r_1 = 10$ mm versus the applied load for $a/b = 0.293$ for all the three repeated tests. Fig. 6.23 also shows best-fit straight lines (solid lines) to the raw data with the corresponding slopes and the correlation coefficients R^2 . As expected, in all the repeated tests, the measured strains are linearly proportional to the applied load as

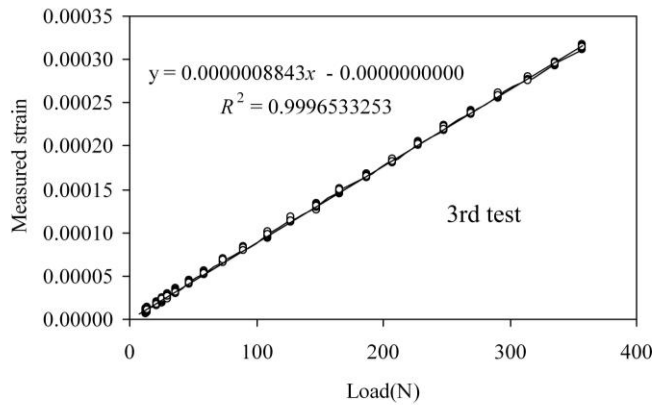
predicted by very good values of R^2 . Further, the slopes of best-fit straight lines in all plots of Fig. 6.23 are nearly same. Thus, these trends clearly reinforces the perfect calibration of the entire experimental setup.



(a)



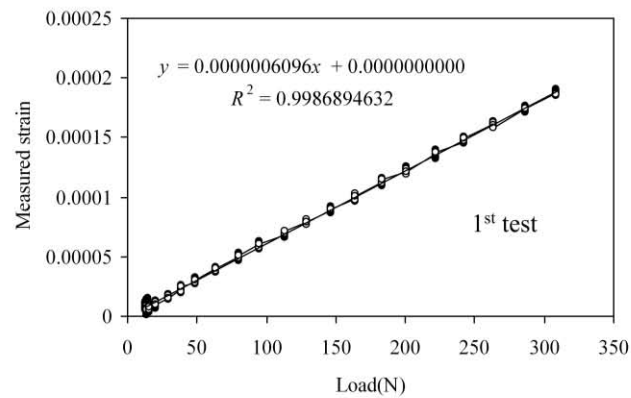
(b)



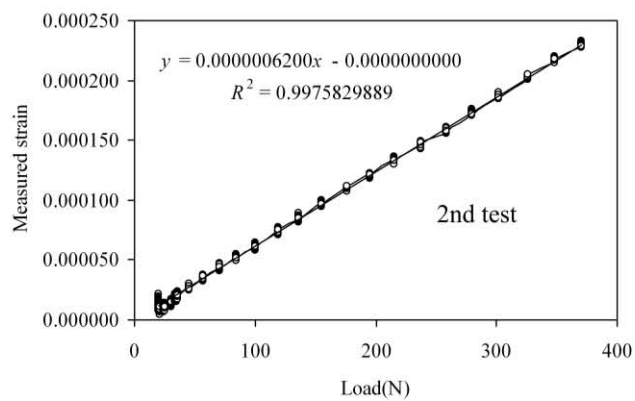
(c)

Figure 6.23 Measured strain (ϵ_{aa}) at $r_1 = 10$ mm for $a/b = 0.293$ for three repeated tests

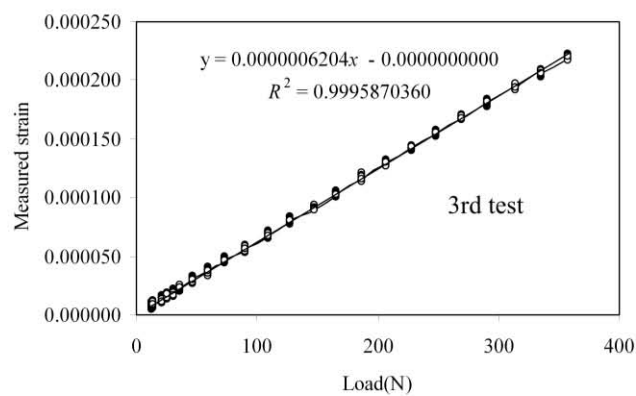
Similarly Fig. 6.24 shows the raw data of measured strains ε_{aa} (circled data points) versus applied load corresponding to the strain gage at $r_2 = 30$ mm for $a/b = 0.293$ for all the three repeated tests.



(a)



(b)



(c)

Figure 6.24 Measured strain (ε_{aa}) at $r_2 = 30$ mm for $a/b = 0.293$ for three repeated tests

The best-fit lines (solid lines) to the raw data along with the corresponding slopes and correlation coefficient R^2 are also shown in Fig. 6.24. Here also, as expected, a perfectly linear trend between the measured strains and the applied load and very nearly same values of slopes of best-fit lines have been observed. Further, comparison of slopes of best-fit lines in Fig. 6.23(a) and Fig. 6.24(a) shows that the magnitude of strain ε_{aa} at $r_2 = 30$ mm is less than that at $r_1 = 10$ mm. This trend can also be noticed in plots of 2nd and 3rd repeated tests in Figs. 6.23 and 6.24. Thus, as expected, the measured strain decreases with increase in distance from the crack tip. The above trends further reinforces the goodness of calibration.

Table 6.8 shows the measured strains ε_{aa} for the strain gage located at $r_1 = 10$ mm obtained from the best-fit equations of a typical test (1st test in Fig. 6.23) for different values of applied loads for $a/b = 0.293$.

Table 6.8 Variation of experimental values of K_I and F_I at $r_1 = 10$ mm with the applied load in the 1st test for $a/b = 0.293$

Load (N)	Measured Strain ε_{aa}	K_I (MPa $\sqrt{\text{mm}}$)	F_I
50	0.0000448	1.17110022	1.67340889
100	0.0000896	2.34220045	1.67340889
150	0.0001344	3.51330067	1.67340889
200	0.0001792	4.68440090	1.67340889
250	0.000224	5.85550112	1.67340889
300	0.0002688	7.02660135	1.67340889

K_I has been computed corresponding to different load values using the measured strain values in Table 6.8 and average material properties (E and ν in Table 6.2) in Eq. (3.30). Then the mode I normalized SIF F_I is computed using the experimental values of K_I by employing Eq. (6.1). Table 6.8 also shows these experimental values

of K_I and F_I for different loads. It could be observed from the Table 6.8 that while K_I is increasing with the increase in applied load, F_I remains constant irrespective of the applied load. All these trends are as expected. Similar trends have also been obtained with the strain data of other repeated tests as the slopes of the straight lines in Fig. 6.23 are almost equal.

Table 6.9 shows the measured strains ε_{aa} for the strain gage located at $r_2 = 30$ mm obtained from Fig. 6.24(a) using best-fit equation for different values of applied load for $a/b = 0.293$. Using these strain values and material properties (E and ν) in Eq. (3.30), K_I have been computed for each load value and are listed in the Table 6.9. Using these experimental values of K_I , the F_I is determined by employing Eq. (6.1) and are listed in Table 6.9. It could be noted that here also K_I is increasing with increasing load while F_I remains constant with the load as expected. It should be noted that similar trends have been obtained with the strain data of other repeated tests as the slopes of the best-fit straight lines in Fig. 6.24 are almost equal.

Table 6.9 Variation of experimental values of K_I and F_I at $r_2 = 30$ mm with the applied load in the 1st test for $a/b = 0.293$

Load(N)	Measured strain	K_I (MPa $\sqrt{\text{mm}}$)	F_I
50	0.00003045	1.38003989	1.9719670
100	0.00006096	2.76007978	1.9719670
150	0.00009144	4.14011967	1.9719670
200	0.00012192	5.52015957	1.9719670
250	0.0001524	6.90019946	1.9719670
300	0.00018288	8.28023935	1.9719670

Table 6.10 shows the F_I obtained at r_1 and r_2 for each of the three repeated experiments for $a/b = 0.293$ and their average values. It could be observed that in all

the three tests at a given location (r_1 or r_2) F_I values are very close to each other showing the precision of the results.

Table 6.10 Experimental values of F_I for three repeated tests for $a/b=0.293$

Test	F_I	
	at $r_1 = 10\text{ mm}$	at $r_2 = 30\text{ mm}$
1	1.6734089	1.9719670
2	1.6799456	2.0056095
3	1.6515575	2.0069034
Average	1.6683040	1.9948267

Table 6.11 shows the comparison of average NSIF obtained from the present experiments at both the locations of strain gages (r_1 and r_2) with the reference solution obtained from ANSYS (Table 6.5) in terms of the % relative error for $a/b=0.293$.

Table 6.11 Experimental values of F_I for $a/b=0.293$ at different gage locations ($r_{\max} = 11.6\text{ mm}$)

Location	F_I		% Relative Error
	Reference solution (Table 6.5)	Experimental value	
Optimal ($r_1 = 10\text{ mm} < r_{\max}$)		1.6683040	1.11
Non-optimal ($r_2 = 30\text{ mm} > r_{\max}$)	1.6500219	1.9948267	20.90

It could be observed from the results in Table 6.11 that the % relative error in F_I which is determined based on the strain gage readings at the optimal location r_1 ($< r_{\max}$) is only 1.11% while that determined based on the strain gage readings at the

non-optimal location r_2 ($> r_{\max}$) is as high as 20.90%. These experimental observations clearly substantiates the theoretical basis of the proposed numerical approach and verify the existence and importance of r_{\max} in deciding the optimal strain gage location for accurate determination of mode I SIF.

6.3.4.2 Results for $a/b = 0.493$

As shown in Table 6.7 for the edge cracked specimen with $a/b = 0.493$, for which $r_{\max} = 36.99$ mm, two strain gages are placed within r_{\max} (i.e., $r_1 = 17.5$ mm, and $r_2 = 35$ mm) and one strain gage is placed beyond r_{\max} at $r_3 = 50$ mm. Fig. 6.25 shows the raw data of measured strains ε_{aa} (circled data points) for the strain gage located at $r_1 = 17.5$ mm versus the applied load for $a/b = 0.493$ for all the three repeated tests. Fig. 6.25 also shows best-fit straight lines (solid lines) to the raw data with the corresponding slopes and the correction coefficients R^2 . As expected, in all the repeated loads, the measured strains are linearly proportional to the applied load and slopes of best-fit lines in all the repeated tests are also nearly same, which again reinforces the perfect calibration of the entire experimental setup.

Fig. 6.26 shows the raw data of measured strains ε_{aa} (circled data points) versus applied load for the strain gage at $r_2 = 35$ mm for $a/b = 0.493$ for all the three repeated loads. The best-fit lines to the raw data (solid lines) along with their corresponding slopes and correlation coefficient R^2 are shown in Fig.6.26. Here also a perfectly linear trend between the measured strains and the applied load and similar slopes of best-fit lines in all the three repeated test have been observed as expected.

Similarly Fig. 6.27 shows the raw data of measured strains versus applied load at $r_3 = 50$ mm for $a/b = 0.493$ for all the three repeated loads. The best-fit lines along with the corresponding slopes and correlation coefficient R^2 are shown in all plots of Fig.6.27. The same trends as observed in the above experiments one again have been obtained at $r_3 = 50$ mm which further substantiates the goodness of the calibration of entire experimental setup. Further, comparison of slopes of best-fit lines

in Figs. 6.25-6.27 show that the measured strain decreases with increase in distance from the crack tip which is as expected. This trend can be noticed in all the three repeated tests. These observations also substantiates the goodness of calibration.

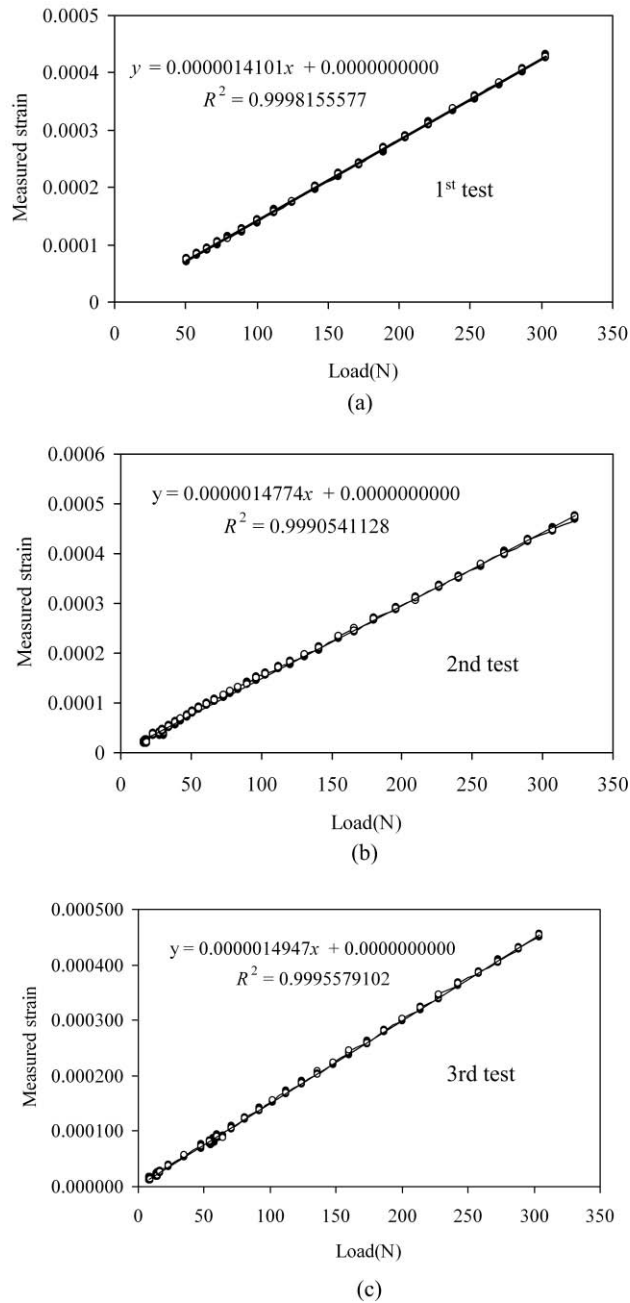
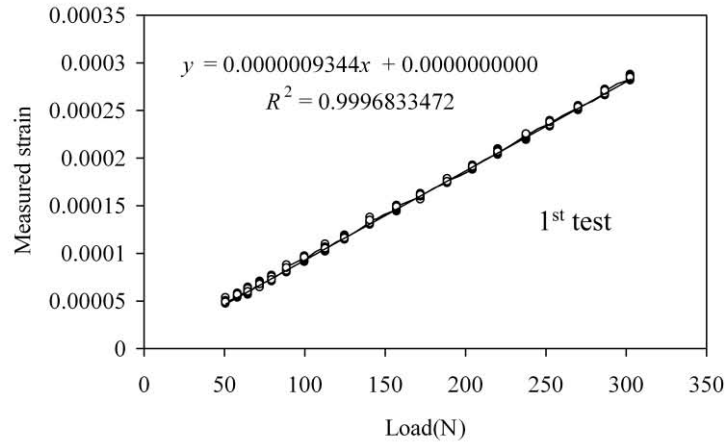
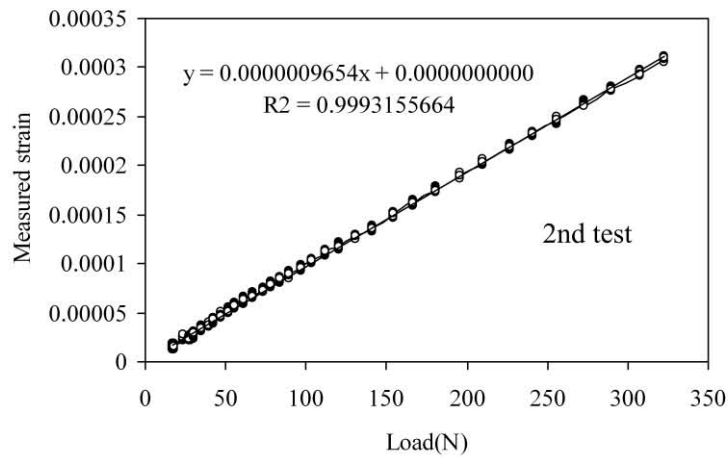


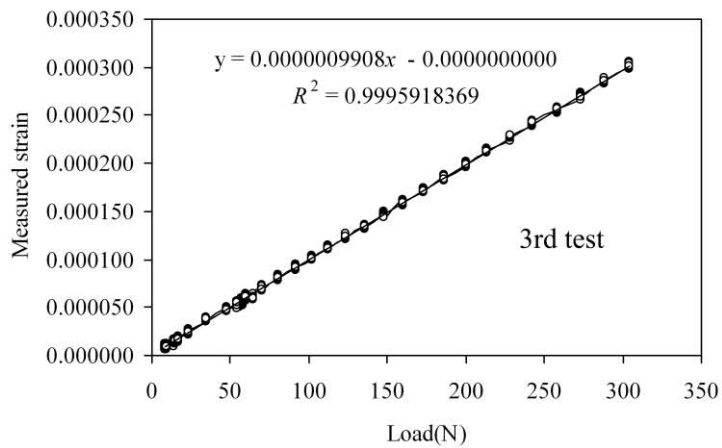
Figure 6.25 Measured strain (ϵ_{aa}) at $r_1 = 17.5$ mm for $a/b = 0.493$ for three repeated tests



(a)

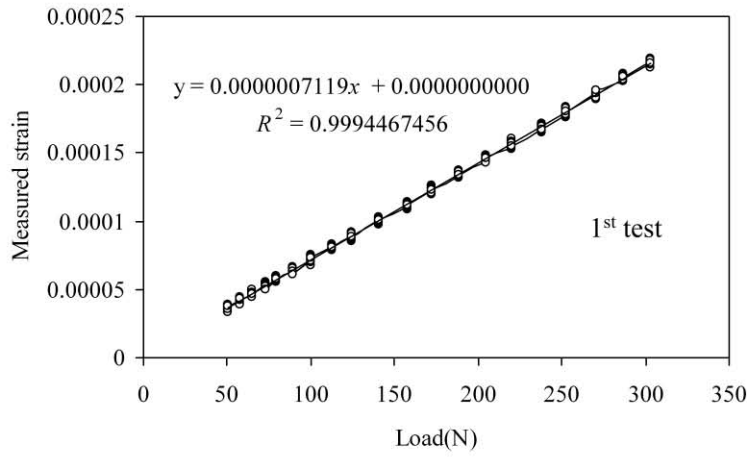


(b)

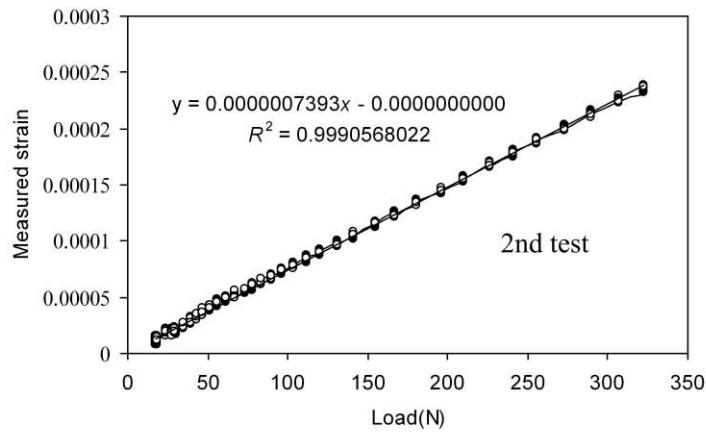


(c)

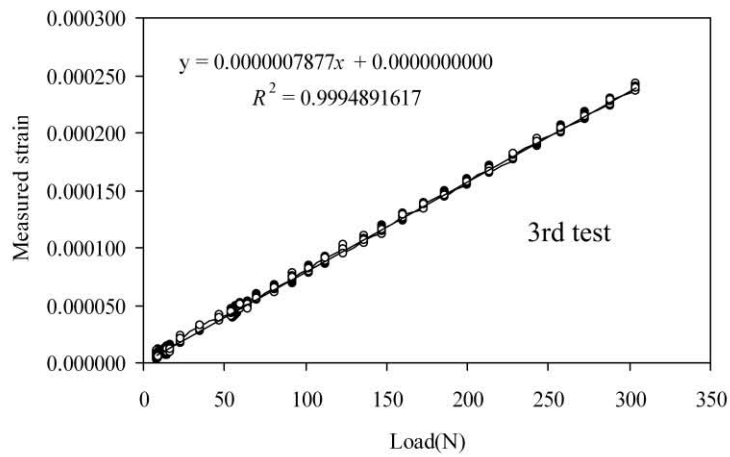
Figure 6.26 Measured strain (ϵ_{aa}) at $r_2 = 35$ mm for $a/b = 0.493$ for three repeated tests



(a)



(b)



(c)

Figure 6.27 Measured strain (ϵ_{aa}) at $r_3 = 50$ mm for $a/b = 0.493$ for three repeated tests

Tables 6.12-6.14 show the measured strains ε_{aa} and the corresponding K_I and F_I determined (using Eqs. (3.30) and (6.1), respectively) for strain gages located at $r_1 = 17.5$ mm, $r_2 = 35$ mm and $r_3 = 50$ mm respectively for different applied loads and for $a/b = 0.493$. As in case of $a/b = 0.293$, here also K_I increases with increasing load but F_I is independent of load as expected at all strain gage locations r_1, r_2 and r_3 .

Table 6.12 Variation of experimental values of K_I and F_I at $r_1 = 17.5$ mm with the applied load in the 1st test for $a/b = 0.493$

Load(N)	Measured strain	K_I (MPa $\sqrt{\text{mm}}$)	F_I
50	0.000070505	2.4381195	2.6864173
100	0.00014101	4.8762390	2.6864173
150	0.000211515	7.3143586	2.6864173
200	0.00028202	9.7524781	2.6864173
250	0.000352525	12.1905976	2.6864173
300	0.00042303	14.6287171	2.6864173

Table 6.13 Variation of experimental values of K_I and F_I at $r_2 = 35$ mm with the applied load in the 1st test for $a/b = 0.493$

Load(N)	Measured strain	K_I (MPa $\sqrt{\text{mm}}$)	F_I
50	0.00004672	2.2848248	2.51751109
100	0.00009344	4.5696496	2.51751109
150	0.00014016	6.8544744	2.51751109
200	0.00018688	9.1392993	2.51751109
250	0.0002336	11.4241241	2.51751109
300	0.00028032	13.7089489	2.51751109

Table 6.14 Variation of experimental values of K_I and F_I at $r_3 = 50$ mm with the applied load in the 1st test for $a/b = 0.493$

Load(N)	Measured strain	K_I (MPa $\sqrt{\text{mm}}$)	F_I
50	0.00003560	2.0806070	2.29249573
100	0.00007119	4.1612139	2.29249573
150	0.00010679	6.2418209	2.29249573
200	0.00014238	8.3224279	2.29249573
250	0.00017798	10.4030349	2.29249573
300	0.00021357	12.4836418	2.29249573

Table 6.15 shows the F_I values obtained from all the strain gage readings for all the three repeated tests and their corresponding average values. Once again very good repeatability of the experiments can be observed from the results presented in Table 6.15.

Table 6.15 Experimental values of F_I for three repeated tests for $a/b = 0.493$

Test	F_I		
	at $r_1 = 17.5$ mm	at $r_2 = 30$ mm	at $r_3 = 50$ mm
1	2.68641731	2.51751109	2.29249573
2	2.81463225	2.60103297	2.38073057
3	2.84759092	2.66946702	2.53659065
Average	2.78288016	2.59600369	2.40327232

Table 6.16 shows the comparison of experimental values of average F_I obtained from the present experiments for $a/b = 0.493$ at the locations of strain gages (r_1, r_2 and r_3) with the reference solutions obtained using ANSYS (Table 6.5). Table 6.16 also shows % relative error in experimental values of F_I . It could be observed from these results that the % relative error in F_I based on the strain gage readings at the selected

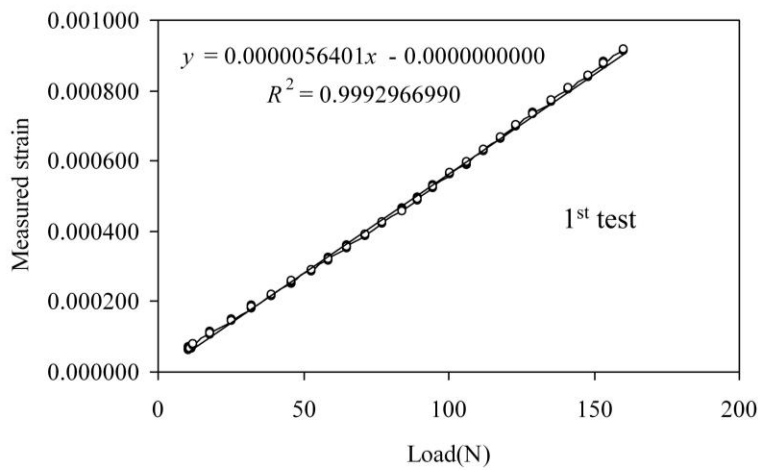
optimal locations $r_1 (<r_{\max})$ and $r_2 (<r_{\max})$ are 0.19% and 6.54% while that based on the strain gage readings at the non-optimal location $r_3 (>r_{\max})$ is as high as 13.48%. These experimental observations undoubtedly substantiates the theoretical basis of the proposed numerical approach and verify the existence and importance of r_{\max} in deciding the optimal strain gage locations for accurate determination of mode I SIF.

Table 6.16 Experimental values of F_I for $a/b=0.493$ at different gage locations ($r_{\max} = 37$ mm)

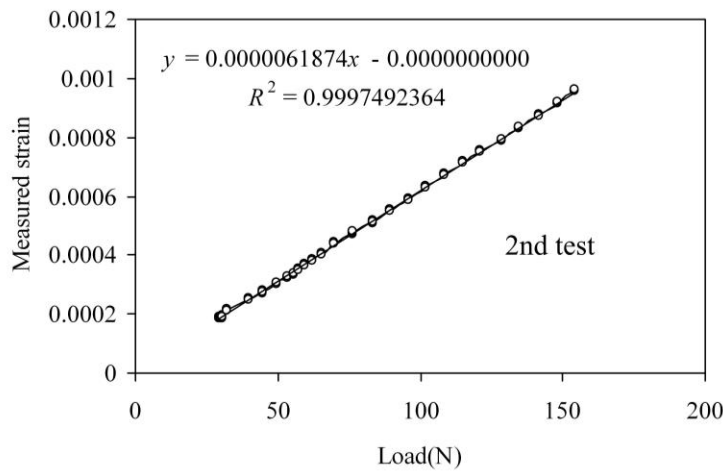
Location	F_I		% Relative error
	Reference solution (Table 6.5)	Experimental value	
Optimal ($r_1 = 17.5 \text{ mm} < r_{\max}$)		2.78288016	0.19
Optimal ($r_2 = 35 \text{ mm} < r_{\max}$)	2.777738	2.59600369	6.54
Non optimal ($r_3 = 50 \text{ mm} > r_{\max}$)		2.40327232	13.48

6.3.4.3 Results for $a/b = 0.693$

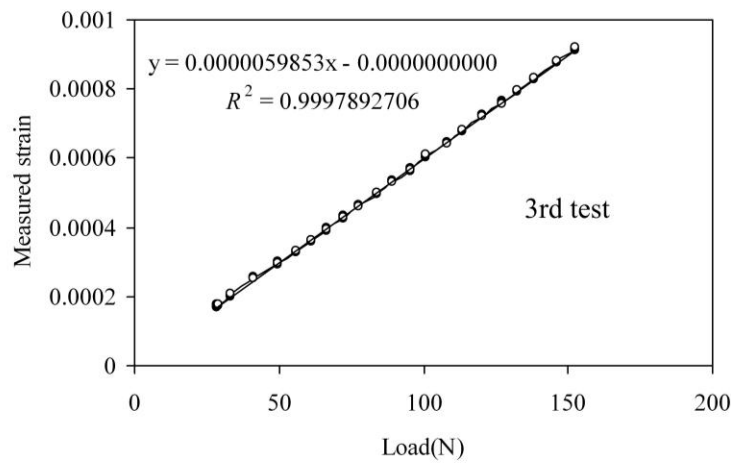
Finally, for the mode I specimen with $a/b = 0.693$, for which $r_{\max} = 8.25$ mm, two strain gage locations (Table 6.7) one at $r_1 = 7$ mm ($<r_{\max}$) and the other at $r_2 = 27$ mm ($>r_{\max}$) are selected for the purpose of experimental verification of optimal strain gage locations. Figs. 6.28 and 6.29 show the raw data of measured strain ε_{aa} (circled data points) versus the applied load for $a/b = 0.693$ for all the three repeated tests at $r_1 = 7$ mm and $r_2 = 27$ mm respectively. Figs. 6.28 and 6.29 also shows best-fit straight lines to the raw data (solid lines) along with the corresponding slopes and the correction coefficients R^2 . As expected, in all the repeated tests, the measured strains in all plots of Figs 6.28 and 6.29 are linearly proportional to the applied load which again reinforces the perfect calibration of the entire experimental setup.



(a)

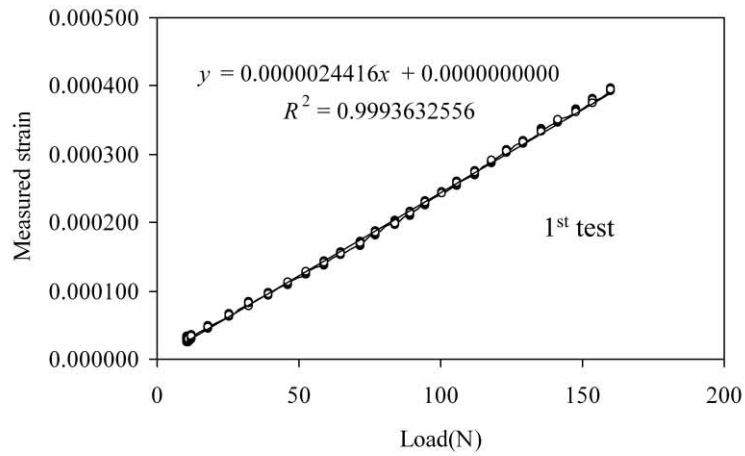


(b)

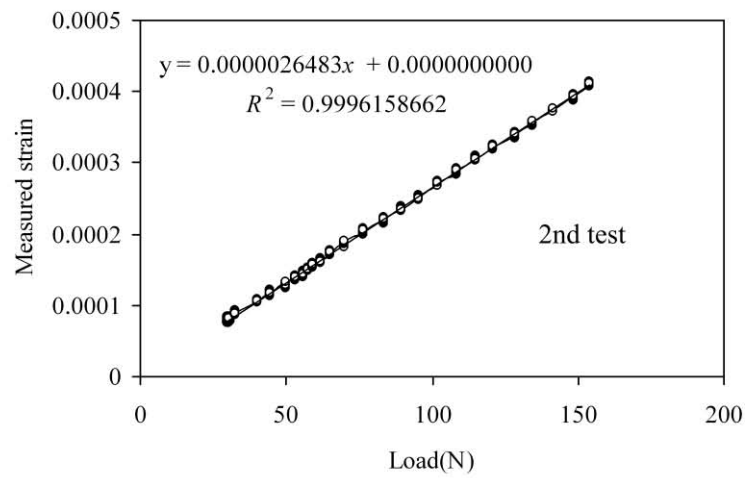


(c)

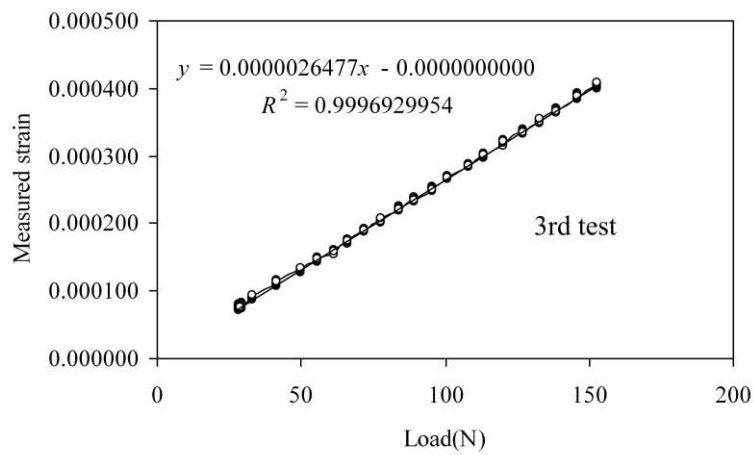
Figure 6.28 Measured strain (ϵ_{aa}) at $r_1 = 7$ mm for $a/b = 0.693$ for all the three repeated tests



(a)



(b)



(c)

Figure 6.29 Measured strain (ϵ_{ad}) at $r_2 = 27$ mm for $a/b = 0.693$ for all the three repeated tests

Tables 6.17 and 6.18 show the measured strains obtained from the best-fit equations for different values of applied loads for $a/b = 0.693$ and for the strain gages located at $r_1 = 7$ mm and $r_2 = 27$ mm . Using these strain values and material properties (E and ν) in Eq. (3.30), the experimental values of K_I have been computed corresponding to different load values. Normalized SIF is then computed using the experimental values of K_I by employing Eq. (6.1). Both K_I and F_I for different loads are also listed in Table 6.17 and 6.18.

Table 6.17 Variation of experimental values of K_I and F_I at $r_1 = 7$ mm with the applied load in the 1st test for $a/b= 0.693$

Load(N)	Measured strain	K_I (MPa $\sqrt{\text{mm}}$)	F_I
50	0.00028201	6.16768065	5.73244048
100	0.00056401	12.33536130	5.73244048
150	0.00084602	18.50304195	5.73244048
200	0.00112802	24.67072260	5.73244048
250	0.00141003	30.83840325	5.73244048
300	0.00169203	37.00608391	5.73244048

Table 6.18 Variation of experimental values of K_I and F_I at $r_2 = 27$ mm with the applied load in the 1st test for $a/b= 0.693$

Load(N)	Measured strain	K_I (MPa $\sqrt{\text{mm}}$)	F_I
50	0.00012208	5.24375573	4.87371499
100	0.00024416	10.48751147	4.87371499
150	0.00036624	15.73126720	4.87371499
200	0.00048832	20.97502293	4.87371499
250	0.0006104	26.21877866	4.87371499
300	0.00073248	31.46253440	4.87371499

It could be observed from these tables that while K_I is increasing with the increase in applied load, F_I remains constant irrespective of the applied load as expected. Table 6.19 shows the experimental values of F_I obtained at r_1 and r_2 for each of the three repeated experiments for $a/b = 0.693$ and the average values of F_I . It could be observed that in all the three tests at a given location (r_1 or r_2) F_I values are very close to each other showing the precision of the experimental results.

Table 6.19 Experimental values of F_I for three repeated tests for $a/b = 0.693$

Test	F_I	
	at $r_1 = 7$ mm	at $r_2 = 27$ mm
1	5.73244048	4.87371499
2	6.28870095	5.28631201
3	6.08329215	5.28511435
Average	6.0348112	5.14838045

Table 6.20 shows comparison of the average F_I obtained from the present experiments for $a/b = 0.693$ (Table 6.19) at both the locations of strain gages (r_1 and r_2) with the reference solution obtained from ANSYS (Table 6.5) in terms of the % relative error in experimental values of F_I .

Table 6.20 Comparison of experimental values of F_I for $a/b=0.693$ with the reference solution ($r_{\max} = 8.25$ mm)

Locations	F_I		% Relative Error
	Reference solution (Table 6.5)	Experimental value	
Optimal ($r_1 = 7$ mm $< r_{\max}$)		6.0348112	1.72
Non optimal ($r_2 = 27$ mm $> r_{\max}$)	6.140603	5.1483805	16.16

It could be observed from these results that the % relative error in F_I at the selected optimal location $r_1 (< r_{\max})$ is only 1.72% while that based on the strain gage reading at the non-optimal location $r_2 (> r_{\max})$ is as high as 16.16%. These experimental observations once again concretely substantiates the theoretical basis of the proposed numerical approach and verify the existence and importance of r_{\max} in deciding the optimal strain gage location for accurate determination of mode I SIF.

6.3.5 Experimental results for verification of optimal strain gage locations in mixed mode I/II

Here mixed mode SIFs, K_I and K_{II} have been determined based on the proposed modified DB technique with strain gages in order to verify the optimal strain gage locations for mixed mode specimens. These experiments also demonstrate the efficacy of the proposed modified DB technique in experimental determination of mixed mode SIFs. As stated earlier, unlike mode I experiments, only one mixed mode specimen with $a/b = 0.497$ has been employed for experiments under mixed mode loading. Fig. 6.30 shows photograph of the mixed mode specimen made of PMMA along with the strain gages pasted on it at the selected radial locations along both the positive and negative gage lines. The specimen in the above figure conforms to the dimensions shown in Fig. 6.1(b) and in Table 6.3.

As the same PMMA sheet is used for mode I and mixed mode specimens, the material properties of PMMA are therefore $E = 2917\text{MPa}$ and $\nu = 0.382$ (Table 6.7) for the mixed mode specimen. Corresponding to $\nu = 0.382$, the angle of orientation of the positive gage line is $\theta^+ = 53.13^\circ$ and that of negative gage line $\theta^- = -53.13^\circ$. The value of strain gage orientation angle $\alpha^+ = 58.28^\circ$ and $\alpha^- = -58.28^\circ$. As shown in Fig. 6.30 six strain gages have been pasted along the positive gage line and another six strain gages have been pasted along the negative gage line maintaining the proper orientation of α^+ and α^- respectively (see also Fig. 3.7).

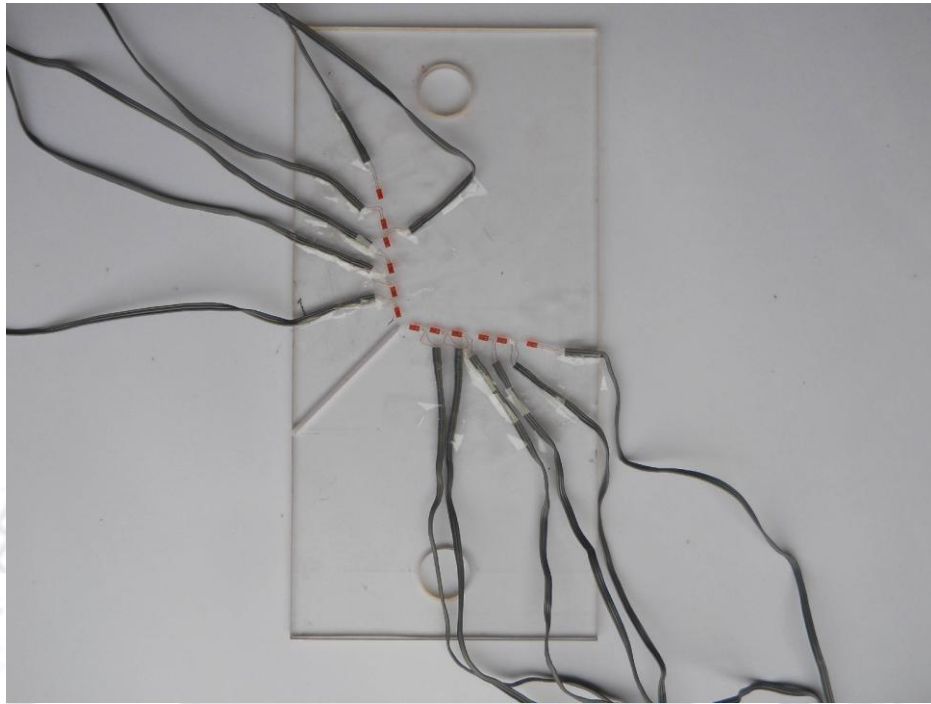


Figure 6.30 Photograph of mixed mode specimen

According to the proposed approach for optimal gage location, the strain gages should be located in the range $t/2 < r < r_{\max}$ along both the gage lines to get the accurate values of SIFs. Strain gages located beyond the r_{\max} will lead to highly erroneous experimental values of SIFs (K_I and K_{II}) and these are non-optimal locations as per the proposed approach. In conforming to the proposed modified DB technique, corresponding strain gages along the positive and negative gage lines are pasted at same radial distance from the crack tip as shown in Fig. 6.30. Table 6.21 shows the selected radial locations for six strain gages each gage line based on the above criteria. For the selected mixed mode specimen, the value of r_{\max} obtained from the proposed method was 29.27 mm (section 3.5). Therefore, along the positive gage line three strain gages are pasted at $r_1 = 6$ mm, $r_2 = 16$ mm and $r_3 = 27$ mm which are within the $r_{\max} = 29.27$ mm and other three strain gages are pasted at $r_4 = 40$ mm, $r_5 = 50$ mm and $r_6 = 65$ mm which are beyond $r_{\max} = 29.27$ mm. Similarly, six strain gages are also pasted along the negative gage line at the same radial locations ($r_1, r_2,$

r_3 , r_4 , r_5 and r_6) from the crack tip as in case of positive gage line. Referring to Table 6.21, three gages at optimal locations and other three gages at non optimal locations are intentionally chosen to verify the importance of optimal strain gage locations in terms of experimentally evaluated values of K_I and K_{II} .

Table 6.21 Selected radial locations of strain gages for SECP specimen ($r_{max} = 29.27$ mm)

Gage line	r_1 (mm)	r_2 (mm)	r_3 (mm)	r_4 (mm)	r_5 (mm)	r_6 (mm)
Positive	6	16	27	40	50	65
Negative	6	16	27	40	50	65

After pasting the strain gages (Fig. 6.30), their precise locations and orientations have been verified using profile projector. It should be noted that in the present investigation, the experiments have been repeated six times on the same mixed mode specimen to ensure the repeatability of results and in all these repeated tests, the magnitude of load applied on the specimen is kept well below the critical load for fracture. Further, foot corrections have been done by subtracting the strain value corresponding to zero load from all the measured strain readings in all repeated mixed mode experiments.

Figs. 6.31(a)-(f) show the raw data of measured strains ε_{aa} (circled data points) at the gage location r_1 on the positive gage line versus the applied load for all the six repeated tests. Figs. 6.31(a)-(f) also show the best-fit straight lines to the raw data (solid lines in plots), along with the corresponding slopes and the correlation coefficients R^2 .

As expected, in all the repeated tests the measured strains are linearly proportional to the applied loads as shown in the Figs. 6.31(a)-(f) with almost same slopes in each test which again reinforces the good calibration of the entire experimental setup.

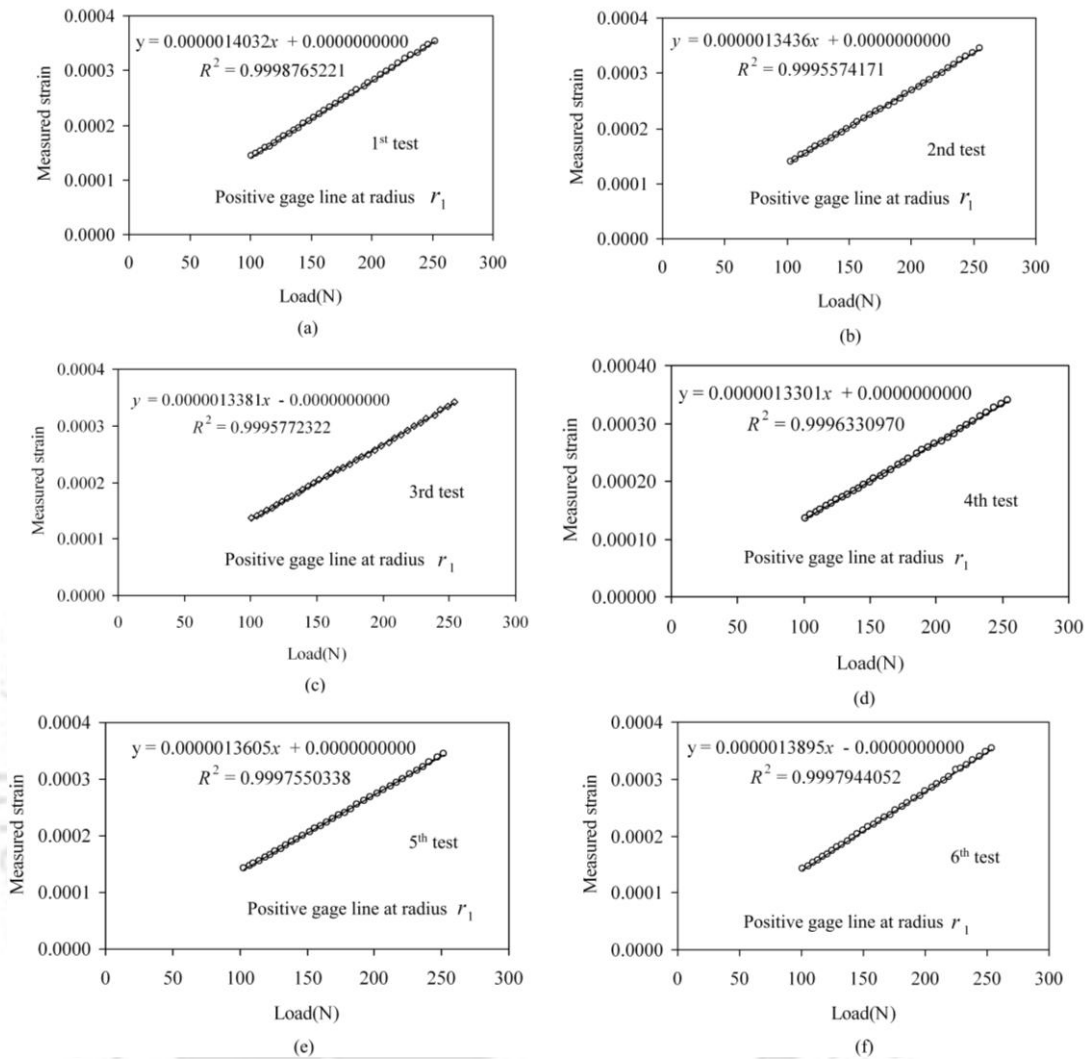


Figure 6.31 Measured strains (ϵ_{aa}) at r_1 on the positive gage line versus applied load for all the six repeated tests

Figs. 6.32 (a) – (e) show raw data of measured strain ϵ_{aa} along the positive gage line versus applied load at other five locations viz. $r_2 = 16$ mm, $r_3 = 27$ mm, $r_4 = 40$ mm, $r_5 = 50$ mm and $r_6 = 65$ mm respectively corresponding to first test. The best-fit lines to the raw data (solid lines) along with the corresponding slopes and R^2 values are also shown in this Figs.6.32 (a) – (e).

It may be noticed from Fig. 6.32 that at all the locations a perfect linear trend between the measured strain and applied load has been observed as expected. Even

though at all these locations strain ε_{aa} have been recorded during the six repeated tests, only data corresponding to 1st test have been presented in Fig. 6.32. It is worth mentioning that excellent repeatability has been observed at all these strain gage locations from all the six tests.

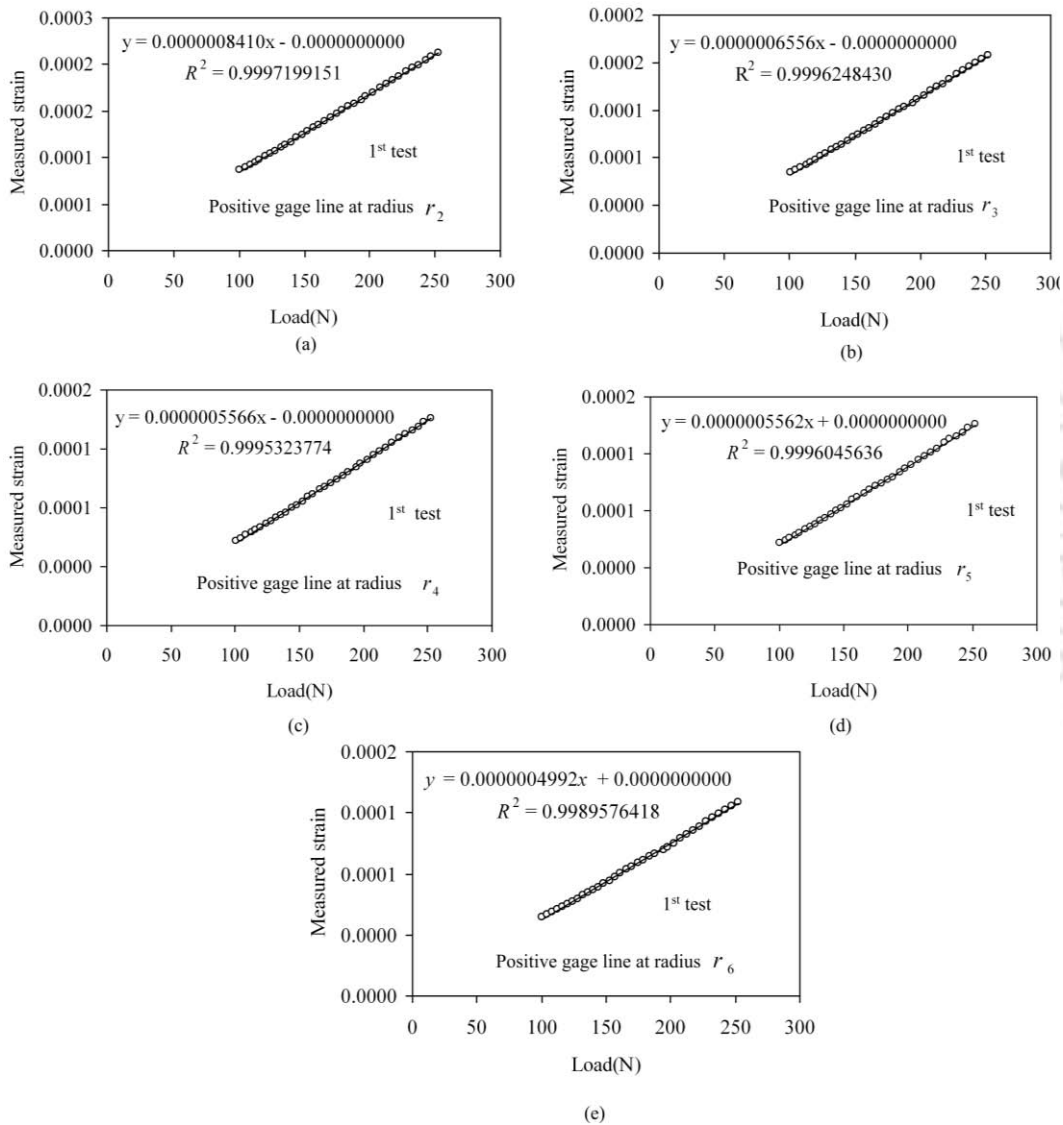


Figure 6.32 Measured strain (ε_{aa}) versus applied load at different radii r_2 to r_6 on the positive gage line for the 1st test

Similarly, Figs. 6.33(a)-(f) show the raw data of measured strain ε_{bb} (circled data points) for the gage location at $r_1 = 6$ mm versus applied load for all the six tests

along the negative gage line. Figs. 6.33 (a)-(f) also show the best-fit straight lines to the raw data (solid lines) with the corresponding slopes and the correlation coefficient R^2 .

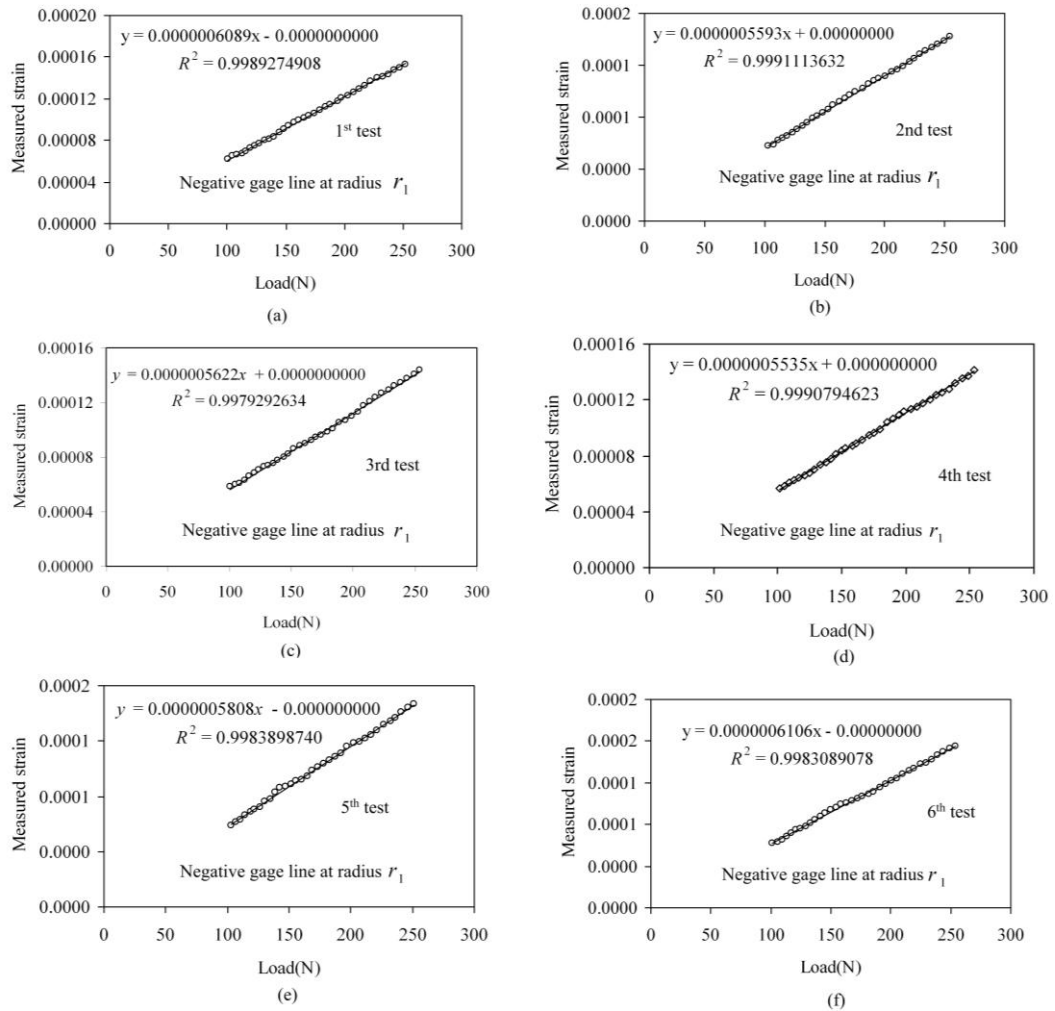


Figure 6.33 Measured strains (ϵ_{bb}) at r_1 on the negative gage line versus applied load for all the six repeated tests

As expected in all the repeated tests, the measured strains ϵ_{bb} are linearly proportional to the applied load with almost same slopes of best-fit lines which again reinforces the perfect calibration of the entire experimental setup.

Figs. 6.34 (a)-(e) show a typical raw data of measured strain ϵ_{bb} (circled data points) along negative gage line versus applied load at other five locations viz. $r_2 = 16$

mm, $r_3 = 27$ mm, $r_4 = 40$ mm, $r_5 = 50$ mm and $r_6 = 65$ mm respectively for the 1st test. The best-fit lines (solid lines) to the raw data along with the corresponding slopes and R^2 values are show in the Figs.6.34 (a)-(e).

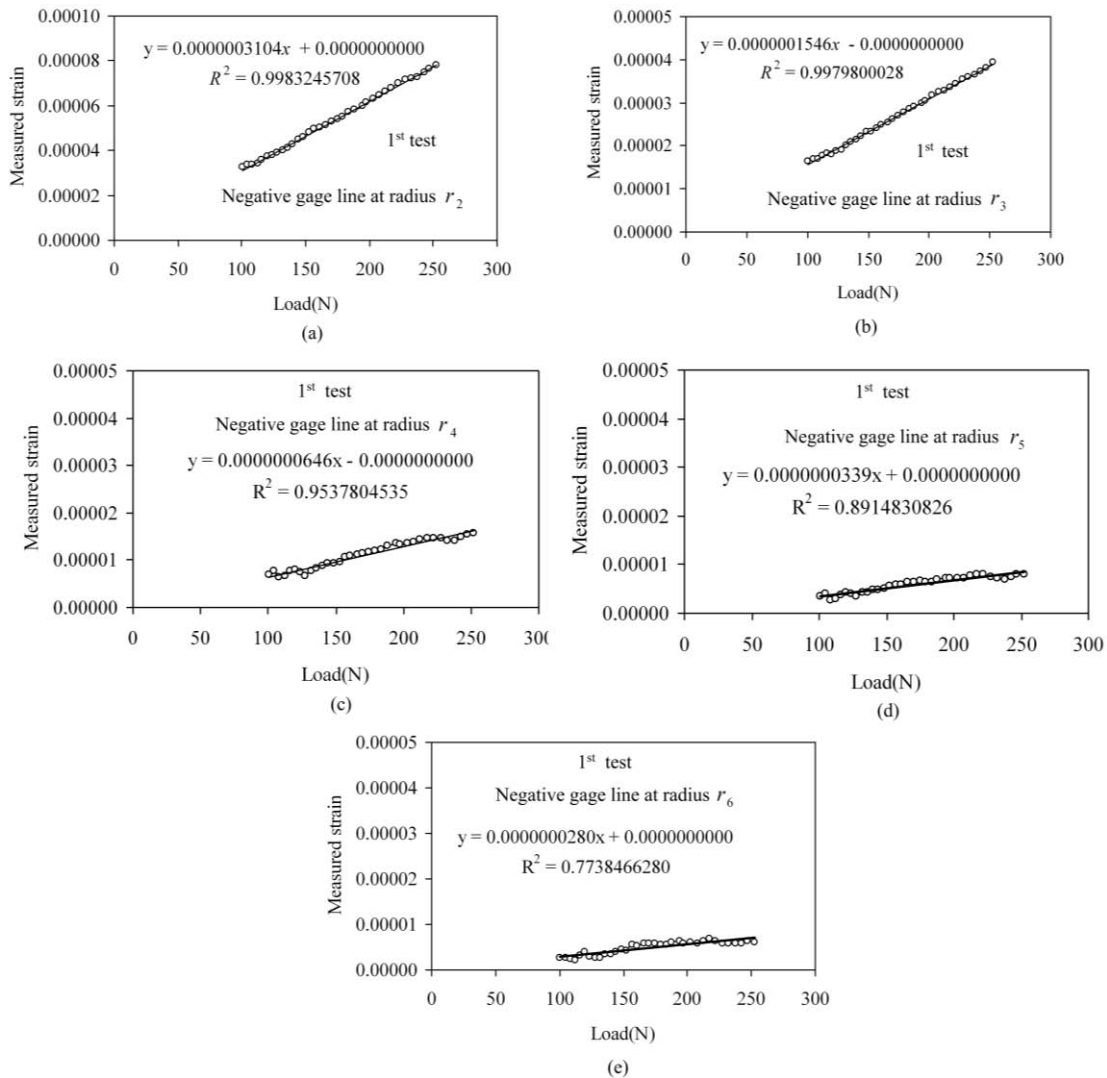


Figure 6.34 Measured strain (ε_{bb}) versus applied load at different radii r_2 to r_6 on the negative gage line for the 1st test

It may be noticed that in all the Figs. 6.34 (a)-(e), an excellent linear trend between the measured strain and the applied load has been observed as expected. It should be noted that even though at all these locations strains ε_{bb} have been recorded during the six repeated tests, only the data corresponding to one typical test (1st test) have been

presented in Fig. 6.34. It is worth mentioning that excellent repeatability has been observed at all these locations from all the six tests.

The following paragraphs demonstrates the existence and importance of optimal strain gage locations using the results obtained from a typical test out of six repeated tests. It should be noted that similar trends and conclusions (which will be demonstrated in the following paragraphs) have also been noticed in all other five repeated tests and hence the in-depth discussion of results of remaining five tests are not presented in this chapter.

Fig. 6.35 shows the variation of measured strains with the radial distance from the crack tip along the positive and negative gage lines for a typical slope. It can be observed from Fig. 6.35 that the magnitude of strain is decreasing with the increasing radial distance from the crack tip as expected. This is true for strain along both the gage lines. It is also observed that magnitude of strains at all the radial locations along with the negative gage line are less than those at the corresponding locations along the positive gage line. In fact, along the negative gage line, the strain gage readings at the farthest location (r_6) from the crack tip approaches to zero. This is also observed for all the loads in Fig.6.34. The above observations further substantiates the goodness of calibration of the entire experimental setup.

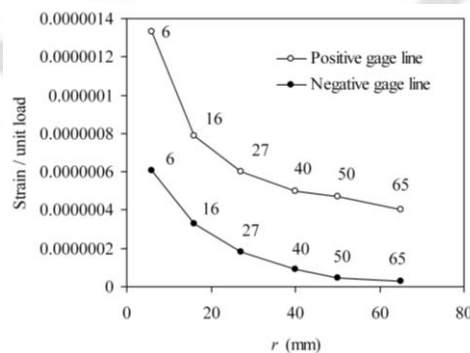


Figure 6.35 Variation of measured strains (ε_{aa}) and (ε_{bb}) with the radial distance from the crack tip

As described earlier the measured strain data at three strain gages on the positive gage line and the data at three corresponding strain gages (which are located at the same

radial distance as that on the positive gage line) on the negative gage line are essential for determination of K_I and K_{II} using the proposed modified DB technique. In the present investigation, these experimentally determined K_I and K_{II} values have been used for demonstration of importance of optimal strain gage locations. Since three strain gages along the positive and negative gage line are required to determine experimentally the mixed mode SIFs, in the present experiment, different combinations of three strain gages have been used in order to demonstrate the importance of optimal strain gage locations. Combinations used are listed in Table 6.22.

Table 6.22 Different combinations of strain gages for determination of mixed mode SIFs

Scheme	Three gage locations on the positive gage line	Three gage locations on the negative gage line
1	r_1, r_2, r_3	r_1, r_2, r_3
2	r_2, r_3, r_4	r_2, r_3, r_4
3	r_3, r_4, r_5	r_3, r_4, r_5
4	r_4, r_5, r_6	r_4, r_5, r_6

In the selected combinations, the first scheme consists of all the three strain gages (along positive and negative gage lines) that are within the r_{\max} ($r_{\max} = 29.27$ mm as determined in section 6.3.2) i.e., all the strain gage locations r_1, r_2 and r_3 are optimal locations with reference to Table 6.22. However, in the second scheme two strain gages at r_2 and r_3 are optimal gage locations and third gage location is a non-optimal location r_4 . In the third scheme, the strain gage at r_3 ($= 27$ mm) is the only gage located optimally (i.e. within the r_{\max}) whereas the other two strain gages at r_4 and r_5 are located at non-optimal locations (i.e. beyond r_{\max}). This scheme is intentionally considered to demonstrate the penalty of placing two out of three strain gages in non-optimal locations (beyond r_{\max}) in determination of mixed mode SIFs. Finally, the fourth scheme consists of all the three strain gages that are located at non-optimal locations (beyond r_{\max}) to show the consequence of placing all the three strain gages

beyond the r_{\max} in terms of error in experimentally determined values of the mixed mode SIFs. This may most likely arise in case where the experimentalist decides the strain gage locations without having any prior knowledge of r_{\max} .

Following the procedure for experimental determination of K_I and K_{II} using the proposed modified DB technique (section 3.5), the value of $0.5653(E\varepsilon_{aa} + E\varepsilon_{bb})\sqrt{r}$ (Eq. (3.61)) and $0.7533(E\varepsilon_{aa} - E\varepsilon_{bb})\sqrt{r}$ (Eq. (3.62)) have been obtained from the strain gage readings for all the schemes presented in Table 6.22. Fig. 6.36(a) shows the measured data of LHS of Eq. (3.61) i.e., $0.5653(E\varepsilon_{aa} + E\varepsilon_{bb})\sqrt{r}$ (circled data points) versus radial distance of strain gages r and Fig. 6.36(b) shows the measured data of LHS of Eq. (3.62) i.e., $0.7533(E\varepsilon_{aa} - E\varepsilon_{bb})\sqrt{r}$ versus r for the gages in scheme 1.

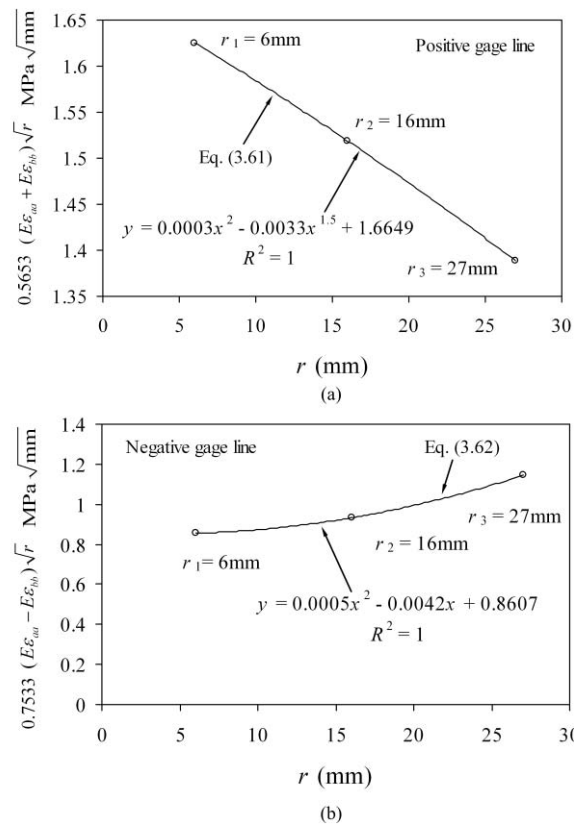


Figure 6.36 Scheme 1: (a) determination of A_0, A_2 and B_1 using the best-fit linear regression (b) determination of C_0, C_1 and C_2 using the best-fit linear regression

Fig. 6.37(a) shows the measured data $0.5653(E\varepsilon_{aa} + E\varepsilon_{bb})\sqrt{r}$ (circled data points) versus r and Fig. 6.37(b) shows the measured data $0.7533(E\varepsilon_{aa} - E\varepsilon_{bb})\sqrt{r}$ (circled data points) versus r for the gages in scheme 3.

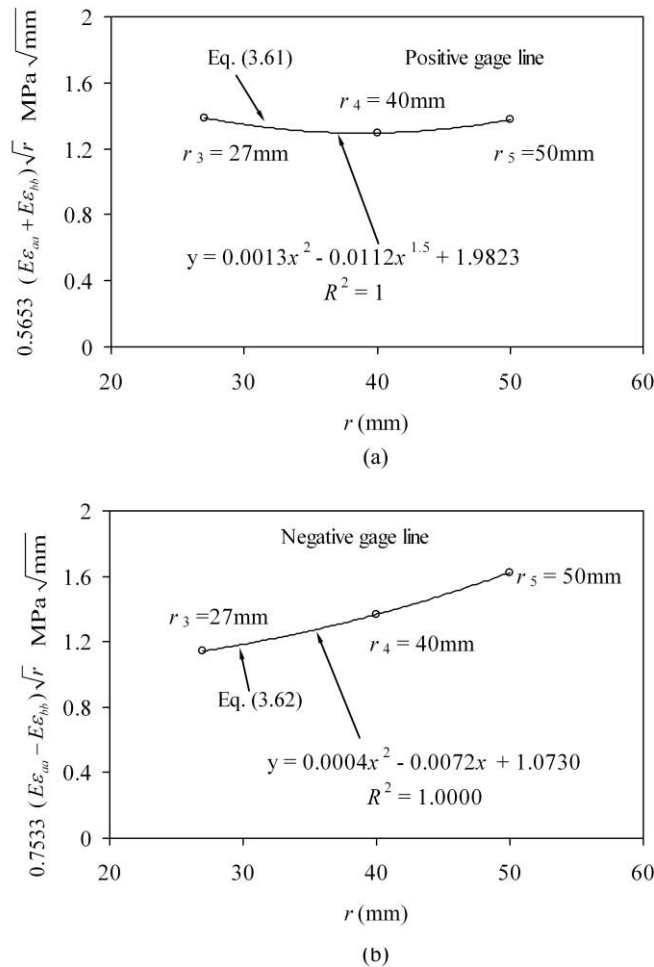


Figure 6.37 Scheme 2: (a) determination of A_0 , A_2 and B_1 using the best-fit linear regression (b) determination of C_0 , C_1 and C_2 using the best-fit linear regression

Similarly, Fig. 6.38(a) and Fig. 6.38(b) shows $0.5653(E\varepsilon_{aa} + E\varepsilon_{bb})\sqrt{r}$ versus r and $0.7533(E\varepsilon_{aa} - E\varepsilon_{bb})\sqrt{r}$ versus r respectively for scheme 4. It should be noted that all the measured data presented in Figs. 6.36-6.38 (circled data points) have been obtained for a typical load of 200 N. According to the proposed modified DB technique (section 3.5), curve of the form $A_0 + \beta_1 A_2 r^2 + \beta_2 B_1 r^{3/2}$ (RHS of Eq.

(3.61)) have been best-fitted to the measured quantity $0.5653(E\varepsilon_{aa} + E\varepsilon_{bb})\sqrt{r}$ in each scheme as shown (with solid lines) in Figs. 6.36(a)-6.38(a). These best-fit curves (solid lines) along with the best-fit coefficients (A_0, A_2 and B_1) are shown in Fig. 6.36(a), Fig. 6.37(a) and Fig. 6.38(a) for scheme 1, scheme 3 and scheme 4 respectively. Similarly, curve of the form $C_0 + \delta_1 C_1 r + \delta_2 C_2 r^2$ (RHS of Eq. (3.62)) have been best-fitted to the measured quantity $0.7533(E\varepsilon_{aa} - E\varepsilon_{bb})\sqrt{r}$ in each scheme as shown (with solid lines) in Figs. 6.36(b)-6.38(b). These best-fit curves (solid lines) along with the best-fit coefficients (C_0, C_1 and C_2) are also shown in Fig. 6.36(b), Fig. 6.37(b) and Fig. 6.38(b) for scheme 1, scheme 3 and scheme 4 respectively.

Using the best-fit coefficients A_0 and C_0 (shown in Figs. 6.36-6.38) the mixed mode SIFs K_I and K_{II} have been determined using Eq. (3.64) for all the schemes at a typical applied load of 200 N. The normalized SIFs F_I and F_{II} are then determined using the above experimental values of K_I and K_{II} by employing Eq. (6.1). Table 6.23 shows experimental values of $A_0, C_0, K_I, K_{II}, F_I$ and F_{II} for all the schemes for a typical load of 200 N. It could be observed from this table that there is a substantial difference in the values of both F_I and F_{II} obtained from the different schemes.

The results in Table 6.23 correspond to the applied load of 200 N. Similar exercise has been carried out for different applied loads for all the four schemes. For example, Table 6.24 shows the values of $A_0, C_0, K_I, K_{II}, F_I$ and F_{II} for different values of applied loads using the experimental data in Fig. 6.36 corresponding to the scheme 1.. The results in Table 6.24, clearly shows invariance of F_I and F_{II} with the applied load and increase in K_I and K_{II} with the increase in load as expected. Similar trends have been obtained for remaining three schemes also.

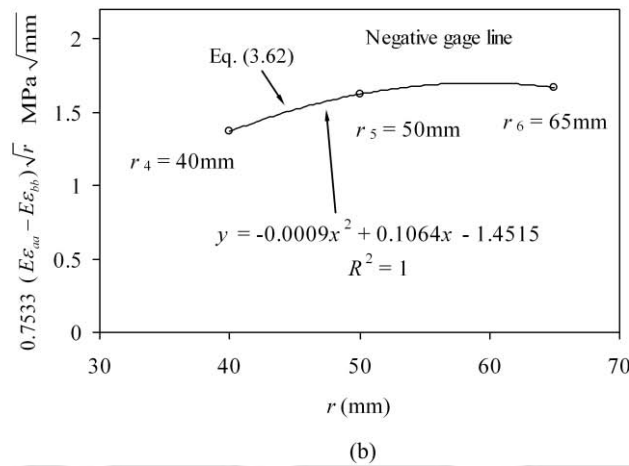
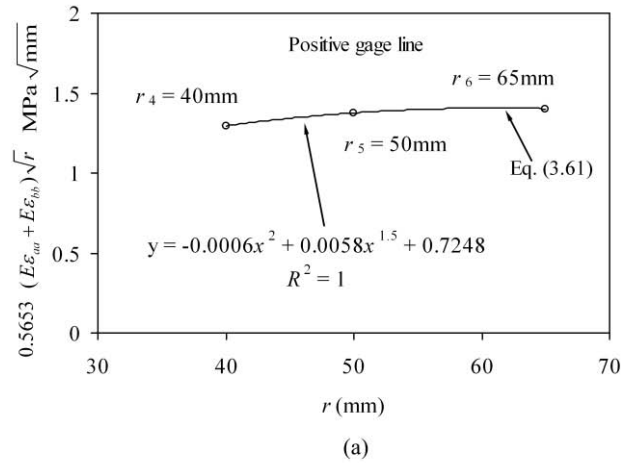


Figure 6.38 Scheme 3: (a) determination of A_0 , A_2 and B_1 using the best-fit linear regression
(b) determination of C_0 , C_1 and C_2 using the best-fit linear regression

Table 6.23 Experimental values of SIFs and normalized SIFs of all the schemes (1st test at load=200N)

Scheme	A_0 (MPa $\sqrt{\text{mm}}$)	C_0 (MPa $\sqrt{\text{mm}}$)	K_I (MPa $\sqrt{\text{mm}}$)	K_{II} (MPa $\sqrt{\text{mm}}$)	F_I	F_{II}
r_1, r_2, r_3	1.6649	0.8607	4.1732	2.1575	1.1457	0.5923
r_2, r_3, r_4	1.7101	0.5889	4.2865	1.4762	1.1768	0.4052
r_3, r_4, r_5	1.9823	1.0730	4.9689	2.6896	1.3641	0.7383
r_4, r_5, r_6	0.7248	-1.4515	1.8167	-3.6384	0.4987	-0.9989

Table 6.24 Experimental values of SIFs and normalized SIFs for the gage locations in scheme 1 (r_1, r_2, r_3) at different loads

Load (N)	A_0 (MPa $\sqrt{\text{mm}}$)	C_0 (MPa $\sqrt{\text{mm}}$)	K_I (MPa $\sqrt{\text{mm}}$)	K_{II} (MPa $\sqrt{\text{mm}}$)	F_I	F_{II}
100	0.832	0.430	2.087	1.079	1.146	0.592
150	1.249	0.646	3.130	1.618	1.146	0.592
200	1.665	0.861	4.173	2.157	1.146	0.592
250	2.081	1.076	5.217	2.697	1.146	0.592

As mentioned earlier, for all the schemes, tests for determination of mixed mode SIFs have been repeated six times in order to ensure the repeatability of the test results. Table 6.25 shows F_I and F_{II} obtained from all the six tests corresponding to scheme 1.

Table 6.25 Experimental values of F_I for all repeated tests corresponding to scheme 1

Tests	F_I	F_{II}
1	1.1457	0.5923
2	1.0863	0.5668
3	1.0924	0.5898
4	1.0750	0.5946
5	1.1033	0.5728
6	1.1299	0.5830

Results in this Table 6.25 shows that excellent repeatability experimental values of F_I and F_{II} from all the six tests performed due to the excellent repeatability of the measured strains. Similar extent of repeatability in F_I and F_{II} has also been observed in scheme 2, scheme 3 and scheme 4 also. Finally, Table 6.26 summarizes results obtained using the experimental data corresponding to a typical test out of the six

repeated tests on the mixed mode specimen. This table shows the comparison of experimentally obtained values of F_I and F_{II} with the reference solutions (obtained using the displacement extrapolation technique of ANSYS). Table 6.26 also shows the % relative error (computed using Eq. (6.2)) in the experimentally obtained normalized mixed mode SIFs F_I and F_{II} for all the four schemes.

Table 6.26 Comparison of experimental values of F_I and F_{II} with the reference solutions

Scheme	Strain gage locations	Reference solution		Experimental values		% Relative Error	
		F_I Eq.(6.3)	F_{II} Eq.(6.3)	F_I	F_{II}	F_I	F_{II}
1	r_1, r_2, r_3	1.1307	0.5951	1.1457	0.5923	1.33	0.47
2	r_2, r_3, r_4			1.1768	0.4052	4.08	31.91
3	r_3, r_4, r_5			1.3641	0.7384	20.64	24.08
4	r_4, r_5, r_6			0.4987	-0.9989	55.89	267.85

From the results in Table 6.26, it could be observed that % relative error in normalized SIFs is only 1.33% for F_I and only 0.47 % for F_{II} in scheme 1 in which all the strain gages are optimally placed. In scheme 2, where two out of three strain gages placed at optimal locations, the % relative error in F_I increases to 4.08 % and 31.91% in F_{II} thus showing effect of non-optimal placement of even a single strain gage on accuracy of measured SIFs. On the other hand, in scheme 3 where two out of three strain gages are placed at non-optimal locations, the % relative error increases to 20.64% in F_I and 24.08% in F_{II} thus showing the effect of non-optimal placement of two strain gages. In the fourth scheme where all the three strain gages are placed non-optimally, the % errors in F_I and F_{II} are as high as 55.89% and 267.85% respectively.

Results in Table 6.26 clearly shows that the % relative error in normalized SIFs obtained using the proposed modified DB technique is negligibly small in

scheme 1. This is because, in the scheme 1, all the strain gages on both the positive and negative gage lines have been located at optimal positions decided by the r_{\max} value obtained using the proposed numerical approach presented in section 3.5. On the other hand, large % relative errors in normalized SIFs obtained in the scheme 3 indicates that these normalized SIFs are unacceptable as compared to that obtained in the scheme 1. This is because, even though one of the strain gages were placed optimally, the fact that the other two strain gages were pasted at non-optimal locations in the scheme 3 lead to such a large error compared to that in the scheme 1. This was expected, as all these strain gage readings (along positive and negative gage lines) contribute to the evaluation of K_I and K_{II} as per the proposed approach but in this case only one strain gage was optimally located. In scheme 4, the % relative errors in normalized SIFs are so high that the experimental values of normalized SIFs are nowhere near the actual values for this experimental configuration and are highly erroneous values. This is because no strain gages were optimally placed in the scheme 4.

All these experimental results in Table 6.26 undoubtedly substantiates the importance of knowing apriori r_{\max} value of specimen for experimental determination of accurate values of the mixed mode SIFs K_I and K_{II} . These results also show what might happen when the strain gages are placed at non-optimal locations due to no prior knowledge of r_{\max} (which is required to decide optimal strain gage locations according to the present work) leading to highly erroneous values of SIFs.

6.4 Summary

In this chapter an experimental setup was made for verification of the developed method for determination of r_{\max} values and hence optimum gage locations. Different specimens were made to carry out mode I and mixed mode (I/II) testing for determination of SIFs using strain gages. In this, PMMA has been used as material for all the specimens. Material properties of the PMMA have been determined experimentally. For mode I testing, specimens having $a/b = 0.293, 0.493$

and 0.693 have been prepared and for mixed mode $a/b = 0.497$ has been prepared. Before conducting experiments, for all these specimens r_{\max} values have been determined using the present method by carrying out FEA using ANSYS. Depending upon these r_{\max} values, strain gages were pasted at locations within the r_{\max} and at locations beyond the r_{\max} to study the importance of the r_{\max} and efficacy of the present method.

Strains at different locations have been recorded from the strain gage readings. Experiments have been repeated number of times and a good repeatability was obtained. Based on these strain readings normalized SIFs have been calculated. It was observed that for mode I, normalized SIF calculated using strain gage placed within the r_{\max} showed a very good agreement with the reference normalized SIF value, where as the normalized SIF calculated using the strain gage readings placed beyond the r_{\max} showed an error in normalized SIF as high as 20.9 % in mode I loading. In case of mixed mode loading, to study the effect of r_{\max} on normalized SIF three strain gages were pasted within the r_{\max} and three strain gages pasted beyond the r_{\max} on the positive gage line. Similarly, on the negative gage line three strain gages were pasted at locations within the r_{\max} and three pasted at locations beyond the r_{\max} .

The normalized SIFs have been calculated considering three strain gage readings of positive gage line within r_{\max} and three strain gage readings of negative gage line within r_{\max} as per the proposed theory. Results showed that the % relative error is very low when compared with the reference solutions obtained using ANSYS. But, when two strain gages are at the optimal locations and one at non-optimal location on both positive and negative gage lines or one strain gage located within the r_{\max} and two strain gages located beyond the r_{\max} on both positive and negative gage lines or when all the three strain gages located beyond the r_{\max} on both positive and negative gage lines the % relative error as high as 267.85% was obtained. Undoubtedly, it substantiates the importance of knowing r_{\max} value for experimental determination of SIFs.

Chapter 7

Conclusions and Scope for the Future Work

In the present work an attempt has been made for the first time to solve an important issue in experimental fracture mechanics in terms of deciding valid strain gage locations a priori for accurate determination of SIFs in mode I and mixed mode I/II loading conditions using DS technique and modified DB technique respectively. Experimental verification of the proposed theory and methodologies has also been carried out in the present investigation. Conclusions drawn from the present work have been categorized as *general conclusions* and *specific conclusions*.

7.1 General conclusions

- 1 A robust and reliable methodology has been developed for estimating the r_{\max} which is the upper bound on valid or optimal strain gage locations for determination of static mode I and mixed mode SIFs in case of homogeneous and isotropic materials.
- 2 The numerical methodology developed for determination of r_{\max} for mode I is supported by strong theoretical background where the generalized Westergaard formulation has been used along with the DS technique and finite element analysis.
- 3 A modification to the DB technique has been proposed for accurate determination of mixed mode SIFs and a numerical methodology developed for determination of r_{\max} supported by strong theoretical formulation based on the generalized Westergaard theory and the proposed modified DB technique along with finite element analysis.
- 4 The methods thus developed have been used to determine the r_{\max} values of different cracked configurations of both mode I and mixed mode I/II

- configurations. In each of these cases appropriate mesh refinement studies have been carried out and the convergence of r_{\max} value has been achieved.
- 5 Effect of different important parameters on the r_{\max} value has been studied using these methods for different cracked configurations and their influences have been explained on the basis of theoretical developments.
 - 6 To assess the impact of optimal and non-optimal strain gage locations on experimental determination of SIF values, experimental setups have been designed for both mode I and mixed mode I/II loading conditions.
 - 7 Comparison of experimentally determined SIF values obtained using the strain gages located at different locations substantiates the importance of placing strain gages with the r_{\max} for accurate determination of SIFs in both mode I and mixed mode I/II loading conditions.
 - 8 From the view point of practical importance, the methodologies developed in the present work (supported by experiments) could be used to recommend valid or optimal strain gage locations apriori for experimental determination of SIFs. This will be of immense help to experimentalist in fracture mechanics as such a recommendation apriori was not available till date.

7.2 Specific conclusions

7.2.1 Conclusions based on numerical analysis of mode I configurations

1. Variation of computed strains (in the direction of α , the orientation of the strain gage) along the gage line with the radial distance from the crack tip follows the trend as per the theoretical predictions.
2. Strains (in the direction of α , the orientation of the strain gage) along the gage line always follows the square root singularity only upto the extent of validity of three parameter zone from the crack tip i.e., r_{\max} for all mode I configurations studied.

3. The results of the present investigation clearly show that determination of the upper bound of valid strain gage locations (r_{\max}) is the solution to the determination of the optimal radial locations for strain gages in experimental determination of mode I SIF.
4. Critical numerical examination of the present work shows that the proposed method could accurately determine the theoretically acceptable values of r_{\max} for cracked configurations under mode I loading.
5. The r_{\max} values of the configurations under mode I loading conditions converge to the theoretically acceptable values as the finite element meshes are refined
6. The r_{\max} is found to be dependent on the ratio of crack length (a) to width (b) of the specimen.
7. At lower values of a/b the crack length dominates the influence on r_{\max} but at higher values of a/b , the net ligament length ($b-a$) dominates the influence on r_{\max} value for all the mode I configurations studied .
8. State of stress (i.e., plane stress or plane strain) has been observed to have influence on the values of r_{\max} for a given configuration and boundary conditions.
9. For all practical considerations, the Poisson's ratio has no significant influence on the r_{\max} value for a given mode I configuration.

7.2.2 Conclusions based on numerical analysis of mixed-mode configurations

- 1 Variation of computed strains (in the directions of α and $-\alpha$, the orientations of the strain gages along the positive and negative gage lines respectively) with the radial distance from the crack tip follows the trend as per the theoretical predictions upto the extent of the validity of five parameter zone i.e., r_{\max} for all the mixed mode configurations studied.

- 2 The results of the present investigation clearly show that determination of the upper bound of valid strain gages locations (r_{\max}) is the solution to the determination of the optimal radial locations for strain gages in experimental determination of mixed mode I/II SIFs.
- 3 Critical numerical examination of the present work shows that the proposed method could accurately determine the theoretically acceptable values of r_{\max} for all the mixed mode cracked configurations.
- 4 The r_{\max} values of the mixed mode configurations converge to the theoretically acceptable values as the finite element meshes are refined.
- 5 The r_{\max} is found to be dependent on the ratio of crack length (a) to width (b) of the specimen and a trend similar to that observed in the case of mode I loading is also observed for mixed mode loading cases.
- 6 State of stress (i.e., plane stress or plane strain) has been observed to have influence on the values of r_{\max} for a given mixed mode configuration and boundary conditions.

7.2.3 Conclusions based on experiments on mode I configurations

Mode I SIFs have been determined using the readings from the strain gages which are placed at radial distances within the r_{\max} and outside the r_{\max} . The r_{\max} for the experimental specimen have been obtained using the proposed approach. Based on these experimental observations the following important conclusions have been drawn

- 1 A linear trend between the measured strain (in the direction of α , the orientation of the strain gage) and the applied load has been observed each time the test is repeated and for all the mode I configurations ($a/b = 0.293, 0.493$ and 0.693).
- 2 Mode I SIF has been determined using the strain data from all the strain gages for each of the tests and for all the configurations. An excellent repeatability in terms of SIF values has been achieved for all repeated tests.

- 3 Experimentally determined mode I SIF corresponding to all the configurations show excellent agreement with the reference SIF when the strain gages are located at optimal locations (i.e., within the r_{\max}) recommended by the present methodology. On the other hand experimentally determined mode I SIF using the data obtained from strain gage placed outside the r_{\max} (i.e., non-optimal location) shows a very high error. This observation is true for all mode I configurations tested.
- 4 It is observed that placing the strain gages within the r_{\max} leads to very accurate SIF values where the error is as low as 0.18% and placing the strain gages outside the r_{\max} can lead to errors in SIF which is as high as 20.9%.
- 5 Excellent agreement of experimentally determined mode I SIF values with the reference solution once again substantiates the dependence of r_{\max} on a/b as obtained in the numerical studies.
- 6 Results from the present experimental investigation very well substantiate the developed method and the associated theory for determination of optimal strain gage locations in determining mode I SIFs using the DS technique.

7.2.4 Conclusions based on experiments on mixed mode I/II configurations

Proposed modified DB technique has been employed for determination of mixed mode SIFs (K_I and K_{II}) using the readings from the strain gages which are placed at radial distances within the r_{\max} and outside the r_{\max} . The r_{\max} for the experimental specimen has been obtained using the proposed approach. Based on these experimental observations the following important conclusions have been drawn.

- 1 A linear trend between the measured strains (in the directions of α and $-\alpha$, the orientations of the strain gages along the positive and negative gage lines respectively) and the applied load has been observed each time the test is repeated and for all the strain gages on both the gage lines.

- 2 Mixed mode SIFs (K_I and K_{II}) have been determined using the strain data from all the strain gages for each of the six repeated tests and an excellent repeatability in terms of K_I and K_{II} values has been achieved for all tests.
- 3 Experimentally determined K_I and K_{II} show excellent agreement with the reference K_I and K_{II} when the strain gages (on both positive and negative gage lines) are located at optimal locations (i.e., within the r_{\max}) recommended by the present methodology. On the other hand experimentally determined K_I and K_{II} using the data obtained from strain gages (on both positive and negative gage lines) placed outside the r_{\max} (i.e., non-optimal location) show very high errors. This observation is true for all the repeated tests.
- 4 It is observed that placing all the three strain gages within the r_{\max} along both the gage lines leads to very accurate values of K_I and K_{II} with an error of as low as 1.32% in the case of K_I and 0.47% in the case of K_{II} . Even placing one of the three strain gages outside the r_{\max} would result in a high error in SIF values. It has been observed that in an extreme case of placing all three strain gages outside the r_{\max} leads to an error in K_I as high as 55.89% and error in K_{II} which is as high as 267.85%. Even though, placing strain gage at those locations might greatly minimize the three dimensional effects, plasticity effects and strain gradient effects but it leads to completely unacceptable values of SIFs. This once again shows the importance of knowing the valid strain gage locations apriori for experimental determination of SIFs.
- 5 Results from the present experimental investigation very well substantiate the developed method and the associated theory for determination of optimal strain gage locations in determining mixed mode SIFs using the proposed modified DB technique.

- 6 Results from the mixed mode experiments also demonstrates the efficacy of the proposed modified DB technique in determination of mixed mode SIFs K_I and K_{II} .

7.3 Scope for future work

1. Experiments could be performed with the specimen made of metallic materials in order to study the effect of plasticity in determination of SIFs using the strain gages placed at optimal locations.
2. The same methodology could be extended to other important mode I and mixed mode I/II cracked configurations for verification of optimal gage locations.
3. A methodology could be developed for estimation of optimal gage locations for determination of dynamic SIFs.
4. An attempt could be made to develop a methodology for estimation of optimal gage locations for determination of SIFs in orthotropic materials.
5. An investigation (based on the works reported in Ref. [13, 65, 66]) similar to the present one is needed for 2D domains containing very small internal cracks.
6. A further investigation is needed for providing recommendations in the form of r_{\max} as a function of a/b over a large range for different important configurations.

References

- [1] **C. E. Inglis**, Stresses in a plate due to the presence of cracks and sharp corners, *Transactions of the Royal Institute of Naval Architects* (1913), 60, 219–214.
- [2] **A. A. Griffith**, The phenomenon of rupture and flow in solids, *Philosophical Transactions Series A* (1920), 221, 163–198.
- [3] **S. Ya. Yarema**, On the contribution G. R. Irwin to fracture mechanics, *Materials Science* (1995), 31, 617-623.
- [4] **H. M. Westergaard**, Bearing pressures and cracks, *Journal of Applied Mechanics* (1939), 61, 49-53.
- [5] **M. L. Williams**, On the stress distribution at the base of a stationary crack, *Journal of Applied Mechanics*, (1957), 24, 109-114.
- [6] **J. J. Duga, W. H. Fisher, R. W. Buxbaum, A. R. Rosenfield, A. R. Buhr, E. J. Honton, and S.C. McMillan**, The economic effects of fracture in the United States, *Battelles's Columbus Laboratories report to the National Bureau of Standards*, March (1983).
- [7] **G. R. Irwin**, Fracture dynamics, Fracture of metals, *American Society for Metals*, Cleveland (1948), 147–166.
- [8] **Y. Murakami**, *Stress intensity factors handbook*. England: Pergamon, (1987).
- [9] **H. Tada, P. C. Paris and G. R. Irwin**, *The stress analysis of cracks handbook*. New York, ASME, (2000).
- [10] **J. R. Rice**, A path independent integral and the approximate analysis of stress concentration by notches and cracks, *Journal of Applied Mechanics*, Transactions ASME (1968), 379–386.
- [11] **J. R. Rice**, Mathematical analysis in the mechanics of fracture, Fracture A path independent integral and the approximate analysis of stress concentration by notches and cracks, *Journal of Applied Mechanics*, Transactions ASME (1968), 379–386.

-
- [12] **A. A. Wells**, Unstable crack propagation in metals: cleavage and fast fracture, *Proceeding of the Crack Propagation Symposium*, Cranfield, U.K (1961), Paper 84.
- [13] **R. J. Sanford**, *Principles of Fracture Mechanics*, Upper Saddle River, NJ: Prentice Hall, (2003).
- [14] **A. J. Rosakis, A. T. Zehnder** and **R. Narashim**, Caustics by reflection and their application to elastic-plastic and dynamic fracture mechanics, *Optical Engineering* (1988), 27, 596–610.
- [15] **E. A. Patterson** and **E. J. Olden**, Optical analysis of crack tip stress fields: a comparative study, *Fatigue and Fracture of Engineering Materials and Structures*, (2004), 27, 623–635.
- [16] **K. Ravi-chandar**, *Fracture Mechanics*. In: W. N. Sharpe Jr. editor, *Springer Handbook of Experimental Solid Mechanics*, New York, (2008), p. 125-58.
- [17] **G. R. Irwin**, Analysis of stresses and strains near the end of a crack traversing a plate, *Journal of Applied Mechanics* (1957), 24, 361–364.
- [18] **D. Broek**, *Elementary Engineering Fracture Mechanics*, Martinus Nijhoff Publishers, Boston, (1987).
- [19] **S. K. Bhandari**, Etude experimentale du factor d' intensine des contraintes au voisinage de la pointe d' une fissure de fatigue centrale dans une tole mince au moyen des mesures extensometriques, *These, Ecole Nat Superiure de L' Aeronautique*, Paris (1969).
- [20] **Monthulet, S. K. Bhandari** and **C. Riviere**, Methods pratiques de determination du factor d'intensite des contraintes pour la propagation des fissures, *La recherché Aerospatiale* (1971), 297-303
- [21] **J. Rosakis** and **K. Ravi-Chandar**, On crack-tip stress state: An experimental evaluation of three-dimensional effects. *International Journal of Solids and Structures* (1986), 22, 121–134.
- [22] **J. W. Dally** and **R. J. Sanford**, Strain gage methods for measuring the opening mode stress intensity factor, *Experimental Mechanics* (1987), 27, 381–88.

-
- [23] **J. R. Berger** and **J. W. Dally**, An overdeterministic approach for measuring K_I using strain gages. *Experimental Mechanics* (1988) 28, 142–145.
- [24] **J. H. Kuang** and **L. S. Chen**, A single strain gage method for K_I measurement, *Engineering Fracture Mechanics* (1995), 51, 871–878.
- [25] **J. Wei** and **J. H. Zhao**, A two-strain-gage technique for determining mode I stress-intensity factor. *Theoretical and Applied Fracture Mechanics* (1997), 28, 135–140.
- [26] **A. Shukla**, **R. K. Agarwal** and **H. Nigam**, Dynamic fracture studies on 7075-T6 aluminum and 4340 steel using strain gages and photoelastic coating, *Engineering Fracture Mechanics* (1988), 31, 501–515.
- [27] **J. R. Berger**, **J. W. Dally** and **R. J. Sanford**, Determining the dynamic stress intensity factor with strain gages using a crack tip algorithm, *Engineering Fracture Mechanics* (1990), 36, 145–156.
- [28] **J. W. Dally** and **R. J. Sanford**, measuring the stress intensity factors for propagating cracks with strain gages, *Journal of Testing and Evaluation* (1990), 18, 240–249.
- [29] **J. R. Berger** and **J. W. Dally**, A spatially overdetermined analysis for propagation toughness using strain gages. *Mechanics research communication* (1990), 17, 93-99.
- [30] **A. Shukla**, **B. D. Agarwal** and **B. Bhushan**, Determination of stress intensity factor in orthotropic composite materials using strain gages, *Engineering Fracture Mechanics* (1989), 32, 469–477.
- [31] **S. K. Khanna** and **A. Shukla**, Development of stress field equations and determination of stress intensity factor during dynamic fracture of orthotropic composite materials, *Engineering Fracture Mechanics* (1994), 47, 345–59.
- [32] **S. K. Khanna** and **A. Shukla**, On the use of strain gages in dynamic fracture mechanics, *Engineering Fracture Mechanics* (1995), 51,933–948.
- [33] **J. W. Dally** and **D. B. Barker**, Dynamic measurement of initiation toughness at high loading rates, *Experimental Mechanics* (1988), 298–303.

- [34] **L. Parnas, O. G. Bilir and E. Tezcan**, Strain gage methods for measurement of opening mode stress intensity factor. *Engineering Fracture Mechanics* (1996), 55, 485–492.
- [35] **S. Rizal and H. Homma**, Dimple fracture under short pulse loading, *International Journal of Impact Engineering* (2000), 24, 69-83.
- [36] **P. R. Marur, R. C. Batra, G. Garcia and A. C. Loos**, Static and dynamic fracture toughness of epoxy/alumina composite with submicron inclusions, *Journal of Material Science* (2004), 39,1437–1440.
- [37] **M. Kirugulige and H. V. Tippur**, Mixed-mode dynamic crack growth in a functionally graded particulate composite. *Experimental Mechanics* (2006), 46:269-281.
- [38] **S. Shirley and H. Homma**, Approach to dynamic fracture toughness of GFRP from aspect of viscoelastic and debonding behaviors, *Journal of Solid Mechanics and Materials Engineering* (2007), 1, 275–286.
- [39] **S. Swamy, M. V. Srikanth, K. S. R. K. Murthy and P.S. Robi**, Determination of the mode I stress intensity factors of the complex configurations using the strain gages. *Journal of Mechanics of Materials and Structures* (2008), 3, 1239–1255.
- [40] **S. C. Wadgaonkar and V. Parameswaran**, Structure of near-tip stress field and variation of stress intensity factor for a crack in a transversely graded material, *Journal of Applied Mechanics* (2009), 76, 011014-1-011014-9.
- [41] **J. F. Kalthoff and A Burgel**, Influence of loading rate on shear fracture toughness for failure mode transition, *International Journal of Impact Engineering* (2004), 30, 957–971.
- [42] **J. W. Dally and J. R. Berger**, A strain gage method for determining K_I and K_{II} in a mixed mode stress field, *Proceeding of the 1986 SEM Spring Conference Experimental Mechanics* (1986), 603-612.
- [43] **T. Kondo, M. Kobayashi and H. Sekine**, Strain gage method for determining stress Intensities of sharp-notched strips. *Experimental Mechanics* (2001), 41, 1–7.

-
- [44] **A. Dorogoy** and **D. Rittel**, Optimum location of a three strain gauge rosette for measuring mixed mode stress intensity factors, *Engineering Fracture Mechanics* (2008), 75, 4127-4139.
- [45] **V. Ricci**, **A. Shukla** and **R. P. Singh**, Evaluation of fracture mechanics parameters in bimaterial systems using strain gages, *Engineering Fracture Mechanics* (1997), 58, 273–283.
- [46] **P. R. Marur** and **H. Tippur**, A Strain gage method for determination of fracture parameters in bimaterial systems, *Engineering Fracture Mechanics* (1999), 64, 87–104.
- [47] **V. Ricci**, **A. Shukla** and **M. Kavaturu**, Using strain gages to investigate subsonic dynamic interfacial fracture in an isotropic–isotropic bi-material, *Engineering Fracture Mechanics* (2003), 70, 1303–1321.
- [48] **V. Ricci**, **A. Shukla**, **V. Chalivendra** and **K. H. Lee**, Subsonic interfacial fracture using strain gages in an isotropic–orthotropic bi-material. *Theoretical and Applied Fracture Mechanics* (2003), 39,143–161.
- [49] **B. Kaushik**, **K. S. R. K. Murthy** and **P. S. Robi**, Determination of strain gage locations for accurate measurement of the opening mode stress intensity factors. *Journal of Mechanics of Materials and Structures* (2008), 3, 1757–1771.
- [50] **R. J. Sanford**, A critical re-examination of the Westergaard method for solving opening mode crack problems, *Mechanics research communications* (1979), 6, 289-294.
- [51] **J. W. Dally** and **W. F. Riley**, *Experimental stress analysis*. Singapore: McGraw- Hill, (1991).
- [52] **R. S. Barsoum**, On the use of isoparametric finite elements in linear fracture mechanics, *International Journal for Numerical Methods in Engineering* (1976), 10, 25–37.
- [53] **R. D. Henshell** and **K. G. Shaw**, *International Journal for Numerical Methods* (1975), 9, 495-507.

-
- [54] **R. D. Cook**, *Concept and application of finite element analysis*, John Wiley & Sons Inc, Singapore, (2002).
- [55] **R. Chona, G. R. Irwin and R. J. Sanford**, The influence of specimen size and shape on the singularity dominated zone (1983), *ASTM STP 791*, p. I3–I23.
- [56] **M. J. Maleski, M. S. Kirugulige and H. V. Tippur**, A method for measuring mode I crack tip constraint under static and dynamic loading conditions, *Experimental Mechanics* (2004), 44, 522-32.
- [57] **Q. Z. Xiao and B. L. Karihaloo**, Implementation of hybrid crack element on a general finite element mesh and in combination with XFEM, *Computer Methods in Applied Mechanics and Engineering* (2007), 196,1864–1873.
- [58] ANSYS, *Theory reference manual, Release 11*, Swanson Analysis Systems, Inc. (2007).
- [59] **T. M. Maccagno and J. F. Knott**, The fracture behaviour of PMMA in mixed modes I and II, *Engineering Fracture Mechanics* (1989), 34, 65-68.
- [60] **B. Mukherjee and D. J. Burns**, Growth of part through thickness fatigue cracks in sheet Polymethylmethacrylate, *Engineering Fracture Mechanics* (1972), 4, 665-685.
- [61] **F. G. Katsamanis and C. G. Delides**, Fracture surface energy measurements of PMMA, A new experimental approach, *Journal of Physics D, Applied Physics* (1988), 21, 79-86.
- [62] **N. T. Younis and B. Kang**, Averaging effects of a strain gage, *Journal of Mechanical Science and Technology* (2011), 25(1), 163–169.
- [63] **N. T. Younis and J. Mize**, Discrete averaging effects of a strain gage at a crack tip, *Engineering Fracture Mechanics* (1996), 55, 147-153.
- [64] **J. R. Berger and J. W. Dally**, An error analysis for a single strain-gage determination of the stress-intensity factor K_I , *Experimental Techniques* (1988), 12, 31-33.

- [65] **R. J. Sanford** and **B. T. Drude**, Determining the Stress Intensity Factors of Internal Cracks Using Local Collocation, *Proceeding of the SEM Spring Conference Experimental Mechanics* (1993), Bethel, CT.
- [66] **K. Bearden**, **J. W. Dally** and **R. J. Sanford**, Experimental determination of K_I for short internal cracks, *Journal of Applied Mechanics* (2001), 88, 937-943.



List of Publications from this Thesis

International Journals

1. **H. Sarangi, K. S. R. K. Murthy and D. Chakraborty**, Optimum strain Gage location for evaluating stress intensity factors in single and double ended cracked configurations. *Engineering Fracture Mechanics* (2010), 77, 3190- 3203.
2. **H. Sarangi, K. S. R. K. Murthy and D. Chakraborty**, Radial locations of strain gages for accurate measurement of mode I stress intensity factor. *Materials and Design* (2010), 31, 2840-2850.
3. **H. Sarangi, K. S. R. K. Murthy and D. Chakraborty**, Extent of three parameter zone and optimum strain gage location for eccentric cracked configurations, *Applied Mechanics and Materials* (2012), 110-116,127-134.
4. **H. Sarangi, K. S. R. K. Murthy and D. Chakraborty**, Optimum strain gage locations for accurate determination of the mixed stress intensity factors. *Engineering Fracture Mechanics* (2012), 88,63-78.
5. **K. S. R. K. Murthy, H. Sarangi and D. Chakraborty**, Experimental verification of optimal strain gage locations for determination of mode I stress intensity factors. *Engineering Fracture Mechanics* (Communicated).

Conferences

1. **H. Sarangi, K. S. R. K. Murthy and D. Chakraborty**, Optimum radial locations of strain gage for accurate determination of mode I stress intensity factor in edge cracked plate. *XVII National Seminar on Aerospace Structures* (XVII NASAS-2011), 169-171, IIT Kanpur.

2. **H. Sarangi, K. S. R. K. Murthy and D. Chakraborty**, Upper bound for radial location of a strain gage for determination of SIF in double edge cracked configurations. *Fifth International Conference on Theoretical, Applied, Computational and Experimental Mechanics (ICTACEM-2010)*, ID-229, 587-589, IIT Kharagpur.
3. **H. Sarangi, K. S. R. K. Murthy and D. Chakraborty**, Location of strain gage on eccentric cracked plates for accurate determination of stress intensity factor. *Proceeding of the 4th International Conference on Advances in Mechanical Engineering (ICAME-2010)*, DD-12, 55-59, SVNIT Surat, Gujarat.
4. **H. Sarangi, K. S. R. K. Murthy and D Chakraborty**, Optimum strain gage location for the accurate determination of stress intensity factor. *National Conference on Emerging Trends in Mechanical Engineering, (ETME-2010)*, DE-03, GCET, Gujarat.
5. **H. Sarangi, K. S. R. K. Murthy, G Venktash and D Chakraborty**, Strain gage locations for accurate measurement of the opening mode stress intensity factors; *Proceeding of the International Conference on Emerging Research and Advances in Mechanical Engineering, (ERA-2009)*, DE-12, 454-459, VEC, Chennai.
6. **K. S. R. K. Murthy, H. Sarangi and D. Chakraborty**, Strain gage locations for experimental determination of the stress intensity factors; 3rd Asian Conference on Mechanics of Functional Materials and Structures, (ACMFMS-2012), IIT Delhi (Accepted for presentation and publication).

About the Author

Mr. Hrushikesh Sarangi

Present address:

Associate Professor
Mechanical Engineering Department
I. T. E. R. Bhubaneswar
Bhubaneswar- 751030
Orissa
E-mail: hrushikesh_sarangi@yahoo.co.in
Cell. No: +91-9437538471

Permanent address:

At/ Post- Balia
Via.- Kujanga
Dist.-Jagatsinghpur
Orissa- 754141

Date of Birth: 19.02.1967

Nationality : Indian

Educational Qualifications

H.S.C. : Board of Secondary Education, Orissa
I. Sc. : Utkal University
AMIE : Mechanical Engineering (Institution of Engineers, India)
M.Tech. : Manufacturing Process Engineering
(Indian Institute of Technology Kharagpur)

Experience

Four years **Industrial Experience** in Machine Shop, Metal Casting and Structural Fabrication

Thirteen years **Teaching Experience** in Manufacturing (ITER, Bhubaneswar)